UC Santa Barbara

Title
Understanding the Limitations of Organic Photovoltaics

Permalink
https://escholarship.org/uc/item/92j791v6

Author
Schopp, Nora

Publication Date
2023

Peer reviewed|Thesis/dissertation

UNIVERSITY OF CALIFORNIA

Santa Barbara

Understanding the Limitations of Organic Photovoltaics

A dissertation submitted in partial satisfaction of the

requirements for the degree Doctor of Philosophy in Chemistry

by

Nora Schopp

Committee in charge:

Professor Thuc-Quyen Nguyen, Chair

Professor Mattanjah De Vries

Professor Lior Sepunaru

Professor Yon Visell

March 2023

The dissertation of Nora Schopp is approved.

_____

Professor Lior Sepunaru

_____

Professor Mattanjah De Vries

_____

Professor Yon Visell

_____

Professor Thuc-Quyen Nguyen, Chair

March 2023

Understanding the Limitations of Organic Photovoltaics

Acknowledgements

I am deeply grateful to all the individuals who have crossed my path toward earning my Ph.D. degree. Their encouragement, support, and guidance have made this journey possible for me. I would like to express my deepest gratitude to all of them.

First and foremost, I would like to express my gratitude to the members of my doctoral committee. I am grateful to my advisor Professor Thuc-Quyen Nguyen for having me in her group for the past five years. I am fortunate to have met her and to have had the opportunity to join her group as a visiting master's student. After spending a few months in her group, I knew that I wanted to return as a Ph.D. student. Over the years, she has taught me how to work independently, provided numerous collaborative opportunities, and encouraged me to become a better mentor. Quyen has fostered a supportive and collaborative research group that holds high scientific standards and has created a valuable scientific network. Her emphasis on effective communication and presentation skills has been one of the most valuable outcomes of my Ph.D. I am grateful for her support and guidance.

I am grateful to Professor Lior Sepunaru for his unwavering support throughout my academic journey. He is an exceptional mentor and teacher who challenges the status quo. It has been a pleasure to work with Lior, and I am thankful for his advice and support, especially in challenging times. My appreciation extends to Professor Mattanjah de Vries for his curiosity about my research, for his compassionate approach to addressing graduate students' concerns, and for always having an open-door. Lastly, I would like to thank Professor Yon Visell for his encouragement, for sharing valuable insights into the industry world, and for bringing fresh perspectives from outside the Chemistry and Biochemistry department.

My sincerest gratitude goes to my friends who made my graduate school experience memorable. Your support and care mean a lot to me, and I am grateful to have shared my journey with you. I want to thank Luana Llanes for being invincible, for being fun and genuine, and for being there when I needed her. Đorđe Nikolić for his support in difficult times, for always having time for me, and for wanting me to thrive. Hiba Wakidi, for never getting tired of encouraging me when in doubt and for listening to my countless problems. Arun Chakraborty for sharing his perspectives on life, for his help with teaching, and for having curious, weird, and fun conversations with me. Ana Pedro for her warm friendship, for her countless words of support, and for always believing in me. Ana, and Hiba, I know you are mentioned twice in this acknowledgment. It is not a mistake, you deserve it.

I thank Christina Kerndal, Geoff Jewel, and Lexi for welcoming me into their home. Christina for showing me new sides of Santa Barbara and Geoff for teaching me about local birds, butterflies, and plants. Christina for her help and the mutual support in a time full of challenges. I wish both you and Geoff could come to my defense to celebrate – I know he will join us in spirit.

I want to thank my friends back home who have not forgotten me in the now almost 7 years since I first left Germany. My gratitude goes to Miriam and Joern for welcoming me back every time as if I had never left. I thank my friend Lydia for giving me a feeling of being deeply connected every time we meet, even though these instances have unfortunately become so rare. I am grateful to my irreplaceable friends who have shaped who I have become and who will continue to do so: Lisa, Marie, Nadine, Johanna, Lennalie, Julian, Chi-Fai, and Andreas.

Lastly, I am deeply grateful to my parents for their unwavering support throughout my life. I am thankful to my mom for instilling in me a sense of scientific curiosity from an early age, which ultimately has led me to where I am now. I am thankful for my dad's support while studying,

including the many dinners we prepared together. I need to thank both of them and Eberhard for their visits to California, numerous video calls, and for welcoming me back whenever I go home. I also want to acknowledge my late grandparents, Ursula and Reinhard Wittfeld, for their support. Thank you all for having been a constant source of encouragement and love.

Vita of Nora Schopp

March 2023

Education

2023	Doctor of Philosophy in Materials Chemistry
	University of California, Santa Barbara, United States
2018	Master of Science in Chemistry (Materials and Catalysis)
	RWTH Aachen University, Aachen, Germany
2015	Bachelor of Science in Chemistry
	RWTH Aachen University, Aachen, Germany

Selected Honors & Awards

2023	Feodor Lynen Research Fellowship for Postdocs (declined)
2021-2023	Link Foundation Energy Fellowship for Ph.D. research in the field of sustainable energy technology (acceptance rate < 2.5%)
2022	Outstanding Service to the Department of Chemistry and Biochemistry Award
2022	Individualized Professional Skills Grant (UCSB)
2021	Environmental Solutions Mentorship Award (Schmidt Family Foundation)
2021	Outstanding Service to the Department of Chemistry and Biochemistry Award
2020	Peter J. Frenkel Foundation Fellowship (Institute for Energy Efficiency) in recognition of an outstanding research contribution to the field of energy efficiency and sustainability
2020	Yzurdiaga Graduate Student Fellowship Award for outstanding graduate research within the Departments of Physics, Chemistry, and Biochemistry, and Biology at UCSB
2019	Phi Lambda Upsilon Award (National Honorary Chemical Society) for top academic performance
2018/2019	Regents in Chemistry Fellowship (UCSB) in recognition of an outstanding scholastic record and confidence in productive scholarship
2017/2018	Promos DAAD Mobility Scholarship for master thesis research abroad
2017	ACalNet Workshop Travel Grant to the 2017 Workshop on Sustainable Chemical Manufacturing (Mellichamp Academic Initiative in Sustainable Materials and Product Design)
2016/2017	Germany Scholarship (RWTH Education Fund and the Ministry of Education and Research) for top academic performance
2016/2017	ACalNet Fellowship for research abroad
2015/2016	Dean's List, Chemistry RWTH Aachen (academic performance in top 5%)
2015/2016	Germany Scholarship (RWTH Education Fund and the Ministry of Education and Research) for top academic performance

2014/2015   Germany Scholarship (RWTH Education Fund and the Ministry of Education and Research) for top academic performance

2012/2013   Dean's List, Chemistry RWTH Aachen (academic performance in top 5%)

Peer-Reviewed Publications

1. **<u>Schopp, N.</u>,** Sabury, S., Chaney, T., Zhang, J., Wakidi, H., Kim, B. M., Sankar, R., Luong, H. M., Therdkatanyuphong, P., Brus, V. V., Marder, S., Toney, M. F., Reynolds, J. R., Nguyen, T.-Q. Organic Photovoltaic Performance Resiliency: Role of Molecular Weight in a PM7 Derivative. *To be submitted.*

2. **<u>Schopp, N.</u>,** Abdikamalov· E., Mostovyi, A. I., Parkhomenko E. A., Bazan, G. C., Nguyen, T.-Q., Smoot, G. F., Brus, V. V. Interstellar Photovoltaics. *submitted.*

3. **<u>Schopp, N.</u>,** Akhtanova, G., Panoy, P., Arbuz, A., Chae, S., Yi, A., Kim, H. J., Promarak, V., Nguyen, T.-Q., & Brus, V. V. (2022). Unraveling Device Physics of Dilute-Donor Narrow-Bandgap Organic Solar Cells with Highly Transparent Active Layers. Advanced Materials, 34(31), 2203796. https://doi.org/10.1002/adma.202203796

4. **<u>Schopp, N.</u>,** & Brus, V. V. (2022). A Review on the Materials Science and Device Physics of Semitransparent Organic Photovoltaics. Energies, 15(13), 4639. https://doi.org/10.3390/en15134639

5. **<u>Schopp, N.</u>,** Luong, H. M., Luginbuhl, B. R., Panoy, P., Choi, D., Promarak, V., Brus, V. V., & Nguyen, T.-Q. (2022). Understanding Interfacial Recombination Processes in Narrow-Band-Gap Organic Solar Cells. ACS Energy Letters, 7(5), 1626–1634. https://doi.org/10.1021/acsenergylett.2c00502

6. **<u>Schopp, N.</u>,** Nguyen, T.-Q., & Brus, V. V. (2021). Optical Expediency of Back Electrode Materials for Organic Near-Infrared Photodiodes. ACS Applied Materials & Interfaces, 13(23), 27217–27226. https://doi.org/10.1021/acsami.1c04036

7. **<u>Schopp, N.</u>,** Brus, V. V., Lee, J., Bazan, G. C., & Nguyen, T.-Q. (2021). A Simple Approach for Unraveling Optoelectronic Processes in Organic Solar Cells under Short-Circuit Conditions. Advanced Energy Materials, 11(1), 2002760. https://doi.org/10.1002/aenm.202002760

8. **<u>Schopp, N.</u>,** Brus, V. V., & Nguyen, T.-Q. (2020). On Optoelectronic Processes in Organic Solar Cells: From Opaque to Transparent. *Advanced Optical Materials*, *9* (3), 2001484. https://doi.org/10.1002/adom.202001484

9. **<u>Schopp, N.</u>,** Brus, V. V., Lee, J., Dixon, A., Karki, A., Liu, T., Peng, Z., Graham, K. R., Ade, H., Bazan, G. C., & Nguyen, T.-Q. (2021). Effect of Palladium-Tetrakis(Triphenylphosphine) Catalyst Traces on Charge Recombination and Extraction in Non-Fullerene-based Organic Solar Cells. *Advanced Functional Materials*, 31(15), 2009363. https://doi.org/10.1002/adfm.202009363

10. Yerlanuly, Y., Zhumadilov, R. Y., Danko, I. V., Janseitov, D. M., Nemkayeva, R. R., Kireyev, A. V., Arystan, A. B., Akhtanova, G., Vollbrecht, J., **Schopp, N.**, Nurmukhanbetova, A., Ramazanov, T. S., Jumabekov, A. N., Oreshkin, P. A., Zholdybayev, T. K., Gabdullin, M. T., & Brus, V. V. (2022). Effect of Electron and Proton Irradiation on Structural and Electronic Properties of Carbon Nanowalls. ACS Omega, 7(51), 48467–48475. https://doi.org/10.1021/acsomega.2c06735

11. Solovan, M. M., Mostovyi, A. I., Parkhomenko, H. P., Kaikanov, M., **Schopp, N.**, Asare, E. A., Kovaliuk, T., Veřtát, P., Ulyanytsky, K. S., Korbutyak, D. V., & Brus, V. V. (2023). A High-Detectivity, Fast-Response, and Radiation-Resistant TiN/CdZnTe Heterojunction Photodiode. Advanced Optical Materials, 11(2), 2202028. https://doi.org/10.1002/adom.202202028

12. Brus, V. V., Solovan, M. M., **Schopp, N.**, Kaikanov, M., & Mostovyi, A. I. (2022). Visible to Near-Infrared Photodiodes with Advanced Radiation Resistance. Advanced Theory and Simulations, 5(3), 2100436. https://doi.org/10.1002/adts.202100436

13. Luginbuhl, B. R., Raval, P., Pawlak, T., Du, Z., Wang, T., Kupgan, G., **Schopp, N.**, Chae, S., Yoon, S., Yi, A., Jung Kim, H., Coropceanu, V., Brédas, J.-L., Nguyen, T.-Q., & Reddy, G. N. M. (2022). Resolving Atomic-Scale Interactions in Nonfullerene Acceptor Organic Solar Cells with Solid-State NMR Spectroscopy, Crystallographic Modelling, and Molecular Dynamics Simulations. *Advanced Materials*, *34*(6), 2105943. https://doi.org/10.1002/adma.202105943

14. Du, Z., Mainville, M., Vollbrecht, J., Dixon, A. L., **Schopp, N.**, Schrock, M., Peng, Z., Huang, J., Chae, S., Ade, H., Leclerc, M., Reddy, G. N. M., & Nguyen, T.-Q. Insights into Bulk-Heterojunction Organic Solar Cells Processed from Green Solvent. Solar RRL, 2100213. https://doi.org/10.1002/solr.202100213

15. Brus, V. V., **Schopp, N.**, Ko, S.-J., Vollbrecht, J., Lee, J., Karki, A., Bazan, G. C., & Nguyen, T.-Q. (2021). Temperature and Light Modulated Open-Circuit Voltage in Nonfullerene Organic Solar Cells with Different Effective Bandgaps. *Advanced Energy Materials*, *11*(4), 2003091. https://doi.org/10.1002/aenm.202003091

16. Ouyang, W., Li, Y., Yurash, B., **Schopp, N.**, Vega-Flick, A., Brus, V., Nguyen, T.-Q., & Liao, B. (2020). Transient grating spectroscopy of photocarrier dynamics in semiconducting polymer thin films. Applied Physics Letters, 117(25), 253302. https://doi.org/10.1063/5.0034773

17. Brus, V. V., Ilashchuk, M. I., Orletskyi, I. G., Solovan, M. M., Parkhomenko, G. P., Babichuk, I. S., **Schopp, N.**, Andrushchak, G. O., Mostovyi, A. I., & Maryanchuk, P. D. (2020). Coupling between structural properties and charge transport in nano-crystalline and amorphous graphitic carbon films, deposited by electron-beam evaporation. *Nanotechnology*, *31*(50), 505706. https://doi.org/10.1088/1361-6528/abb5d4

18. Karki, A., Vollbrecht, J., J. Gillett, A., Shuyong Xiao, S., Yang, Y., Peng, Z., **Schopp, N.**, L. Dixon, A., Yoon, S., Schrock, M., Ade, H., Manjunatha Reddy, G. N., H. Friend, R., & Nguyen, T.-Q. (2020). The role of bulk and interfacial morphology in charge generation, recombination, and extraction in non-fullerene acceptor organic solar cells. *Energy & Environmental Science*, *13*(10), 3679–3692. https://doi.org/10.1039/D0EE01896A

19. Karki, A., Vollbrecht, J., Dixon, A. L., **Schopp, N.**, Schrock, M., Reddy, G. N. M., & Nguyen, T.-Q. (2019). Understanding the High Performance of over 15% Efficiency in Single-Junction Bulk Heterojunction Organic Solar Cells. *Advanced Materials*, *31*(48), 1903868. https://doi.org/10.1002/adma.201903868

20. Karki, A., Vollbrecht, J., Gillett, A. J., Selter, P., Lee, J., Peng, Z., **Schopp, N.**, Dixon, A. L., Schrock, M., Nádaždy, V., Schauer, F., Ade, H., Chmelka, B. F., Bazan, G. C., Friend, R. H., & Nguyen, T.-Q. (2020). Unifying Charge Generation, Recombination, and Extraction in Low-Offset Non-Fullerene Acceptor Organic Solar Cells. *Advanced Energy Materials*, *10*(29), 2001203. https://doi.org/10.1002/aenm.202001203

21. Barrett, J. A., Jones, Z. R., Stickelmaier, C., **Schopp, N.**, & Ford, P. C. (2018). A Pinch of Salt Improves n-Butanol Selectivity in the Guerbet Condensation of Ethanol over Cu-Doped Mg/Al Oxides. *ACS Sustainable Chemistry & Engineering*, *6*(11), 15119–15126. https://doi.org/10.1021/acssuschemeng.8b03589

22. Rösener, T., Bienemann, O., Sigl, K., **Schopp, N.**, Schnitter, F., Flörke, U., Hoffmann, A., Döring, A., Kuckling, D., & Herres-Pawlis, S. (2016). A Comprehensive Study of Copper Guanidine Quinoline Complexes: Predicting the Activity of Catalysts in ATRP with DFT. *Chemistry – A European Journal*, *22*(38), 13550–13562. https://doi.org/10.1002/chem.201602223

Theses

Bachelor Thesis: Isoeugenol Functionalized Microgels with Antibacterial Properties
Master Thesis: Characterization of Organic Semiconductor Materials and Devices for Organic Solar Cell Applications with Conductive and Photoconductive Atomic Force Microscopy

Presentations

Material Research Society Fall Meeting Boston, MA, 2022, Poster Presentation
Material Research Society Spring Meeting Honolulu, 2022, Oral Presentation
University of California Chemical Symposium, online, 2021, Oral Presentation
University Potsdam-UCSB Mini-Symposium, online, 2021, Research Talk
Center for Polymers and Organic Solids, Santa Barbara, CA, 2021, Seminar
Center for Polymers and Organic Solids, Santa Barbara, CA, 2020, Seminar
Workshop on Sustainable Chemical Manufacturing, Santa Barbara, CA, 2017, Poster Presentation

Abstract

Understanding the Limitations of Organic Photovoltaics

by

Nora Schopp

Organic Photovoltaics (OPVs) harvest energy directly from sunlight. They comprise a molecular or polymeric carbon-based donor:acceptor blend (bulk heterojunction or BHJ) in between two electrodes. OPVs underwent tremendous progress in the past few years, now reaching Power Conversion Efficiencies (PCEs) of over 19%. In contrast to their well-established inorganic counterparts, OPVs are lightweight, thin, and flexible, and they can be tuned on the molecular level, allowing the modification of color and transparency. These unique properties make OPVs ideal candidates for integrated energy harvesting solutions as their optical tunability and solution-processability are favorable for integration into buildings. However, to date, OPVs do not meet the requirements for widespread commercialization. *I*) High-performing systems suffer from reproducibility challenges due to batch-to-batch variations and *II*) a systematic in-depth understanding of the structure-property relationships is absent. Lastly, *III*) Semitransparent OPVs (ST-OPVs) still suffer from poor performances even though theoretical calculations predict high PCEs even for systems with 100% average visible transmittance (AVT). This work focuses on the understanding of these limitations through a multidimensional approach, including both experimental and simulation-based methods. After an introduction to OPVs in Chapter 1, various techniques used in this work are discussed in Chapter 2. Chapter 3 investigates residual catalysts traces as a possible cause for batch-to-batch variations, addressing *I*) and *II*). The systematic addition of $Pd(PPh_3)_4$ to PTB7-Th:IOTIC-4F devices and its effect on the morphology

and the optoelectronic processes is studied. A drop in performance is observed that is due to altered material properties and different loss mechanisms, but the system showed robustness to 0.75% Pd(PPh$_3$)$_4$, an amount typically not exceeded after purification. Next, Chapter 4 presents a new approach to unravel the optoelectronic processes under short-circuit conditions, facilitating the study of *II)*. We propose a new method to obtain the geminate prefactor P_g, the mobility-lifetime product $\mu\tau$, and the extraction efficiency η, using only standard measurements and simulations. Our simple method also predicts the optimal device configuration and active layer thickness with greater accuracy than optical transfer matrix simulations, providing a fast and cost-effective alternative to the experimental device optimization. The following chapters focus on narrow-band gap ST-OPVs for integrated energy harvesting solutions, addressing *III)*. Chapter 5 identifies changes in ST-OPVs that are concomitant with increased transparency. Reduced generation rates and altered generation rate profiles lead to a reduced open-circuit voltage (V_{oc}) and changes in the recombination dynamics. We show that high-purity and low-trap-density active layers are crucial. Furthermore, transparent devices are sensitive to shunt-leakage, highlighting the need for high-quality active layers even more. The impact of surface recombination decreases with increased AVT and limitations due to high series resistance decrease, suggesting considering a wider range of transparent electrode materials. Chapter 6 focuses on the interfacial recombination in the narrow-band gap system PCE10:COTIC-4F. Our findings indicate that ZnO is the most suitable front electrode due to low interfacial recombination, efficient charge extraction, and favorable energy level alignment. Other electrodes are studied, including ZnO functionalized with PFN-Br, PEDOT:PSS and CPE-K. The present results show that interfacial recombination plays a significant role in narrow band gap OPV systems and future research in this direction will be necessary to overcome the PCE bottleneck arising from surface traps. Lastly, Chapter 7 introduces an experimental approach to obtain OPVs

with highly transparent active layers, addressing *II)* and *III)*. Devices with donor concentrations of 40% to 20% show high average visible transmittance (AVT) values of 64% to 77%. The AVT increases with lower donor concentration due to reduced visible range donor absorption and increased near-IR acceptor absorption. We investigate morphology, charge generation, charge recombination, and charge extraction, and propose further optimization of the interfaces and active layer morphology.

Table of Contents

Chapter 1: Introduction

Energy (Ancient Greek: ἐνέργεια, enérgeia, 'activity', SI unit *joule*) is a conserved physical property; it cannot be created or destroyed. However, energy can be transferred from one system to another through work, the exchange of heat, or light. The complex metabolic processes that sustain living organisms are one of many fascinating examples of energy conversion; without energy, there is no life.

Electricity is one of the most prominent forms of energy. The flow of charged particles, such as electrons, results in an electric current that is associated with electric power. Electric power (SI unit *joule per second* or *watt*) is the rate at which electric energy is transferred in an electric circuit. Electricity is a so-called 'secondary energy source' as it can only be obtained through the conversion of primary energy sources such as coal, petroleum, wind, or solar energy.

Our modern lifestyle relies heavily on electricity in all aspects. It increases our comfort, frees up our time, and allows us to push the boundaries of what humankind is capable of. Electric heating and lighting in buildings gave us independence from nature's rhythm – we stay warm in the winter, and we can read after sundown. Electronic features have increased our safety in the transportation sector and help to created countless automated systems. Information exchange and electronic devices connect and entertain us. All of this would be impossible without electricity.

1.1 The Energy Landscape

The energy landscape in the United States is made of a mix of non-renewable and renewable energy sources and is expected to undergo a shift over the next decades towards more sustainable energy.
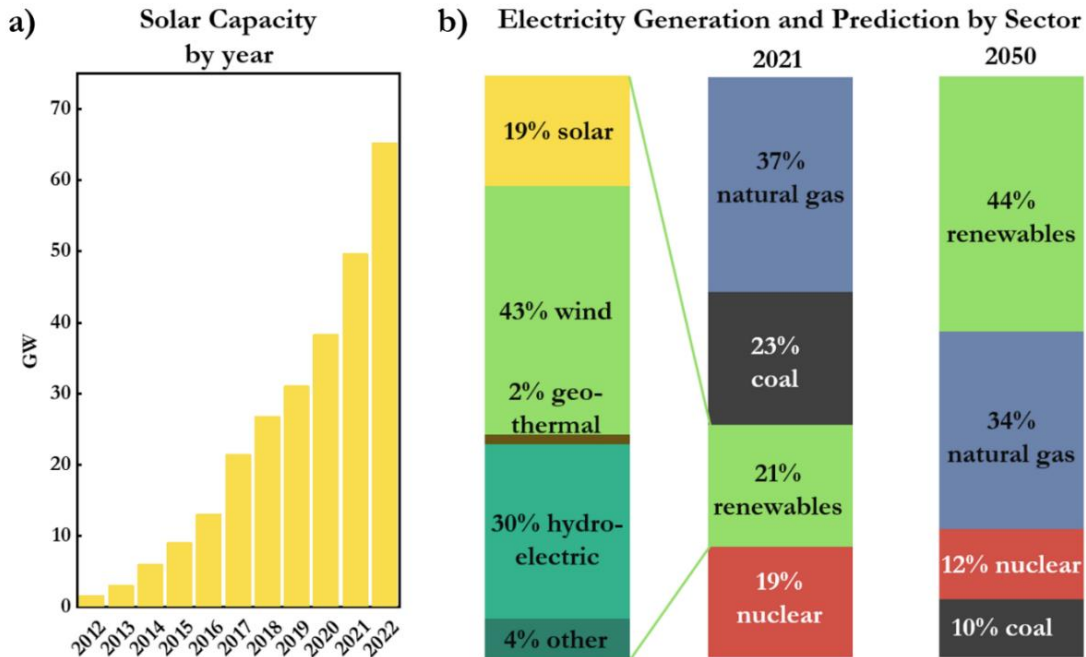
Figure 1.1. a) Rise of the solar capacity in the U.S. b) The Energy Landscape in the United States by technology in 2021 and predicted for 2050. Data obtained from the Annual Energy Outlook 2022 and the US Energy Information Administration.[1,2]

Currently, the energy landscape in the United States is dominated by fossil fuels. Natural gas (methane, CH_4) combustion is the main source of energy and is produced from on- and off-shore natural gas and oil wells and coal beds, making up 37% of the total electricity generation Natural gas is followed by coal, contributing with 23% significantly to the total electricity generation as well. Coal is a carbon- and carbon hydrate-rich substance, formed over millions of years from plants under pressure and heat.[3,4] Due to its carbon-rich composition, its combustion releases large quantities of carbon dioxide (CO_2) into the atmosphere. It is well understood that carbon dioxide is a main driving force for climate change and that CO_2 emissions need to be reduced or eliminated to mitigate the climate crisis. In addition, the burning of coal leads to emissions that pose a serious health hazard to the public that has been linked not only to respiratory symptoms but also to cardiovascular diseases, resulting in increased mortality.[5–7] CO_2 emissions can be reduced by about 50% when switching from coal to natural gas for electricity production. While

not providing a long-term answer to the climate crisis, an immediate reduction of emissions is necessary and thus natural gas plays a critical role in the transition to a sustainable energy landscape.[8]

One way to generate CO_2 emission-free electricity is through nuclear power. As of 2021, 19% of the electricity in the US is generated through nuclear fission, the process in which large quantities of energy are released due to the splitting of heavy atomic nuclei. In this process, a neutron splits a heavy atom such as uranium into lighter atoms, releasing energy in form of heat and radiation and new neutrons. These neutrons then collide with other uranium atoms, leading to a chain reaction.[9] While sometimes considered a technology that can help mitigate climate change, utility-scale nuclear power has very limited potential to contribute to a sustainable future.[10–12] Not only are uranium sources limited, but also a growing social opposition, complex licensing, and long-term costs are major bottlenecks.[12] It can furthermore be argued that no complex case studies are needed to underline that nuclear power is everything but an environmentally friendly solution to the climate crisis, since modern history has shown repeatedly that we are incapable of controlling nuclear technology reliably. Nuclear accidents have resulted in detrimental environmental impacts and adverse health outcomes for millions of people due to radiation.[13–16] Furthermore, waste management bears unforeseeable intergenerational conflicts due to the necessity of extremely long-term ($\approx$ 10,000 years) solutions.[17,18] Thus, while possibly 'cheap' for the energy provider, nuclear power comes with incredibly high long-term costs.

In contrast to the above-discussed non-renewable energy sources, each coming with their own drawbacks, renewable energy sources such as wind and solar pose low risks for the population and environment. These energy sources combined account for about 21% of the total energy generation.[1] The largest share of the renewable energy production goes to wind energy (43%), followed by hydro-electric (30%) and solar energy (19%).[1] Renewable energy sources can

contribute to minimizing the further rise of the global temperatures by reducing emissions. The drastic change in climate is caused by the emission of greenhouse gases, which leads to an expected temperature rise of about $1.5 - 5$ °C by 2050 with detrimental outcomes.[19,20] The increase in temperature comes with negative impacts on agriculture and ecosystems, an increase of extreme weather events, increased mortality due to heat-related deaths, as well as various socio-economic impacts.[21–23] Renewables play a critical role in meeting the climate goals established by the 2015 United Nations Climate Change Conference in Paris (COP21) aiming to keep global temperatures < 2 °C above pre-industrial levels. To meet the goals, renewable energy technologies can be implemented with a mix of an increased energy-efficiency, reforestation, changes in agriculture and manufacturing, electrification of transport and buildings, and potentially carbon-capture technology.

In the case of wind energy, wind directly generates electricity in a wind turbine and in the case of hydro-electric power turbines are moved by the flow of water, for example a river or a waterfall. Both technologies have a low footprint, mainly related to the manufacturing and installation of the turbines. Critics of these renewable technologies cite concerns about the local ecosystems; however, these risks must be assessed in comparison to the global long-term environmental impacts that come with non-renewable technologies. Wind and hydro-electric power generation are emission free after construction and installation of the turbines, offer low-cost energy, and thus can contribute to a shift to clean energy production. Wind is the result of uneven heating though solar energy, thus can be considered a secondary form of solar energy, that is constantly replenished. Both on-shore and off-shore wind parks exist for utility-scale power generation. While providing clean energy, low-frequency noise concerns and the impact on the scenery are often cited by critics of this technology and wind power fluctuation lead to uncertainty and pose a challenge for grid integration.[24–26]

Hydro-electric power can be stored by pumping water into higher elevation reservoirs, that can then be released later. The adaptability to demand is a big advantage of this technology, however, the construction of dams can impact the local environment, require relocation of populations and harm biodiversity.[27] Therefore, a sustainable development of hydropower is crucial. If done right, this technology can play a big part in sustainable electricity generation and can help meet the electricity need in developing countries.[27–29]

Geothermal, bio energy, and marine energy make up small fractions of the energy landscape. The remaining 19% of the renewable energy production originates from solar power, that harvests energy from sunlight. Solar energy includes electricity generation with photovoltaic (PV) panels or through mirrors that concentrate solar radiation (solar concentrators). The former convert electromagnetic radiation into electricity though the photoelectric effect and the latter convert the energy into heat, which can then be used to produce electricity or stored for later use. Solar energy is cost-effective and underwent enormous growth in the past decade, as illustrated in **Figure 1.1a**. Due to this special role of photovoltaic technology and its central position to this work, the next sub-chapters will be dedicated to solar energy and PV technology.

1.2 Solar Energy and the Solar Spectrum

The energy of the sun reaches the earth in the form of electromagnetic radiation. The temperature in the core of the sun is about $1.5 \cdot 10^7$ K. At such a high temperature atoms form plasma, a mix of ions and electrons, and nuclei move fast enough to collide and fuse, releasing large amounts of energy in the form of radiation.[30] The sun's electromagnetic radiation is partially absorbed in the earth's atmosphere. The remaining radiation that reaches the earth's surface is described by the AM1.5 spectrum (red), shown in **Figure 1.2**. The spectral intensity depends on the wavelength and constitutes IR-radiation, visible light, and UV radiation. Visible light is the

part of the electromagnetic spectrum in the wavelength region between 380-780 nm and the sensitivity of the human eye is described by the so called photopic response function $V(\lambda)$ (black).
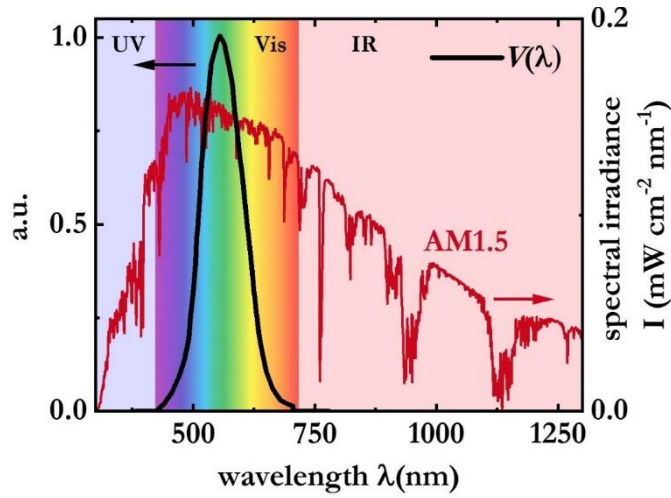
Figure 1.2. AM1.5 spectrum and the photopic response V in different wavelengths regions.

Because of the wave-particle duality, the radiation can be described as particles (photons) with a certain momentum p, or as waves with a certain wavelength λ, convertible according to the *de Broglie formula* $\lambda = h/p$ where h is the *Planck constant*.

$$E = h\,\nu = h\frac{c}{\lambda} \tag{1.1}$$

The energy E of a single photon is proportional to its frequency ν, or to the speed of light c divided by the wavelength λ. Photovoltaic cells convert this energy into electricity.

1.3 Photovoltaic Technologies

The photoelectric effect describes the observation of the emission of photo electrons upon irradiation of a material with electromagnetic radiation. The discovery of the photoelectric effect in 1839 by Becquerel laid the groundwork for solar energy generation. A few decades later, in

1888, the first patents (U.S. 389124 and U.S.389125) for solar cells were issued to Ed. Weston.[31,32] Then, in the 1950s, intense research efforts at Bell labs led to the first photovoltaic cell based on Si, reaching photoconversion efficiencies (PCEs) of 4%.[33] The PCE describes the fraction of solar power that is converted to electric power. Within few years, the PCEs increased to 14% (1960) and solar cells became a viable technology with their first applications in satellite and space technology.[34] Since then, the PV field has evolved dramatically. A large spectrum of different technologies has emerged, including inorganic single-crystal and polycrystalline Si cells, CdTe-based cells, GaAs-based cells, polycrystalline thin-film photovoltaics, as well as perovskite, dye-sensitized, and organic photovoltaics (OPVs)[35–37] **Figure 1.3** shows the evolution of the record laboratory cell efficiencies for technologies based on different semiconductor materials.
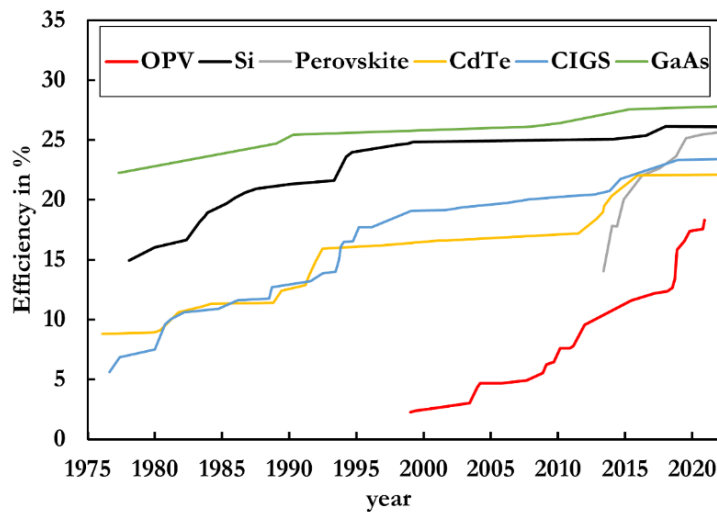
Figure 1.3. Solar cell efficiency timeline. Adapted from the NREL Best Research-Cell Efficiency Chart.[37] Si and GaAs data shown is for single crystal cells.

Inorganic solar cells are based on Si, CdTe, CuInGaSe (CIGS) or GaAs. Single crystal Si cells are the most common type, making up about 95% of the sold PV modules.[38] They feature PCEs of over 25% and offer long-term stability of 25+ years at costs that have steadily declined in the past decade[39,40]. Thanks to the abundance of Si and the maturity of the technology, Si solar cells

can nowadays be found in many places worldwide. Besides utility-scale power generation, they can serve off-grid applications such as parking meters, portable chargers, or streetlights and they can be integrated into buildings, greenhouses, or vehicles. They also play an important role in the electricity generation and (waste-)water treatment in developing countries.[41–55]

The second most common PV technology are CdTe-based PVs, which reach PCEs of up to 22%.[37] CdTe, in contrast to Si, is a direct band gap semiconductor material with an optimal band gap of about 1.5 eV to harvest energy from sunlight, therefore only thin ($\approx$ 1 µm) films are needed. In a direct band gap semiconductor, the momentum of electrons and holes at the top of the valence band and the bottom of the conduction band are the same, and absorption can occur easily. In contrast, in an indirect band gap material an electron must interact not only with the photon to gain energy, but also with a lattice vibration called a phonon in order to either gain or lose momentum. Light can therefore penetrate farther before being absorbed in an indirect band gap material than a direct band gap material.[56]

CdTe modules can be manufactured at low costs with even shorter payback times than for Si.[57] In contrast to Si, CdTe modules are not subject to photodegradation and degradation at elevated temperatures, bearing an important advantage in harsh conditions (module operating conditions: −40 to 85 °C).[57,58] Moreover, CdTe is upcycled from mining waste and recycling of the material at the end of the panel lifetime lowers the environmental impact.[57] Due to its stability, toxicity concerns are minimal. Thanks to these advantages and the improvements in the PV design, the market share of CdTe is expected to grow in the next years.[59]

Copper indium diselenide ($CuInSe_2$) also called CIGS cells are another thin-film PV technology. These cells show high efficiencies of about 20% in the lab, however, the transition from lab to manufacturing remains challenging and commercial modules have efficiencies of 12-

14%.[60,61] GaAs PV are expensive due to epitaxial growth of the III-V semiconductor, but high performing, thus a good option for space applications.[62] They reach PCEs of up to 30.8%.[37]

Perovskite PVs are an emerging thin-film technology. Thanks to their solution-processability they can be printed, spin-coated, or vacuum-deposited onto a substrate. The technology underwent impressive progress in the past decade and PCEs that are comparable with the inorganic technologies have been reached (current record 25.7%).[63,64] Perovskite PVs are named after the crystal structure of the hybrid organic-inorganic photoactive material, which contains lead, leading to environmental concerns.[63,64] In contrast, organic PV are lead free and are based on carbon-based molecules and polymers. The next chapter will describe this technology in detail.

1.4 Organic Photovoltaics

Organic Photovoltaics are a thin-film PV technology that relies on carbon-based photoactive materials. In contrast to their inorganic counterparts, they are solution-processable, lightweight, thin, flexible and tunable on the molecular level, enabling the modification of color and transparency.[55,65,66] OPVs promise cost-effective and environmentally friendly energy harvesting from sunlight and are prime candidates for new integrated energy-efficient solutions.[65,67–69] However, to compete with their inorganic counterparts, OPVs still need to overcome several challenges. The following sub-chapters introduce the photoactive materials and the working principle of OPV devices.

1.4.1 Organic Semiconductors

Organic PVs rely on organic semiconductors that are of molecular or polymeric nature. The carbon-based molecules exhibit semiconducting properties due to their specific electronic configuration.[70–72] The first observation of electronic conductivity in organic materials was made

9

on anthracene crystals in the early 20th century.[70,73] In 2000, the Nobel prize in Chemistry was awarded to Alan J. Heeger, Alan G. MacDiarmid and Hideki Shirakawa '*for the discovery and development of conductive polymers'*.[74] The field has evolved since, and a plethora of organic semiconducting molecules is known, ranging from small molecules to oligomers and polymers. They all have a so-called *conjugated π-electron system* in common, that arises from alternating carbon-carbon single and double bonds.
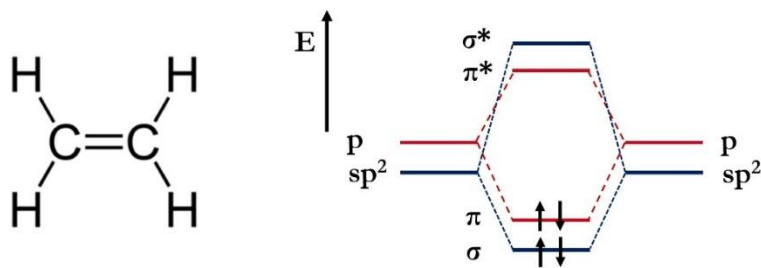
Figure 1.4. Chemical structure of ethene and its molecular orbital diagram.

The simplest example of a molecule with a double bond is ethene, which can be polymerized to polyethylene (see **Figure 1.4**). In ethene, the C-atoms are sp^2-hybridized and each C-atom forms two σ-bonds with H-atoms and one with the neighboring C atom.[55,70,75] Carbon, being positioned in group 4 in the periodic table, has four valence electrons. Thus, one electron remains unhybridized in the p_z orbital. These p_z electrons overlap and form the conjugated, delocalized systems of electrons that is responsible for the semiconducting properties.[76] The interactions of the p_z orbitals give weaker bonding (π) and antibonding (π*) energy levels than the σ-σ bonds (smaller split in the molecular orbital scheme). As a result, the highest occupied molecular orbital (HOMO) and the lowest unoccupied molecular orbital (LUMO) correspond to the bonding π-orbital and anti-bonding π* orbitals. Commonly, only the π and π* are depicted for simplicity.
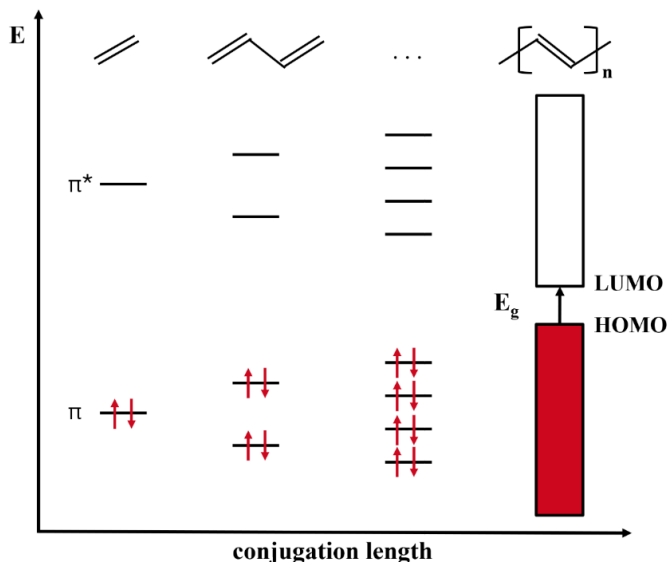
Figure 1.5. Chemical structures of ethene, 1,3-butadiene, and polyethylene (top) and schematic representation of their π and π^* orbitals, demonstrating the band gap narrowing with extended conjugation length.

When polymerizing ethene to polyethylene, first a dimer is formed (1,3-butadiene). In this case, the molecule has two double bonds and four π-electrons. For each additional repeat unit, the conjugated system is extended by two additional π-electrons. Figure 1.5 shows schematically how the degree of polymerization impacts the electronic structure. For *n* repeat units, *n* π-orbitals are formed. By the laws of quantum mechanics, these cannot be degenerate and must have distinct energies.[56,77] As more and more repeat units are added, the energetic difference between each energy level becomes smaller and smaller. Eventually, in a polymeric material, the energy differences become infinitesimal small and quasi-continuous bands are formed. The HOMO level can therefore be seen as an analogue to the top of the valence band and the LUMO as an analogue to the bottom of the conduction band in inorganic semiconductors. It becomes furthermore evident, that the gap between the HOMO and LUMO shrinks with extension of the conjugation length.[55,78] This HOMO-LUMO gap is also referred to as the band gap E_g, a fundamental material

parameter for semiconductors that defines the material's interaction with light and its conductivity.
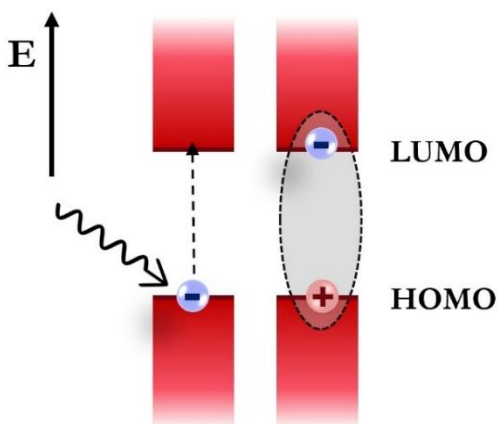
Figure 1.6. Schematic illustration of the interaction of light with an organic semiconductor and promotion of an electron from the HOMO to the LUMO, forming a coulombically bound exciton.

Upon irradiation with light that has an energy larger than the band gap, an electron is excited from the HOMO to the LUMO level. In organic semiconductors, a coulombically bound electron-hole pair is formed, a so-called exciton, as shown in **Figure 1.6**.[79,80] In the case of inorganic semiconductors, free charge carriers (not coulombically bound electrons and holes) are generated immediately upon charge excitation due to higher dielectric constants (more screening of the charges), corresponding to small exciton binding energies. Organic semiconductors however have low dielectric constants of $\varepsilon \approx$ 2-3, meaning that the electron and hole are initially coulombically bound and therefore possess a large exciton binding energy.[81,82] To overcome this large exciton binding energy, so called bulk heterojunction solar cells have been developed that are comprised of a blend of two organic semiconductor materials: a donor and an acceptor material. The blend forms a percolating network with large interfacial areas of the donor- and acceptor-rich domains. At the interfaces, charges can separate into free charge carriers.[79,83,84] A more detailed explanation can be found in the following sub-chapter 1.4.2.
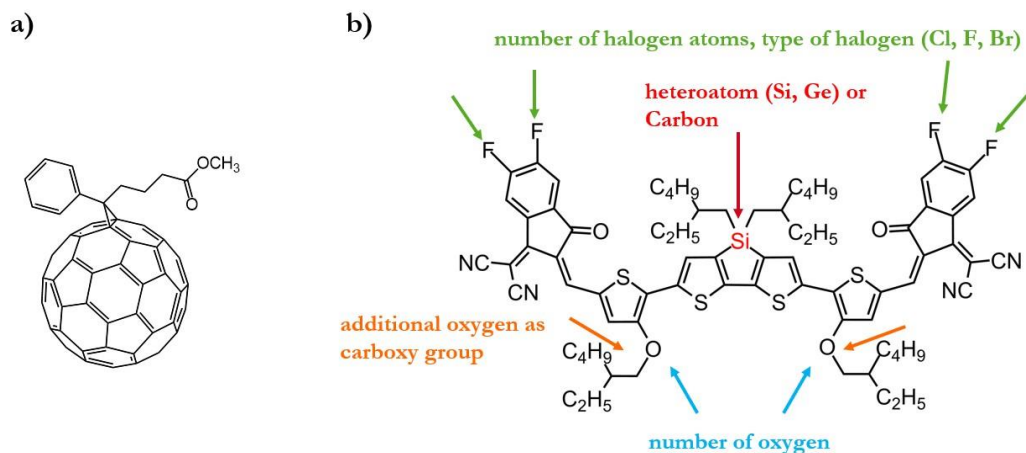
Figure 1.7. a) Chemical structure of the fullerene acceptor $PC_{61}BM$. b) Chemical Structure of the non-fullerene acceptor COTIC-4F and examples of chemical modifications.

Common donor polymers are P3HT, PTB7-Th, PM6, and PM7, to name a few. These donor polymers are more electron-rich than the acceptor molecules they are paired with. In the past, OPVs relied on so called fullerene acceptors.[85–87] Nowadays, so called non-fullerene acceptors (NFAs) outperform fullerene acceptors thanks to strong absorption, ease of synthesis, improved stability, solubility, and crystallinity, as well as lower energy losses.[66,88,89] The transition to NFAs has improved the PCEs tremendously and thanks to the chemical design freedom of the newer class of acceptors, the materials can be fine-tuned for an optimal OPV performance.[66,88,89]

1.4.2 OPV Device Structure and Working Principle

The mixture of donor and acceptor in a BHJ solar cell is called the *photoactive layer* or simply the *active layer*. It is placed between two electrodes, an anode (hole extraction) and a cathode (electron extraction), as shown in **Figure 1.8a**. The BHJ blend forms a percolating network of donor and acceptor domains that can vary in domain size, the domain purity, the degree of mixing, the crystallinity, and the molecular packing.[90–93] These aspects of the BHJ layer are called

morphology. Morphology plays a critical role in the device performance and a set of techniques exists to address these material characteristics.
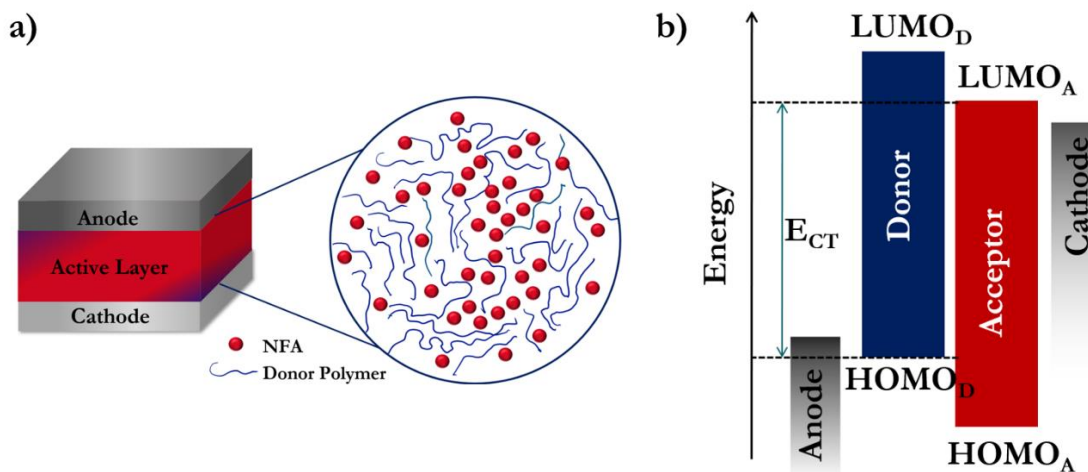
Figure 1.8. a) Schematic device structure of a BHJ solar cell. b) Energy level diagram of the solar cell.

Figure 1.8b shows a schematic of the energy diagram of an organic solar cell. The HOMO and LUMO of the donor and acceptor molecules as well as the energy levels of the respective electrodes align in such way, that a photogenerated electron can cascade down from the LUMO of the donor to the LUMO of the acceptor and to the cathode. Electrons lose energy as they cascade down in the potential energy landscape, holes lose energy when they move up. Likewise, a hole can move up in the energy gradient from the HOMO of the acceptor to the HOMO of the donor and to the anode. Note, that the energy levels for the anode and cathode, which are conductive materials, represent their Fermi levels.[94] It becomes evident that the selection of suitable material combinations and suitable electrode materials is critical to obtain a working device.
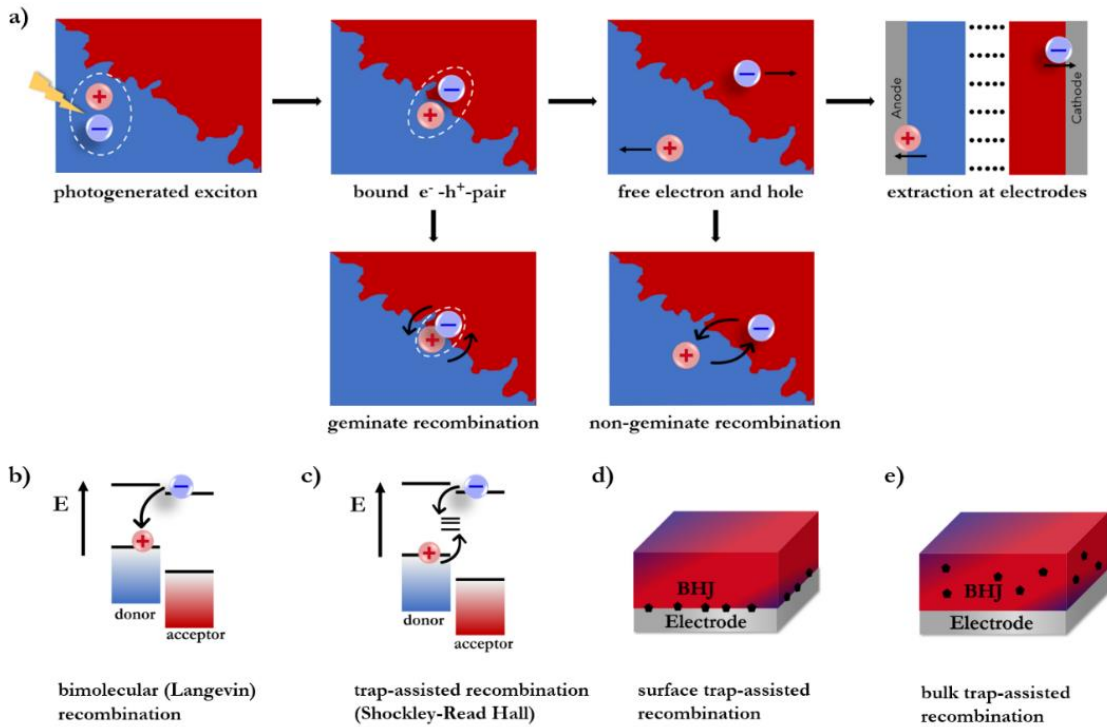
Figure 1.9. a) Schematic illustration of the optoelectronic processes in an OPV. b) schematic representation of bimolecular and c) trap-assisted recombination. d) Illustration of surface traps and e) bulk traps, both causing trap-assisted recombination.

Upon shining light onto the device, a photogenerated exciton is formed, which is coulombically bound, as discussed above. It migrates to the interface of a donor- and an acceptor-rich domain, where it can split into free electron and hole. The electron migrates though the acceptor material and the hole though the donor material until the charge carriers are extracted at the respective electrodes to perform work in the outer circuit.[75,86] This is the ideal description of the optoelectronic processes, shown in **Figure 1.9a** in the top row. In reality, different recombination loss mechanisms can occur. First, the bound electron hole pair can recombine before the charge carriers split apart. This type of recombination of charge carriers that originated from the same photo-excitation is called *geminate recombination*.[95–98]

The recombination of free electrons and holes (from different photo-excitations) is summarized as *non-geminate recombination*. Different subcategories of non-geminate recombination

15

are shown in Figure 1.9b-e. *Bimolecular recombination* occurs when free electron and free hole meet in the blend and annihilate each other. When one of the charge carriers is localized in a trap state and the other charge carrier migrates though the blend to meet and recombine with the trapped charge carrier, it is referred to as trap-assisted recombination.[99–102] Trap-assisted recombination can further be sub-divided into bulk trap-assisted recombination and surface trap-assisted recombination, depending on the location of the traps. Trap states are any energy levels in the band gap of the photoactive blend. They can be of different origin, for example, they can be due to chemical impurities such as catalyst residues or synthesis side products, due to oxygen and water contamination, or due to morphological irregularities.[100,103–105]

The sum of these optoelectronic processes and the recombination contributions govern the solar cell efficiency (see section 2.3). They can be probed though various experimental techniques that are discussed in Chapter 2:.

1.5 Summary of Chapters

Chapter 2: Material and Device Characterization

Chapter 2 provides an overview of common OPV characterization techniques. It provides the reader with the fundamental background information about the techniques used in this dissertation work. Morphological characterization, optical characterization, electrical characterization, determining energy levels, and probing recombination losses are covered.

Chapter 3: Effect of Palladium-Tetrakis(Triphenylphosphine) Catalyst Traces on Charge Recombination and Extraction in Non-Fullerene-based Organic Solar Cells

The effect of the cross-coupling catalyst tetrakis(triphenylphosphine)palladium(0) (Pd(PPh$_3$)$_4$) on the performance of a model organic bulk-heterojunction solar cell composed of a blend of

poly([2,6'-4,8-di(5-ethylhexylthienyl)benzo[1,2-b;3,3-b]dithiophene]{3-fluoro-2[(2-ethylhexyl)carbonyl]thieno[3,4-b]thiophenediyl}) (**PTB7-Th**) donor and 3,9-bis(2-methylene-((3-(1,1-dicyanomethylene)-6,7-difluoro)-indanone))-5,5,11,11-tetrakis(4-hexylphenyl)-dithieno[2,3-d:2',3'-d']-s-indaceno[1,2-b:5,6-b']dithiophene (**IOTIC-4F**) non-fullerene acceptor is investigated. (Pd(PPh$_3$)$_4$) is commonly used in the synthesis of organic semiconductor materials. The effect of intentional addition of different amounts of Pd(PPh$_3$)$_4$ on morphology, free charge carrier generation, non-geminate bulk trap- and surface trap-assisted recombination as well as bimolecular recombination and charge extraction is quantified. This work shows that free charge carrier generation is affected significantly, while the impact of Pd(PPh$_3$)$_4$ on non-geminate recombination processes is limited because the catalyst does not facilitate efficient trap-assisted recombination. The studied system shows substantial robustness towards the addition of Pd(PPh$_3$)$_4$ in small amounts.

Chapter 4: A Simple Approach for Unraveling Optoelectronic Processes in Organic Solar Cells Under Short-Circuit Conditions

The short-circuit current (J_{sc}) of organic solar cells is defined by the interplay of exciton photogeneration in the active layer, geminate and non-geminate recombination losses and free charge carrier extraction. The method proposed in this work allows the quantification of geminate recombination and the determination of the mobility-lifetime product ($\mu\tau$) as a single integrated parameter for charge transport and non-geminate recombination. Furthermore, the extraction efficiency is quantified based on the obtained $\mu\tau$ product. Only readily available experimental methods (current-voltage characteristics, external quantum efficiency measurements) are employed, which are coupled with an optical transfer matrix method simulation. The required optical properties of common organic photovoltaic (OPV) materials are provided in this work.

The new approach is applied to three OPV systems in inverted or conventional device structures, and the results are juxtaposed against the $\mu\tau$ values obtained by an independent method based on the voltage–capacitance spectroscopy technique. Furthermore, it is demonstrated that the new method can accurately predict the optimal active layer thickness.

Chapter 5: On Optoelectronic Processes in Organic Solar Cells: From Opaque to Transparent

ST-OPVs promise integrated, sustainable, low-cost energy harvesting solutions. However, current efficiency limitations must be overcome to make ST-OPV a competitive technology. In this simulation-based work, the effect of the selective transparency on the photoelectronic processes in ST-OPVs is studied and changes in the generation–recombination dynamics and the extraction efficiency are demonstrated that are causally linked to the increased transparency. The study of five model systems with transparent indium tin oxide (ITO) back electrodes and systematically varied extinction coefficients and an opaque cell with Ag back contact allows to quantify these changes in the photoelectronic processes. We further address the role of the series and the shunt resistors while keeping all other parameters of the modeled devices identical. The findings demonstrate the increased importance of the active layer quality in ST-OPVs and indicate that ST-OPVs benefit from a wider choice of transparent electrode materials.

Chapter 6: Understanding Interfacial Recombination Processes in Narrow Band Gap Organic Solar Cells

Recombination losses in OPVs remain a performance-limiting factor, including bulk trap-assisted recombination and interfacial recombination at the electrode:active layer interface. In this work, we demonstrate the role of the front electrode:active layer interface in a narrow-band-gap system,

PCE10:COTIC-4F, a promising candidate for semitransparent organic photovoltaics. We systematically address charge generation, recombination, and extraction, with a focus on interfacial recombination via surface traps by a comparison of four device structures with electrodes based on ZnO, ZnO/PFN-Br, PEDOT:PSS, and a self-doped conjugated polyelectrolyte (CPE-K). The amount of interfacial recombination is affected significantly by the electrode choice, while similar levels of bulk recombination are maintained. For the studied blend, we identify ZnO as a suitable choice, as it pairs low surface recombination rates with beneficial charge carrier generation, favorable energy level alignment, and efficient extraction. In contrast, PEDOT:PSS-based devices suffer from increased interfacial recombination, which can be suppressed when CPE-K is used instead.

Chapter 7: Unraveling Device Physics of Dilute-Donor Narrow Band Gap Organic Solar Cells with Highly Transparent Active Layers

The charge generation–recombination dynamics in three narrow band gap near-IR absorbing non-fullerene (NFA) based OPV systems with varied donor concentrations of 40%, 30%, and 20% are investigated. The dilution of the polymer donor with visible-range absorption leads to highly transparent active layers with blend average visible transmittance (AVT) values of 64%, 70%, and 77%, respectively. Opaque devices in the optimized highly reproducible device configuration comprising these transparent active layers lead to PCEs of 7.0%, 6.5%, and 4.1%. The investigation of these structures yields quantitative insights into changes in the charge generation, non-geminate charge recombination, and charge extraction dynamics upon dilution of the donor. Lastly, this study gives an outlook for employing the highly transparent active layers in ST-OPVs.

1.6 Permissions and Attributions

Chapter 3: Effect of Palladium-Tetrakis(Triphenylphosphine) Catalyst Traces on Charge Recombination and Extraction in Non-Fullerene-based Organic Solar Cells

The contents of chapter 3 previously appeared in N. Schopp, V. V. Brus, J. Lee, A. Dixon, A. Karki, T. Liu, Z. Peng, K. R. Graham, H. Ade, G. C. Bazan, T.-Q. Nguyen, *Advanced Functional Materials* 2021, *31*, 2009363. The contents have been reproduced with permission from John Wiley and Sons (license #5470930977045).

Chapter 4: A Simple Approach for Unraveling Optoelectronic Processes in Organic Solar Cells Under Short-Circuit Conditions

The contents of chapter 4 previously appeared in N. Schopp, V. V. Brus, J. Lee, G. C. Bazan, T.-Q. Nguyen, *Advanced Energy Materials* 2021, *11*, 2002760. The contents have been reproduced with permission from John Wiley and Sons (license #5470930460732).

Chapter 5: On Optoelectronic Processes in Organic Solar Cells: From Opaque to Transparent

The contents of chapter 5 previously appeared in N. Schopp, V. V. Brus, T.-Q. Nguyen, Advanced Optical Materials 2021, 9, 2001484. The contents have been reproduced with permission from John Wiley and Sons (license #5472691507149).

Chapter 6: Understanding Interfacial Recombination Processes in Narrow Band Gap Organic Solar Cells

The contents of chapter 6 previously appeared in N. Schopp, H. M. Luong, B. R. Luginbuhl, P. Panoy, D. Choi, V. Promarak, V. V. Brus, T.-Q. Nguyen, *ACS Energy Lett.* 2022, *7*, 1626.

The contents have been reprinted with permission from ACS publications, the American Chemical Society.

Chapter 7: Unraveling Device Physics of Dilute-Donor Narrow Band Gap Organic Solar Cells with Highly Transparent Active Layers

The contents of chapter 7 previously appeared in N. Schopp, G. Akhtanova, P. Panoy, A. Arbuz, S. Chae, A. Yi, H. J. Kim, V. Promarak, T.-Q. Nguyen, V. V. Brus, *Advanced Materials* 2022, *34*, 2203796. The contents have been reproduced with permission from John Wiley and Sons (license #5470931075576).

Chapter 2: Material and Device Characterization

2.1 Morphological Characterization

The morphological features of BHJ blends impact the device performance by influencing charge generation, recombination, transport, and extraction.[91,106] Morphology is an overarching term for the various aspects of the orientation and distribution of the materials in the three-dimensional volume of a film, including the features of the percolating donor-acceptor network, the phase separation, domain size and purity, film roughness, the order, crystallinity, and the molecular interactions. The understanding of these features in the nm- and µm-scale can pose a challenge and special techniques are necessary to gain insights into the different morphological aspects which can guide the material and device development. This chapter serves as an overview of various morphological characterization techniques that are used in the OPV field.

2.1.1 AFM, c-AFM and pc-AFM

2.1.1.1 AFM

Atomic Force Microscopy (AFM) is a technique to probe the surface morphology on the nanometer-scale. In AFM, an atomically sharp tip is mounted on a cantilever that scans the film's surface, schematically shown in **Figure 2.1**.

A laser beam is reflected at the cantilever which then hits a photodetector. Depending on the local height of the surface of the sample, the cantilever is positioned in a different angle and the laser beam is deflected to a different location on the position sensitive photodetector (PD). This way, information about the surface height can be deducted, giving the topography image. This mode of AFM is called contact mode.[107,108]
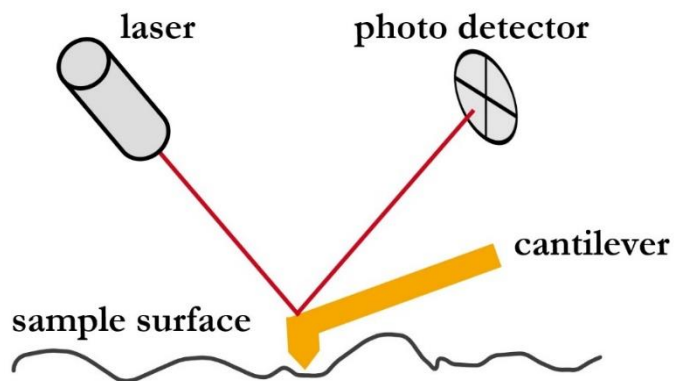
Figure 2.1. Schematic of an AFM setup in contact mode.

The AFM can also operate in tapping-mode. In this case, the tip oscillates near its resonance frequency while scanning the surface. Changes in the oscillation amplitude are measured, which are related to the sample-tip interaction, and the topography information is obtained.[109,110] Various examples of tapping-mode and contact-mode AFM images can be found in the following chapters. Their roughness-mean-square value is commonly reported as a measure for the surface roughness. It can be obtained with various image editing software packages, such as with Gwyddion.[111]

2.1.1.2 c-AFM and pc-AFM

Conductive-AFM or c-AFM is a variation of the contact-mode AFM technique in which a conductive probe is used. The probe can collect or inject charge carriers from/into the sample. While scanning the surface, not only a topography image but also a current image is obtained. If the c-AFM setup has the addition of a light source than can illuminate the sample from the bottom through a transparent substrate, photo-conductive AFM (pc-AFM) measurements can be carried out.[112–115] In c-AFM and pc-AFM, both the tip and the substrate must be conductive.

This technique has the unique benefit of visualizing donor- and acceptor rich domains in a BHJ blend of a solar cell. Typically, a high work function tip (Au or Pt/Ir) scans the BHJ film

which must be deposited on a conductive substrate. A small positive bias can be applied to the sample to direct the flow of photogenerated electrons toward the substrate. As the high work function tip collects holes from the blend, a high photocurrent signal corresponds to efficient hole extraction from a donor-rich domain. Consequently, low photocurrent signals correspond to the collection of electrons from acceptor-rich domains.

2.1.2 GIWAXs

GIWAXs stands for *Grazing Incidence Wide Angle X-ray Scattering.* This technique belongs to the scattering techniques and gives insights into the molecular orientation (face-on or edge-on), crystalline lattice spacing, crystalline correlation length (CCL) and the relative crystallinity.[116] The drawback of this technique is that it only probes the crystalline regions of the film.

In contrast to AFM, GIWAXs probes the bulk morphology. Because of the translation to the reciprocal space, large scattering vectors correspond to small distances and *vice versa*. As a result, the small π-π stacking distance in the horizontal plane in a face-on orientation correspond in large q_z vectors. A schematic illustration of typical GIWAXs images obtained for a purely face-on and edge-on orientation is shown in **Figure 2.2.** Detailed descriptions of the technique and its applications can be found in the literature.[116–118]
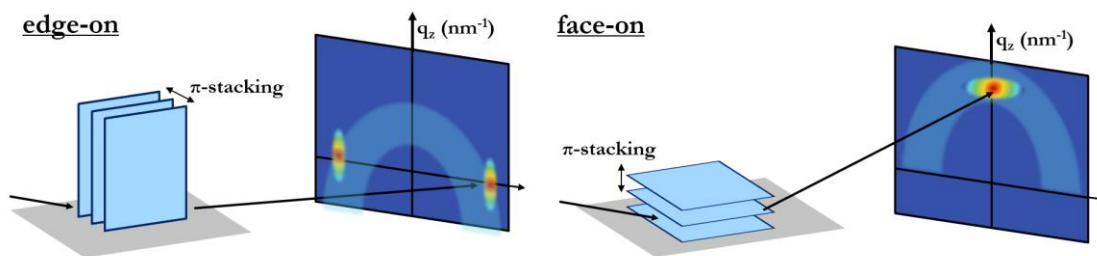
Figure 2.2. Schematic drawings of edge-on and face on oriented crystal planes and the resulting GIWAXs patterns.

2.1.3 Transmission Electron Microscopy

Transmission electron microscopy (TEM) provides detailed information about the structural characteristics on the nanoscale, which cannot be resolved with optical microscopy. The technique relies on the interactions of a high energy electron beam with the sample. These accelerated electrons have a very small de Broglie wavelength λ_B (λ_B= h/p, with p being the momentum), allowing to probe nanoscale features that cannot be resolved with visible light due its much larger wavelengths. For example, if the incoming electron beam has an energy of 100 keV, the corresponding wavelength of the electrons 3.88 pm. In comparison, visible light falls in the wavelength region between 380 nm and 780 nm.[119]

The electron beam passes through a thin sample, such as a thin film (<100 nm) deposited on a TEM grid (a nanosized mesh for example made from copper, nickel or gold, available in different mesh sizes and shapes). The beam then reaches a fluorescent screen to create an image. The image contrast depends on the difference in electron density within the sample, the thickness and density of the sample, and on the energy of the electrons.[120,121] Examples of TEM images of OPV blends can be found in Chapter 7.

2.1.4 Resonant Soft X-Ray Scattering

Resonant Soft X-ray Scattering (RSoXS) is an emerging scattering technique that can probe the nano- to meso-scale morphology. The technique combines soft X-ray spectroscopy with X-ray scattering, providing statistical morphological information from nanometer to micrometer length scales and is sensitive to orientation and chemical composition. RSoXs can give insights into the phase separation and the average domain purity.[122–124] Example RSOXs data for OPV BHJ blends can be found in Chapter 3.

2.2 Optical Characterization

Optical characterization tools give information about how a material, such as a BHJ film, interacts with light. The absorption of ultraviolet (*UV*) or visible light, and sometimes near-infrared (IR), corresponds to electronic transitions in the materials and to the exciton generation rate. Therefore, absorption it is a critical aspect for the OPV performance.[97,125] Absorption in the IR typically caused by molecular vibration or by free charge carriers.[126]

The absorption coefficient α is a measure for the rate of the light intensity I decrease in a material along the propagation path x (Beer's law, Equation 2.1), with I_0 being the initial light intensity:

$$I = I_0 e^{-i\alpha x} \tag{2.1}$$

$$\leftrightarrow \quad \alpha = \frac{1}{I(\lambda)} \frac{d\,[I(\lambda)]}{dx} \tag{2.2}$$

The optical properties of a material are described by the refractive index n and the extinction coefficient k. The refractive index n describes the refraction of light at an interface via the Snell's relationship $n_1 \sin \theta_1 = n_2 \sin \theta_2$ and defines the phase velocity v of an electromagnetic wave in a material.

$$v = \frac{c}{n} \tag{2.3}$$

The extinction coefficient k corresponds to the amplitude damping of the electromagnetic wave, or, in simple words, describes how quickly light vanishes in a material. The extinction coefficient k is proportional to α and the wavelength λ.[127]

$$k = \frac{\alpha\lambda}{4\pi} \tag{2.4}$$

Together, they are part of the complex refractive index n^*.[127]

$$n^* = n + ik \tag{2.5}$$

The complex dielectric function ε^* is an alternative description related to n^* *via* $\varepsilon^* = n^{*2}$.[127]

$$\varepsilon^* = \varepsilon_1 + i\varepsilon_2 \tag{2.6}$$

2.2.1 UV-Vis Spectroscopy

The most common optical characterization method is UV-visible spectroscopy. In this setup, a light beam passes though the sample and depending on the mode of operation the absorbance A or the transmission T is obtained.[128,129] The sample can be a liquid in a cuvette or a film on a transparent substrate, as in the case of BHJ or polymer films. If equipped with an integrating sphere, the reflection R of the film can be measured as well.
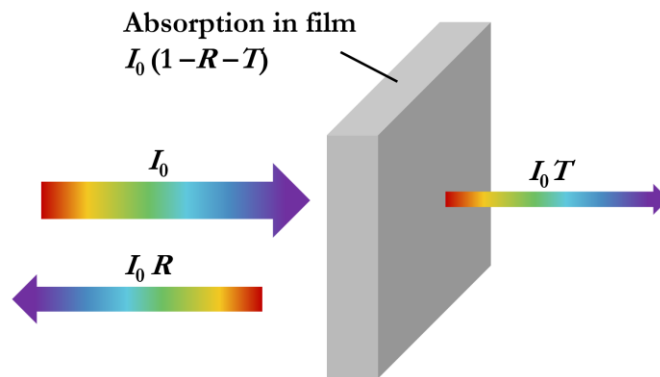
Figure 2.3. Schematic drawing of incident light with intensity I_0, reflected light I_0R, transmitted light I_0T and absorbed light $I_0(1-R-T)$.

The transmission T is defined as the fraction of light that passes though the sample (I) normalized by the total incident light (I_0). The reflectance R is the faction of light reflected at the

sample surface, normalized by the total incident light intensity. A remaining fraction of light is absorbed by the sample, called absorptance a (sometimes denoted as A).

$$R + T + a = 1 \tag{2.7}$$

Both the definitions of R and T are straightforward and pose little risk of confusion. However, commonly the absorbance A is reported, which must not be confused with the fraction of light absorbed. Instead, A is defined as[75]:

$$A = -\log\left(\frac{I}{I_0}\right) = -\log(T) \tag{2.8}$$

Note that log denotes the decadic logarithm, not the natural logarithm ln. To give an example, if a sample reflects no light and absorbs 10% of the incident light, T is 90% or 0.9. The corresponding absorbance is $A = -\log(0.9) = 0.045$. If a sample reflects no light and absorbs 98% of the incident light, T is 2% or 0.02. The corresponding absorbance is $-\log(0.02) = 1.7$. Due to the unintuitive decadic-logarithmic dependance of A, the risk of confusion with the absorptance a, or with the absorption coefficient α, the use of the transmittance T should be encouraged instead of the absorbance A.

R and T are related to the optical properties (n and k) of a film *via* the following relationships[125,127].

$$R = \frac{(n-1)^2 + k^2}{(n+1)^2 + k^2} \tag{2.9}$$

$$T = \frac{(1-R)^2 \left[1 + \left(\frac{\lambda\alpha}{4\pi n}\right)\right]}{e^{\alpha x} - R^2 e^{-\alpha x}} \tag{2.10}$$

Based on R and T measurements, the absorption coefficient can be calculated:[125]

$$\alpha = \frac{1}{d} \, ln \left(\frac{(1-R)^2}{2T} + \left(\frac{(1-R)^4}{4T^2} + R^2 \right)^{0.5} \right) \tag{2.11}$$

The extinction coefficient can then be obtained from α *via* the above-described relationship $k = \frac{\alpha\lambda}{4\pi}$. Assuming interference effects are absent and if $n^2 \gg k^2$, the refractive index n can be approximated based on R as:[127]

$$n = \left| \frac{1+R^2}{1-R^2} \right| \tag{2.12}$$

Typically, organic semiconducting materials possess refractive indices between 2 and 3.[97,130]

2.2.2 Ellipsometry

Spectroscopic Ellipsometry is an optical characterization method to obtain the optical properties and thicknesses of thin film materials, such as metals, semiconductors and oxides.[131] In the measurement, linearly polarized light hits the sample, which interacts with the sample and then is reflected and detected. The light undergoes amplitude and phase changes when it interacts with the sample, which are recorded.[132]
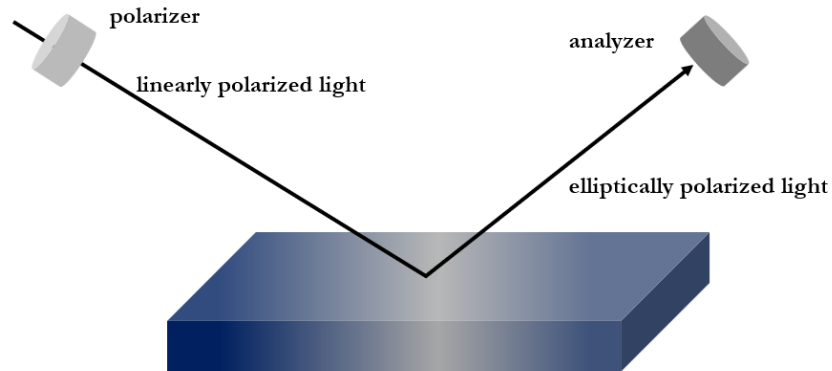
Figure 2.4. Schematic illustration of an ellipsometry measurement.

In case of an isotropic material, two parameters (Ψ and Δ, also called ellipsometric angles) are sufficient to describe the change in polarization ρ, if no depolarization takes place:

$$\rho = \tan(\Psi)e^{i\,\Delta} \tag{2.13}$$

Different dispersion relationships describe the dependence of the optical constants on the wavelength for different materials. For example, transparent materials can be described by the Cauchy or the Sellmeier relationship. Oscillator theory helps to describe dispersion relationships for many other materials. Some of the models are Kramers-Kronigs consistent, meaning the real and imaginary part depend on each other.[131,133,134] However, not all materials are well described by such models, and it is an inherent challenge to choose the right model when fitting ellipsometry data of organic semiconductor. Organic semiconductor blends are often anisotropic, which complicates the correct determination of the optical properties further.[97,135]

The preparation of ellipsometry samples, the measurement, and the fitting must be done with utmost care to obtain relevant data for organic semiconductor films. Practical recommendations for ellipsometry measurements for OPVs include the consideration of the substrate and the film processing. Due to the different polarities and wetting behaviors of different materials, OPV blends can orient differently on different substrates. With that, their optical properties can vary. This can pose an additional challenges, and a full characterization of the substrate or substrate stack is recommended. To obtain relevant data, the substrate should be the same as the back electrode in the device. For example, in a conventional device structure, this would be glass/ITO/PEDOT:PSS. The stack can then be incorporated into the model as a base layer to obtain the optical constant of the BHJ film deposited on this substrate.[97] To increase the accuracy of measurements further, it is recommended to incorporate transmission mode measurements into the model. Many variable angle spectroscopic ellipsometers (VASE) can take such

measurements. Lastly, it is important to dry the BHJ film under vacuum, to obtain films that are a close match to the BHJ layers in the working device, which are pumped down to low pressure to evaporate back electrodes. The optical properties of common OPV materials, such as PEDOT:PSS, ZnO, Ba, Al can be found in sub Chapter 4.2.1.

2.3 Electrical Characterization

The electrical characterization of OPVs is typically the first step in the OPV device characterization. It includes obtaining current-density-voltage (JV-curves) or current-voltage (IV) characteristics and measuring the External Quantum Efficiency (EQE) spectrum. The current density J is the current I per area, and often the symbols are used interchangeably. The JV-characteristics allows to quantify the OPV performance and to compare different devices and different blend systems.
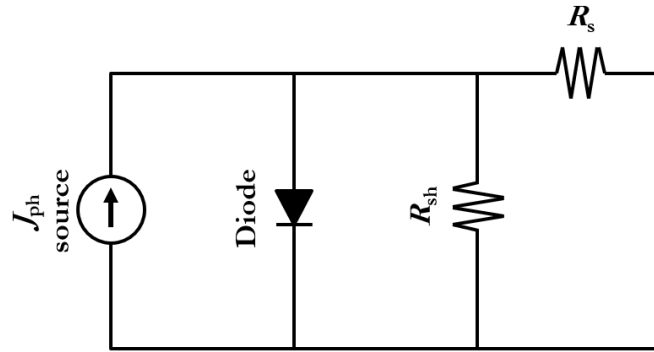
Figure 2.5. Equivalent circuit of a solar cell.

A solar cell can be represented by an electrical equivalent circuit, shown in **Figure 2.5**, that consists of a photocurrent source and a diode in parallel. A high series resistance R_s (in series) and a large leakage current due to a low shunt resistance R_{sh} (in parallel) can limit the OPV performance. In the presence of both resistors the IV-characteristics can be described as:

$$I = I_0 \exp\left[\frac{q/(V+IR_s)}{n\,k_BT} - \frac{V+IR_s}{R_{sh}}\right] \tag{2.14}$$

31

The values of the two resistances can be found *via* the differential resistance dV/dJ.[136] Examples can be found in Chapter 3:. The description with the equivalent circuit will help to understand the current-voltage characteristics of a solar cell.

2.3.1 *JV*-Characteristics and OPV Performance Metrics

JV-curves are measured by connecting to the anode and cathode of the device to apply voltage. The voltage is typically swept from a small reverse bias (*e.g.*, −0.5 V) to the maximum voltage (e.g. 1.5 V) and then back to the maximum reverse bias (*e.g.*, −2 V). The current *I* is measured and divided by the active device area to obtain the current density *J*. The active area can be defined by a mask of a known size. The reverse (backward) scan is then used for the analysis.

$$FF = \frac{\text{(orange)}}{\text{(gray)}} = \frac{J_{MPP} \cdot V_{MPP}}{J_{sc} \cdot V_{OC}}$$

$$PCE = \frac{P_{out}}{P_{in}} = \frac{FF \cdot V_{OC} \cdot J_{sc}}{P_{in}}$$
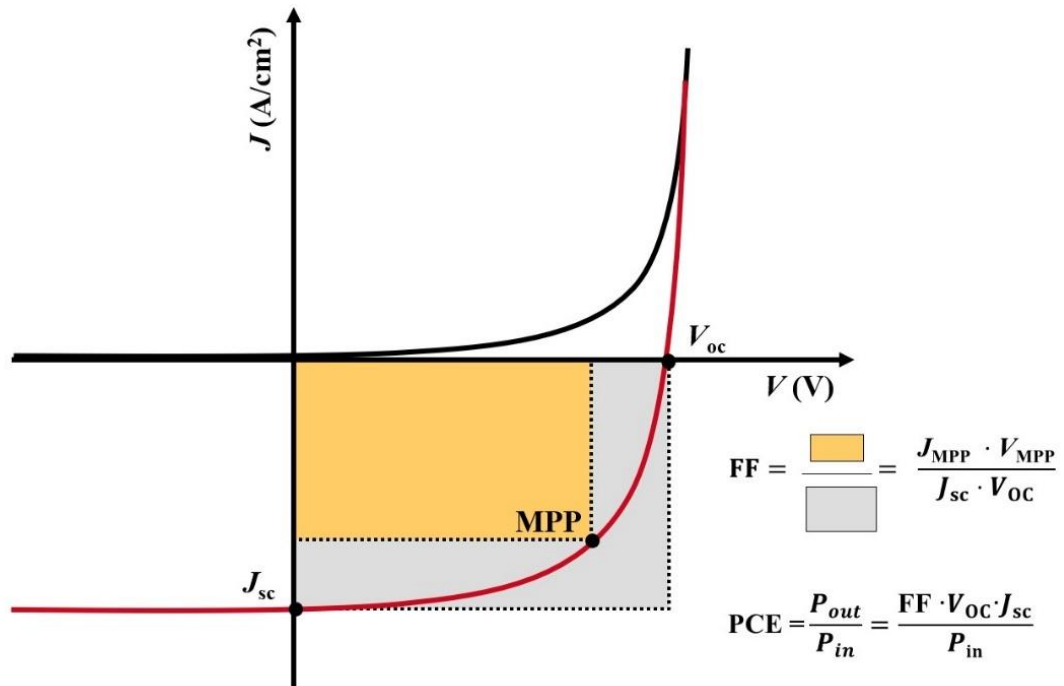
Figure 2.6. Schematic OPV *JV*-characteristics in the dark (black) and under illumination (red) and the performance parameters.

Under dark conditions, the dark JV-curve is measured, which follows the diode behavior described by the Shockley equation, with the reverse saturation current J_0, the ideality factor n_{id}, the elementary charge q, the absolute temperature T, and the Boltzmann constant k_B:

$$J(V) = J_0 \left(e^{\frac{qV}{n_{id}k_B T}} - 1 \right) \qquad (2.15)$$

Under reverse bias, only a small current close to zero is detected, which arises from thermalization and leakage (which is more pronounced at larger reverse bias). At forward bias, the exponential dependence of the current on the voltage can be observed. Under illumination, the photocurrent (negative) J_{ph} is added to the dark current, shifting the JV-curve down. From the JV-curve the performance defining parameters can be obtained.

The short-circuit current J_{sc} is the current at 0 V. It is largely governed by the photogeneration of charge carriers but also by geminate recombination, non-geminate recombination and extraction.[97] An in-depth discussion of the factor governing the J_{sc} can be found in Chapter 4:.

The open circuit voltage V_{oc} is the voltage at which the current is zero. This implies that charge generation and charge recombination are balanced.[100] Under V_{oc} conditions, specifically bimolecular recombination plays a role due to the n^2 dependence on the charge carrier concentration.[137]

The V_{oc} can also be defined by the splitting of the quasi-Fermi levels of electrons $E_{f,n}$ and holes $E_{f,p}$ as $(E_{f,n} - E_{f,p})/q$. The maximum V_{oc} is limited by the effective band gap as $E_{g,eff}/q$, but commonly the splitting is smaller because of interfacial losses, disorder and recombination.[138,139] To understand this definition, a short excursion to semiconductor physics is needed. The Fermi energy is the energy level to which all states are filled with electrons at 0 K, while all states above are empty.[56] Under dark conditions (thermal equilibrium), the electron concentration n can be

calculated with the effective density of states at the conduction band edge, N_c, and the Fermi energy, E_F:[56]

$$n = N_C e^{-\frac{E_c - E_F}{k_B T}} \tag{2.16}$$

Under illumination, the quasi-Fermi level for electrons $E_{f,n}$ describes the electron concentration n, and the quasi-Fermi level for holes $E_{f,p}$ describes the hole concentration p, with N_v being the effective density of states at the valence band edge.[56]

$$n_{photo} = N_C e^{-\frac{E_c - E_{Fn}}{k_B T}} \tag{2.17}$$

$$p_{photo} = N_V e^{-\frac{E_{Fp} - E_V}{k_B T}} \tag{2.18}$$

The Fill Factor FF is the ratio of the power at the maximum power point (the JV-product is maximized at this point) and the product of J_{sc} and V_{oc}. The PCE is the product of these three parameters per incident power. The three parameters govern the device performance *via* the following relationship, with P_{in} and P_{out} being the incident power of the light and the output power of the cell:

$$PCE = \frac{P_{out}}{P_{in}} = \frac{FF \cdot V_{oc} \cdot J_{sc}}{P_{in}} \tag{2.19}$$

2.3.2 External Quantum Efficiency

The External Quantum Efficiency (EQE) is a wavelength-dependent quantity that is described by the ratio of the electron flux in the outer circuit per incident photon flux.[75,97]

$$EQE(\lambda) = \frac{J_{sc(\lambda)/q}}{I(\lambda)/h\nu} \qquad (2.20)$$

The features in the EQE are governed by the wavelength-dependent absorption of the donor and acceptor of the blend, as well as by the absorbance of light in all other device layers and the reflection at all interfaces, leading to a complex interference pattern and wavelength-dependent electrical field distribution in the device stack. This complex interference pattern can be simulated with optical transfer matrix simulations, based on the thickness of each layer and based on the optical properties of each layer.[97] This approach is outlined in detail in Chapter 4:.
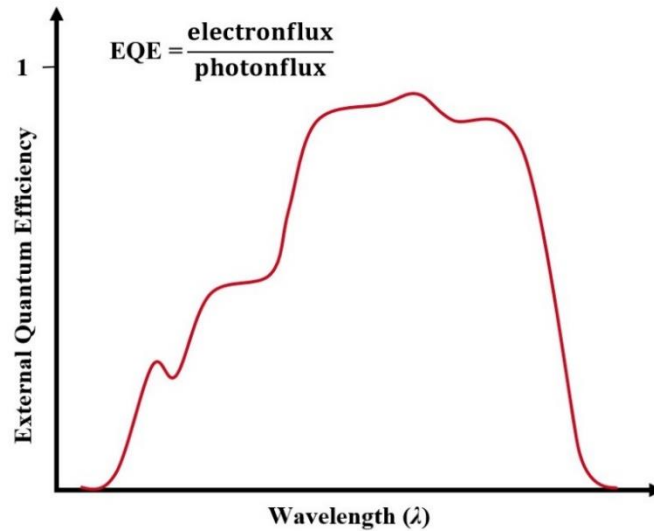
Figure 2.7. Example of an External Quantum Efficiency (EQE) spectrum.

The EQE is experimentally measured by shining monochromatic light onto the device, chopped at a certain frequency, and recording the photovoltage signal with a lock-in amplifier, while sweeping the wavelength. For OPVs it is commonly recorded without an external sample bias. The EQE(λ) and J_{sc} are related *via* the following equation, with $S(\lambda)$ being the spectral distribution, if the EQE is measured at 0 V:

$$J_{sc} = q \int_{\lambda'}^{\lambda''} \text{EQE}(\lambda) \cdot S(\lambda) d\lambda \qquad (2.21)$$

It follows that the integration of the EQE spectrum can be used to check the measured J_{sc} value for correctness. It is worth notingthat the actual solar simulator spectrum must be used to cross-check the two measurements, rather than the ideal AM1.5 spectrum.

The EQE can be used to derive the Urbach energy E_U, which is a measure of the energetic disorder.[140–142] Disorder in organic semiconductors causes absorption of light with wavelength below the band gap E_g, due to transitions from or to localized tail states. The absorption follows the expression $\alpha = \alpha_0 \exp(h\nu/E_U)$, thus the plot of the natural logarithm of the EQE as a function of incident photon energy can yield the E_U, as shown below.
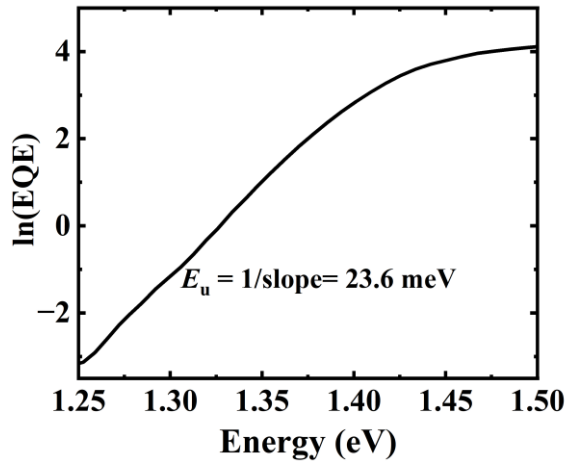
Figure 2.8. Example Urbach energy plot for an organic semiconductor blend.

36

2.4 Determining the Energy Levels and the Band Gap

The HOMO and LUMO levels as well as the Fermi energy and band gap have been introduced in the previous chapter. Different techniques are available to experimentally probe the HOMO and LUMO energy levels and to obtain the band gap as an important material parameter.
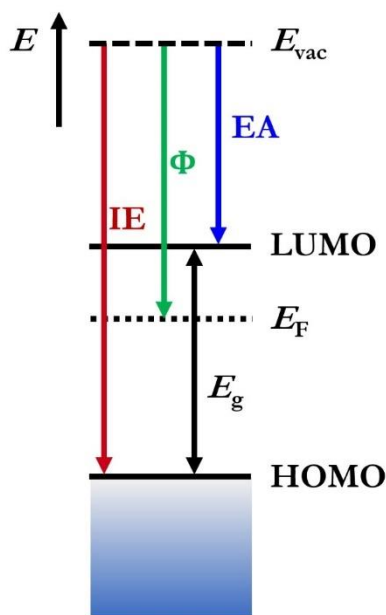
Figure 2.9. Energy levels in an organic semiconductor, including HOMO and LUMO, as well as the Fermi energy E_F, the vacuum level E_{vac}, the ionization energy (IE), electron affinity (EA) and the work function Φ.

2.4.1 Determining the Optical Band Gap *via* the Tauc Plot

The optical data obtained from UV-Vis or ellipsometry measurements can be used to derive the optical band gap *via* the so-called Taucplot. The absorption coefficient relates to the band gap *via* the relation $(\alpha \cdot h\nu)^{1/\gamma} = C \cdot (h\nu - E_g)$, where C is a constant. The exponent $1/\gamma$ is equal to $1/2$ or 2 for direct and indirect band gap semiconductors, respectively. The absorption coefficient α can be calculated from the extinction coefficient k as described earlier. However, if optical data are not available, the EQE spectrum can be used instead as will be shown in Chapter

3. The band gap value is obtained from the x-intercept of a linear regression in the low energy region. An example Tauc plot for an organic semiconductor blend (PCE10:IOTIC-4F) is shown in **Figure 2.10**.
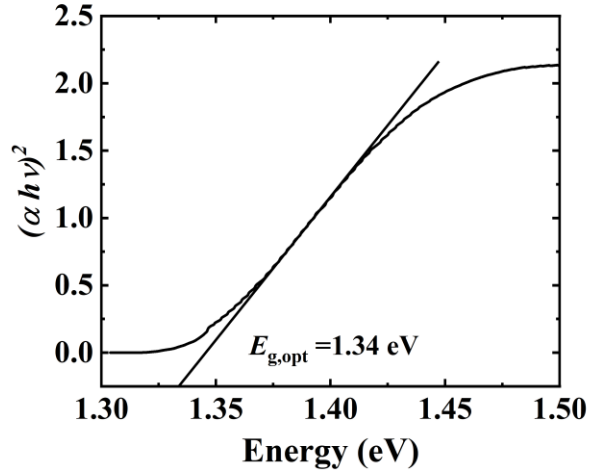
Figure 2.10. Tauc plot and linear regression in the low energy region for the determination of the optical band gap.

2.4.2 Ultraviolet Photoelectron Spectroscopy

Ultraviolet Photoelectron Spectroscopy (UPS) uses ionizing UV radiation to probe the HOMO level (top of the valence band) or the ionization energy and the work function Φ. The photons used for UPS have energies of approximately 10-40 eV, which allows the photoexcitation of valence band electrons, with an approximate information depth of 2-3 nm.[143] Once the energy of the photons is sufficient to overcome the work function, electrons will be emitted. The energy of the incoming photon hυ minus the binding energy E_B is the kinetic energy E_K of the emitted electrons since the total energy is conserved:

$$E_K = h\nu - E_B \tag{2.22}$$

The Fermi level can be calculated from high kinetic energy electrons, being the highest energy level from which electrons can be emitted. In the recorded spectrum, this corresponds to the high kinetic energy cutoff of the signal. The ionization energy (IE) can be calculated from this equation using the binding energy cutoff at low kinetic energies for E_K. Here, the emitted electrons are slow and have just enough energy to reach the vacuum level.[144] In UPS, the photons do not have sufficient energy to excite any core levels. In contrast, X-ray photo electron spectroscopy (XPS) uses higher energy photons (>1000 eV) to probe the elemental composition of a sample surface.[145]

2.4.3 Inverse Photoemission Spectroscopy

Inverse photoemission spectroscopy (IPES) can probe unoccupied states (LUMO or conduction band minimum) or the electron affinity. In this technique, electrons occupy empty states in the sample material and a photon is emitted with an energy that corresponds to the difference of the initial kinetic energy and the energy of the electron in the empty level. In the case of an electron occupying the LUMO level the emitted photon energy corresponds to $h\nu = E_K - E_{LUMO}$. IPES and UPS are complementary techniques. Having determined the HOMO level from UPS and the LUMO from IPES, the difference between these levels gives the band gap.

2.4.4 Cyclic Voltammetry

Cyclic voltammetry is an electrochemical method that records the current response I of an electrochemical cell in dependence on an applied potential and the resulting cyclic voltammogram reveals the oxidation and reduction processes of the material under investigation.[146,147] In the three-electrode setup, a current flows between working electrode and counter electrode, which

are employed together with a reference electrode with defined equilibrium potential, such as a saturated calomel electrode (SCE) or Ag/AgCl electrode.[146,148]
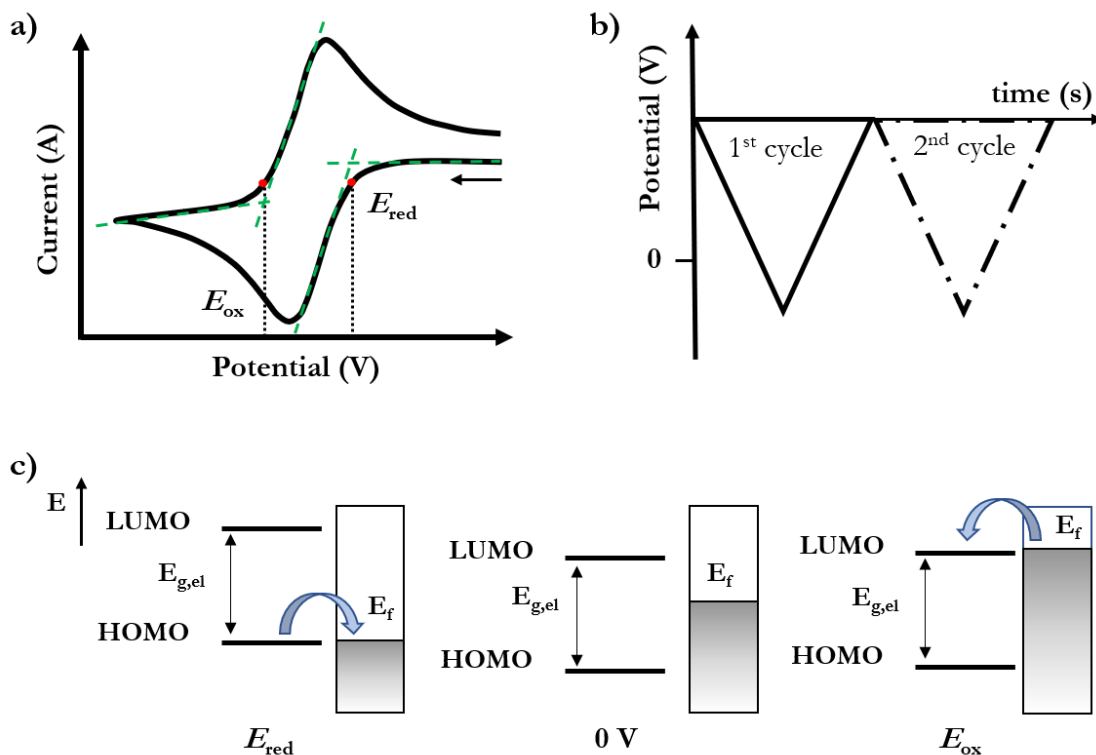
Figure 2.11. a) Current-Potential dependence in a CV measurement. b) Applied potential versus time and c) the energy level alignment at the reduction potential, at 0 V, and at the oxidation potential.

The analyte can be either dissolved in a conductive electrolyte solution or absorbed onto the working electrode; for example in the case of polymers or inorganic nanocrystals, a thin film can be cast onto the electrode.[146,149,150] The varying potential that is applied to the working electrode results in a voltage drop over a thin layer of analyte near the electrode, inducing a change in the relative positions of the energy levels of the electrode and analyte molecule.[75,147] When applying an increasingly negative potential, the electrode's Fermi level is raised and once the position matches energetically with the position of the LUMO, electrons are transferred from the electrode to the analyte and the onset of the reduction peak is observed.[75,146,147] To probe the oxidation,

the potential is thus swept towards higher values and the onset of the oxidation occurs once the Fermi level of the electrode is lowered sufficiently to match the HOMO level of the analyte.[75,146,147] Only if the analyte can be reversibly oxidized and reduced, both the ionization energy and the Electron affinity can be determined.[146,149] To relate the measured redox behavior to the IE (HOMO) and EA (LUMO), an empirical relationship is commonly used, originally proposed by Brédas *et al.*[149–152] Here, potentials E_{ox} and E_{red} refer to the onset of the oxidation and reduction peak and EA and IE can be calculated as $EA = E_{LUMO} = (E_{red} + 4.4)eV$ and $IE = E_{HOMO} = (E_{ox} + 4.4)eV$.

The electrochemical band gap determined by CV has values smaller than those obtained from optical measurements due to the exciton-binding energy - typically a difference of up to 0.2 eV is reported.[150,153,154] While commonly employed due to ease and accessibility, CV measurements and data interpretation may not always be straightforward and a wide range of considerations may be necessary due the complexity of the redox processes, including the scan rate of the experiment, the reversibility of the redox system, the diffusion and undesired convection processes in the solution, the choice of electrolyte and electrodes, as well as multi-electron transfers, to name only a few.[146,147,155]

2.5 Probing Recombination Losses

Chapter 1.4.2 outlined the different recombination mechanisms that play a role in OPVs. Due to the different mechanisms and time scales, geminate recombination and the different non-geminate recombination mechanisms can be deconvoluted.

2.5.1 Geminate Recombination

Geminate recombination of charge carriers that originate from the same photoexcitation can be measured with time-delayed collection field (TDCF) measurements.[156] In TDCF, a pre-bias is applied, followed by a short (≈10 ns) photoexcitation laser pulse (low pulse fluence). Under these conditions non-geminate recombination is negligible. A larger collection bias is then applied after a fixed delay time to collect the photogenerated charge carriers. Variation of the pre-bias can give insights into the voltage-dependence of the geminate recombination losses.[95,157,158] State-of-the-art OPV systems, such as PM6:Y6, have been shown to have a negligible dependence of photogenerated charge carriers on voltage, and no voltage dependence has been found for the CT-state dissociation.[98]

An alternative approach to quantify geminate recombination that does not require any specialized equipment is outlined in Chapter 4. It relies on the simple measurement of the saturated photocurrent at reverse bias, coupled with optical simulations.[97]

2.5.2 Qualitative Insights into Non-geminate Charge Recombination

A simple measurement to get qualitative insights into the dominant recombination mechanism is probing the dependence of the V_{oc} on the natural logarithm of the light intensity.[99,100,159] This measurement can be carried out by measuring JV-curves while modulating the light intensity with a set of neutral density filters. If bimolecular recombination is dominant, a slope of 1 k_BT is expected. In the case of dominant trap-assisted recombination *via* bulk traps, the slope is increased to > 1 k_BT. In contrast, in the case of dominant trap-assisted recombination *via* surface traps, the slope is reduced to values < 1 k_BT.
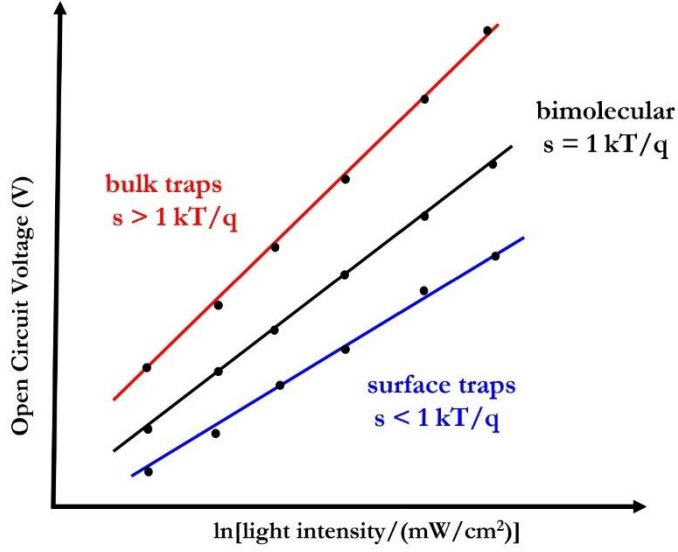
Figure 2.12. Illustration of three example systems with different V_{oc} values and different slopes.

2.5.3 Quantitative Insights into Non-geminate Charge Recombination

The different recombination current contributions for bimolecular (J_{bm}), bulk trap-assisted (J_{bulk}) and surface trap-assisted (J_{sf}) recombination that were introduced in sub-chapter 1.4 can be mathematically described as:

$$J_{rec,bm} = q \, d \, k_{bm} \, n^2 \tag{2.23}$$

$$J_{rec,bulk} = q \, d \, k_{bulk} \, n \tag{2.24}$$

$$J_{rec,sf} = q \, d \, k_{sf}(V_{cor}) \, n \tag{2.25}$$

Here, k_{bm}, k_{bulk}, and k_{sf} are the recombination coefficients, d is the thickness of the active layer, n is the free charge carrier density, and the voltage corrected for the series resistance $V_{corr} = V\text{-}JR_s$. It is worth noting the n^2-dependence in the case of bimolecular recombination and the

43

voltage-dependence in the case of surface recombination. The sum of the individual contributions is the total recombination current $J_{\text{rec,total}}$:[137]

$$J_{rec,total} = J_{rec,bm} + J_{rec,bulk} + J_{rec,sf} \qquad (2.26)$$

The following sub chapter explains how to quantify these recombination contributions with impedance spectroscopy.

2.5.3.1 Impedance Spectroscopy

To gain quantitative insights into the recombination dynamics, impedance spectroscopy, also called capacitance spectroscopy, can be carried out. A small perturbing AC-bias is applied to the sample across a frequency range. The frequency f can also be expressed as angular frequency $\omega = 2\pi f$. Impedance spectroscopy probes the relaxation processes that follow this perturbation, such as lattice distortions, electrode polarization, dipole rearrangement, and electrical and ionic conduction, by measuring the alternating current response $I(t)$ that follows the perturbation signal $V(t)$ with a time delay (the signal has a phase shift ϕ).[160] The impedance Z is the complex, frequency-dependent resistance of the sample.

$$V(t) = V_0 \sin(\omega t) = V_0 e^{i\omega t} \qquad (2.27)$$

$$I(t) = I_0 \sin(\omega t + \phi) = V_0 e^{i(\omega t + \phi)} \qquad (2.28)$$

$$Z = \frac{V(t)}{I(t)} = \frac{V_0}{I_0} e^{-i\phi} \qquad (2.29)$$

The impedance Z is a complex number that can be expressed as:

$$Z = Z' - i Z'' \qquad (2.30)$$

Z' is the real component of Z corresponding to $\phi = 0$ and Z'' is the imaginary component of Z, corresponding to $\phi = 90°$. Z' is equivalent to the resistance described by Ohm's law and Z'' is the reactance, describing the sample's opposition to the change of voltage.

2.5.3.2 Impedance Spectroscopy for OPVs

To probe the recombination dynamics in OPVs, measurements in the range of $10\text{-}10^6$ Hz are carried out. The impedance is measured in the dark and under illumination with varying frequency and bias. The bias ranges from V_{sat} (typically -2 or -3 V) to the V_{oc} of the device. Before carrying out the impedance measurements, the JV-characteristics in the dark and under illumination must be obtained to determine the experimental recombination current J_{rec}. There are two possible ways to define the recombination current.

$$J_{ph} = J_{light} - J_{dark} \tag{2.31}$$

$$J_{rec} = J_{ph} - J_{light,sat} \tag{2.32}$$

or: $$J_{rec} = J_{light} - J_{light,sat} \tag{2.33}$$

Here, J_{ph} is the photocurrent and $J_{light,sat}$ the current measured under illumination at the saturated reverse bias. Further, the series resistance needs to be determined from the differential resistance in the dark and under illumination as well as the device area A (the measurements are carried out without aperture). The thickness of the active must be known as well as the built-in voltage V_{bi}, for example obtained from the JV-curve as V_0.

First, the recorded Z' and Z'' values from the dark measurement can be used to calculate the corrected capacitance C_{corr} of the BHJ layer. It consists of a frequency-dependent component, the

chemical capacitance C_{chem}, and a frequency-independent capacitance C_g. C_{chem} originates from free charge carriers and C_g from the Maxwell displacement current. The latter can either be a voltage-independent geometrical capacitance or a voltage-dependent capacitance of a space charge region if the width of the space charge region is not occupying the whole active layer.[136] C_{corr} can be calculated with corrections for the inductance L from the wires of the setup and for the series resistance as follows:[136,161]

$$C_{corr}(\omega, V_{corr}) = -\frac{1}{\omega}\frac{Z'' - \omega L}{(Z' - R_s)^2 + (Z'' - \omega L)^2} \qquad (2.34)$$

The corrected capacitance at reverse bias in the dark is constant across the frequency range and its average across the frequencies is C_g. It serves to calculate the dielectric constant, with ε_0 being the vacuum permittivity, d the thickness of the BHJ layer and A the device area.[64,136]

$$\varepsilon_{BHJ} = \frac{C_g d}{\varepsilon_0 A} \qquad (2.35)$$

When electrode layers introduce additional capacitive effects, the capacitance of the BHJ can be overestimated, leading to too-low values for the dielectric constant of the active layer. If only highly conductive metal electrodes and thick active layers are present, the above equation is a good approximation to obtain ε. However, for example in the inverted device structure, the capacitance of ZnO should be taken into account. The dielectric constant of sol-gel-deposited ZnO has been determined to be 4.7, as shown in Chapter 3:.[112] Considering the ZnO layer changes ε_{BHJ} typically by about $\approx$ 30%, therefore, it is important to consider the device architecture in the impedance analysis.[64,112]

$$\varepsilon_{BHJ} = \frac{C_g \cdot C_{ZnO}}{C_{ZnO} - C_g}\frac{\cdot d_{BHJ}}{\varepsilon_0 \cdot A} \qquad (2.36)$$

Under illumination, the capacitance at saturated reverse bias, $C_{sat,light}$, is obtained as the average value across the frequencies in which the values are constant. The difference of $C_{sat,light}$ and C_g is the saturated capacitance $C_{sat.}$ The saturated charge carrier density n_{sat} follows from it.

$$C_{sat} = C_{sat,light} - C_g \qquad (2.37)$$

$$n_{sat} = \frac{C_{sat}}{qAd}(V_0 - V_{sat}) \qquad (2.38)$$
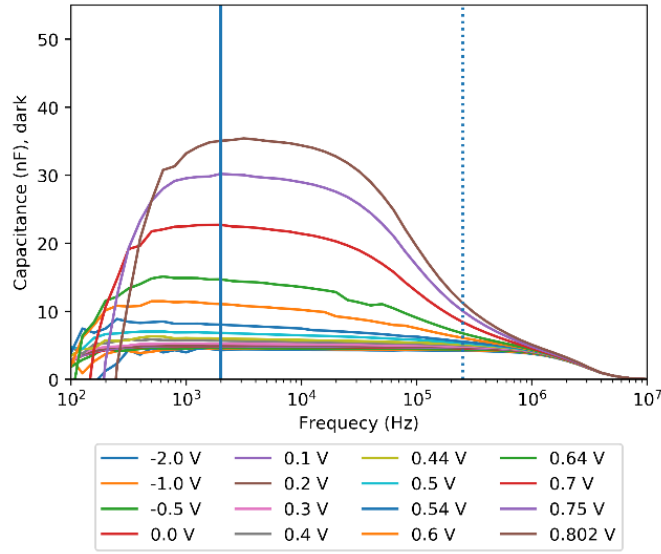
Figure 2.13. Example of a capacitance spectrum of an OPV device obtained under illumination and with the low frequency indicated by the solid blue line.

A low frequency maximum of the capacitance spectrum under illumination is typically observed around 10^3 to 10^4 Hz. The chemical capacitance $C_{chem}(V_{corr})$ is the difference between the low frequency capacitance $C_{LF,light}(V)$ and C_g.

$$C_{chem}(V_{corr}) = C_{LF,light}(V_{corr}) - C_g \qquad (2.39)$$

Then the charge carrier concentration $n(V_{corr})$ can be calculated *via* the following integration:[136,137]

$$n(V_{\text{corr}}) = n_{\text{sat}} + \frac{1}{q\,A\,d} \int_{V_{\text{sat}}}^{V_{\text{corr}}} C_{\text{chem}}(V_{\text{corr}})\,dV_{\text{corr}} \qquad (2.40)$$

The integration can follow a numerical trapezoidal rule. Note that alternative approaches exist in which low- and high-frequency capacitance are used for the analysis (dashed line in **Figure 2.13**).[136] In some cases, an extrapolation of n at values close to V_{oc} is recommended, when impedance data at high voltages shows a decrease in $C_{\text{LF,light}}$. Following the calculation of n, the effective mobility can be obtained:

$$\mu_{\text{eff}} = \frac{J(V_{\text{corr}})d}{2qn(V_{\text{corr}})[V_{\text{corr}} - V_{OC}]} \qquad (2.41)$$

The effective mobility lets us define the recombination coefficients for bimolecular (k_{bm}), bulk trap-assisted (k_{bulk}), and surface trap-assisted (k_{sf}), recombination.

$$k_{\text{bm}} = \frac{2\,q\,\mu_{\text{eff}}\,\xi}{\varepsilon\varepsilon_0} \qquad (2.42)$$

$$k_{\text{bulk}} = \frac{q\,\mu_{\text{eff}}N_{\text{bulk}}}{\varepsilon\varepsilon_0} \qquad (2.43)$$

$$k_{\text{sf}} = \frac{q\,\mu_{\text{eff}}\,N_{\text{sf}}}{\varepsilon\varepsilon_0}\,e^{-q\frac{V_{\text{bi}} - V_{\text{oc}}}{k_{\text{B}}T}} \qquad (2.44)$$

In the equations for the recombination currents, the only unknown parameters are the Langevin prefactor for bimolecular recombination ξ, and the bulk and surface trap densities N_{bulk} and N_{sf}. Fitting the sum of the recombination current (Equation 2.26) to the experimental recombination current yields the three variables as fitting parameters. Example fits are shown in **Figure 2.14**.
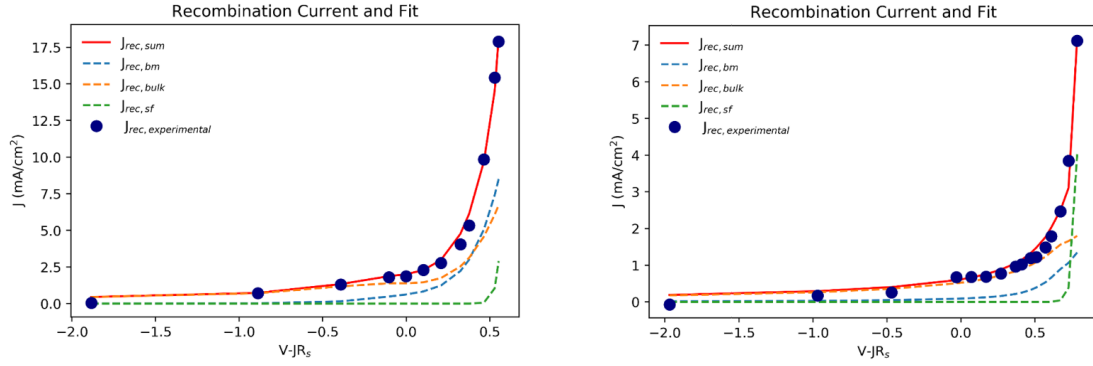
Figure 2.14. Example recombination current fits with different magnitudes of the total recombination current and different relative contributions of the different recombination mechanisms.

To improve the fitting accuracy, it is recommended to carry out a preliminary fit to determine the number of bulk traps by fitting from moderate negative to positive bias with two fitting parameters only, excluding N_{sf}.
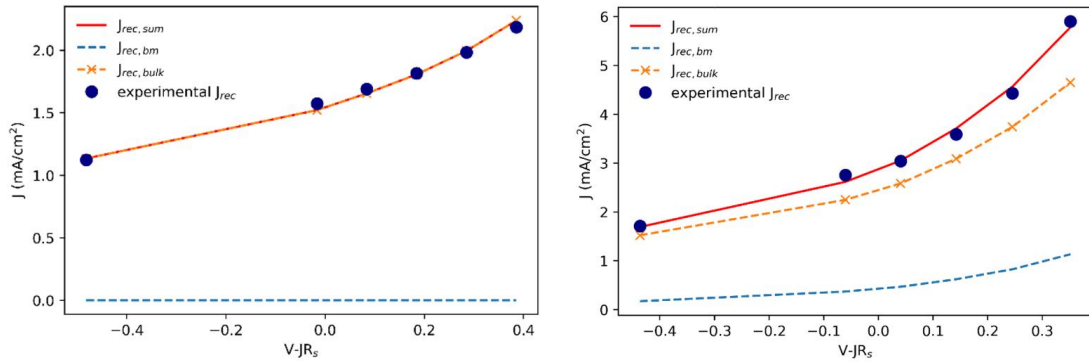
Figure 2.15. Examples of preliminary fits for two solar cells with different ratios of bulk trap-assisted recombination and bimolecular recombination.

In this region, surface traps play a minor role, and the overall fit accuracy can be improved. In the next fitting step, $N_{t,bulk}$ can be fixed and the remaining two parameters ξ and N_{sf} determined by fitting across the whole bias range. The previously optimized value for ξ can serve as the initial value in the second fit. Recommended bounds for the fit parameters are 0 - 1 for ξ and 0 - 10^{18} for N_{bulk} and N_{sf}.

2.6 Optical Transfer Matrix Simulations

The Optical Transfer Matrix Method (TMM) has been described by Pettersson et. al in 1999 and applied to OPV devices by McGhee and Burkhard.[130,162] Documentation and a freely available python version of the TMM code is available online.[163,164] The TMM software requires the optical constants n and k as input parameters as well as the device architecture, including the thickness of all layers. It then computes the electrical field distribution within the device stack and the theoretical photocurrent $J_{ph,theo}$ that would be obtained for the device if no losses occurred. An expanded software package that allows to visualize the three dimensional exciton generation rates $G(x, \lambda)$ and the calculation of the EQE spectra is discussed in Chapter 4:.[97] An example is shown in **Figure 2.16** below.
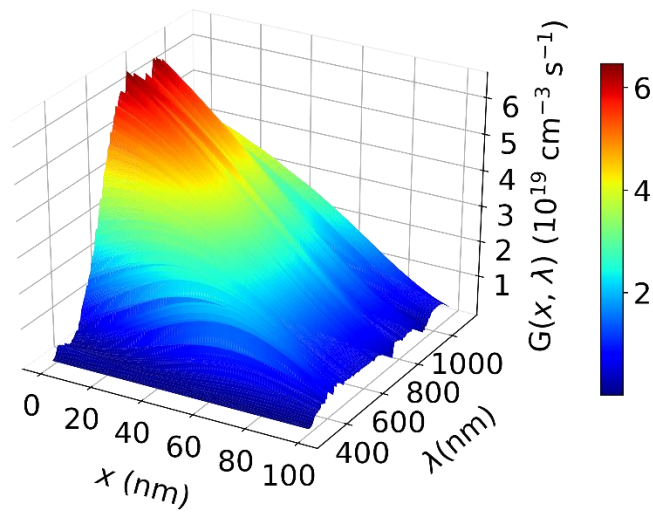
Figure 2.16. Example exciton generation rate $G(x, \lambda)$ as a function of depth in the device x and photon wavelength λ.

Numerical simulations to gain insights into the device physics, coupling experiments, and simulations are outlined in Chapter 4. The determination of the geminate recombination prefactor as well as non-geminate losses will be discussed using only standard measurements and optical simulations.[97]

Chapter 3: Effect of Palladium-tetrakis(triphenyl-phosphine) Catalyst Traces on Charge Recombination and Extraction in Non-Fullerene-based Organic Solar Cells

3.1 Introduction

Organic Photovoltaics (OPVs) promise flexible, lightweight, and solution-processable solar cells for low-cost energy harvesting. The development of donor-acceptor copolymers and non-fullerene acceptors (NFAs) has facilitated the realization of OPVs with higher efficiencies, now reaching record photoelectrical conversion efficiencies (PCEs) of up to 18.2% (single junction).[165–169] However, a further improvement of the material science and device engineering of organic solar cells is required to employ them in portable, lightweight, and semitransparent energy-harvesting solutions.[170–172]

The standard device architecture of organic solar cells is based on the bulk heterojunction (BHJ) active layer, sandwiched between an electron- and a hole-selective electrode with different work functions. The BHJ active layer consists of a nanoscale percolating network of a polymer donor and fullerene or non-fullerene acceptor material blend, which is commonly considered as an effective medium with uniform photoelectrical properties.[173–175] The material of the active layer should be an intrinsic semiconductor, free from unintentional doping or impurities, to reach high PCEs.[176,177] However, it is a challenge to meet the requirements for a reproducible high purity of organic semiconductors, especially in the case of conjugated polymers.

In the synthesis of both polymer donor materials and state-of-the-art NFAs, Pd-based catalytic cross-coupling reactions are most widely employed, offering mild reaction conditions and allowing a wide range of molecular functionalization.[72,167,169,178–183]

51

Tetrakis(triphenylphosphine)palladium(0) (Pd(PPh$_3$)$_4$) is one of the most frequently used cross-coupling catalysts, employed in Stille coupling[184], Suzuki coupling[185], Negishi coupling[186] and Songashira coupling reactions.[187] Purification protocols aim to remove impurities, including the catalyst residuals, but the purification of high molecular weight compounds can be difficult since efficient techniques such as distillation, crystallization, or column chromatography cannot be employed.[188,189] In addition, Pd(PPh$_3$)$_4$ and similar organometallic palladium complexes can decompose to Pd nanoparticles, which exhibit a strong affinity to conjugated polymers and heteroatoms.[188–191] As a consequence, Pd(PPh$_3$)$_4$ related trace impurities can remain in the synthesized products; to quantify their amount and impact on the device performance is challenging.

The role of trace impurities, such as intentionally added chemical impurities,[192–195] monomeric units,[196] or side products,[197] has been investigated in several reports and was identified as a major parameter of influence on the photoelectrical processes in BHJ solar cells.[193–195,195,198,199] The deterioration of the device performance in the presence of impurities has been mainly attributed to increased trap-assisted recombination,[191,193,195,198–200] but also to reduced charge carrier generation and extraction[194] as well as exciton-charge annihilation.[192]

In the case of trap-assisted recombination, the impurity creates a distribution of localized energy levels in the band gap at which one charge carrier gets trapped and then recombines with the respective free charge carrier of the opposite sign.[198,201–204] According to the Shockley-Read-Hall statistics, trap-assisted recombination losses are most detrimental for the device performance in the case of deep traps that are located near the mid-gap energy of the semiconductor, facilitating efficient recombination through the trap-states.[203,204]

Among the impurities that are well studied is PC$_{80}$BM, which has been associated with an increase in trap-assisted recombination in PCDTBT:PC$_{60}$BM solar cells, leading to a reduction in

the J_{sc}, $V_{oc,}$ and FF. The observed deterioration of the performance is attributed to the formation of localized deep electron traps that lead to impeded carrier transport caused by reduced electron mobility.[192,193,205] Similarly, the addition of 7,7,8,8-tetracyanoquinodimethane (TCNQ) leads to trap-assisted recombination and reduced electron mobility but also has been attributed to the stabilization of holes and increased exciton charge annihilation.[192] Another well-studied impurity is oxygen, which is known to cause device degradation.[206–211] It has been shown that oxygen can cause the formation of deep traps and a reduction of the mobility in P3HT:PCBM blends and it can lead to p-doping of the active layer.[207,208]

The effects of residual Pd(PPh$_3$)$_4$ catalyst traces, which can potentially lead to dramatic performance deterioration due to trap-assisted recombination, has gathered only a little attention despite being one of the most common impurities in OPV materials. Few studies have addressed the effect of Pd nanoparticles or intentionally added Pd(PPh$_3$)$_4$ on BHJ solar cell performance, limited to the scope of fullerene-based BHJ.[191,199,212,213]

A drop in PCE from 4.55% to 2.42% was reported for a PCDTBT:PC$_{70}$BM solar cell as the polymer Pd concentration was increased to 2570 ppm in the polymer, leading to reduced shunt resistance, R_{shunt}, while no changes in electron or hole mobility were observed.[212] Residual Pd catalyst has been shown to reduce the hole mobility in a fluorene-thiophene-benzothiadiazole copolymer-based BHJ solar cell, PFB-co-FT:PCBM, lowering the PCE from 0.23% to 0.1% when using PFB-co-FT with 3600 ppm Pd.[199] A study on P3HT:PCBM solar cells reported reduced performance from 3.19% to 1.95% upon addition of Pd(PPh$_3$)$_4$ in concentrations as low as 0.2 wt% of Pd(PPh$_3$)$_4$ relative to P3HT.[213] The same study suggests an increase of charge carrier lifetime for higher catalyst concentrations of up to 5 wt%, leading to stable performances at higher concentrations (1.74 - 1.84%).[213] Contradicting this observation of a saturation regime for higher Pd(PPh$_3$)$_4$ concentrations, the opposite was found

for PTB7:PC$_{71}$BM solar cells, which showed no significant change in performance for Pd concentration of up to 1 wt%.[191] For higher concentrations, a steep drop in performance was observed due to the reduction of the open-circuit voltage (V_{oc}), the short-circuit current (J_{sc}), and the fill factor (FF).[191]

While still lacking a systematic understanding of the processes induced by the residual catalyst in fullerene BHJ solar cells, no attention has been paid to the role of residual Pd(PPh$_3$)$_4$ in emerging high-performance non-fullerene BHJ solar cells, despite their significance for the further development of OPVs. It remains an open question how Pd(PPh$_3$)$_4$ impacts NFA-based OPVs and it is unclear if a threshold level exists that has to be exceeded to observe a noticeable impact on the performance. A very low threshold level would for example indicate that the current purification efforts are of utmost importance and the poor performance of certain batches of OPV materials may be explained by residual catalyst traces, whereas in the case of a high threshold level mainly other origins of a poor device performance should be in focus.

Partially, this may be because the quantification of remaining catalyst traces in the material blend is difficult. Nevertheless, to overcome current performance limitations in non-fullerene organic solar cells, the in-depth understanding of the dependence of the photoelectrical parameters on the presence of catalyst traces in the active BHJ layer is indispensable. One way to understand the impacts of impurities such as residual catalysts on the film morphology, charge recombination, and, therefore, the device performance is to intentionally add Pd(PPh$_3$)$_4$ with known amounts into the donor:acceptor blend. In this contribution, we carried out a comprehensive quantitative analysis of the effect of the controllably and systematically added Pd(PPh$_3$)$_4$ impurity, with concentrations up to 7 wt% (~ 55700 ppm), on the charge carrier photogeneration, recombination and extraction processes in a model polymer:non-fullerene acceptor system poly([2,6'-4,8-di(5-ethylhexylthienyl)-benzo[1,2-b;3,3-b]dithiophene]{3-fluoro-

2[(2-ethylhexyl)carbonyl]thieno[3,4-b]thiophenediyl}) (**PTB7-Th**): 3,9-bis(2-methylene-((3-(1,1-dicyanomethylene)-6,7-difluoro)-indanone))-5,5,11,11-tetrakis(4-hexylphenyl)-dithieno[2,3-d:2',3'-d']-s-indaceno[1,2-b:5,6-b']dithiophene (**IOTIC-4F**). PTB7-Th is selected as the donor polymer because it is a common polymer used in high performance NFA-based solar cells. To demonstrate the applicability to other NFA based systems, we further show the performance changes upon catalyst addition to the PM6:Y6 system, which has gathered much attention due to its performance of over 15%.[214–216]

3.2 Results and Discussion

Figure 3.1a shows the chemical structures of the donor PTB7-Th and the acceptor IOTIC-4F as well as the structure of Pd(PPh$_3$)$_4$. We studied reference devices with an active layer based on the donor and acceptor material, as well as devices with PTB7-Th:IOTIC-4F:Pd(PPh$_3$)$_4$ in a weight ratio of 1:1.5:0.0075, 1:1.5:0.03 and 1:1.5:0.07, in the following, referred to as devices with 0%, 0.75%, 3% and 7% catalyst, respectively. The XPS analysis (Figure S3.2) of a film with 0% added catalyst revealed no detectable amounts of Pt or Pt compounds, suggesting successful purification of the starting materials. The devices were fabricated in the inverted device architecture with Indium Tin Oxide(ITO)/Zinc Oxide(ZnO) as electron collecting bottom contact and molybdenum(VI) oxide(MoOx)/Silver(Ag) as hole collecting top contact, shown in Figure 3.1c. More details on the device fabrication and characterization are described in the experimental section.

The HOMO level of Pd(PPh$_3$)$_4$ was found to be located at −7.28 eV by Ultraviolet Photon Spectroscopy (UPS) (Figure S3.1), and a band gap of 2.98 eV was obtained from optical measurements leading to a LUMO level at −4.30 eV. The energy levels of PTB7-Th and IOTIC-

4F were taken from literature.[217,218] The resulting energy band diagram of the PTB7-Th, IOTIC-4F and Pd(PPh3)4 system is displayed in Figure 3.1 b).
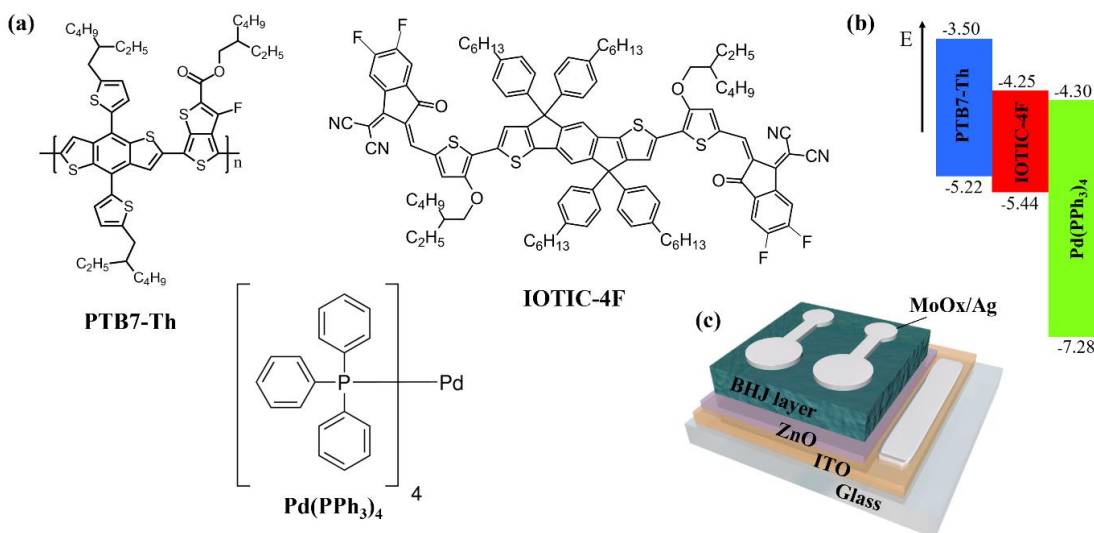
Figure 3.1. a) Chemical structures of the BHJ blend system and the Pd-catalyst, b) Energy Band Diagram, c) a schematic of the device architecture.

First of all, we obtained the electrical and photoelectrical properties of the BHJ solar cells to assess the impact of Pd(PPh3)4 on the solar cell performance. The current-voltage characteristics of the PTB7-Th:IOTIC-4F solar cells with and without Pd(PPh3)4 under 1 sun AM 1.5 illumination are shown in **Figure 3.2,** and the extracted photoelectrical parameters are displayed in **Table 3.1**. The addition of Pd(PPh3)4 most noticeably reduces the J_{sc} and FF and slightly lowers the V_{OC}. Upon addition of 7% of Pd(PPh3)4 to the active layer the J_{sc} drops from 24.6 mA/cm² to 16.7 mA/cm², the V_{OC} decreases from 0.71 V to 0.67 V and the FF is reduced from 60.5% to 45.5%, resulting in a large decrease of the performance from 10.5% to 5.1%. We notice that the addition of only a small amount (0.75% catalyst) does not lead to a decreased device performance. The threshold amount that yields significant changes is reached when 3% of Pd(PPh3)4 are added, resulting in a PCE of 5.9%.

We further applied the same approach to PM6:Y6 based OPVs. PM6:Y6 has gathered much attention due to performances of over 15% and has become a well-studied model system for solar cells based on Y-series acceptors.[180,182,214–216] Overall, the behavior of this system is very similar to the discussed performance changes of the PTB7-Th:IOTIC-4F system. The PCE of 15.4% (0% added catalyst) decreases to 15.0%, 12.5%, and 10.5% for devices with 0.75%, 3%, and 7% $Pd(PPh_3)_4$, respectively (see Table S3.4 and Figure S3.24). Again, mainly the J_{sc} and the FF are reduced (from 26.3 to 20.1 mA/cm^2 and from 0.71 to 0.64) and only a slight change in the V_{oc} observed (from 0.83 V to 0.81 V). The changes of the J_{sc} are reflected in the EQE spectra as well, as seen in Figure S24b, and no shift in the EQE response can be seen. The addition of small amounts (0.75%) of catalyst does not significantly impact the performance of the PM6:Y6 cells.

The EQE spectra of the PTB7-Th:IOTIC-4F solar cells (Figure 3.2b) show that the EQE decreases with the catalyst concentration and a lower EQE is observed for systems with more catalyst at the same wavelength. It is important to note that this does not indicate that the self-absorption edge is blue-shifted with added catalyst. The absorption range is in fact not altered by the addition of $Pd(PPh_3)_4$, as can be seen from the discussion of the band gap values further below and from Figure S3.16.

Further, they reflect the decrease in J_{sc}, lowering the maximum EQE from 75.5% to 53.6% upon the addition of 7% catalyst to the active layer blend. Next, we will focus on the understanding of these performance changes.

Table 3.1. Photoelectrical parameters of the PTB7-Th:IOTIC-4F BHJ solar cells with different amounts of $Pd(PPh_3)_4$ under 100 mW/cm^2 AM1.5 illumination. (wt% and mol% with respect to the PTB7-Th repeat unit).

$Pd(PPh_3)_4$ (wt%)	$Pd(PPh_3)_4$ (mol %)	J_{sc} (mA/cm^2)	V_{OC} (V)	FF (%)	PCE (%)
0	0	24.6 ± 0.5	0.71 ± 0.01	60.5 ± 1.7	10.5 ± 0.5
0.75	0.60	24.0 ± 0.5	0.72 ± 0.01	62.5 ± 1.6	10.8 ± 0.3
3	2.37	19.0 ± 0.9	0.67 ± 0.01	46.9 ± 1.0	5.9 ± 0.3
7	5.57	16.7 ± 0.2	0.67 ± 0.01	45.5 ± 0.3	5.1 ± 0.2

(a)

(b)
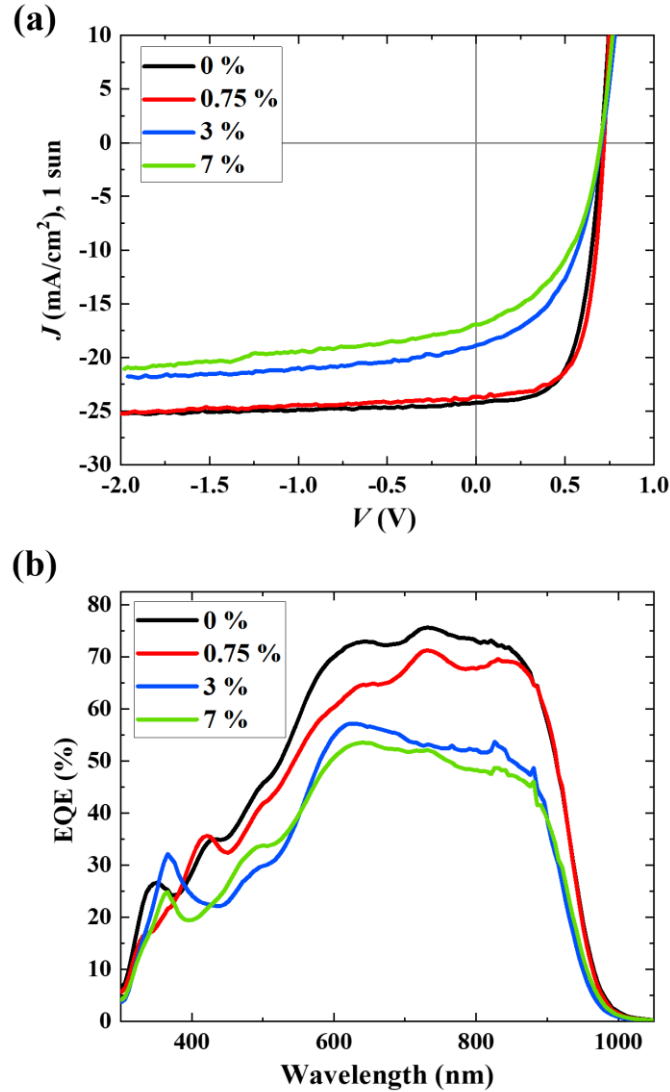
Figure 3.2. Current-Voltage characteristics of solar cells with different amounts of Pd(PPh$_3$)$_4$ added to the active layer under 100 mW/cm^2 AM 1.5 illumination

An optimized morphology is crucial for the performance of organic BHJ photovoltaics, as many previous studies have shown that morphological changes impact the device performance.[215,219–225] It is well understood that the structure of the percolating network of the donor and acceptor material in the BHJ and the degree of crystallinity of the active layer influence the device characteristics, as both charge transport and charge extraction can be altered.[215,223,226] Further, the degree of mixing and the interfacial orientation influences the generation of free

59

charge carriers and the recombination processes.[220,221,227] The degree of phase separation of the material blend can change the generation of free charge carriers in the solar cell as well.[224,228]

As a first step towards the in-depth understanding of the observed changes in the device performance, we studied the surface morphology, the molecular ordering, and orientation as well as the mesoscale phase separation. The surface morphology of the active layers with 0% and 7% $Pd(PPh_3)_4$ was characterized by Atomic Force Microscopy (AFM), shown in Figures S3.3 and S3.4 and S3.5, respectively. The 5 μm x 5 μm AFM topography scans of the PCE10:IOTIC-4F solar cell active layers with 0% and 7% $Pd(PPh_3)_4$ show a similar nanoscale morphology with comparable surface roughness with a root-mean-square (RMS) of 2.2 nm and 1.4 nm (Figure S3.3a and S3.4a. Higher resolution images (2 μm x 2 μm) show indistinguishable features (Figure S3.3b and S3.4b), indicating that the presence of $Pd(PPh_3)_4$ does not alter the surface morphology. In addition, wider area morphology AFM images of the sizes 20 x 20 μm and 50 x 50 μm were obtained in tapping mode (Figure S3.5). No larger features were revealed, and the surface morphology appears similar in the films with and without added catalyst. The 20 x 20 μm and 50 x 50 μm blend film images without catalyst showed a roughness of 1.75 nm and 0.97 nm respectively, and the ones with 7% $Pd(PPh_3)_4$ revealed comparable RMS values of 1.24 and 1.07 nm.

Photoconductive AFM probes simultaneously the nanoscale morphology and the photocurrent (current under illumination minus dark current). Photoconductive AFM images of the active layers obtained at 0 V bias using a gold-coated tip reveal well-mixed donor:acceptor phases for the 0% catalyst film (Figure S3.3c and S3.3d). A positive photocurrent is due to the extraction of photo-generated holes, and a negative photocurrent is due to the extraction of photo-generated electrons by a high work function metal tip from the sample; therefore, the bright and dark features correspond to donor and acceptor rich domains, respectively. The

magnitude of the photocurrent is a measure of how efficiently charge carriers are extracted. Figure S3.6 shows the current histograms for the 5 µm x 5 µm nanoscale current images. It can be seen, that 95% of the measured points for the 0% sample lie between −18.6 pA and +27.0 pA, whereas the sample with added catalyst has a narrower distribution of current values with 95% of them being in the range from −6.36 pA to 8.00 pA, which is also reflected by the scales of the photocurrent images (Figure S3.4c and d). The reduced magnitude of the photocurrent indicates that fewer holes and electrons are extracted, which implies either reduced charge generation or increased charge recombination or inefficient extraction of charge carriers from the device with added $Pd(PPh_3)_4$. This result agrees with the observed changes in the device performance, and we will discuss the altered charge generation, recombination, and extraction further in the remaining text.

Next, grazing-incidence wide-angle X-ray scattering (GIWAXS) was performed to gain insight into the molecular ordering of the PTB7-Th:IOTIC-4F blends and of the neat components. The 2D-GIWAXS patterns are provided in Figure S3.7. The 1D linecuts show the scattered intensity in the q_z plane, perpendicular to the substrate, and the q_{xy} plane, parallel to the substrate (Figure S3.8). The use of the Scherrer equation allows for the determination of coherence lengths (L_c).[229] These values indicate the distance over which each observed molecular ordering feature is maintained in the film. Both blend components orient face-on relative to the substrate as indicated by the presence of intense scattering at high q_z and low q_{xy}. This means that the π-conjugated backbones in these materials are oriented face-on with respect to the substrate, which is beneficial for the charge transport in OPV devices.[230] The orientation is unaltered by the addition of $Pd(PPh_3)_4$. Lamellar stacking in the donor PTB7-Th appears at 0.27 q_{xy} (d = 2.34 nm; L_c = 6.39 nm) with a higher-order reflection at 0.86 q_{xy} (d = 0.73 nm; L_c = 2.77 nm). The donor displays π-stacking at 1.63 q_{xy} (d = 0.39 nm; L_c = 1.06 nm). These stacking distances are in good

agreement with those previously reported for this material.[231] IOTIC-4F lacks higher-order diffraction peaks often observed in small molecule non-fullerene acceptors signaling a relatively low degree of ordering.[228] Scattering due to π-stacking is present at 1.86 q_z (d = 0.34 nm; L_c = 2.93 nm); lamellar stacking appears at 0.31 q_{xy} (d = 2.00 nm; L_c = 14.12 nm). Except for the off-axis scattering from IOTIC-4F, the scattering features from both blend components are present in the PTB7-Th:IOTIC-4F blend film.

Comparison of the scattering of the blend film without catalyst with the neat donor and acceptor films shows that the stacking distances do not change significantly. However, the L_c for lamellar stacking from IOTIC-4F is reduced in the blend, indicating a decrease in the ordering of the NFA. Upon addition of the catalyst Pd(PPh$_3$)$_4$, the L_c for lamellar stacking in IOTIC-4F slightly decreases further. This does not appear to be correlated with the amount of catalyst present. The coherence length L_c for lamellar stacking in PTB7-Th decreases in the blend compared to the neat film from L_c = 6.39 nm to L_c = 4.55 nm. Upon addition of 0.75% Pd(PPh$_3$)$_4$, the lamellar stacking rises back to L_c =5.97 nm, whereas the addition of larger quantities of the catalyst leads to a decrease of the stacking distance (3%: L_c =4.97 nm, 7%: L_c =2.98 nm), suggesting that small amounts of Pd(PPh$_3$)$_4$ may be beneficial for the ordering. These observations are in line with the decrease in performance only beyond catalyst concentrations of 3% or more, suggesting that the stacking on the nanoscale is one parameter that governs the performance in the studied systems. Other stacking distances and coherence lengths are not significantly altered for the blend components upon catalyst addition.

To investigate the morphology on the mesoscale and to probe phase separation, we performed Resonant Soft X-ray Scattering (RSoXS) (Figures S3.9 and S3.10, Table S3.1) on films with 0%, 0.75%, 3% and 7% catalyst added. For all films, a bimodal size distribution is observed. The most noticeable change upon addition of the catalyst is the increase of the long period L_1 of the larger

domain from 87 nm to 179 nm, comparing the films with 0% and 7% Pd(PPh$_3$)$_4$. An increase in the domain size decreases the surface to volume ratio and thus reduces the donor-rich and acceptor-rich domain's interfacial area. A resulting decrease of exciton splitting for free charge carrier generation and with that, a reduction of J_{sc} and PCE is expected and in line with the observed drop in the device performance.[232–234] The altered domain size can influence the percolating network structure, and therefore, a change in extraction and recombination (reflected in lowering J_{sc}, V_{oc} , FF and PCE) is possible as well. This change of the morphology upon addition of the catalyst is pronounced, but not linear, as slightly reduced domain sizes are found for the other catalyst concentrations (68 nm and 76 nm), and the scattering intensities (Figure S3.9) do not decrease monotonically. Therefore, we conclude that other parameters of influence contribute to the changes in performance as well. The size of the smaller domains does not change significantly with catalyst addition (L_2= 27 nm $\pm$ 6 nm in all films). Further, the RSoXs analysis allows a comparison of the degree of mixing.[222,225] The overall variance of the composition σ^2 integrated overall lengths scales is measured *via* the scattering intensity, and the resulting standard deviation σ serves as a relative parameter to assess the average domain purity. The difference of σ between the films is small, ranging from 0.96 to 1, indicating a comparable degree of mixing. Overall, the presence of the catalyst reduces the magnitude of the nanoscale current, it impacts the mesoscale morphology and alters the nanoscale stacking distance in IOTIC-4F, whereas the surface morphology and other nanoscale stacking distances/coherence lengths remain the same.

Energetic disorder in organic semiconductors, often given rise to by the morphology, is known to be another factor that can impact the device performance. The energetic disorder is directly related to the width of the density of states (DOS), and a broader distribution of states leads to inferior transport properties that lower the PCE.[141,235,236] To investigate whether the addition of the catalyst induces changes in the energetic disorder, the Urbach energy E_u was determined from

the low energy tail of the external quantum efficiency (EQE) spectra (see Figure S3.11 and Table S3.3). For the devices with 0% to 7% catalyst comparable E_u values of 26.8 meV, 25.5 meV, 24.5 meV and 27.0 meV with standard deviations below 0.7 meV are obtained, respectively, showing that E_u does not correlate with the Pd(PPh$_3$)$_4$ concentration. Therefore, we assume that energetic disorder can be excluded as a parameter of influence on the electronic processes in the devices and the catalyst does not broaden the DOS distribution.

To exclude shunt leakage current as another possible reason for the performance losses, we determined the shunt resistance R_{sh} from the differential resistance at 0 V (see Figure S3.17 for the differential resistance in dependence on the voltage for representative devices and Table S3.3 for average values of R_{sh}). The shunt resistance remains high upon the addition of Pd(PPh$_3$)$_4$, with $R_{sh} > 4.3 \cdot 10^4 \pm 1.3 \cdot 10^4$ for all concentrations, demonstrating that unlike observed in other studies, the devices show robustness towards the addition of Pd(PPh$_3$)$_4$ for the studied concentrations.[212] Furthermore, we observe no change in the optical band gap which was found to be 1.31 eV from extrapolation of the low energy tail in the $(EQE \cdot h\nu)^2$ or $(\alpha \cdot h\nu)^2$ versus energy plot, with α being the absorption coefficient (see Figure S3.16), indicating that the energy levels are not altered by the addition of the catalyst.

As the next step towards the understanding of the observed changes in the photoelectrical parameters with an increase of Pd(PPh$_3$)$_4$, and, more specifically, to understand the decrease in J_{sc} we focus our attention on the photogeneration and on losses that occur before the formation of free charge carriers. Upon absorption of a photon, an exciton is generated in the active layer that diffuses to the donor:acceptor interface to form a charge transfer (CT) state, which then can separate into free electron and hole.[158,237–240] Not all of these coulombically bound geminate pairs split into free charge carriers, though, because of geminate recombination.[237,158,238–241] Further,

since we investigate a system with an added impurity, the formed excitons likely undergo quenching even before a geminate pair can be formed.[80,105,242,243]

To probe the combined effect of these fast losses, we first simulated the charge generation in the BHJ active layer. To do so, we prepared four films of the different blends with and without added catalyst and calculated the refractive index n and the extinction coefficient k of each film from the measurement of reflectance R and transmittance T (see Supporting Information Figure S3.11, Equation S3.1 to Equation S3.3). Only minor unsystematic changes in k around 900 nm, as well as a slight reduction in the refractive index n for all films with the catalyst, can be seen, indicating that the absorption of photons is only marginally changed. The optical properties of the active layer, in conjunction with those of all other device layers as well as the device architecture, determine the amount of light absorbed and the interference pattern within the device and the active layer.[130,241,244] A change in the optical properties will result in a change of the generation rate G of charge carriers that are photo-generated in the active layer, and with that, the theoretical maximum of the J_{sc} changes. We illuminated the devices with a solar simulator and measured the current voltage-characteristics to obtain the saturated photocurrent $J_{ph,sat}$ at large reverse bias. The photocurrent J_{ph} was determined by subtracting the light current J_l from the dark current J_d. At -2 V, most charge carriers are extracted due to the high internal electric field in the active layer. It is possible to assume 100% extraction at this bias, but for accuracy, we further corrected the measured photocurrent at −2 V (Figure S3.13, Table S3.2) by the extraction efficiency at this bias, which was determined by applying the Hecht equation (discussed later) to calculate the saturated photocurrent $J_{ph,sat}$ (Table S3.2). Next, we simulated the J_{sc} for the same illumination condition with transfer matrix method based simulations.[162] The simulated J_{sc} is a theoretical value that would be obtained if the absorbed photon flux yields electron flux in the outer circuit without any losses.[241] The difference between the experimentally obtained $J_{ph,sat}$ that

excludes extraction losses (and with that non-geminate recombination losses), and the simulated J_{sc} is therefore attributed to geminate recombination losses, and, in this system with added impurity, also to exciton quenching by $Pd(PPh_3)_4$. The ratio of $J_{ph,sat}$, and the simulated J_{sc}, here called $P_{e,g}$, is shown in **Figure 3.3a**.

The PTB7-Th:IOTIC-4F solar cell system without catalyst does not suffer from exciton quenching or geminate recombination losses, and $P_{e,g}$ approaches unity. The added catalyst in the active layer increases these fast losses (Figure 3.3a, Table S3.2) and $P_{e,q}$ values of 0.93, 0.78, and 0.73 are found, which directly correlate with the reduced J_{sc} and FF. To elucidate further whether exciton quenching plays a role in the reduction of $P_{e,g}$ as suspected upon addition of an impurity, we performed steady-state photoluminescence measurements of the neat materials, with and without the added catalyst. The fluorescence intensity of a pure PTB7-Th film is reduced to 63% (integrated area over the measured range from 685 nm to 1007 nm) upon the addition of 7 wt% of $Pd(PPh_3)_4$ (Figure S3.14a), whereas the addition of 7 wt% $Pd(PPh_3)_4$ to a film of pure IOTIC-4F causes a much steeper drop in fluorescence to 3% of its original value (based on the integration of the obtained data from 726 nm to 1077 nm, see Figure S3.14b. From these results, we conclude that in the BHJ solar cell, the catalyst molecule causes exciton quenching leading to a reduction of free charge carriers and a reduction of J_{sc} and FF. Geminate recombination is known to be closely linked to changes in the nanoscale morphology.[96,245,246] Since we did not observe major changes in the nanoscale morphology and the nanoscale packing (pc-AFM, GIWAXs), we assume that the contribution of exciton quenching is the main factor for the reduction of $P_{e,q}$ and with that for the reduction of the performance. To instill further confidence in this hypothesis, time-resolved photoluminescence (PL) measurements were performed on the blend, the donor, and the acceptor material, as well as on the donor and acceptor materials with added catalyst. In the case of the blend, the obtained PL decay shows only the instrument response function. (Figure

S3.15a This indicates that the BHJ blend efficiently separates electron-hole pairs at the interfaces, quenching the emissive decay pathway to the extent that a PL lifetime could not be resolved. The time-correlated single photon counting results (Figure S3.15) for PTB7-Th films show about 30% reduction of the PL lifetime from 0.46 ns to 0.32 ns upon addition of 7% $Pd(PPh_3)_4$. In the case of IOTIC-4F films, the addition of catalyst leads to a PL lifetime reduction of 25% from 0.24 ns to 0.18 ns. These results demonstrate that the catalyst acts as a collisional quencher. After the exciton is formed upon light absorption, it diffuses until it reaches the catalyst where it undergoes non-radiative exciton decay to the ground state. Shorter lived excitons do not diffuse far enough to reach a quencher and are able to return to the ground state radiatively. This results in the shortening of the photoluminescence lifetime upon the addition of the catalyst quencher to the film. We can conclude that the catalyst indeed acts as an exciton quencher in both donor and acceptor domains.

To further investigate the effect of $Pd(PPh_3)_4$ on the electronic processes in the solar cells, we examined the voltage dependence of the photocurrent J_{ph} as a measure of charge extraction, shown in Figure 3.3b. The corrected voltage was determined from the applied voltage V, corrected for the effect of the series resistance R_s, as $V_{corr}=V-JR_s$. The effective voltage is then calculated as $V_{eff} = V_0-V_{corr}$. Figure 3.3b shows that the photocurrent decreases with increasing catalyst concentration indicating that the free charge carrier generation is not efficient, which is in agreement with the previously discussed results. Additionally, the saturation regime is shifted to higher effective voltages for higher catalyst concentration and not reached for the system with 7% added catalyst within the measured voltage range, indicating that higher internal fields are required to sweep out charge carriers. This adds to the explanation of reduced photocurrents that were seen in the photoconductive AFM scans, as discussed earlier and to the reduction of J_{sc}. Poor extraction can be caused by a decrease in the charge carrier effective mobility μ_{eff} or by a

reduction of the effective recombination lifetime τ_{eff}.[247–250] We will explore these possibilities in detail in the remaining text. The dependence of the photocurrent on the effective voltage can further give information about the presence of space-charge. In the case of built-up space-charge, a square-root dependence is expected.[197,247,251] In all cases, this dependence is not observed, indicating the absence of built-up space-charge, which can result from imbalanced mobilities.
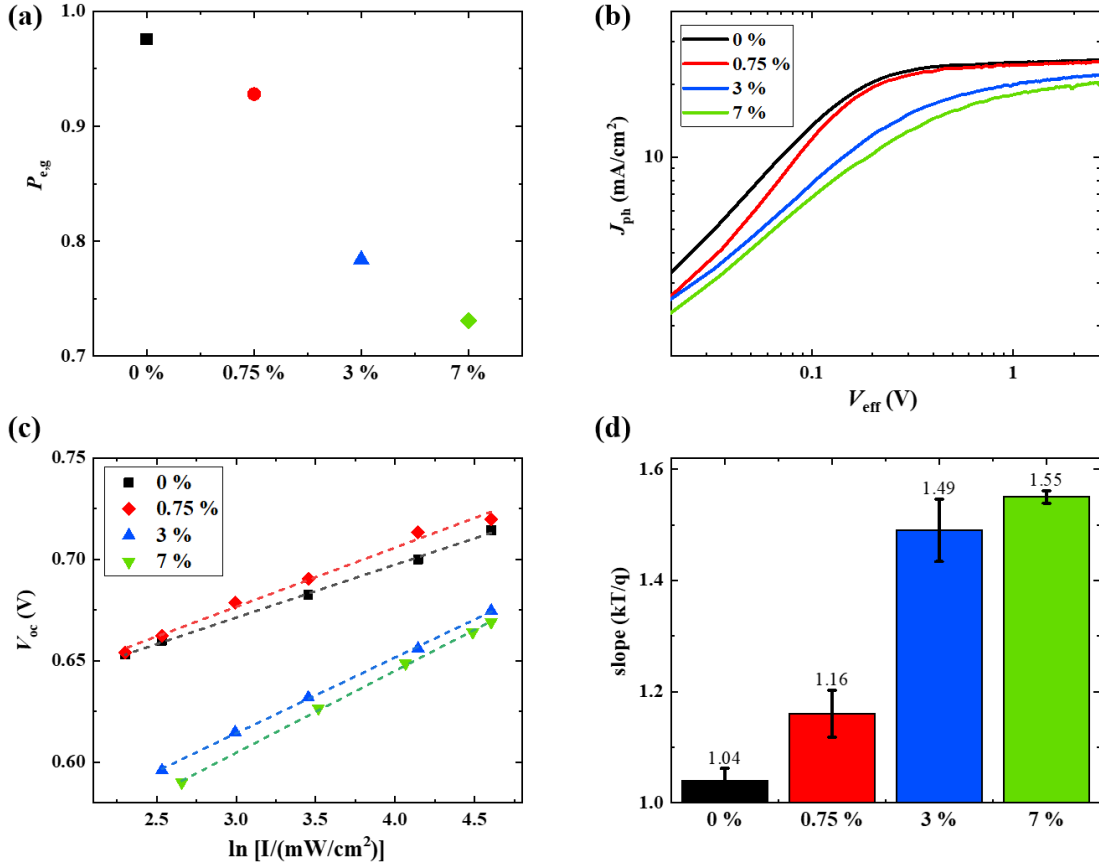
Figure 3.3. a) Geminate recombination and exciton quenching prefactor $P_{e,g}$ with added catalyst, b) photocurrent versus corrected voltage $V_{eff}=V_0-V_{corr}$, c) V_{oc} versus light intensity and d) the respective slopes of the PTB7-Th:IOTIC-4F solar cells with different amounts of Pd(PPh$_3$)$_4$ added to the active layer.

Having discussed the effect of losses before the formation of free charge carriers, we now consider non-geminate losses, which can lower J_{sc}, V_{OC} and FF. Investigating the dependence of

the V_{oc} on the light intensity I is a widely used approach to study recombination under V_{oc} conditions. This technique serves as a first qualitative assessment of the dominant recombination mechanism. Depending on the slope of the V_{oc} on the natural logarithm of the light intensity I, information about the dominant recombination mechanism can be inferred, according to the relationship $V_{oc} \propto kT/q \cdot \ln(I)$, with the k being the Boltzmann constant, T the temperature and q the elementary charge. In the case of systems with dominant bimolecular recombination, a slope of 1.0 kT/q is expected. Surface trap-assisted recombination can lower this value, whereas the presence of bulk trap-assisted recombination is known to increase the slope.[99,100,159] The dependence of the V_{oc} on $\ln(I)$, displayed in Figure 3.3c, reveals a strong dependence on the catalyst concentration. The reference system without catalyst exhibits a slope close to 1.0 kT/q, the addition of 0.75% catalyst increases the slope slightly to 1.16 kT/q, and adding 3% and 7% catalyst increases the slope further to 1.49 and 1.55 kT/q, respectively, indicating an increase of bulk traps upon addition of $Pd(PPh_3)_4$ (Figure 3.3d).

To further investigate both charge recombination and extraction quantitatively, we employed impedance-voltage spectroscopy followed by the fitting of the experimental recombination current to quantify important recombination parameters as well as both effective mobility and effective recombination lifetime.[136] By measuring the frequency and voltage-dependent real and imaginary parts of the impedance, and after correcting for series resistance and inductance, we obtained the corrected capacitance spectra that are shown in Figure S3.19 for the devices with different catalyst concentrations under 1 sun illumination and in the dark.

In a first step, we calculated the dielectric constant of the BHJ active layer with different catalyst concentrations from the capacitance spectra measured in the dark. The dielectric constant of the BHJ active layer is not only an important material characterization parameter to be studied in the framework of investigating the effect of residual catalyst but also required to study the

recombination processes. The recombination current is inversely proportional to ε.[252,253] Typically, only the voltage-independent capacitance at large reverse bias, referred to as the geometric capacitance C_g, is considered to determine the dielectric constant of the BHJ active layer, neglecting capacitive effects of the electrodes. In the case of highly conductive metal electrodes or very thick active layers, this approximation is justified but as we employed ZnO as bottom contact, its capacitive effects should be considered.[64] Figure S3.18 shows the Nyquist plot and the capacitance of a 170 nm thick ZnO film, prepared in the same fashion as the electrode by a sol-gel method, sandwiched between ITO and a top metal contact. The dielectric constant obtained for the ZnO was found to be 4.74 ± 0.14 and its capacitance $C_{ZnO} = \varepsilon_{ZnO}\, \varepsilon_0 A / d_{ZnO}$ was taken into account for the analysis of the devices, assuming two capacitors in series, according to Equation 3.1.

$$\varepsilon = \frac{\frac{C_g \cdot C_{ZnO}}{C_{ZnO} - C_g} d}{\varepsilon_0 A} \tag{3.1}$$

We found that the dielectric constant of the BHJ active layer is not affected by the incorporation of $Pd(PPh_3)_4$, with ε in the narrow range from 3.00 ± 0.28 to 3.16 ± 0.15 (compare Table S3.3).
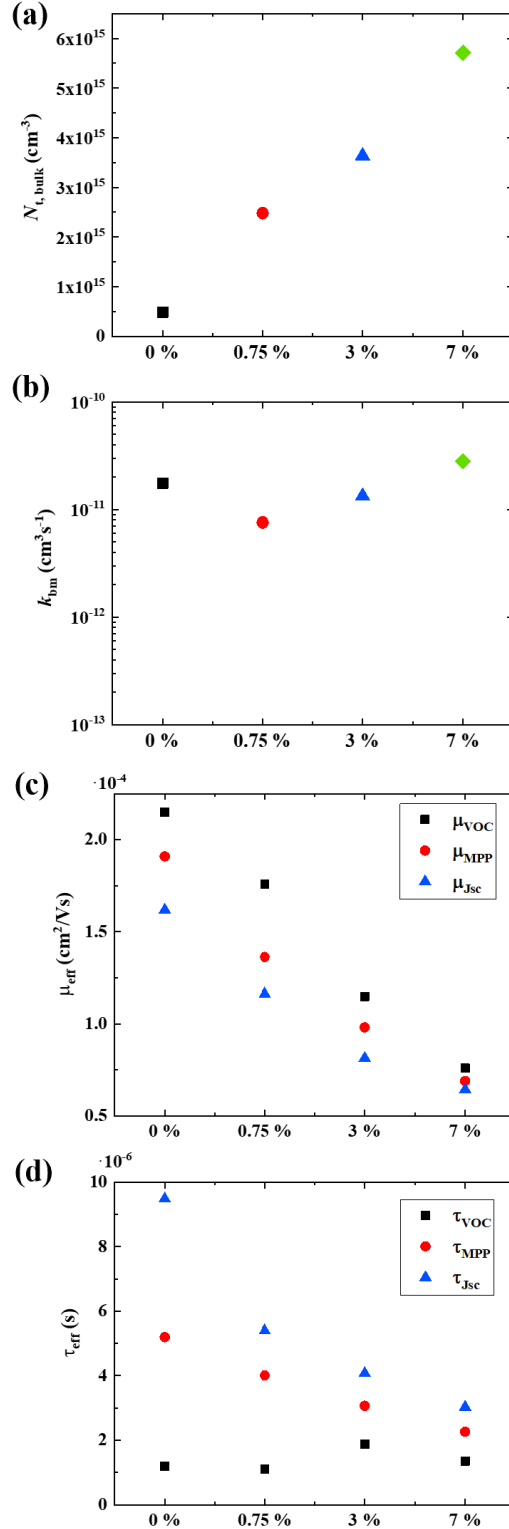
Figure 3.4. a) Bulk trap concentration N_t, b) bimolecular recombination coefficient k_{bm} c) μ_{eff} and d) τ_{eff} at MPP, V_{oc} and J_{sc} for devices with different Pd(PPh$_3$)$_4$ concentrations (0%, 0.75%, 3%, and 7%) determined by impedance-voltage spectra analysis.

The recombination current $J_{rec} = J_{ph} - J_{ph,sat}$ was fitted according to the recently published model by Vollbrecht and Brus et. al.,[137] taking into account the contributions of bimolecular recombination, surface trap and bulk trap assisted recombination, resulting in the Langevin prefactor ξ for bimolecular recombination, the density of surface traps $N_{t,surf}$ and the density of bulk traps N_t, from which the effective recombination lifetime τ_{eff} can be calculated (fits of the recombination current are shown in Figure S3.20). Surface recombination plays a minor role in all devices that were investigated with $N_{t,surf} < 1.1 \times 10^{12} \, cm^{-3}$, values that are low for this recombination mechanism.[137]

N_t, is of particular interest in the context of studying the effect of residual catalyst, since impurities are expected to facilitate bulk trap assisted recombination, which is possibly detrimental for the performance as explained earlier. **Figure 3.4a** correlates the bulk trap concentration with the amount of added $Pd(PPh_3)_4$. A steady increase with increasing $Pd(PPh_3)_4$ concentration in the active layer is observed, the difference between the system with 7% and the system with 0% catalyst, exceeding one order of magnitude (Table 3.2). We now consider these numbers further and relate them with the amount of added $Pd(PPh_3)_4$ to determine the 'trap efficiency' (E_t), which is the number of created deep bulk traps that act as efficient recombination centers per added molecule of $Pd(PPh_3)_4$. To do so, we determined the density of a PTB7-Th:IOTIC-4F film with X-ray reflectivity (the fit is shown in Figure S3.23). Based on the weight fraction of the catalyst in each blend, the determined film density, and the molecular weight of $Pd(PPh_3)_4$, we calculate the number of added $Pd(PPh_3)_4$ molecules per cubic centimeter of the BHJ active layer N_{cat} (Table 3.2). The increase of the concentration of bulk traps of each system with added catalyst compared to the reference system with 0% catalyst is also shown in Table 3.2. We define the ratio of the introduced traps per introduced $Pd(PPh_3)$ molecule as the trap efficiency E_t, with values of 0.03%, 0.1% and 0.07%, demonstrating that only a small fraction of

the added $Pd(PPh_3)_4$ leads to the formation of deep bulk traps. One explanation is that $Pd(PPh_3)_4$ and its decomposition products may cluster, as it is known for Pd nanoparticles, into larger aggregates.[188] Another possible explanation for this result is supported by the proposed energy band diagram, which shows that the introduced catalyst traces do not have an energy level that is near the mid-gap. Shallow traps are expected to play a minor role in recombination according to the Shockley-Read-Hall theory. To summarize, a fraction of added $Pd(PPh_3)_4$ creates bulk traps and thus, trap assisted recombination is a concern for the PTB7-Th:IOTIC-4F solar cells and explains the reduction of free charge carriers and reduction of V_{oc} and reduction of the FF.

The bimolecular recombination coefficient k_{bm} is derived from the Langevin reduction factor ξ. From Figure 3.4b, it is evident that k_{bm} changes with catalyst concentration. The reference system has a k_{bm} of $1.76 \cdot 10^{-11}$ $cm^3 s^{-1}$. The reduction of k_{bm} to $0.76 \cdot 10^{-11}$ $cm^3 s^{-1}$ for 0.75% added catalyst resonates with the performance and the slightly increased L_c observed in GIWAXS. Further increase of the $Pd(PPh_3)_4$ content increases k_{bm} to $1.33 \cdot 10^{-11}$ $cm^3 s^{-1}$ and $2.82 \cdot 10^{-11}$ $cm^3 s^{-1}$. This correlates with the L_c values for the 3% and 7% blend films found determined with GIWAXS. Considering that the range of reported k_{bm} values is approximately between 10^{-14} to 10^{-9} $cm^3 s^{-1}$, the observed changes are minor.[170] We conclude that bimolecular recombination contributes to a moderate extent to the reduced device performance in these systems and assume that the observed changes originate from the morphological alterations that are seen on the nanoscale.

The effective mobility was determined assuming similar mobilities for electrons and holes as:[136]

$$\mu_{\text{eff}}(V) = \frac{J_L}{2\,q\,d\,n(V)\,|V_0 - V_{\text{corr}}(V)|} \tag{3.2}$$

The addition of 0.75% Pd(PPh$_3$)$_4$ causes a drop of the mobility by about 30% compared to the reference system from 1.90 ·10^{-4} cm^2/Vs to 1.36 ·10^{-4} cm^2/Vs (at MPP). The addition of larger quantities results in a further decrease of μ_{eff}, to roughly half of the original values for 3% (μ_{eff} = 0.98 ·10^{-4} cm^2/Vs) and to about one-third of the original value (μ_{eff} = 0.0.69 ·10^{-4} cm^2/Vs) for 7% added Pd(PPh$_3$)$_4$. The drop in μ_{eff} is evident at J_{sc}, at the maximum power point (MPP) and at V_{oc} in a similar magnitude. The reduction of the mobility matches with the earlier described indication of poor extraction with added catalyst. The changes in mesoscale morphology in cooperation with the nanoscale morphology may explain these results.

Table 3.2. Density of introduced catalyst molecules N_{cat} calculated based on the density determined by X-ray reflectivity (Figure S3.23), bulk trap concentrations N_t, the difference in bulk trap concentration compared to the system without added catalyst $N_{t,0\%}$-$N_{t,i\%}$ and the resulting trap efficiency E_t.

Pd(PPh$_3$)$_4$ (%)	N_{cat} (cm^{-3})	N_t (cm^{-3})	$N_{t,0\%}$ - $N_{t,i\%}$ (cm^{-3})	E_t
0		4.87 · 10^{14}		
0.75	7.79 · 10^{17}	2.48 · 10^{15}	1.99 · 10^{14}	0.03%
3	3.09 · 10^{18}	3.63 · 10^{15}	3.14 · 10^{15}	0.1%
7	7.09 · 10^{18}	5.71 · 10^{15}	5.22 · 10^{15}	0.07%

With all recombination contributions being quantified by the recombination rates k_{bm}, k_{sf}, k_b for bimolecular, surface, and bulk trap-assisted recombination, the effective recombination lifetime τ_{eff} can be calculated. (Equation 3.4)

$$\tau_{eff}(V) = \frac{1}{k_{bm}\, n(V) + k_{sf} + k_b} \tag{3.4}$$

From Figure 3.4d it is evident that added Pd(PPh$_3$)$_4$ impacts the effective charge carrier lifetime significantly for all concentrations, which is most dominant under short circuit conditions but also evident at the MPP. This shows that the outlined contributions of bulk traps and bimolecular

recombination are significant for the studied systems. At V_{oc} the lifetime is short due to the lack of an internal field as a driving force for extraction and charges recombine fast, and as expected, no trend can be seen.

To quantify the result of the reduced mobility and lifetime on the extraction of charge carriers, we first determined the built-in field of the devices from the dark JV-curves (Table S3.3). The extraction efficiency η depends on the internal field F in the active layer, which can be expressed as $F=(V_{bi}-V_{corr})/L$, with L being the active layer thickness. The Hecht Equation originally describes the extraction efficiency of photo-generated electron-hole pairs, spatially dependent on the distance to the anode and cathode.[254] We assume the charge carriers to be on average separated by $L/2$ from the extracting contact. Then the probability of charge being extracted can be described as:

$$\eta = \frac{\mu \tau F}{L/2}\left(1 - exp\left(\frac{-L/2}{\mu \tau F}\right)\right) \tag{3.5}$$

The resulting voltage-dependent extraction efficiency is shown in Figure S3.21c. **Figure 3.5** shows η for the PTB7-Th:IOTIC-4F solar cells with different concentrations of Pd(PPh$_3$)$_4$ at J_{sc} and the MPP. With increasing Pd(PPh$_3$)$_4$ concentration, a decrease in η can be observed, which is most prominent under small forward bias, adding to the explanation why the addition of Pd(PPh$_3$)$_4$ decreases the performance of the solar cells. At the MPP, originally η exceeds 90%, whereas when 7% catalyst are added η is only about 60%. Further, we can determine the extraction efficiency of charge carriers at a reverse bias of -2 V, which we used to quantify geminate recombination losses more accurately than by assuming 100% extraction at -2 V.
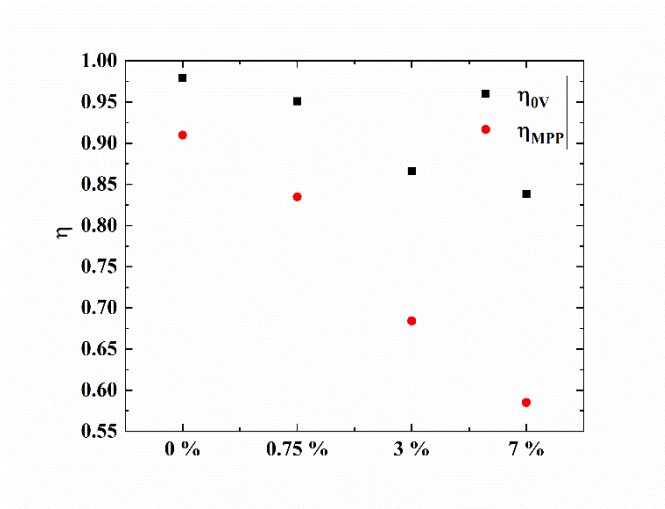
Figure 3.5. Extraction efficiency η in dependence on the amounts of catalyst added to the active layer.

3.3 Conclusions

To conclude, the addition of controlled amounts of 0.75%, 3% and 7% Pd(PPh$_3$)$_4$ leads to a decrease of the performance in the NFA-based PTB7-Th:IOTIC-4F BHJ solar cell from 10.5% to 5.1%. We have shown that the nanoscale molecular ordering and the mesoscale morphology are altered, whereas the effective band gap, and energetic disorder are not significantly impacted by the addition of Pd(PPh$_3$)$_4$. The analysis of impedance spectroscopy data of the blend systems with different amounts of catalyst revealed a small increase in bimolecular recombination when amounts of Pd(PPh$_3$)$_4$ larger than 3% were added (1.76 10^{-11} cm^{3}s^{-1} to 2.82 ·10^{-11} cm^{3}s^{-1}). Effective mobility and effective charge carrier lifetime are reduced upon the addition of Pd(PPh$_3$)$_4$, which we have shown to result in less efficient extraction (> 90% to < 60% at MPP). A moderate increase of bulk traps with increased amounts of Pd(PPh$_3$)$_4$ was observed (4.87 × 10^{14} cm^{-3} to 5.71 × 10^{15} cm^{-3}), based on the fitting of impedance spectroscopy data, that contributes to the decrease

of the performance. However, the catalyst does not act as an efficient recombination center and less than 0.1% of the introduced molecules act as a trap.

The study of fast losses, based on our approach of combining experimental saturated photocurrent and optical modeling, revealed that the addition of catalyst has a major impact on the generation of free charge carriers (P_g reduced from unity to 0.73 for 7% added catalyst). Steady-state photoluminescence measurements confirmed that $Pd(PPh_3)_4$ acts as an exciton quencher and time-resolved photoluminescence revealed that the catalyst causes a reduction of the exciton lifetime in both the donor and acceptor. In contrast to previous reports on fullerene-based OPVs, the observed drop in performance cannot be solely attributed to trap-assisted recombination but is the result of the interplay of altered material properties and different loss mechanisms. As a final note, we state that the PTB7-Th:IOTIC-4F system showed substantial robustness to the addition of $Pd(PPh_3)_4$ in moderate amounts (0.75%), which are expected typically not to be exceeded after the material purification process.

3.4 Experimental Section

Ultraviolet Photon Spectroscopy (UPS)

UPS measurements were carried out in a PHI 5600 ultrahigh vacuum system with an 11-inch diameter hemispherical electron energy analyzer and a multichannel plate detector. The solution-processed $Pd(PPh_3)_4$ films were prepared through spin casting a 5 mg/mL $Pd(PPh_3)_4$ solution from chloroform at 2000 rpm for 30 s in an N_2 environment glovebox (<0.1 ppm H_2O and O_2) and transferred into the analysis chamber with no air exposure. The UV light source was an Excitech H Lyman-α lamp (E-LUX™121) equipped with a 90° ellipsoidal mirror (E-LUXTM EEM Optical Module). The UV beam path was in a high-purity dried O_2 purge with the pressure

of 8-9 Torr.[1] UPS measurements were performed with a -5 V sample bias and a 2.95 eV pass energy.

Surface Morphology

Atomic Force Microscopy and photoconductive AFM were performed with an Asylum Research MFP-3D setup with conductive gold-coated probes with a resonant frequency of 13 kHz and a spring constant of 0.2 N m^{-1}, purchased from ContGB Budged Sensors. All measurements were done under nitrogen atmosphere in contact mode at 0 V sample bias and at a scan rate of 0.30 Hz. For photocurrent measurements, the sample's current at 0 V was measured in the dark, and the obtained value was used as the offset for photocurrent measurement under illumination.

Grazing Incidence Wide Angle X-ray Scattering (GIWAXS)

GIWAXS measurements were performed at the Advanced Light Source at Lawrence Berkeley National Lab on the 7.3.3 beamline. The sample was scanned with an incidence angle of 0.12° and a photon energy of 10 keV (λ = 1.24 Å), while under a helium environment to minimize beam damage and reduce air scattering. The width of the incident X-ray beam is about 1 mm, and silver behenate was used to calibrate the lengths in the reciprocal space. A 2D detector (PILATUS 2 M from Dectris) with a sample-to-detector distance of 276.9 mm was used to collect the images. The Nika software package for Igor (by Wavemetrics) and the Igor script WAXStools were used to process the image[228].

Resonant Soft X-ray Scattering

RSoXS measurements were performed with transmission geometry at beamline 11.0.1.2[255] at the advanced light source (ALS), Lawrence Berkeley National Laboratory. The samples were

prepared in the same manner as the active layers for solar cells but were spin-cast onto a PSS-coated substrate. A photon energy of 283.8 eV was used.

Fabrication of Organic Solar Cells

Photovoltaic devices were fabricated in inverted structure with glass/ITO/ZnO/PCE10:IOTIC-4F:Pd(PPh$_3$)$_4$/MoOx/Ag architecture. In a first step, the ITO on glass substrates, purchased from Naranjo, were cleaned with commercially available dish soap and distilled water. Next, they were ultra-sonicated in acetone and isopropyl alcohol subsequently for 15 minutes each. The substrates were dried in an oven overnight at 130 ℃. The ZnO bottom contact was fabricated from a mixture of tetrahydrofuran and diethylzinc (15% w/w in toluene) in a 2:1 volume ratio, which was spin-coated (30 µl at 4000 rpm for 15 seconds in air) to form ZnO films. The substrates were annealed for 20 minutes at 150 ℃ before the active layer was prepared under nitrogen atmosphere by spin coating 25 µl PTB7-Th:IOTIC-4F solution (1:1.5 weight ratio, c = 20 mg/mL) in chlorobenzene with 2% chloronaphtalene at 1300 rpm for one minute on top of the ZnO layer. The active layer solution was stirred for more than 3 hours at 56℃ before spin coating. For the devices containing Pd(PPh$_3$)$_4$, a Pd(PPh$_3$)$_4$ stock solution was prepared using chlorobenzene with 2% chloronaphthalene as solvent under inert atmosphere. The solvent and the stock solution were added in the respective ratios to obtain concentrations of 0.75%, 3% and 7% w/w Pd(PPh$_3$)$_4$ per PTB7-Th. The MoO$_3$/Ag top electrodes with an area of 0.22 cm^2 were fabricated by thermal evaporation at pressures of less than 10^{-6} Torr using an Ångstrom evaporator.

Device Characterization

Current-voltage characteristics were measured with a Keithley 2602 semiconductor analyzer system under nitrogen atmosphere in the dark and under illumination. A solar simulator with a 300 W Xenon lamp with AM 1.5 global filter was used to irradiate the devices with 100 mW/cm^2 AM 1.5G illumination. The light intensity was calibrated with a standard silicon solar cell with KG1 filter, which was calibrated by the National Renewable Energy Laboratory. This setup was used to quantify geminate recombination by measurement of *JV*-curves to obtain photocurrents and its tabulated spectrum was used as software input for the transfer matrix method software[162] to predict the theoretical J_{sc}. To determine the performance, the solar cell device area was defined by an aperture of 0.094 cm^2. The V_{oc} in dependence of the light intensity was measured with the same setup using a set of Newport 5215 neutral density filters. EQE spectra were measured under nitrogen atmosphere as well, and the intensity of the monochromatic light, chopped at 155 Hz, was determined with a Newport Si photodiode. A Solartron SI1260 analyzer was used to measure frequency-dependent impedance (10^1–10^6 Hz) under 1 sun illumination and in the dark with a small AC perturbation of 40 mV, starting at a negative sample bias and increasing the bias up to V_{oc}. The device thickness was measured with an Ambios XP-100 profilometer.

Optical measurements

Absorption measurements were performed on a Perkin Elmer Lambda 750 UV–vis/NIR spectrophotometer. Thin-film absorption of Pd(PPh$_3$)$_4$ was determined from films spin-coated from chlorobenzene on quartz substrates and measured in an optical cryostat. To obtain the optical properties of PTB7-Th:IOTIC-4F: Pd(PPh$_3$)$_4$ blends, the reflectance and transmission of films on glass were measured with a Filmetrics FT-R1-RTX system. The film thickness was measured with an Ambios XP-100 profilometer. All non-polymer-based materials were

characterized with a Woollam M-2000DI Variable Angle Spectroscopic Ellipsometer to obtain the optical properties of all device layers as input for the transfer matrix simulation.

The steady-state photoluminescence (PL) measurements were performed on a home-built fluorometer setup. The PL was excited by a He-Ne laser beam (JDS Uniphase) with 633 nm wavelength at 45 degrees angle of incidence. The PL was collected in 90 degrees geometry with an optical lens system and focused on the input slit of a spectrometer (Acton SP-500) equipped with charge-couple device (CCD) camera (Princeton Instruments PIXIS:400) which can detect light in the range 300-1050 nm. The laser beam was cleaned from plasma emission with a bandpass filter, and the CCD detector was protected from the excitation light by a long-pass interference filter (Thorlabs). The excitation light intensity was controlled with a neutral density gradient filter (Thorlabs). The spectrum, collected by the CCD camera, was corrected for the instrument response by measuring the spectrum of a black body-like light source (Ocean Optics HL-1) and calculating appropriate correction factors. PL spectra at wavelengths longer than ~800 nm often exhibit fringe-like modulation caused by etaloning in the CCD camera sensor. These artifacts were not removed from the data collected. The obtained data were corrected for the film thickness by absorption measurements. Films of pristine PTB7-Th and IOTIC-4F, each with and without catalyst, were prepared in Chlorobenzene with 2% chloronaphthalene with a concentration of 20 mg/ml. Films were spin-coated under inert atmosphere onto UV/Ozone treated glass substrates, which were encapsulated for the steady-state photoluminescence measurements.

3.5 Supplementary Information for Chapter 3
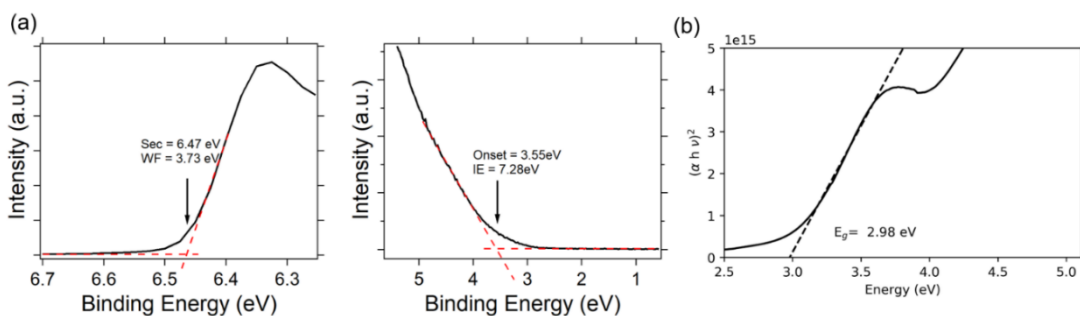
Figure S3.1. a) High energy (left) and low energy (right) region of the UPS spectrum of Pd(PPh$_3$)$_4$ and linear fits to determine the work function and the HOMO onset. b) Absorption coefficient α, determined from absorbance measurements of Pd(PPh$_3$)$_4$ in solution (CB2%CN), and linear extrapolation of the absorption onset for the determination of the band gap E_g.
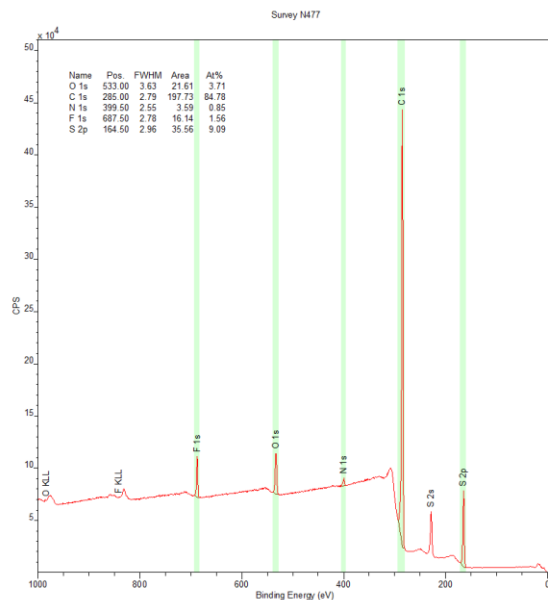
Figure S3.2. X-ray photoemission spectroscopy survey scan of the PCE10:IOTIC-4F film without added catalyst, showing no Pt signal.
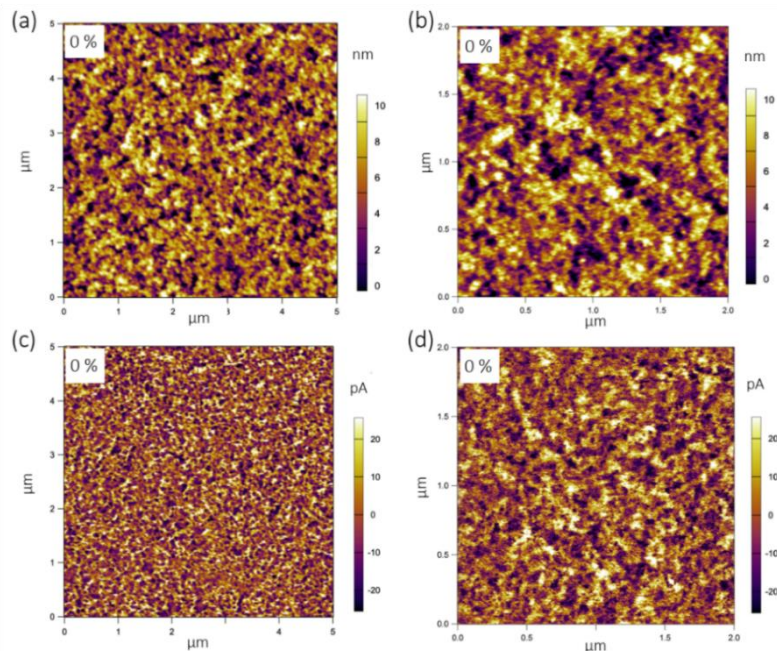
Figure S3.3. a) 5µm x 5 µm and b) 2 µm x 2 µm contact mode nanoscale morphology images of the blend film with 0% catalyst, c) 5µm x 5 µm and d) 2 µm x 2 µm photocurrent images of the active layer at 0 V sample bias.
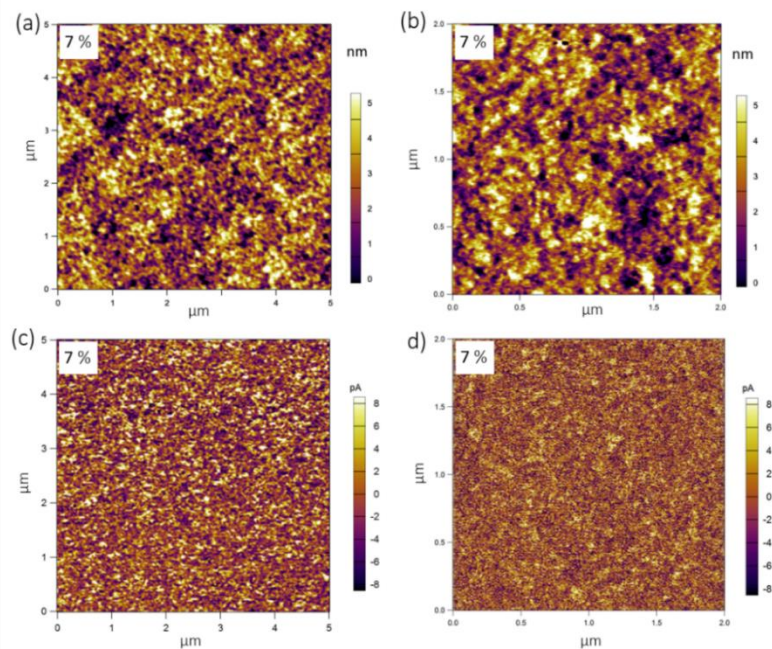
Figure S3.4. a) 5 µm x 5 µm and b) 2 µm x 2 µm contact mode nanoscale morphology images of the blend film with 7% catalyst, c) 5µm x 5 µm and d) 2 µm x 2 µm photocurrent images of the active layer at 0 V sample bias.
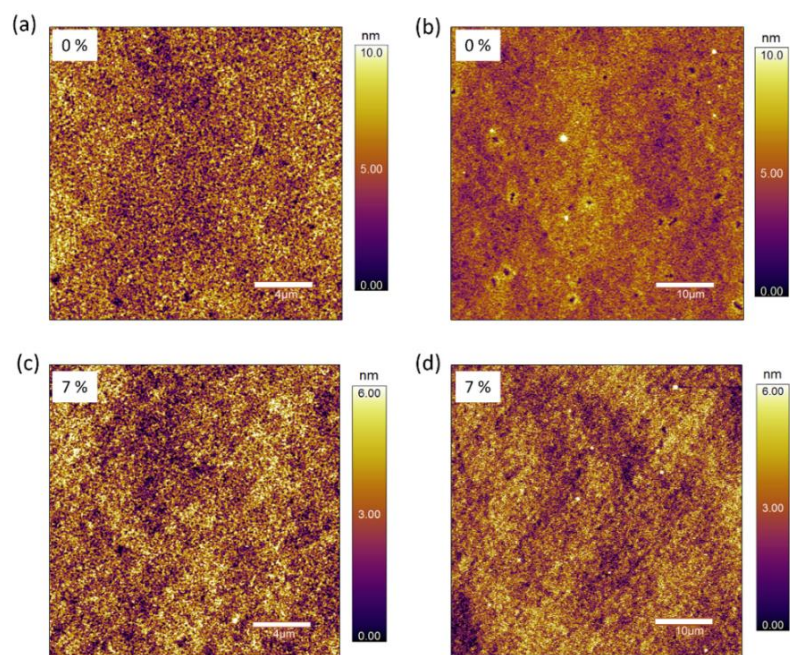
Figure S3.5. Wide area tapping mode AFM scans of the PCE10:IOTIC4F blend film. a) 20 x 20 μm scan of the blend film without Pd(PPh$_3$)$_4$ added, b) 50 x 50 μm scan of the blend film without Pd(PPh$_3$)$_4$ added, c) 20 x 20 μm scan of the blend film with 7% Pd(PPh$_3$)$_4$ added and d) 50 x 50 μm scan of the blend film with 7% Pd(PPh$_3$)$_4$ added.
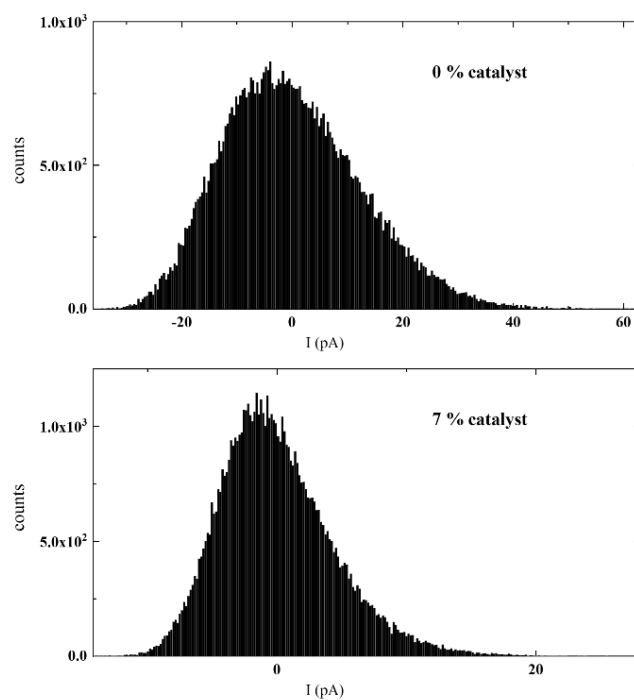
Figure S3.6. Current histograms obtained by pc-AFM for the device without (top) and with 7% catalyst (bottom).
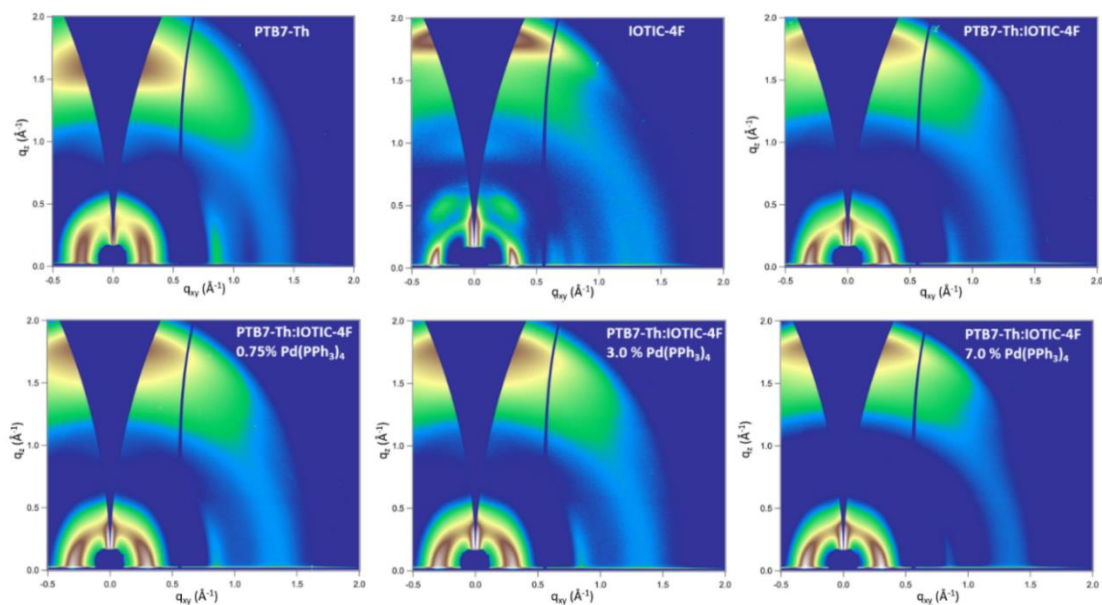
Figure S3.7. GIWAXs patterns for the pristine donor material PTB7-Th, the acceptor IOTIC-4F and the four blend systems without and with Pd(PPh$_3$)$_4$ added.
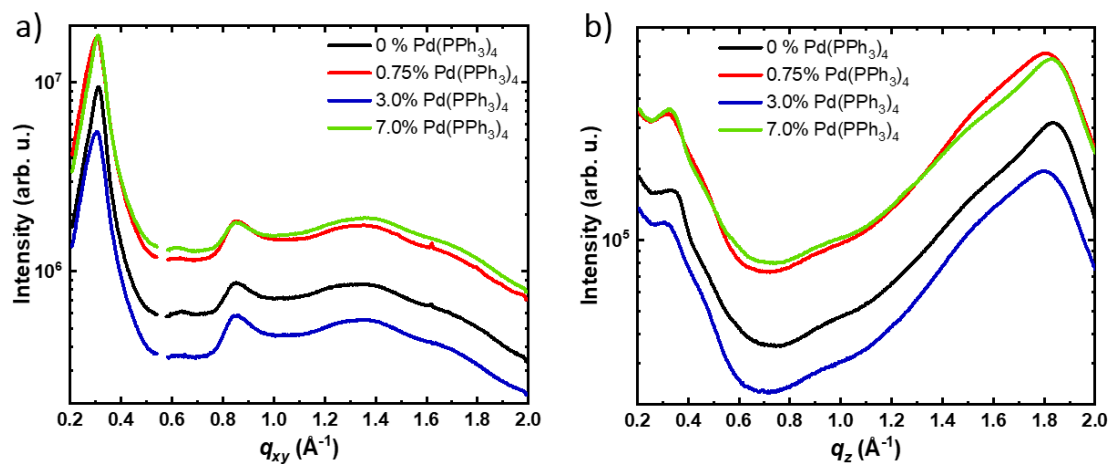
Figure S3.8. GIWAXs 1D linecuts displaying the scattered intensity in the q_z plane (perpendicular to the substrate) and the q_{xy} plane (parallel to the substrate).
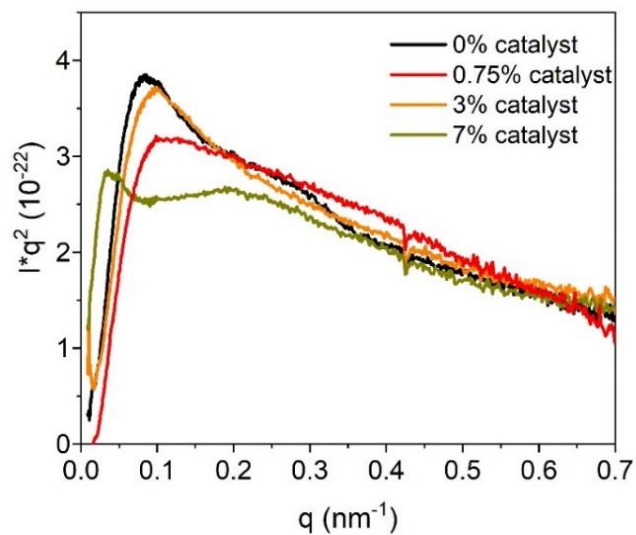
Figure S3.9. RSoXs profiles extracted at an x-ray energy of 284.2 eV and normalized by the film thickness.
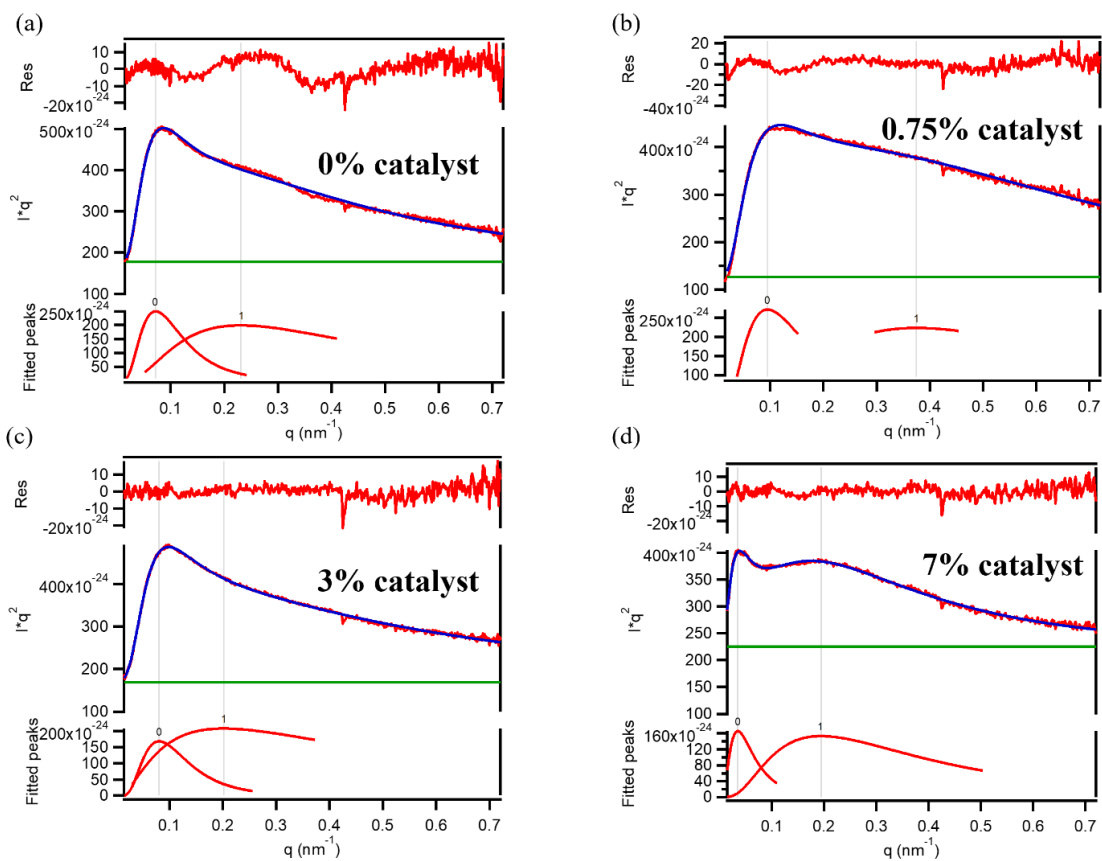
Figure S3.10. RSoXs fits and peak deconvolution for the data extracted at an x-ray energy of 284.2 eV.

Table S3.1. Parameters extracted from RSoXs profiles for blend films with different content of Pd(PPh$_3$)$_4$ Position q1 of the peak observed at low q, its long period L1 and the domains' relative volume fraction, position q2 of the peak observed at high q, its long period L2 and the its relative volume fraction and the relative overall standard deviation σ of the composition variation.

Pd(PPh$_3$)$_4$	q_1 (nm^{-1})	L_1 (nm)	Rel. volume fraction of L$_1$	q_2 (nm^{-1})	L_2 (nm)	Rel. volume fraction of L$_2$	σ
0%	0.072	87	19%	0.231	27	81%	1
0.75%	0.095	68	20%	0.375	18	80%	0.97
3%	0.081	76	10%	0.20	31	90%	0.99
7%	0.035	179	14%	0.194	32	86%	0.96

Disorder in organic semiconductors causes absorption below the band gap E_g, due to transitions from or to localized tail states below E_g. The absorption follows the expression $\alpha = \alpha_0 \exp(h\nu/E_U)$ and the width of the absorption tail is tail is a measure for the disorder of the material, described by the Urbach Energy E_u.[256–258] The exponential fit of the EQE values below the band gap to determine E_u is shown in Figure S3.11. The average values across several device with standard deviation can be found in Table S3.3.
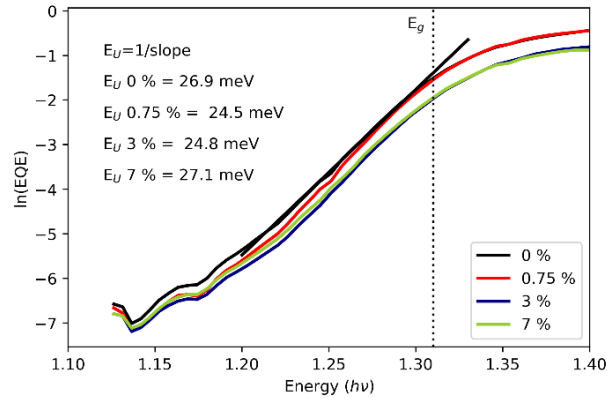
Figure S3.11. a) EQE spectra of device with different amount of added catalyst. b) Plot of the natural logarithm of the EQE versus energy. The slope of the exponential fit of the EQE values below the band gap allows the determination of the Urbach energy.
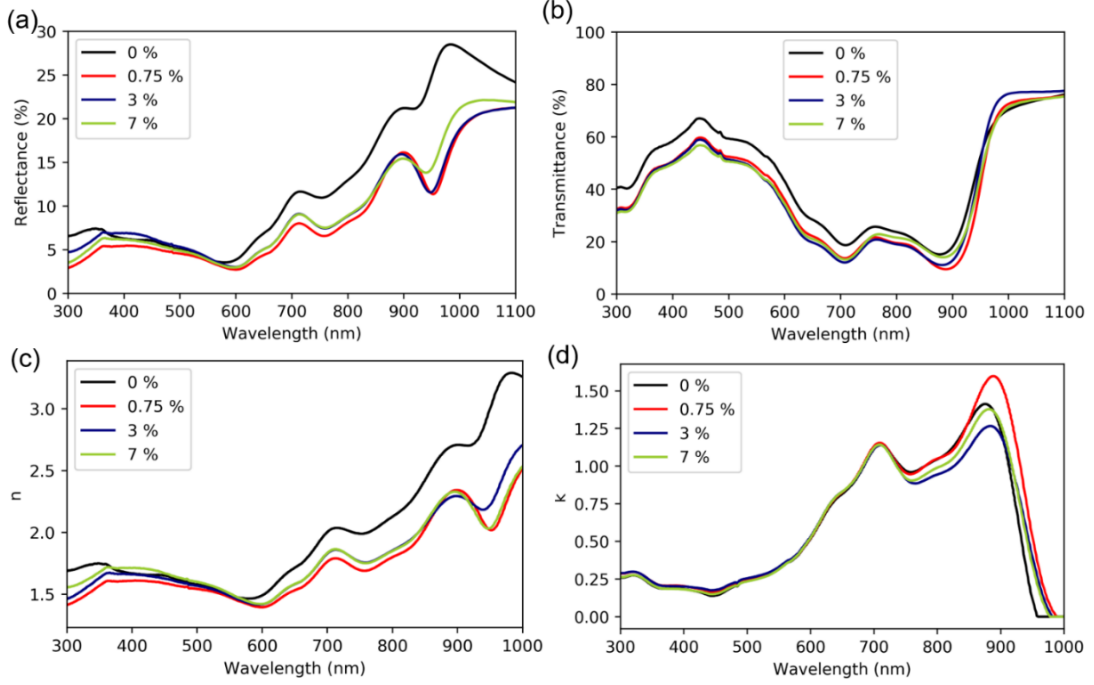
Figure S3.12. a) Reflectance and b) transmittance spectra of films with different amount of added catalyst and refractive index *n* and extinction coefficient *k*.

Equations for the determination of α, n and k.[259,127]

$$\alpha = \frac{1}{d}\ ln\left(\frac{(1-R)^2}{2T} + \left(\frac{(1-R)^4}{4T^2} + R^2\right)^{0.5}\right)$$ (S3.1)

$$k = \frac{\alpha\lambda}{4\pi}$$ (S3.2)

$$n = \left|\frac{1+R^2}{1-R^2}\right|$$ (S3.3)
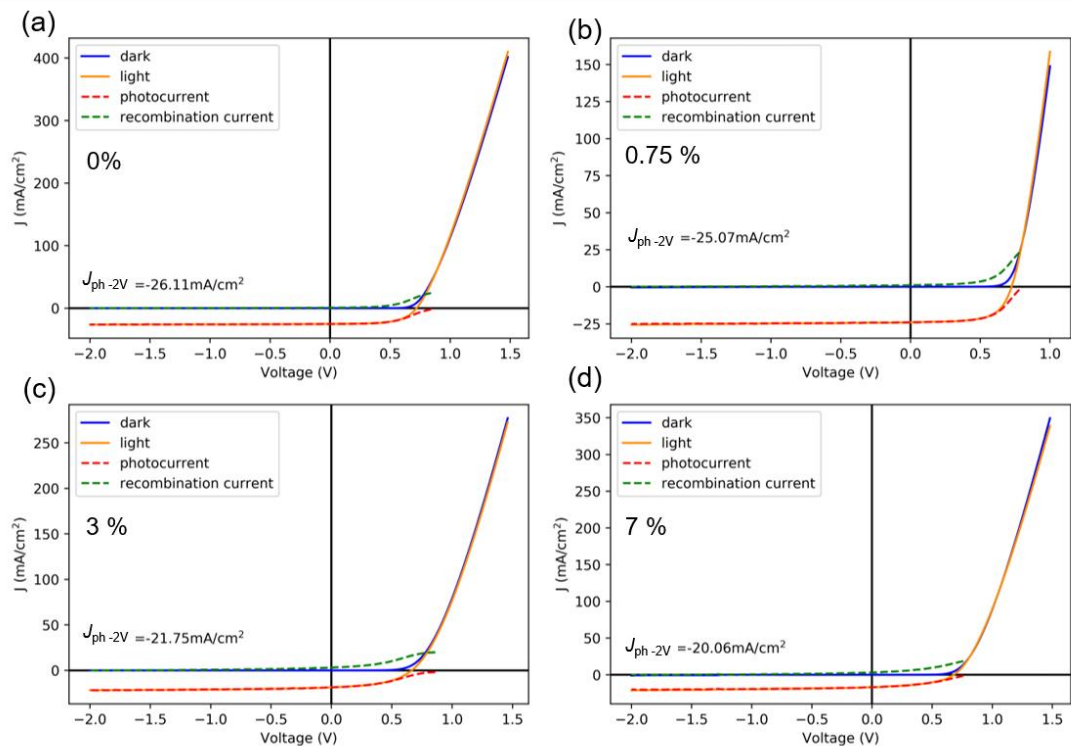
Figure S3.13. Experimental current voltage characteristics of those devices that were simulated based on the transfer matrix method. The photocurrent at -2 V is indicated.

Table S3.2. Experimental photocurrent $J_{ph\,-2V}$ at -2V, extraction efficiency η_{-2V} at -2 V and the corresponding calculated saturated photocurrent J_{sat}, theoretical photocurrent J_{theo} based on optical simulations and the resulting geminate recombination prefactor P_g.

Pd(PPh$_3$)$_4$ (wt%)	$J_{ph\,-2V}$ (mA/cm²)	η_{-2V}	$J_{ph,sat}$ (mA/cm²)	J_{theo} (mA/cm²)	P_g
0	26.11	0.996	26.21	27.69	0.98
0.75	25.07	0.987	25.40	27.36	0.93
3	21.75	0.967	22.49	28.69	0.78
7	20.06	0.967	20.74	28.36	0.73
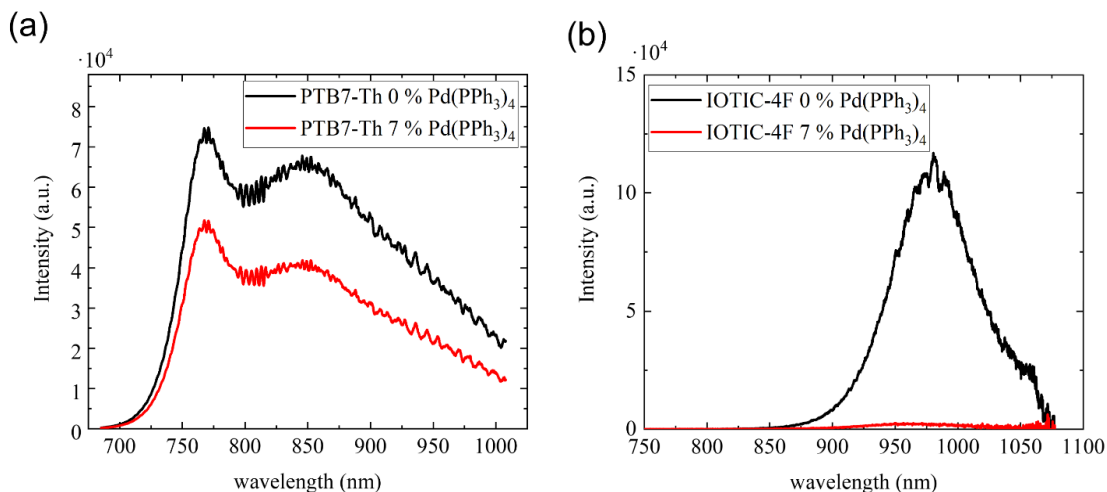
Figure S3.14. a) Fluorescence intensity of a neat PTB7-Th film and of a film with 7 wt% added Pd(PPh$_3$)$_4$ b) Fluorescence intensity of a neat IOTIC-4F film and of a film with 7 wt% added Pd(PPh$_3$)$_4$.
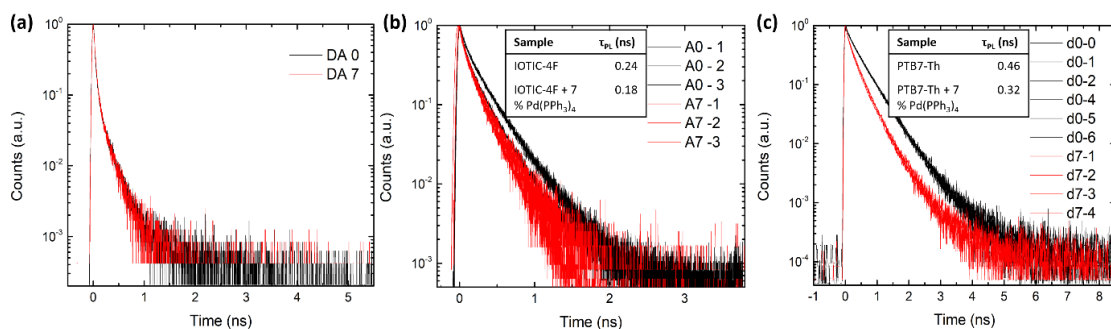
Figure S3.15. a) TCSPC measurements of the blend film were only able to display the instrument response function and this result was the same with and without the catalyst. Time-resolved photoluminescence measurements for b) the IOTIC-4F acceptor (800 nm λ_{ex}, 960 nm $\lambda_{detection}$) and c) the PTB7-Th donor films (400 nm λ_{ex}, 760 nm $\lambda_{detection}$), with (red) and without catalyst (black) show a reduction in the PL lifetime.
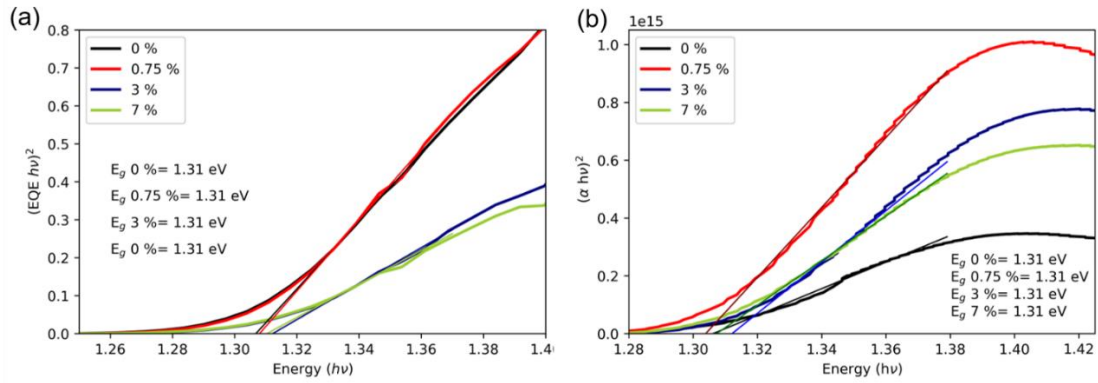
90

Figure S3.16. a) $(\text{EQE} \cdot h\nu)^2$ versus energy plot and linear fit to determine the optical band gap of the devices with different amount of added catalyst. b) $(\alpha \cdot h\nu)^2$ versus energy plot and linear fit to determine the optical band gap of the devices with different amount of added catalyst.
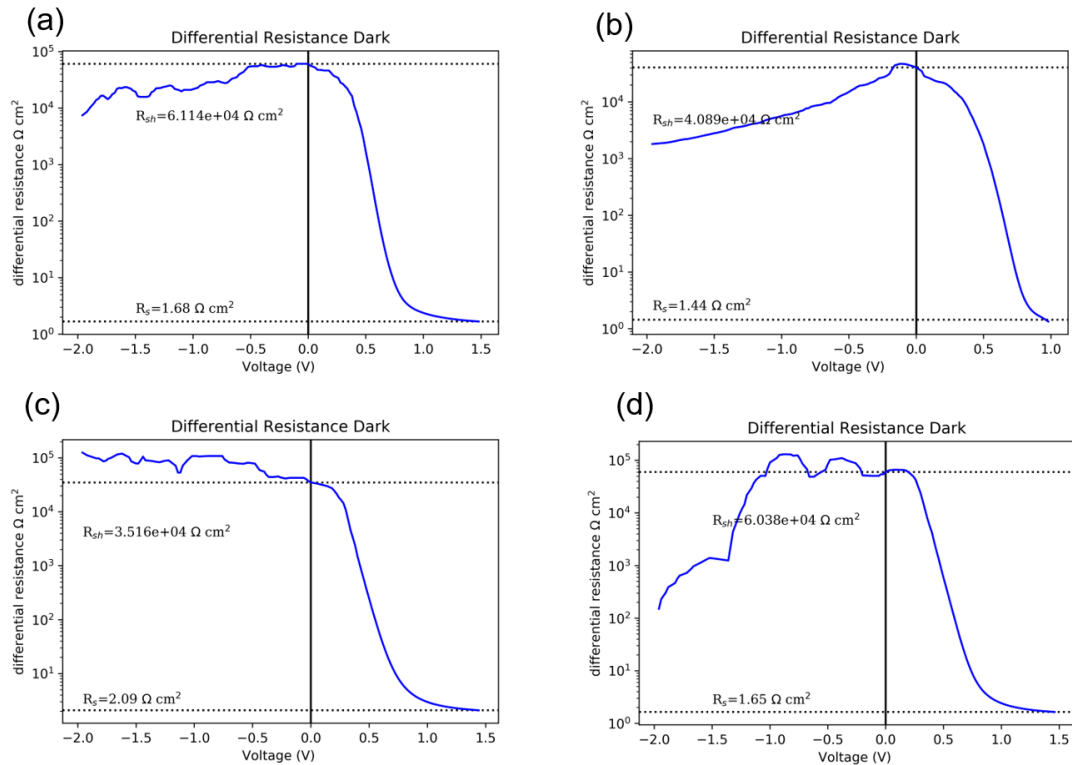
Figure S3.17. Differential resistance for solar cells with a) 0% catalyst, b) 0.75% catalyst, c) 3% catalyst and d) 7% catalyst.
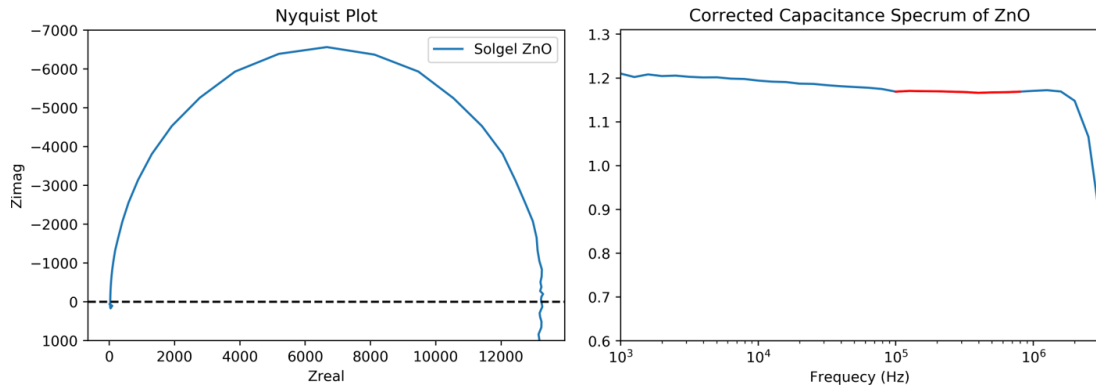
Figure S3.18. Nyquist plot of a film of sol-gel ZnO of 170 nm thickness and its corrected capacitance spectrum used for the determination of the dialectic constant of the ZnO electrode material.

Table S3.3. Urbach Energy E_U, band gap E_g, shunt resistance R_{sh} (average of devices) and dielectric constant ε of PTB7-TH:IOTIC-4F devices with different amount of $Pd(PPh_3)_4$ as well as average build-in field V_{bi}.

$Pd(PPh_3)_4$ (wt%)	E_U (meV)	E_g (eV)	R_{sh} (Ω cm²)	ε	V_{bi} (V)
0	26.8 ± 0.4	1.31 ± 0.01	$5.9 \cdot 10^4 \pm 1.5 \cdot 10^4$	3.16 ± 0.15	0.771
0.75	25.5 ± 0.5	1.31 ± 0.01	$4.3 \cdot 10^4 \pm 1.3 \cdot 10^4$	3.00 ± 0.28	0.782
3	24.5 ± 0.7	1.31 ± 0.01	$4.53 \cdot 10^4 \pm 1.4 \cdot 10^4$	3.05 ± 0.14	0.706
7	27.0 ± 0.0	1.31 ± 0.01	$4.4 \cdot 10^4 \pm 1.6 \cdot 10^4$	3.13 ± 0.18	0.712
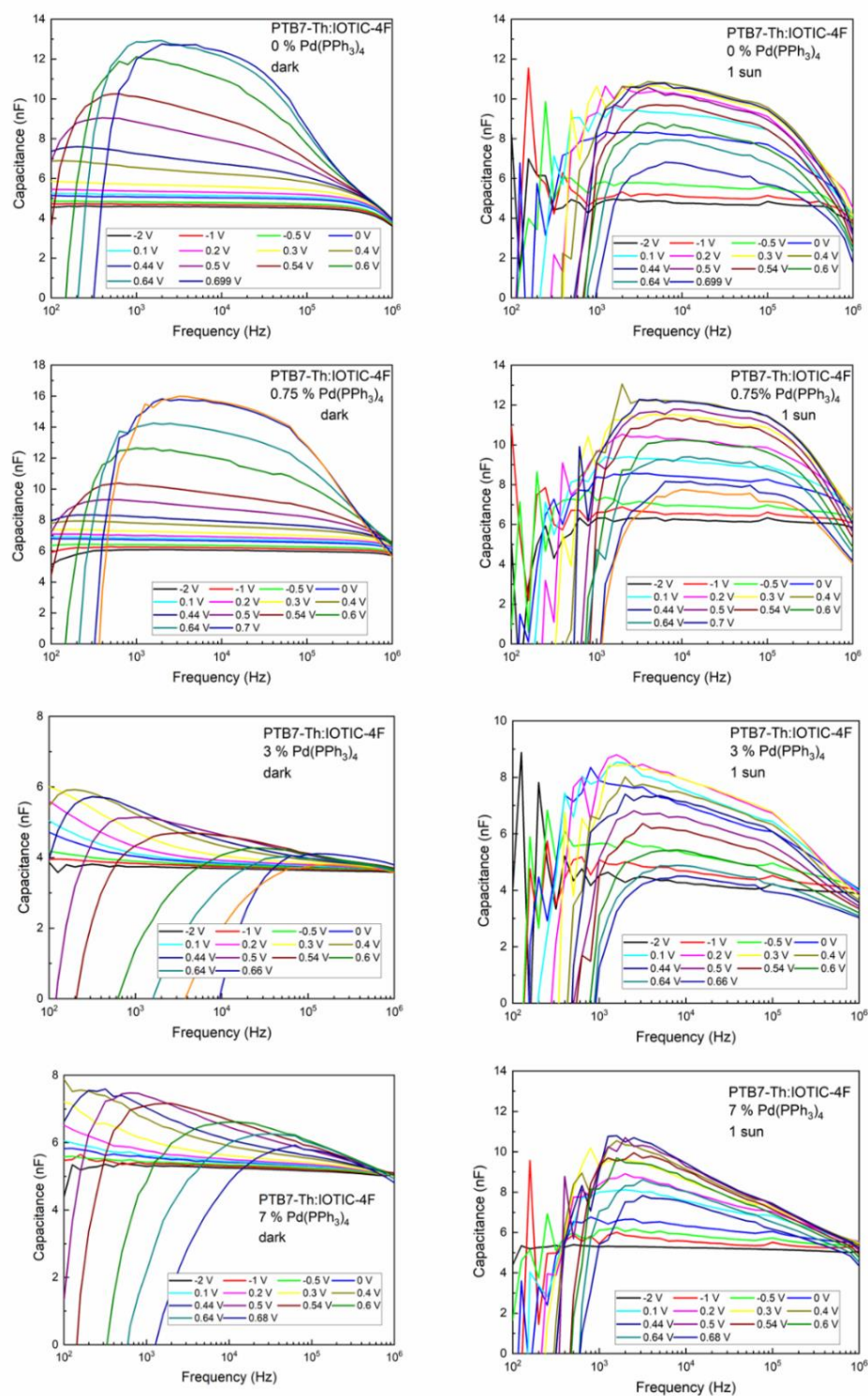
Figure S3.19. Capacitance spectra of devices with different amount of Pd(PPh₃)₄ in the dark and under 1 sun illumination.
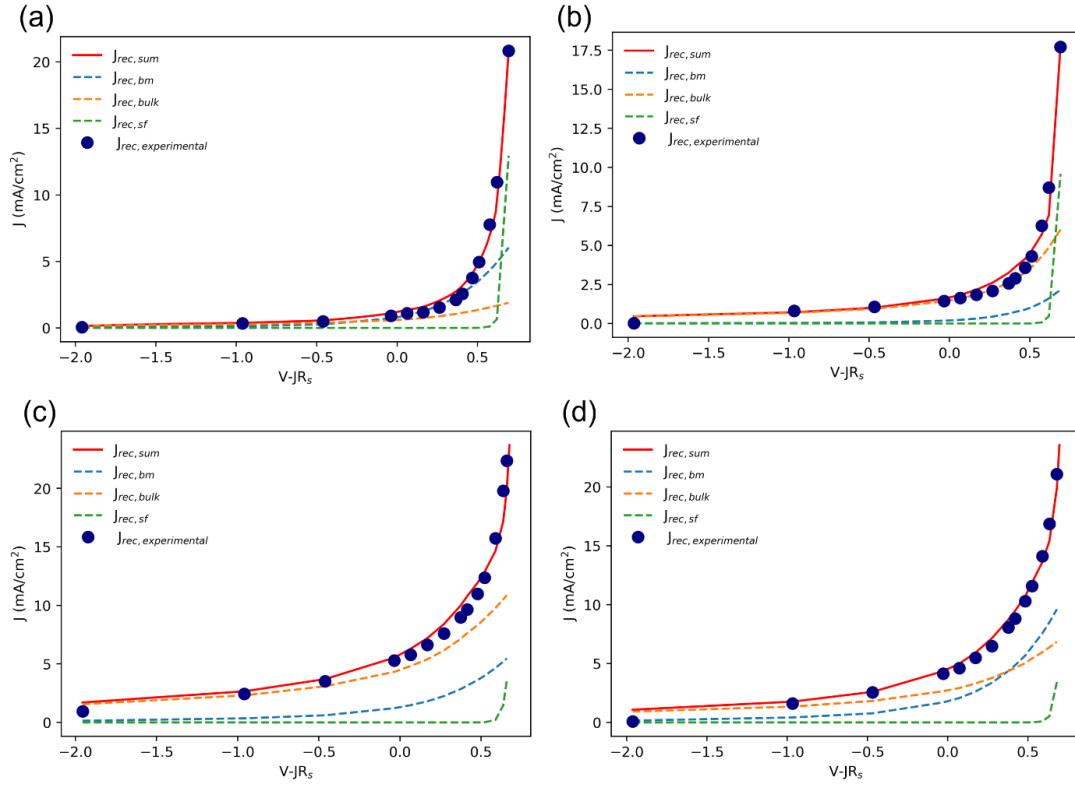
Figure S3.20. Recombination currents ($J_{rec} = J_{ph} - J_{ph,sat}$) and fits based on the parameters determined by analysis of impedance spectroscopy data for devices with a) 0%, b) 0.75%, c) 3% and d) 7% added catalyst.
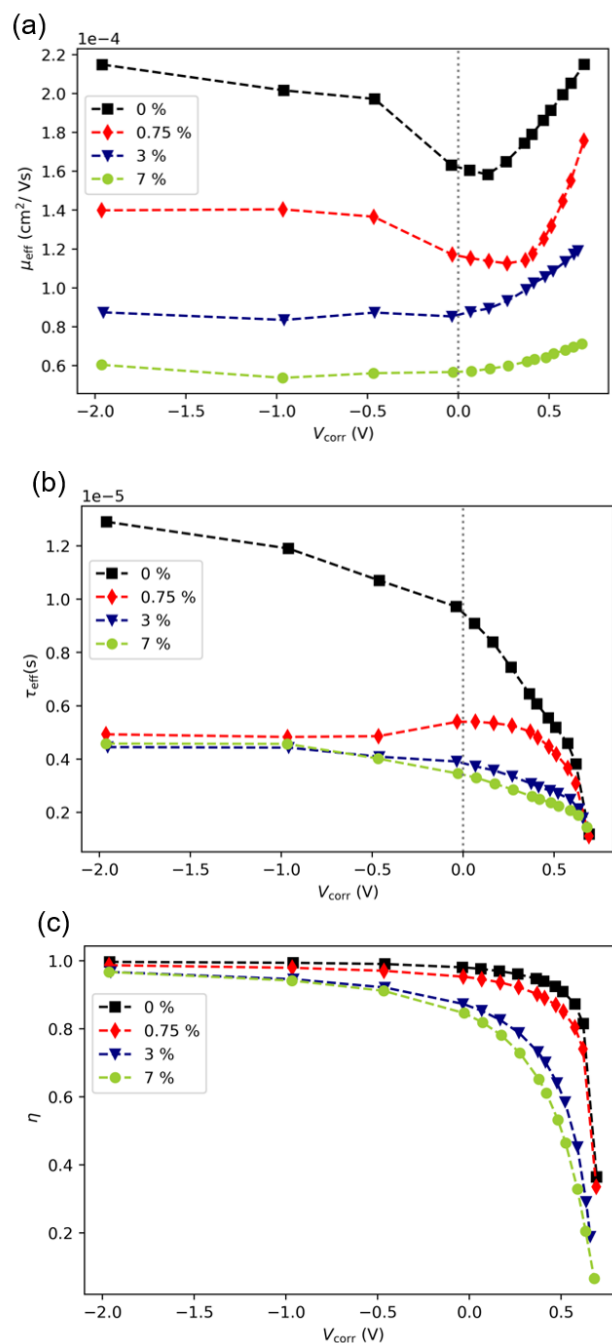
Figure S3.21. a) Effective mobility, b) lifetime, and c) extraction efficiency in dependence of the corrected voltage.

In addition to the determination of the effective mobility, we quantified the hole mobility of the PTB7-Th:IOTIC-4F system and the system with 0.75% added Pd(PPh$_3$)$_4$ by fabricating hole only diodes. In these devices with symmetric contacts, which are favorable for hole injection, and

unfavorable for electron injection, the transport is dominated by the donor material. Fitting to the Mott Gurney Law, Equation S3.4, results in similar mobility values of $\mu_{SCLC} = 2.29 \cdot 10^{-4} \pm 0.03 \cdot 10^{-4} \text{cm}^2/\text{Vs}$ for the 0% diode and in $\mu_{SCLC}= 1.27 \cdot 10^{-4} \pm 0.01 \cdot 10^{-4} \text{cm}^2/\text{Vs}$ for the 0.75% diode (Figure S3.22).

$$J(V) = \frac{9}{8}\frac{\epsilon\epsilon_0\mu V^2}{d^3} \tag{S3.4}$$
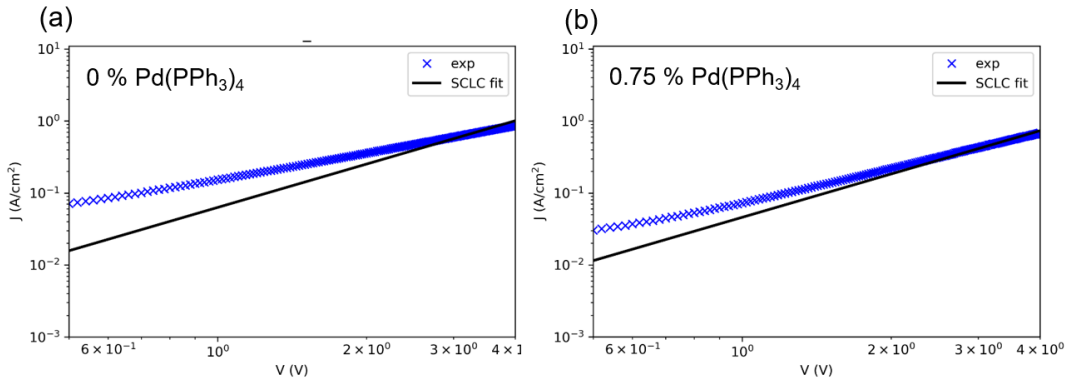
Figure S3.22. Space charge limited current fits and experimental current voltage characteristics of a ITO/PEDOT:PSS/PCE10:IOTIC-4F/MoOx/Ag hole only diode with a) no catalyst and b) 0.75% catalyst in the active layer.
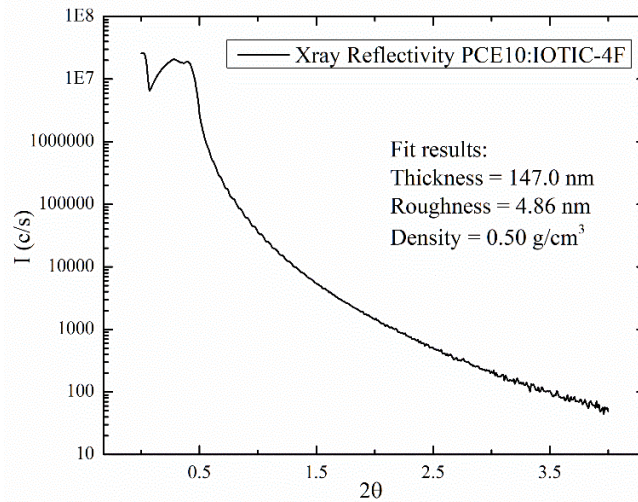
Figure S3.23. X-ray reflectivity fit and fitting parameters of PCE10:IOTIC-4F film.

Below, we summarize the performance change on the **PM6:Y6** solar cell system. The cells were fabricated in inverted device structure, as described for the PTB7-Th:IOTIC-4F system in the experimental part of the main text, but with an active layer comprised of PM6 and Y6 in a 1:1.2 ratio in chloroform (18 mg/mL) with 0.5% 1-chloronaphthalene as additive, that was spin coated at 3000 rpm. The devices were annealed for 10 min at 110 °C before evaporation of the back electrodes.

Table S3.4. Photoelectrical parameters of the PM6:Y6 BHJ solar cells with different amounts of Pd(PPh$_3$)$_4$ under 100 mW/cm^2 AM1.5 illumination.

Pd(PPh$_3$)$_4$ (wt%)	J_{sc} (mA/cm^2)	V_{OC} (V)	FF (%)	PCE (%)
0	26.27	0.83	0.707	15.4
0.75	25.47	0.82	0.718	15.0
3	22.96	0.81	0.67	12.5
7	20.07	0.81	0.644	10.5
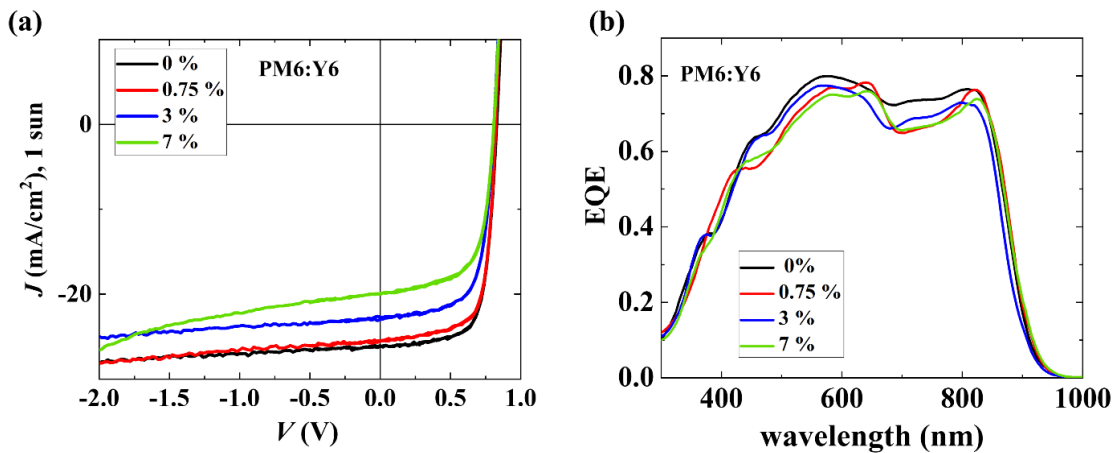
Figure S3.24. Current-Voltage characteristics of PM6:Y6 solar cells with different amounts of Pd(PPh$_3$)$_4$ added to the active layer under 100 mW/cm^2 AM 1.5 illumination.

Chapter 4: A Simple Approach for Unraveling Optoelectronic Processes in Organic Solar Cells Under Short-Circuit Conditions

4.1 Introduction

Organic Photovoltaic (OPV) materials promise the fabrication of flexible, lightweight and semitransparent solar cells for integrated energy harvesting while allowing low-cost, large scale and solution-based processing.[170,260,261] Advancement in synthesis, specifically the development of non-fullerene acceptors, as well as progress in device design and processing, has led to continuous improvements of the performance in the last decade.[262,166,106] Most recently, remarkable photoconversion efficiencies (PCEs) up to 18.2% were achieved.[169,214,263] This progress in the field of OPVs is intricately linked to the correct assessment of material and device parameters and to efforts towards deconvoluting the electronic processes and the contributions of different loss mechanisms.[264,265]

Under short-circuit conditions, the interplay of exciton photogeneration in the active layer, geminate and non-geminate recombination processes and free charge carrier extraction define the measured electron flux (photocurrent).[245,253,266–268] The complexity of the photoelectronic processes complicates the analysis, and advanced techniques are frequently applied to characterize a single aspect.[136,137,269,270] For example, impedance spectroscopy is commonly used to gauge the losses due to non-geminate recombination, and Time-Delayed Collection Field (TDCF) is employed to investigate geminate recombination losses.[136,137,269,270]

In this work, we propose a comprehensive technique that allows the quantification of geminate recombination and the determination of the mobility-lifetime product $\mu\tau$. We couple optical transfer matrix method-based simulations with simple experimental methods (JV-characteristics,

EQE) that are readily available in most laboratories. The geminate recombination losses are quantified by a geminate recombination prefactor P_g, which is a material parameter of the active layer's donor:acceptor blend. P_g describes the fraction of excitons splitting into free electrons and holes; thus, P_g approaching unity is desirable for efficient OPVs.[86] We determine P_g from experimental current-voltage characteristics combined with optical simulations.

Next, we propose a new approach to obtain the mobility-lifetime product $\mu\tau$ based on the measurement of the external quantum efficiency (EQE), the previously determined P_g and the simulation of the EQE. The effective mobility μ defines a charge carrier's drift velocity v_d in a given electric field E and the effective lifetime τ describes the time between the generation of a free charge carrier and its subsequent annihilation *via* recombination. Thus, the mobility-lifetime product $\mu\tau$ as a single integrated parameter includes both charge transport and non-geminate recombination features.[271] Efforts to provide accessible means to determine the $\mu\tau$ product are reported in the OPV community only rarely, and, if so, they are based on substantial simplifications, and the results are not juxtaposed with those obtained by any independent method.[272] Since $\mu\tau$ determines the distance that a photogenerated charge carrier travels in the active layer before it recombines, we can quantify the extraction efficiency η under short-circuit conditions.[254,273,274] Having quantified all contributions under short-circuit conditions, we can predict the J_{sc} in dependence on the active layer thickness, taking into account geminate and non-geminate recombination losses.

4.2 Results and Discussion

We apply our developed technique to three solar cells with different donor:acceptor blends and device architectures. We show how the obtained results allow the comparison of material-

and device architecture-specific features across different organic photovoltaic devices. First, the proposed technique is applied to a solar cell in inverted structure based on the non-fullerene acceptor (NFA) 2,2'-((2Z,2'Z)-((5,5'-(4,4-bis(2-ethylhexyl)-4H-cyclopenta[1,2-b:5,4-b']-dithiophene-2,6- diyl)bis(4-((2-ethylhexyl)oxy)thiophene-5,2-diyl))bis(methanylylidene))bis(5,6-difluoro3-oxo-2,3-dihydro-1H-indene-2,1-diylidene))dimalononitrile (**COTIC-4F**) and the polymer donor poly[4,8bis(5-(2-ethylhexyl)thiophen-2-yl)benzo[1,2-b;4,5-b']dithiophene-2,6-diyl-alt-(4-(2-ethy-lhexyl)3-fluorothieno[3,4-b]thiophene-)-2-carboxylate-2-6-diyl)] (**PCE10**). Second, we investigate devices in conventional structure with an active layer blend composed of **PCE10** donor and the NFA 2,2'-((2Z,2'Z)-((5,5'-(4,4,9,9-tetrakis(4-hexylphenyl)-4,9-dihydro-s-indaceno[1,2-b:5,6-b']dithiophene-2,7-diyl)bis(4-((2-ethylhexyl)oxy)thiophene-5,2-diyl))-bis(methanylylidene))bis(6-fluoro-3-oxo-2,3-dihydro-1H-indene-2,1-diylidene))dimalononitrile and its isomers **(IOTIC-2F$_a$)** and third we use a solar cell system based on the polymer donor poly[(2,6-(4,8-bis(5-(2ethylhexyl-3-fluoro)thiophen-2-yl)-benzo[1,2-b:4,5-b']dithiophene))-alt-(5,5-(1',3'-di-2-thienyl5',7'-bis(2-ethylhexyl)benzo[1',2'-c:4',5'-c']dithiophene-4,8-dione)] (**PM6**) and the NFA 2,2'-((2Z,2'Z)-((12,13-bis(2-ethylhexyl)-3,9-diundecyl-12,13-dihydro-[1,2,5]thiadiazolo[3,4-e]thieno[2'',3'':4',5']thieno[2',3':4,5]pyrrolo[3,2-g]thieno[2',3':4,5]thieno[3,2-b]indole-2,10-diyl)bis(methanylylidene))bis(5,6-difluoro-3-oxo-2,3-dihydro-1H-indene-2,1-diylidene))dimalononitrile (**Y6).** The chemical structures are shown in **Figure 4.1a** and the device architectures are displayed in Figure 4.1 b). The photoelectrical parameters of the solar cells are summarized in Table S4.1 in the supporting information and current-voltage characteristics of respective devices in the dark and under 1 sun illumination are shown in Figure S4.1. We chose the three non-fullerene based systems since they provide a suitable basis for a study across different device structures (conventional, inverted), across different performances (PCEs from 6.8% to 12.1%), different built-in voltages (0.623 V to 0.920 V) and different active layer

100

thicknesses (80 nm to 140 nm) and most importantly different short circuit current densities of 16.5 mA/cm² (PCE10:IOTIC-2F$_a$), 20.9 mA/cm² (PCE10:COTIC-4F) and 24.0 mA/cm²(PM6:Y6). The system with COTIC-4F features the narrowest band gap NFA currently reported (E_g = 1.10 eV), which is of special interest for the fabrication of IR photodetectors and semitransparent OPVs.[170,275] The PM6:Y6 system has been recognized for its high performance of over 15%.[214,215] A recent report shows that the FF and J_{sc} drop with the increase of the low molecular weight fraction (LMWF).[216] Here, we investigate a system with 7% LMWF PM6 donor polymer, which has efficiency limitations compared to PM6:Y6 blends with a smaller (1%) LMWF. At the same time, it is still performing higher than the other two chosen systems of our study. This way, we hope to shed light onto the question whether the PCE or the J_{sc} directly correlate with the $\mu\tau$ product or if it is necessary to quantify extraction and recombination losses to understand what governs the J_{sc}. Further, the IOTIC-2F$_a$ based system was chosen, since has a high built-in voltage is and its relatively low J_{sc} is rather unexpected.[218] Here we will unravel the processes in this system that cause the limitations of the J_{sc}.
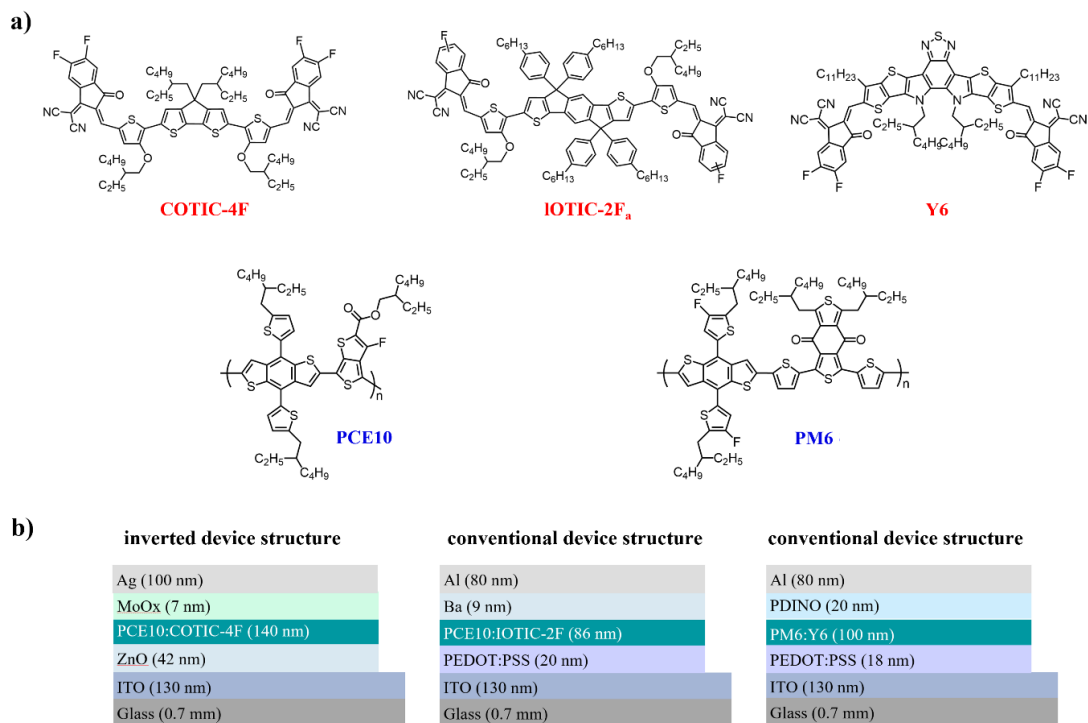
Figure 4.1. a) Chemical structures of the non-fullerene acceptors (red, top row) and the polymeric donor materials (blue, bottom-row) used in this work in the BHJ solar cells in the combinations PCE10:COTIC-4F, PCE10:IOTIC-2F$_a$ and PM6:Y6. b) Schematic inverted or conventional device architectures of the solar cells fabricated for this work.

4.2.1 Optical Properties and Simulation of the Generation Rate in the Active Layer

The exciton generation rate $G(x,\lambda)$ in the active layer of a solar cell under illumination is determined by the optical properties of all layers, the refractive index $n(\lambda)$ and extinction coefficients $k(\lambda)$, in conjunction with the device architecture.[162,163,276] More specifically, the fraction of reflected and transmitted light at each interface depends on the difference in the refractive index $n(\lambda)$ of adjunct layers, whereas the ability of each layer to absorb the incident light of a certain wavelength is described by the extinction coefficient $k(\lambda)$.[162,163,276] The thickness of each layer is of importance because the wavelength-specific interference pattern of the optical

field will vary depending on the exact device architecture.[162,163] We determined the optical constants of all materials that were used in this work, except those of Ba,[277] Al,[278] and PEDOT:PSS,[279] which are reported in the literature.
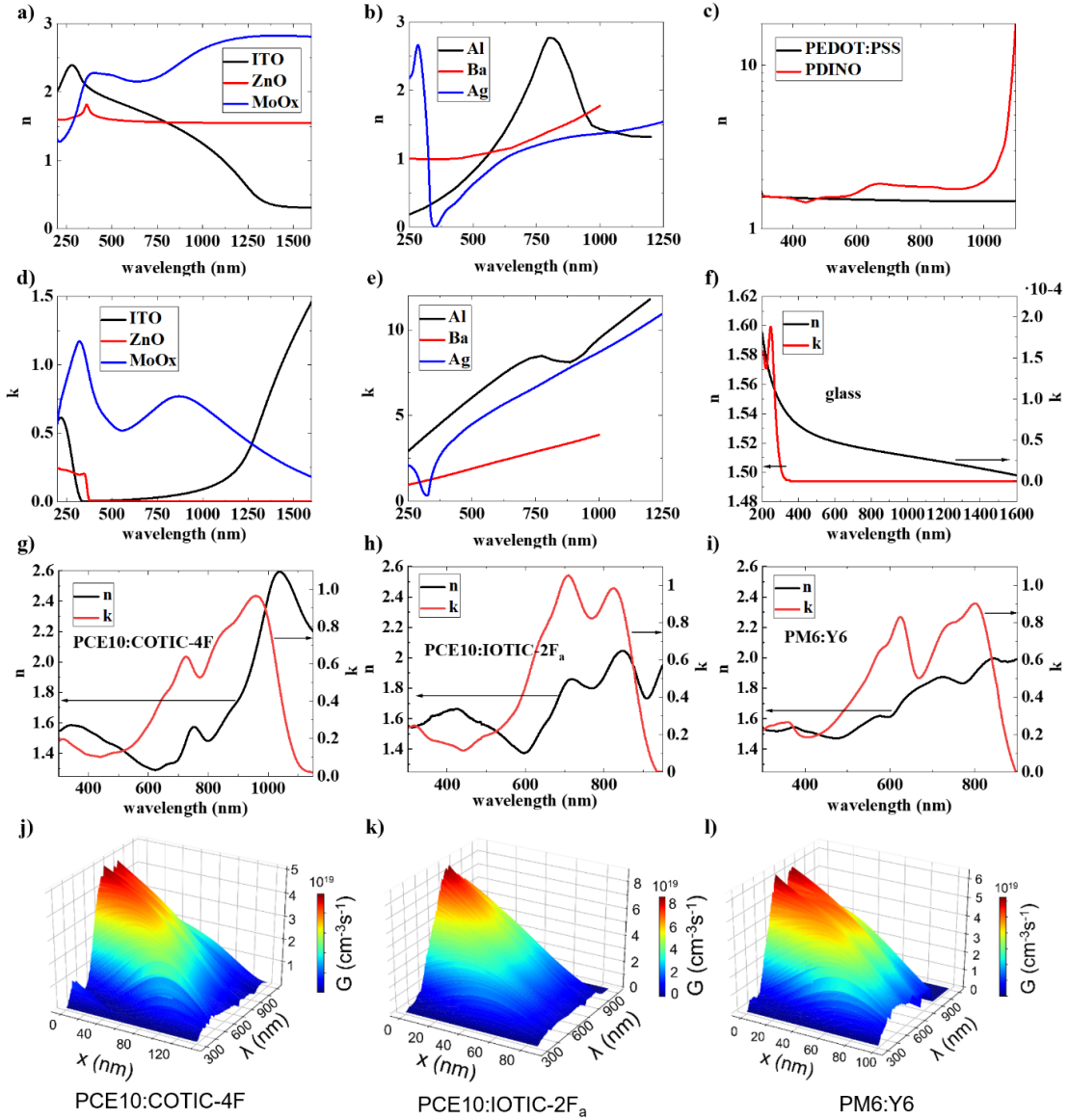
Figure 4.2. a), b), c) Refractive index *n* of metal oxides, metals and organic materials used in the device fabricated in this work. d), e), f) Extinction coefficients *k* of metal oxides, metals and organic materials used in the device fabricated in this work. g), h), i) Refractive index and extinction coefficient of the active layers. j), k), l) The resulting generation rates $G(x,\lambda)$ under 100 mW/cm^2 AM 1.5 illumination.

The refractive indices, n, of the metal oxides Indium-Tin Oxide (ITO), Zinc Oxide (ZnO) and Molybdenum(VI)oxide (MoOx) are shown in **Figure 4.2a**, n of the metals Al, Ba and Ag are shown in Figure 4.2b and n of the organic materials poly(3,4-ethylenedioxythiophene) polystyrene sulfonate (PEDOT:PSS) and 2,9-Bis[3-(dimethyloxidoamino)propyl]anthra[2,1,9-def:6,5,10-d'e'f']diisoquinoline-1,3,8,10(2H,9H)-tetrone (PDINO) are shown in Figure 4.2c. The extinction coefficients $k(\lambda)$ of these materials are displayed in Figure 4.2d-f. The glass substrate's optical properties can be found in Figure S4.3. The optical properties of the active layers PCE10:COTIC-4F, PCE10:IOTIC-2F$_a$ and PM6:Y6 are shown in Figure 4.2g-i and Figure S4.2 shows the corresponding absorption coefficients. The comparison of the three blends reveals that the refractive index is in the narrow range between 1.3 and 2.6 for all three blends over the measured spectrum, in good agreement with the common assumption than most organic semiconducting materials have values of n $\approx$ 2.[130] The extinction coefficient of the PCE10:COTIC-4F blend peaks around 960 nm at a value slightly below 1. This absorption in the infrared, caused by the NFA, is in agreement with the reported ultra-narrow band gap of COTIC-4F.[275] The PCE10:IOTIC-2F$_a$ is slightly more absorbing at its peak values, which are located at 709 nm and 824 nm, but the absorption window is narrower than in the previous blend; its extinction coefficient does not extend much beyond 900 nm. The values of the extinction coefficient of the PM6:Y6 blend and its absorption window are of similar magnitude as to those of the PCE10:IOTIC-2F$_a$ blend but a blueshift of both absorption onset and offset can be observed.

Having obtained all optical constants, we then simulated the exciton generation rates $G(x,\lambda)$ under 100 mW/cm^2 AM1.5 illumination with the available transfer matrix method software.[162,163,253] The generation rates are shown in Figure 4.2-l for the three solar cell systems. The position x ranges from $x = 0$, which describes the interface of the active layer with the ZnO layer in inverted and the PEDOT:PSS layer in conventional structure, to $x = L$, for the device

active layer thicknesses of j) $L = 140$ nm, k) $L = 86$ nm and l) $L = 100$ nm. From all three generation rate profiles, it is evident that the absorbing nature of the active layer causes the maximum absorption to be in the vicinity of the $x = 0$ interface. It is noteworthy, that the devices based on the COTIC-4F:PCE10 and the PM6:Y6 blend benefit from generation rates that extend more into the bulk of the active layer, which becomes visible when comparing $G(x,\lambda)$ beyond 80 nm for each system; in the case of the solar cell that is based on PCE10:IOTIC-2F$_a$, the generation is strongly reduced at positions beyond 80 nm despite high generation ($> 810^{19}$ cm^{-3}s^{-1}) near $x = 0$. In general, a high generation rate is expected to be beneficial for the device performance as it is expected to increase the short-circuit current. We will demonstrate though, that a direct correlation cannot be made as other factors impact the performance under short-circuit conditions as well.

4.2.2 Quantifying Geminate Recombination: Determination of the Geminate Recombination Prefactor

The integration of $G(x,\lambda)$ over the known spectrum $I(\lambda)$ leads to an only spatially dependent generation rate $G(x)$, as schematically depicted in **Figure 4.3a**. When this spatially dependent generation rate $G(x)$ is integrated once more over the active layer thickness L, we obtain the photogenerated charge carrier flux in the active layer. Multiplication with the elementary charge q, therefore, directly yields the theoretically obtainable short-circuit current $J_{sc,theo}$ that is based on the optical simulations.
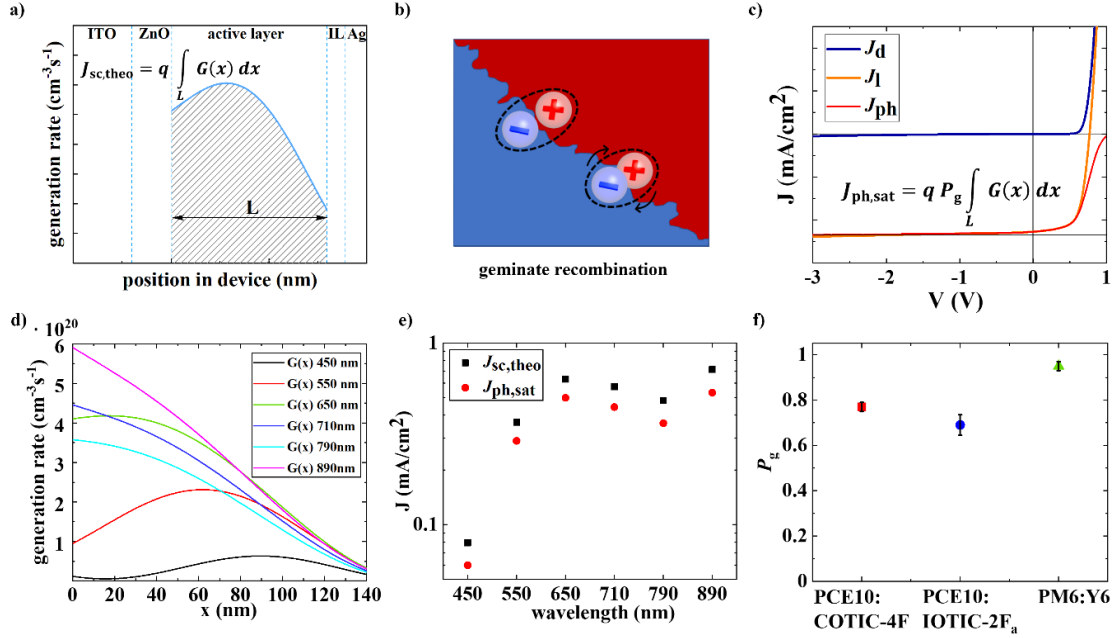
Figure 4.3. a) Schematic of the generation rate $G(x)$ in dependence of the position in the device under illumination from the $x = 0$ side, to visualize the relationship between the theoretical short-circuit current $J_{sc,theo}$ and $G(x)$. b) schematic of geminate recombination of a coulombically bound electron-hole pair at the donor-acceptor interface in the active layer. c) schematic of a solar cell's dark current J_d, light current J_l and the resulting photocurrent J_{ph}, which saturates at large reverse bias as $J_{ph,sat}$, and the relationship with $G(x)$. d) spatially resolved exciton generation rates in the same device under the chosen monochromatic illumination. e) measured saturated photocurrent $J_{ph,sat}$ and theoretical short-circuit current $J_{sc,theo}$ for different monochromatic illumination conditions of a PCE10:COTIC-4F solar cell, showing negligible wavelength dependence. f) Geminate recombination prefactor P_g for the PCE10:COTIC-4F, PCE10:IOTIC-2F$_a$ and PM6:Y6 solar cells.

In practice, not all absorbed photons create free charge carriers to yield $J_{sc,theo}$, since a fraction of the created excitons in the active layer recombines geminately at the donor/acceptor interface before the electron-hole pair separates into free electron and hole (Figure 4.3b).[156,245,280,281] These geminate recombination losses can be quantified by comparison of the simulated theoretical short-circuit current $J_{sc,theo}$ with the experimental saturated photocurrent $J_{ph,sat}$, which is reached at large reverse bias (see Figure 4.3c). The photocurrent J_{ph} is defined as $J_{ph} = J_l\text{-}J_d$, with J_l being the current under illumination and J_d the current in the dark, as schematically shown in Figure 4.3c. At high reverse bias, the internal electrostatic field in the active layer of the solar cell is large and

in good approximation, all free photogenerated electrons and holes are extracted at the respective electrodes and non-geminate losses are negligible.[98,282,283] Therefore, the difference between the simulated $J_{sc,theo}$ and the experimental $J_{ph,sat}$ can be only attributed to geminate recombination losses.[98,282,283] Consequently, we can define the geminate prefactor P_g as $P_g = J_{ph,sat}/J_{sc,theo}$, which describes the fraction of free electrons or holes per created exciton.

To quantify the geminate recombination losses, we combine the simulation of the generation rate under monochromatic illumination of known intensity with experimental JV-characteristics under the same illumination conditions. The use of monochromatic illumination eliminates errors that would arise if the illumination spectrum were not well defined (e.g., due to changes in the solar simulator spectrum over time or more generally due to a not well-defined spectral distribution). Further, it can reveal inaccuracies of the simulation input if repeated at multiple wavelengths. Since the simulated short circuit current/the measured saturated photocurrent both depend on the absorption in the active layer (proportional to k) and on the optical field distribution in the active layer (which is determined by the optical properties of all layers in the device due to interference, reflection on the interfaces and parasitic absorption), a constant ratio and with that a constant P_g is only expected if all input parameter (thicknesses, optical properties, illumination conditions) are set correctly. Therefore, a repetition of the experiment at multiple wavelengths allows checking for potential errors in any of these parameters.

To determine P_g for the first blend system based on PCE10:COTIC-4F, we first illuminated a solar cell at monochromatic illumination of known intensity at a wavelength of 450 nm. We obtained the saturated photocurrent $J_{ph,sat}$ under this illumination condition experimentally and simulated the $J_{sc,theo}$ of the device for this illumination condition, which yields $P_g = 0.75$. We then repeated the experiment and the simulation for monochromatic light at different wavelengths of 550 nm, 650 nm, 710 nm, 790 nm and 890 nm. Figure 4.3d visualizes the Generation rates at

these chosen monochromatic illumination conditions. The $J_{ph,sat}$ and $J_{sc,theo}$ values that we obtained are shown in Figure 4.3e. The geminate recombination prefactor P_g as the average across the $J_{ph,sat}/J_{sc,theo}$ ratios under illumination at different wavelengths amounts to $P_g = 0.77 \pm 0.02$ for the PCE10:COTIC-4F system, as shown in Figure 4.3f.

We obtained P_g for the other two blend systems in the same manner. Figure 4.3f shows that the geminate losses in the PCE10:IOTIC-2F$_a$ system, with $P_g = 0.69 \pm 0.04$, are slightly increased in comparison to the geminate losses in the PCE10:COTIC-4F. The higher-performing PM6:Y6 system though shows only minimal geminate recombination losses, with $P_g = 0.95 \pm 0.02$. This result is in good agreement with a recent study of the geminate losses of the PM6:Y6 system with the time-delayed collection field, EQE, and V_{oc} measurements.[98]

4.2.3 Simulation of the External Quantum Efficiency: Determining $\mu\tau$

After the determination of the geminate recombination prefactor, we obtain the $\mu\tau$ product by simulating and fitting the external quantum efficiency (EQE(λ) or EQE) to the experimental EQE. The EQE of a solar cell is defined as the electron flux in the outer circuit per wavelength-dependent photon flux of the incident light and is typically measured at 0 V. The electron flux can be described by the short circuit current as J_{sc}/q, and the incident photon flux is the light Intensity $I(\lambda)$ divided by the photon energy $h\nu$, as shown in Equation 4.1. In contrast to the J_{sc}, the EQE is not sensitive to the exact illumination conditions of the experimental setup, as is evident from its definition.

We simulate the exciton generation rate $G(x)$ under monochromatic illumination considering the standard AM1.5 spectral distribution and divide the simulated $J_{sc,theo}$ by the photon flux of the monochromatic illumination known from the same AM1.5 spectrum. This way, we obtain the

simulated EQE_{theo}, which is the theoretical maximum of the EQE, based on only the optical simulations, assuming full extraction and no geminate recombination ($\eta = 1$ and $P_g = 1$).

Under real working conditions, a part of photogenerated excitons will be lost due to geminate recombination, and, in addition, free charge carriers will recombine non-geminately. Thus, the measured J_{sc} is defined by P_g and the charge extraction efficiency $\eta(x)$. The apparent EQE can, therefore, be calculated by using Equation 4.1.

$$EQE_\lambda = \frac{electron\ flux\ in\ circuit}{incident\ photon\ flux} = \frac{J_{sc}}{I(\lambda)}\frac{h\nu}{q} = P_g \frac{\int_0^L G(x,\lambda)\ \eta(x)\ dx}{I(\lambda)}\frac{h\nu}{q} \tag{4.1}$$

The Hecht equation (Equation 4.2) describes the spatially resolved extraction efficiency $\eta(x)$, here shown for the inverted structure, for which light enters the device from the electron collecting electrode.[254,273] As the sum of the extraction efficiency for electrons $\eta_n(x)$ (Equation 4.2b) and the extraction efficiency for holes $\eta_p(x)$ (Equation 4.2c), $\eta(x)$ depends on the mean free path w that a charge carrier travels in the active layer before recombining, on the active layer thickness L and the position x within the active layer. The mean free path is directly proportional to the mobility-lifetime product $\mu\tau$ and the internal electrostatic field V_{bi}/L.

$$\eta(x) = \eta_n(x) + \eta_p(x) \tag{4.2a}$$

$$\eta_n = \frac{w}{L}\left(1 - \exp\frac{-(L-x)}{w}\right) \tag{4.2b}$$

$$\eta_p = \frac{w}{L}\left(1 - \exp\frac{-x}{w}\right) \tag{4.2c}$$

$$w = \frac{\mu\tau V_{bi}}{L} \tag{4.3}$$
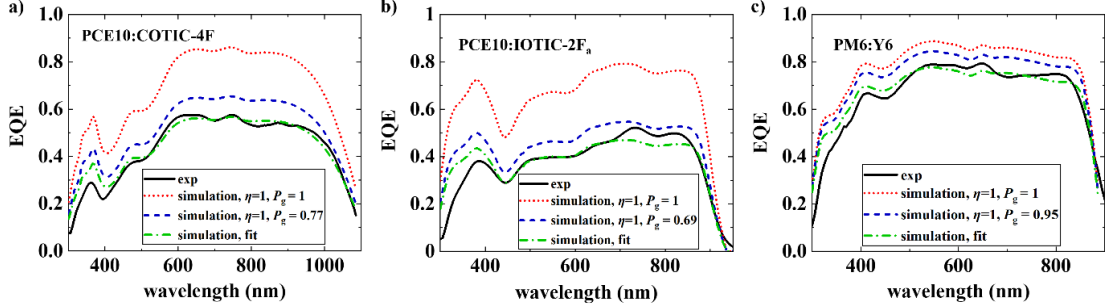
Figure 4.4. Experimental EQE spectra (black solid curves) and simulated EQE spectra for η =1 and P_g=1 (red dotted curves), simulated EQE spectra for η=1 and P_g as determined experimentally (blue dashed curves) and fit of the simulated EQE to the experimental EQE (green dash-dotted curves) for solar cells based on a) PCE10:COTIC-4F, b) PCE10:IOTIC-2Fa and c) PM6:Y6.

We determined the built-in potential, V_{bi}, from the dark current-voltage characteristics and used the AM1.5 spectral distribution to calculate the theoretical EQE_{theo} (Equation 4.1) for the case of $P_g = 1$ and $\eta = 1$, shown in **Figure 4.4** (dotted red curves) for the three blend systems. The solar cells based on PCE10:COTIC-4F and PM6:Y6 exceed high external quantum efficiencies of 0.8, which is expected based on the generation rates that were discussed earlier. Specifically, the PM6:Y6 system has a relatively flat high response over a wide wavelength range (400-850 nm) thanks to the efficient charge generation in this system.

Next, we take the geminate losses into account, which reduce the EQEs to different extends (dashed blue curves). The EQEs that would be obtained if only geminate losses would occur are significantly lower than the EQE_{theo} (> 20% reduction) for the PCE10:COTIC-4F and the PCE10:IOTIC-2F$_a$ device, showing that geminate losses govern the experimental EQE to a significant extent in these systems, whereas the higher-performing PM6:Y6 system shows only a negligible reduction of the EQE by geminate losses. We will discuss the implication for the short-circuit current in more detail below.

The remaining difference to the experimental EQE is attributed to the extraction efficiency $\eta(x)$ as a function of $\mu\tau$. Least-square fitting, with $\mu\tau$ as the only fitting parameter, yields the

110

green dash-dotted curves in Figure 4.4. The simulated and fitted EQEs capture the overall shape and the wavelength-dependent features of the experimental EQEs very well, implying that the device architecture and optical properties were determined accurately and confirming the simulation of the generation rates. In the inverted PCE10:COTIC-4F solar cell, the EQE is slightly overestimated around 400 nm, whereas the rest of the spectrum shows an exceptionally good fit, including the infrared wavelength region beyond 1000 nm. Inhomogeneities of the ZnO film thickness might cause the deviation around 400 nm since the absorption of ZnO is limited to wavelengths around this wavelength region. Similarly, a small overestimation at short-wavelengths can be seen in the case of PCE10:IOTIC-2F$_a$ and to a lesser extend for PM6:Y6. Here, it might be caused by either an underestimation of the reflection from the Al back electrode, which would lead to a lower generation around 320 nm, possibly caused by minor deviations of the Ba or PDINO interlayer thickness. Around 700 to 800 nm, the EQE is slightly underestimated in the PCE10:IOTIC-2F$_a$ solar cell. A possible reason could, in this case, be the absorption of the ITO layer, which has an onset around 700 nm. We note that these explanations, which are based on the simulated fraction of absorbed light in each layer, are speculative in nature, as the interplay of the optical properties of all layers and their thicknesses that govern the simulated EQE is complex. Further, we cannot exclude that minor changes in the processing conditions of the materials employed in the device structure do not impact their optical properties. Considering all these aspects, we want to highlight again the very good agreement of simulated and experimental *EQE* for most parts of the spectrum. The values for the mobility-lifetime products obtained by this fitting are summarized in **Figure 4.5**.

4.2.4 Comparison with Impedance Spectroscopy

To validate our new approach, we analyzed the solar cells based on PCE10:COTIC-4F, PCE10:IOTIC-2F$_a$ and PM6:Y6 with an independent method. We employed voltage-capacitance spectroscopy (impedance spectroscopy) and used a conventional approach to determine the $\mu\tau$ product by fitting the recombination current.[136,137] The values for $\mu\tau$ obtained by this method are also shown in Figure 4.5. Figure S4.5 shows the capacitance spectra in the dark and under illumination, and Figure S4.6 shows the fits of the total recombination current and separate contributions of all dominant recombination mechanisms.
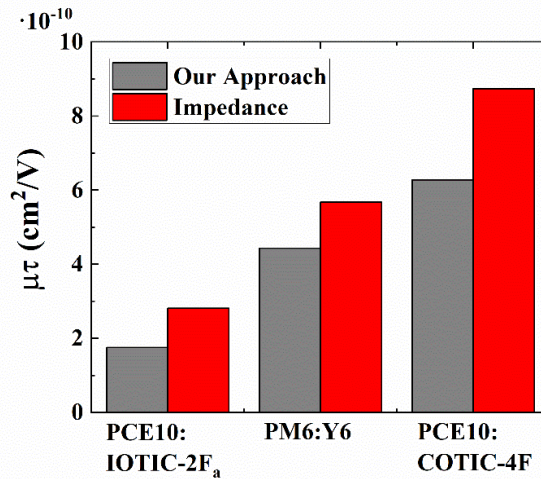
Figure 4.5. Comparison of the determined mobility-lifetime product based on our proposed approach with the one based on the analysis of capacitance-voltage spectra 'impedance'.[136,137]

From this comparison, good agreement between our proposed method and the established impedance spectroscopy technique can be seen, confirming the validity of our approach to determine P_g and $\mu\tau$. To further demonstrate the applicability of our approach to fullerene systems, we carried out the analysis for a P3HT:PC$_{60}$BM based solar cell as described in the S9. Good correlation between the results obtained by our approach and those obtained with impedance spectroscopy were found for this system as well as shown in Figure S4.9.

While the impedance spectroscopy technique yields besides the $\mu\tau$ product also non-geminate recombination parameters for bulk trap-assisted, surface trap-assisted and bimolecular recombination as well as bias-dependent charge carrier densities, it has several short-comings.[136,137] First, the technique requires the measurement of the *JV*-characteristics and the real and imaginary parts of the impedance of the solar cell in the dark and under illumination at different biases with an impedance analyzer, an instrument that is not always available. Second, a rather complex multi-step analysis and fitting process follow. The measurement and analysis of impedance spectroscopy data are not only time-consuming but can be challenging for inexperienced users.

In contrast, our approach uses only *JV*-curves and EQE measurement, two quick standard measurements that are available in most, if not all, OPV laboratories. Second, the transfer matrix method-based simulations combined with our python-based software and the optical properties of standard OPV materials are available at no cost and allow the reproducible automated fitting of the EQE. However, the most significant advantage of our approach is that it allows us to obtain information about the generation process and the geminate recombination losses, which is crucial for the understanding of the electronic processes under short-circuit conditions. Finally, it can be employed for material- and time-conserving device optimization, as outlined after the discussion of the results.

4.2.5 Discussion of the Processes under Short-Circuit Conditions

The analysis of the three systems provides a comprehensive picture of the limitations under short-circuit conditions. The results are summarized in **Table 4.1** and the spatially dependent extraction probability is displayed in Figure S7.

Table 4.1. Geminate recombination prefactor P_g, mobility-lifetime product $\mu\tau$ and average extraction efficiency $\bar{\eta}$ (AEE) determined by our approach for the three studied solar cells and theoretical J_{sc} that would be obtained without any geminate recombination and extraction losses, theoretical J_{sc} that would be obtained without extraction losses and J_{sc} based on the experimental EQE, all under 100 mW AM1.5 illumination.

	P_g	$\mu\tau$ [cm²/V]	$\bar{\eta}$ (AEE)	J_{sc} $\bar{\eta}$=1, P_g=1 [mA/cm²]	J_{sc} $\bar{\eta}$=1 [mA/cm²]	J_{sc} [mA/cm²]
PCE10:COTIC-4F	0.77 ± 0.02	$6.3\cdot10^{-10}$	0.86	30.8	23.7	20.4
PCE10:IOTIC-2F$_a$	0.69 ± 0.04	$1.8\cdot10^{-10}$	0.86	24.4	16.9	14.5
PM6:Y6	0.95 ± 0.02	$4.4\cdot10^{-10}$	0.92	27.0	25.7	23.6

The integration of the EQE of the ultra-narrow band gap system PCE10:COTIC-4F, using the AM1.5 spectrum, gives a J_{sc} of 20.4 mA/cm². Note that this value varies slightly from the experimental J_{sc}, due to the small mismatch between the used solar simulator's spectrum and the AM1.5 spectrum. The J_{sc} is close to the values of the most efficient systems currently reported. Nevertheless, the theoretical J_{sc} that would be obtained without the contribution of geminate recombination and extraction losses is even higher (30.8 mA/cm²) and with that the highest among the three systems, due to a thick active layer (140 nm) and absorption in a broad spectral range. A geminate prefactor of 0.77 reduces the number of photogenerated free charge carriers to a considerable extend. If all of them were extracted, a J_{sc} of 23.7 mA/cm² would be achieved. Despite the thick active layer and a low build-in field (V_{bi} = 0.623 V) an average extraction efficiency (AEE) of 0.86 is reached, which is explained by the large $\mu\tau$ of $6.3\cdot10^{-10}$ cm²/V.

The PCE10:IOTIC-2F$_a$ system absorbs in a narrower range, and its active layer is thinner (86 nm). If all charge carriers would be efficiently separated and extracted, a maximum J_{sc} of 24.4 mA/cm² could be reached. Geminate recombination plays a significant role in this system as well, reducing the number of free charge carriers by a factor of P_g = 0.69. The low $\mu\tau$ of $1.8\cdot10^{-10}$ cm²/V does not limit extraction in this device as much as it would in the previous case: In fact,

the thin active layer combined with a high $V_{bi} = 0.920$ V leads to the same AEE (0.86) as in the previously discussed PCE10:COTIC-4F system, yielding a J_{sc} of 14.5 mA/cm^2 under 1 sun AM1.5 illumination according to the experimental EQE.

PM6:Y6 has the highest J_{sc} of the three systems; under 100 mW AM1.5 illumination 23.6 mA/cm^2 is obtained. This value is close to the maximum obtainable J_{sc} (27.0 mA/cm^2). Geminate recombination losses are almost absent in this high performing system ($P_g = 0.95$) and an intermediate $\mu\tau$ of $4.4 \cdot 10^{-10}$ cm^2/V and $V_{bi} = 0.849$ V lead to a high AEE of 0.92 in the 100 nm thick device. These results explain the above-average performance of this blend system and illustrate that the three chosen blend systems and their short-circuit currents are predominantly defined by geminate recombination losses and not extraction losses. This is expected because the active layer thicknesses have been experimentally optimized before this work. Further morphological optimization may be of interest for the PCE10:IOTIC-2F$_a$ and the PCE10:COTIC-4F system, whereas we see that the PM6:Y6 system already performs close to its intrinsic limits.

4.2.6 Application for Device Optimization

These examples illustrate how our approach allows making an in-depth assessment of the photoelectronic processes under short-circuit conditions and how it can guide the device optimization. In fact, we can take this a step further and predict the J_{sc} for different active layer thicknesses, taking into account the determined spatially- and wavelength-dependent exciton generation, the geminate recombination prefactor, and the thickness-dependent extraction efficiencies. Figure S4.8 shows the theoretical $J_{sc,theo}$ that is calculated based on the optical transfer matrix method-based simulations (blue curve) and the AEE (black curve) as a function of the active layer thickness, calculated according to Equation 4.2 and averaged across the position in

the active layer. The red curve represents the predicted J_{sc} based on our approach, which is the product of the geminate prefactor, the extraction efficiency and the $J_{sc,theo}$ as a function of different active layer thicknesses L. We see that the active layer thicknesses of the devices used in this study (dashed lines) are all within the green 98% range of the maximum J_{sc} that we predict. Experimental data of several devices (black squares) fit exceptionally well with our predictions. Figure S4.8 illustrates how our approach goes beyond an active layer thickness optimization that is based solely on the maximization of the J_{sc} with optical simulations. In the case of PCE10:IOTIC-2F$_a$, for example, it is evident that a thin active layer is crucial for good extraction due to the low $\mu\tau$. We predict a maximum J_{sc} for this system around 98 nm, whereas optical transfer matrix method-based simulations predict an optimum active layer thickness of 133 nm to obtain the highest J_{sc}. A summary of the procedure for applying our approach for the device optimization can be found in the SI. To conclude, we expect our new method to be a useful tool for the characterization of the optoelectronic properties and for optimizing the active layer thickness for a maximum J_{sc} by fabrication and analysis of a single solar cell. While having discussed the analysis of three OPV systems in this work, we would like to highlight that our approach can be applied to Perovskite solar cells as well.

4.3 Conclusion

In this work, we provide the optical constants of relevant OPV materials and used a simple approach to quantify geminate recombination losses, coupling experimental JV-characteristics, measured under different monochromatic illumination, with optical transfer matrix-based simulation. Based on this, we then proposed a new method to obtain the $\mu\tau$ product in OPVs, which requires only the standard measurement of the EQE spectrum. We applied our new approach to three different non-fullerene acceptor based organic solar cell systems in inverted or

conventional device configurations and determined the geminate prefactor P_g, the mobility-lifetime product $\mu\tau$ and the extraction efficiency η. We have found very good agreement between the results for $\mu\tau$ obtained by the proposed method and those derived from the established advanced analysis of voltage-capacitance-spectroscopic data. We further show that our simple method can predict the optimal device configuration/active layer thickness with accuracy that goes beyond the predictions based on only optical transfer matrix simulations, offering a fast and cheap alternative to the time- and material-consuming experimental device optimization.

4.4 Experimental Section

Fabrication of Organic Solar Cells

Organics Photovoltaic devices were fabricated in inverted and conventional structure with the configurations glass/ITO/ZnO/PCE10:COTIC-4F/MoOx/Ag, glass/ITO/PEDOT:PSS/PCE10:IOTIC-2F$_a$/Ba/Al and glass/ITO/PEDOT:PSS/PM6:Y6/PDINO/Al. ITO substrates were purchased from Naranjo, cleaned with commercial detergent and distilled water and subsequent sonication in distilled water, acetone and isopropyl alcohol, for 20 minutes each. The substrates were dried overnight in an oven at 130 ℃. In the case of the inverted device structure, the ZnO bottom contact was prepared by spin-coating a solution of Tetrahydrofuran and Diethylzinc (15% w/w in toluene) in a 2:1 volume ratio (30 µl at 4000 rpm for 15 seconds in air). After annealing the substrates for 20 minutes at 150 ℃ under normal atmosphere, they were transferred into a nitrogen-filled glove box for the preparation of the active layer. A solution of PCE10:COTIC-4F (20 mg/mL, 1:1.5 D:A mass ratio in chlorobenzene with 2% chloronaphthalene) was prepared beforehand and stirred for a minimum of three hours at 56 ℃. 25 µl of this solution was spin-coated at 1500 rpm

for 1 minute. The deposition of the top electrodes by thermal evaporation followed with an Ångstrom evaporator at pressures of less than 10^{-6} Torr.

For the devices in conventional structure, the ITO substrates were treated with UV-ozone for 15 minutes and a layer of poly(3,4-ethylenedioxythiophene): poly(styrenesulfonate) (PEDOT:PSS, Clevios P VP Al 8043) was spin-coated outside the glovebox at 2500 rpm for one minute. The substrates were annealed for 20 minutes at 140 ℃. For each batch of conventional devices, a substrate with PEDOT:PSS that was processed and annealed at the same time as those that were used for the device fabrication to determine the thickness of the PEDOT:PSS layer of that particular batch of devices.

The active layers were prepared in the same manner as for the inverted structure, from a solution of PCE10:IOTIC-2F$_a$ (21.5 mg/mL, 1:1.5 D:A mass ratio in Chlorobenzene with 1% 1,8-Diiodooctane at 3000 rpm) and PM6:Y6 (18 g/mL,1:1.5 D:A mass ratio in Chloroform with 1.5% chloronaphthalene, spin-coated at 4000 rpm), respectively. For the devices based on PM6:Y6, a PDINO solution in methanol with a concentration of 1 mg/mL was spin-coated on top of the active layer before Al was deposited by thermal evaporation.

Solar Cell Characterization

Current-voltage characteristics were measured inside a glove box using a Keithley 2602Bsourcemeter. J-V curves were measured in the dark and under illumination of 10 mW cm^{-2} (using an OD1 Newport 5215neutral density filter) and at 100 mW cm^{-2} with a solar simulator with a 300 W Xe lamp and an aperture of 9.4 mm^2 was used to define the illuminated area. The solar simulator's light intensity was calibrated with a standard silicon solar cell with KG1 filter, which was calibrated by the National Renewable Energy Laboratory.

The external quantum efficiency (EQE) was measured using a 75 W Xe light source, monochromator, optical chopper (155 Hz), and a lock-in amplifier. Power-density calibration was performed with a calibrated Newport silicon photodiode. The focused monochromatic beam of the EQE lamp onto the device was photographed with respect to the known device substrate's dimensions, and the area was obtained by the pixel count of the illuminated area, and a light intensity between OD1 and 1 sun was found.

For the determination of the geminate prefactor, the solar cells were illuminated with a monochromatic light source (300 W Xe lamp with a set of interference filters) inside a glove box. The current-voltage characteristics under monochromatic illumination were measured with a Keithley 4200 semiconductor characterization system. The monochromatic light's power was measured with a Thor Labs silicon photodiode.

A Solartron SI1260 impedance analyzer was used to obtain the impedance spectra (frequency range 10^1–10^6 Hz). The devices were illuminated at 1 sun and 0.1 sun with the same solar simulator used for the measurement of the JV-characteristics. A small amplitude AC signal with 40 mV was used.

Optical Simulations and Fitting

The device architecture was determined by profilometry measurements with an Ambios XP-100 profilometer. The optical properties were determined by ellipsometry with a Woollam M-2000DI 4 Variable Angle Spectroscopic Ellipsometer. As the substrate, either quartz glass or silicon was used and included in the model for fitting the layer of interest. The software for the Transfer Matrix Model was used as available from the literature to simulate the profile of the optical field in the active layer and to obtain the spatially and wavelength-dependent generation rates.[163] The python-based code created for this work works in conjunction with the optical modeling

software. More details about the code and its availability are described in the Supporting Information.

4.5 Supplementary Information for Chapter 4

4.5.1 Supplementary Data

Table S4.1. Average photoelectrical parameters of the solar cells used in this work under 1 sun solar simulator illumination.

	J_{SC} (mA/cm²)	V_{OC} (V)	FF (%)	PCE (%)
PCE10:COTIC-4F	20.9 ± 0.1	0.57 ± 0.01	57.5 ± 0.6	6.8 ± 0.1
PCE10:IOTIC-2F$_a$	16.5 ± 0.4	0.80 ± 0.01	55.3 ± 0.1	7.3 ± 0.2
PM6:Y6	24.0 ± 0.9	0.78 ± 0.01	64.9 ± 2.7	12.1 ± 0.4
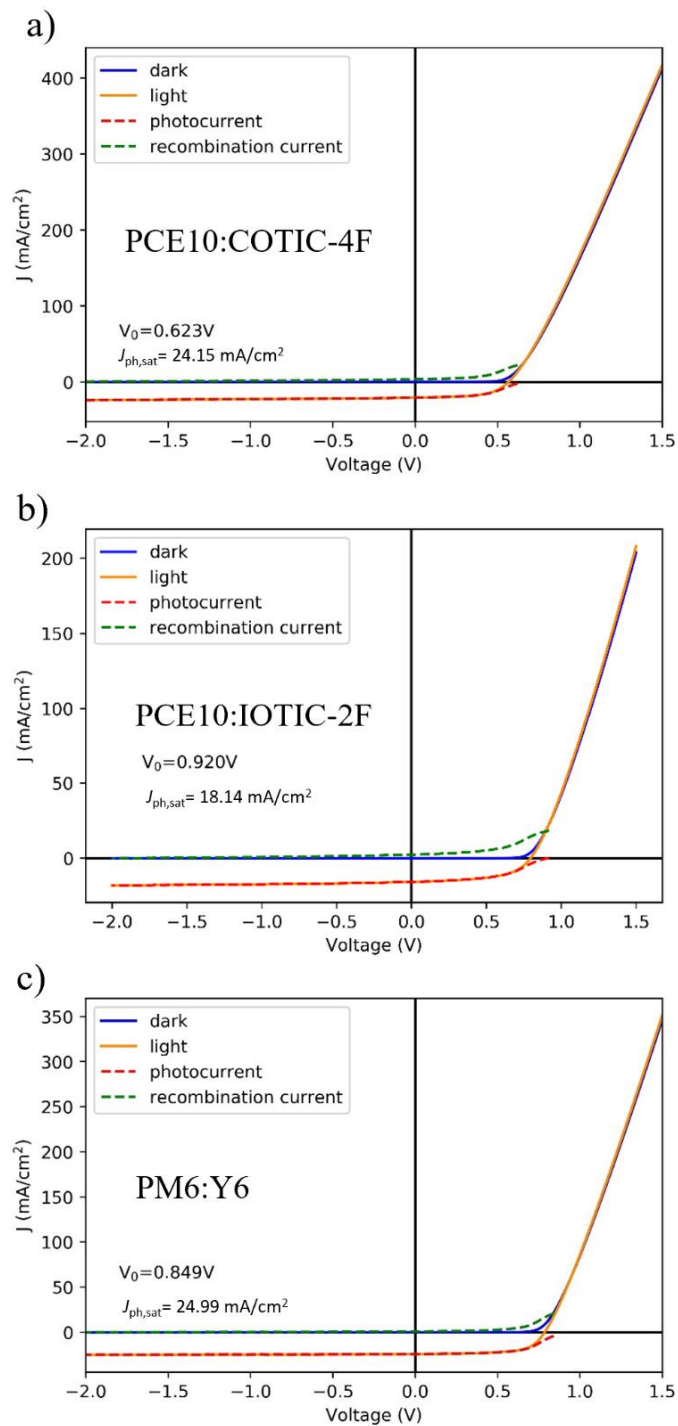
Figure S4.1. Current-voltage characteristics in the dark and under 1 sun illumination, photocurrent, saturated photocurrent and V_0 of a a) PCE10:COTIC-4F, b) PCE10:IOTIC-2F$_a$ and c) PM6:Y6 solar cell.
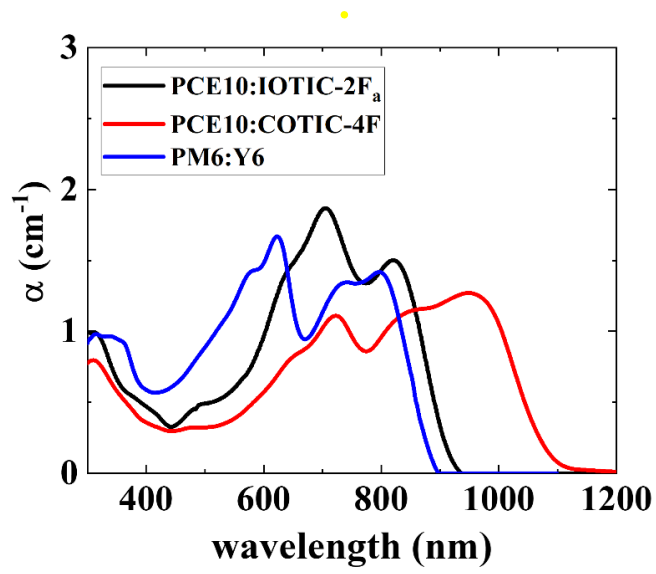
Figure S4.2. Absorption coefficient α of the three solar cell blends.
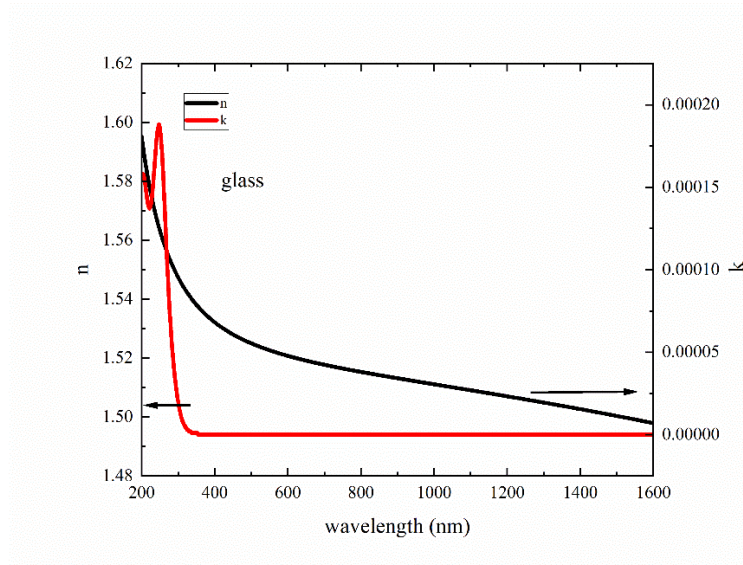
Figure S4.3. Optical constants of glass, determined with spectroscopic ellipsometry.
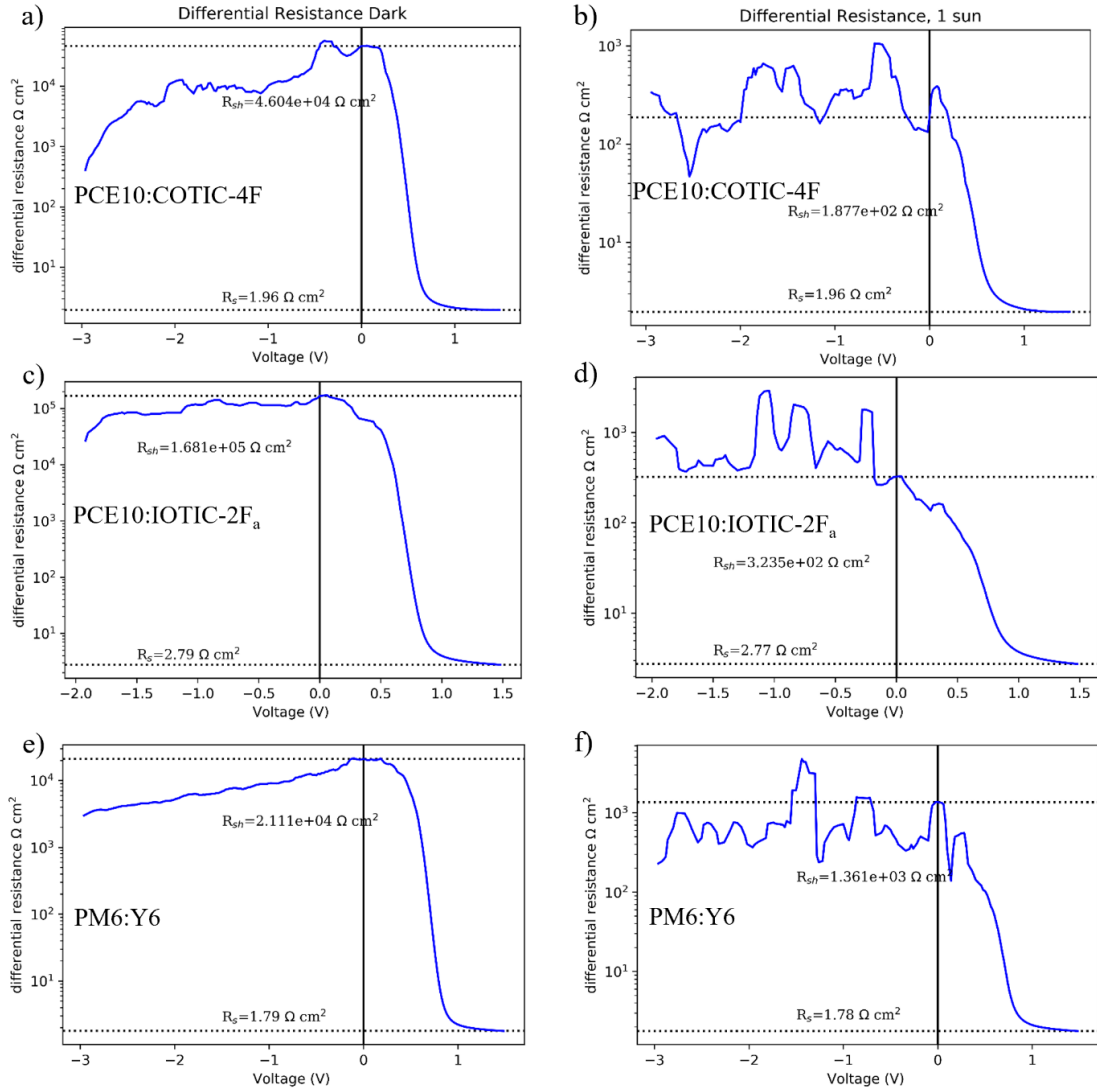
Figure S4.4. Differential Resistance of a),b) the PCE10:COTIC-4F solar cells in the dark and under 1 sun illumination, of c),d) the PCE10:IOTIC-2F$_a$ solar cells in the dark and under 1 sun illumination and e),f) the PM6:Y6 solar cells in the dark and under 1 sun illumination.

We determined the $\mu\tau$ at two illumination conditions (OD1 and 1 sun) since the illumination intensity of the used EQE setup is in between OD1 and 1 sun illumination. The average of the obtained values is displayed in Figure 4.5. The differential resistance at OD1 was assumed to be identical with the data for 1 sun for the analysis, which is justified by the minor changes observed comparing the differential resistance in the dark and under 1 sun illumination.
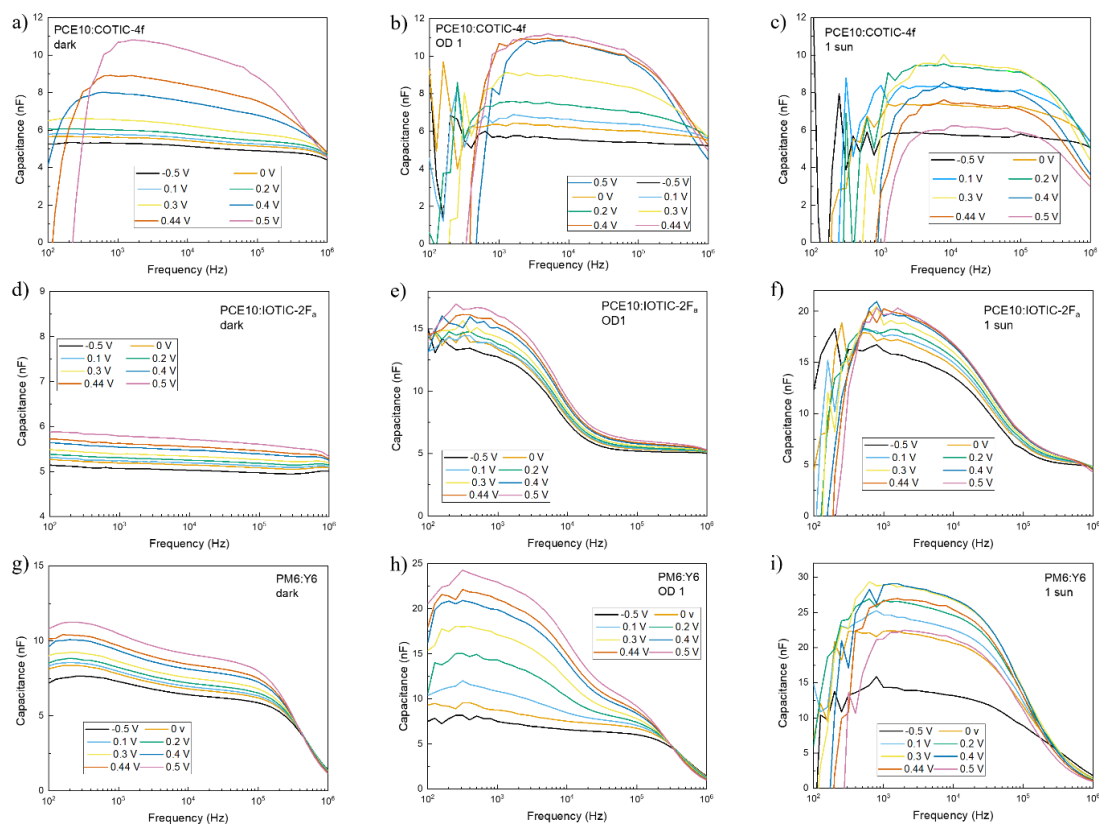
Figure S4.5. Frequency-dependent capacitance-voltage spectra of a) a PCE10:COTIC-4F solar in the dark, b) at an illumination of 0.1 sun and c) at an illumination of 1 sun, d) capacitance-voltage spectra of a PCE10:IOTIC-2F$_a$ solar in the dark, e) at an illumination of 0.1 sun and f) at an illumination of 1 sun, g) capacitance-voltage spectra of a PM6:Y6 solar in the dark, h) at an illumination of 0.1 sun and i) at an illumination of 1 sun.
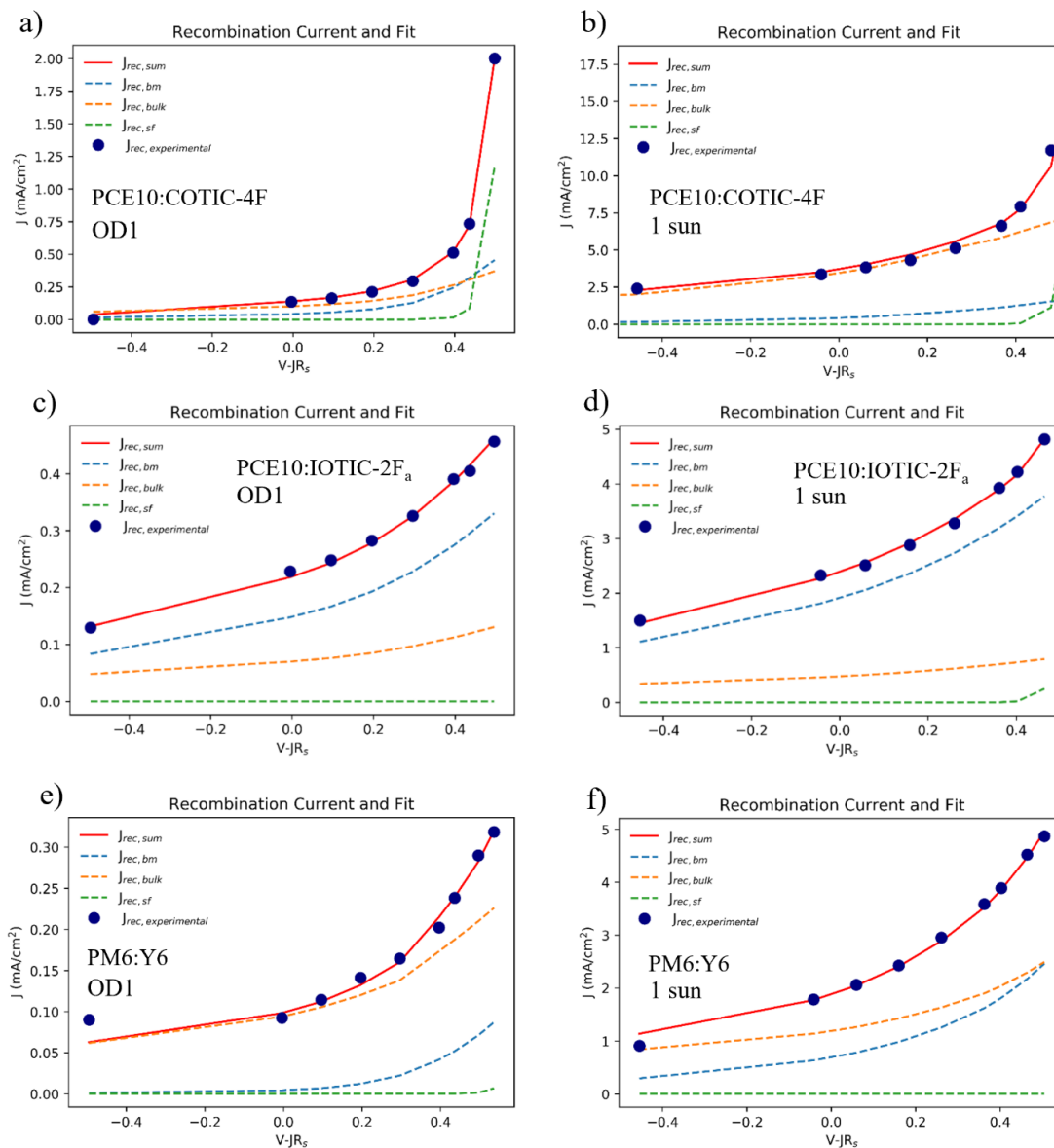
Figure S4.6. Experimental recombination current and fit of the recombination current based on the parameters determined by the analysis of the impedance spectroscopy data of a) a PCE10:COTIC-4F solar cell under 0.1 sun and b) 1 sun illumination, of c) a PCE10:IOTIC-2F$_a$ solar cell under 0.1 sun and d) 1 sun illumination and e) a PM6:Y6 solar cell under 0.1 sun and f) 1 sun illumination.
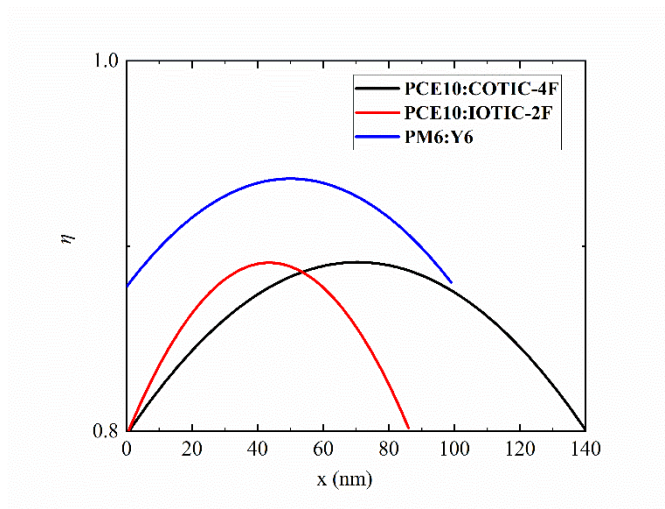
Figure S4.7. Spatially resolved and extraction efficiencies for the three investigated solar cells at 0 V and spatially averaged value of the extraction efficiencies $\bar{\eta}$.
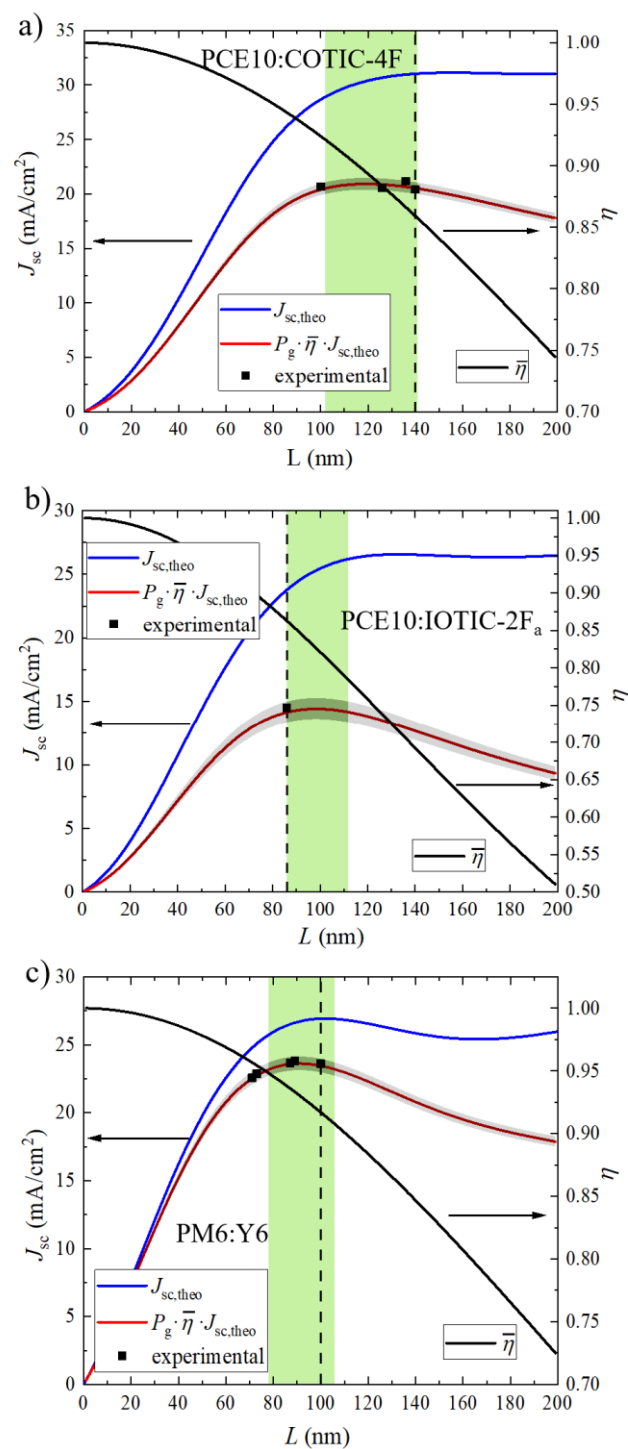
Figure S4.8. $J_{sc,theo}$, calculated based on optical transfer matrix method simulations, extraction efficiency $\bar{\eta}$ and the predicted J_{sc} as the product of P_g, $J_{sc,theo}$ and $\bar{\eta}$, in dependence on the active layer thickness L for the three studied systems, as well as experimental data points. The green range indicates the thickness range in which the highest J_{sc} is expected (98% of maximum). The dashed line indicates the active layer thickness that was used in this study.

4.5.2 Applicability to Fullerene Systems:

To demonstrate the applicability of the approach for fullerene systems, a P3HT:PC$_{60}$BM solar cell with the device architecture glass/ITO (130 nm)/ PEDOT:PSS (20 nm)/P3HT:PC$_{60}$BM (123 nm)/Al (63 nm) was fabricated and analyzed. The approach was carried out as described in the main text but the µτ was calculated from the EQE at 550 nm. We find good agreement between the impedance spectroscopy results, which were obtained in the same manner as described for the other systems, and those delivered by our approach for $\mu\tau$. The optical properties were used as reported in literature for films processed under the same conditions.[284]
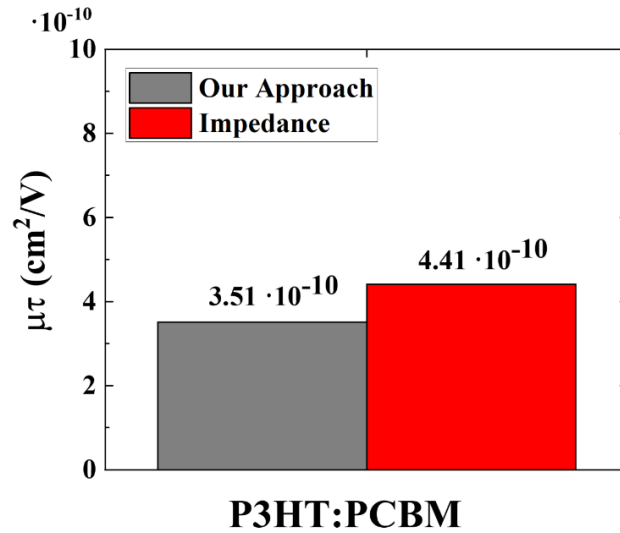
Figure S4.9. Comparison of the results obtained by our approach and by impedance spectroscopy for a P3HT:PCBM solar cell.

4.5.3 Step-by Step Guide for the Application of our Approach to the Device Optimization

After obtaining the optical constants of the active layer and of other layers that are not provided in this work or other literature, the following steps lead to the prediction of the thickness-dependent J_{sc}.

Experimental steps:

1. Fabrication of at least one solar cell (thickness measurement should be done after completing the other experimental steps)

2. Measurement of the JV-characteristics at 1 sun and in the dark (to obtain V_{bi})

3. Measurement of the EQE

4. Measuring JV-characteristics under monochromatic illumination

Simulation and Calculation Steps:

5. Simulating the $J_{sc,theo}$ under the monochromatic illumination used in step 4. (It is important to set other wavelengths to zero in the spectral distribution file.)

6. Calculation of P_g

7. Using the provided software (see below) to obtain $\mu\tau$ and the extraction efficiency η by fitting to measured EQE.

8. Calculation of the extraction probability $\eta(x)$ for each thickness L of interest, then averaging $\eta(x)$ to get extraction efficiency $\bar{\eta}$ for each L.

9. Simulation of the $J_{sc,ideal}$ for each L (no losses) with TMM under 1 sun AM 1.5 or the spectrum of your interest. (blue curve)

Product of $P_g, \eta(L)$ and simulated $J_{sc,ideal}$ give predicted $J_{sc.}$ (red curve)

4.5.4 Software

The python-based software created for this work operates in conjunction with the transfer matrix method software that was developed by George F. Burkhard, Eric T. Hoke at Stanford University.[130]

Our part of the code includes:

- the visualization of the 3D Generation rate

- the calculation of the EQE in dependence on the position x in the device, the wavelengths and the $\mu\tau$

- fitting of the calculated $EQEs$ to the experimental EQE and the output of the $\mu\tau$

- the calculation of the J_{sc} from measured EQE for AM1.5 illumination

- a visualization of the extraction efficiency $\eta(x)$ of electrons and holes at 0 V in dependence of the position in the device based on the determined $\mu\tau$

- a visualization of the extraction efficiency $\eta(x)$ of electrons and holes at -3 V in dependence of the position in the device based on the determined $\mu\tau$

- the average extraction efficiency $\bar{\eta}$ for different active layer thicknesses (required for device optimization)

The combined software can be accessed publicly and used under the GNU license agreement after the date of publication of this work. It can be found together with the optical constants provided in the manuscript under https://github.com/nschopp/Optoelectronic-Processes-in-Organic-Solar-Cells-Under-Short-Circuit-Conditions.

Chapter 5: On Optoelectronic Processes in Organic Solar Cells: From Opaque to Transparent

5.1 Introduction

Organic photovoltaics (OPVs) offer a cost-effective, sustainable alternative for energy harvesting. In the past few years, OPVs underwent enormous progress, with power conversions now reaching over 18%.[165,166,168,169,180] In contrast to their inorganic counterparts, OPVs are lightweight, thin and flexible, and their fabrication is less energy-intensive.[170,285,286] These advantages alone open up an entire range of new applications for remote energy harvesting. The perhaps most striking feature of organic materials is their molecular tunability, which has brought colorful and transparent or semitransparent (ST-) OPVs to reality.[167,170,275,287] ST-OPVs can be integrated into windows to harvest energy on-site, allowing unlimited architectural design possibilities and natural lighting for buildings.[67,68,170,288–290] When integrated into greenhouses, they can generate electricity while selectively transmitting the spectral range necessary for unhindered plant growth.[52,53,170] To meet the requirements for semitransparency, the active layer of the solar cell must absorb light outside the visible range (380 nm to 780 nm) while maintaining high transparency in the visible range.[291,292] The emergence of versatile non-fullerene acceptor (NFA) molecules for bulk heterojunction (BHJ) solar cells played a leading role in the development of ultra-narrow band gap systems. These have paved the way for the desired high absorption in the infrared range that is accompanied by a high average visible transmittance (AVT).[275,293,294] While NFA based donor:acceptor BHJ solar cells have been studied intensively in the past few years, efforts to understand the photoelectrical processes in BHJ solar cells mainly focused on opaque systems with high photo-conversion efficiencies (PCEs).[137,215,295] The inherent effects of semitransparency on the device physics in OPVs have rarely been addressed. One of the

challenges that arise is that the AVT cannot be experimentally varied as an independent parameter without altering other material properties. This work takes advantage of a simulation-based approach to unravel the effect of (semi)transparency on charge generation, non-geminate recombination and extraction processes in organic ST-OPVs and discusses the impact of series and shunt resistance on the solar cells with respect to the AVT. With that, the study aims to guide the further development of efficient ST-OPVs by underlining changes that are causally linked to the increased transparency, pointing out aspects of special considerations for the fabrication of efficient ST-OPVs.

5.2 Results and Discussion

5.2.1 Properties of the Designed Model Device Systems

The effects of increased transparency are investigated by performing a comprehensive simulation-based study in which the absorption in the visible range is selectively varied while keeping all other parameters constant. We choose six fictive model device systems that are based on the physical properties of the previously reported state-of-the-art donor:NFA system PM6:Y6. The device structures are schematically depicted in **Figure 5.1**.[215]

Figure 5.2a shows the optical constants that are the starting point of the simulations carried out in this work. The active layers labeled as k 0.75, k 0.5, k 0.25 and k 0 are obtained by a reduction of the extinction coefficient k 1 of the original blend to 75%, 50%, 25% and 0% of its initial values in the visible range (380 - 780 nm). Due to the variation of k in only the visible part of the spectrum, an increased transmittance/increased transparency is equivalent to an increased AVT in this work. It is worth noting that, generally, the terms AVT and

transparency/transmittance cannot be used interchangeably because changes in the absorption outside the visible range would not lead to a change in the AVT.
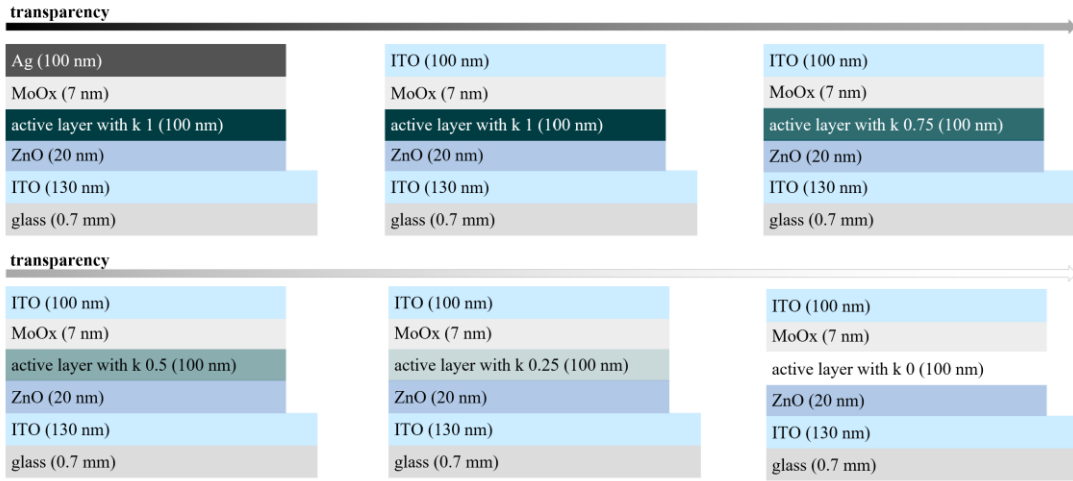
Figure 5.1. Device architectures of the solar cells studied by simulation in this work and schematic indication of the device stack's transparency.

The refractive index $n(\lambda)$ used for all devices is shown in Figure 5.2a. The variation of only k without any change in the refractive index n may not represent the physical relationship of n and k. Yet, it allows the study of the effect of the reduced absorption without introducing the complexity of changes in reflectance and interference patterns due to refractive index changes. This approach is supported by work that has shown that variation in the refractive index of organic semiconductors has a minor impact on the absorption and the accuracy of the transfer matrix optical simulation.[296]
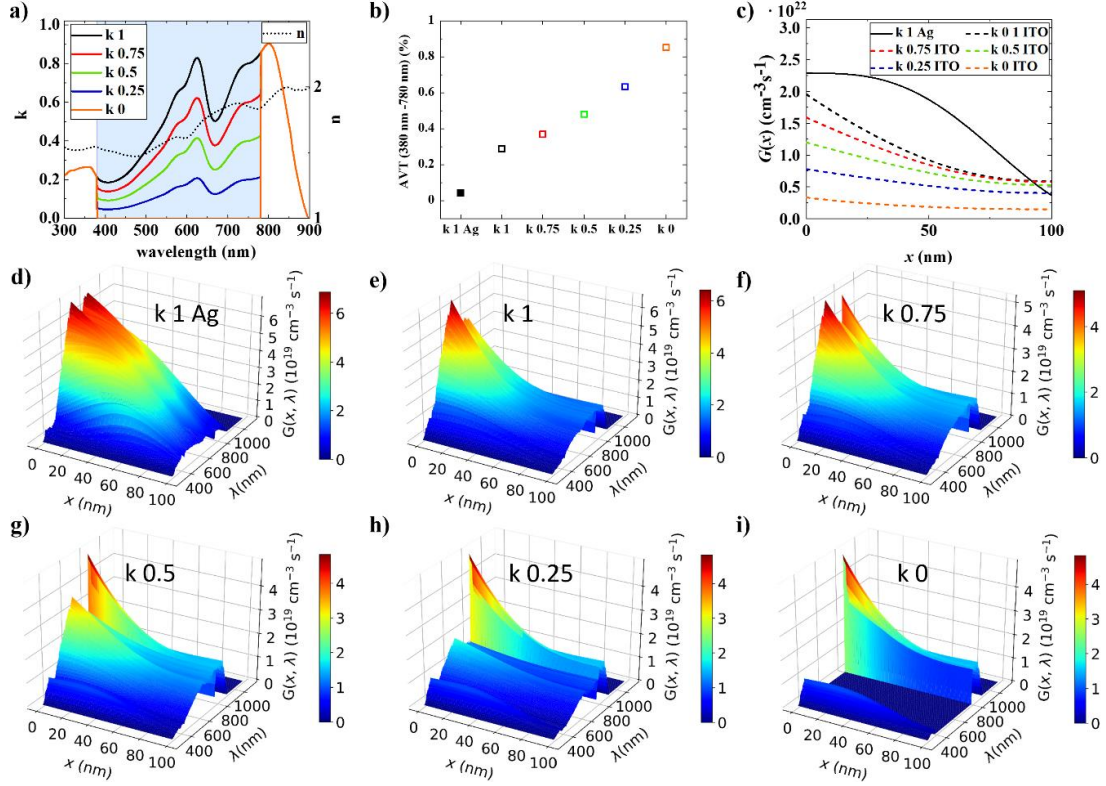
Figure 5.2. Optical properties of the model systems and the resulting AVT and generation rates. a) Refractive index *n* and systematically varied extinction coefficient *k* of the active layers. Optical constants of all device layers available from the literature.[215,297] b) The resulting increased AVT of the devices with different active layers. c) Simulated spatially dependent generation rate $G(x)$ for AM1.5 illumination reveal changes in the spatial distribution and the magnitude of charge carrier generation upon variation of the AVT. d–i) Simulated spatially- and wavelength-dependent generation rates for all devices reflect the systematically reduced absorption in the visible range.

The device configurations studied in this work are based on an inverted device structure comprised of an indium tin oxide (ITO) coated glass substrate with an electron collecting layer of zinc oxide (ZnO), followed by the active layer with the systematically modified extinction coefficient *k* and a hole collecting layer of molybdenum(VI) oxide (MoOx) with either silver or ITO as the back contact. The device architecture of the Ag k 1 device is *glass(0.7 mm)/ITO(130 nm)/ZnO(20nm)/active layer with original k 1 (100 nm)/ MoOx (7 nm)/Ag (100 nm)*. In the devices k 1, k 0.75, k 0.5, k 0.25 and k 0 the Ag electrode is replaced by a transparent ITO top contact, and, thus, the device structures are *glass(0.7 mm)/ITO(130 nm)/ZnO(20nm)/active layer k 1, k 0.75,*

k 0.5, k 0.25 or k 0 (100 nm)/ MoOx (7 nm)/ITO(100 nm). These devices are referred to as Ag k 1, k 1, k 0.75, k 0.5, k 0.25 and k 0. In a first step, the AVTs of the solar cells are calculated based on the transmittance of each device stack, the spectral intensity distribution of the AM1.5 spectrum $I(\lambda)$ and the photopic spectral response of the human eye $V(\lambda)$, as $AVT = \frac{\int I(\lambda)\cdot T(\lambda)\cdot V(\lambda)\, d\lambda}{\int T(\lambda)\cdot V(\lambda)\, d\lambda}$.[298,299] The transmittance $T(\lambda)$ of each device stack is obtained from optical transfer matrix method simulations and the resulting AVT values are shown in Figure 5.2b. Device k Ag 1 with Ag back contact is opaque, with an AVT of only 4%. Replacing Ag with ITO leads to a vastly increased AVT of 29%, which was then further increased upon the reduction of the active layer's absorbance in the visible range to 37% for k 0.75, to 48% for k 0.5, to 63% for k 0.25 and 85% for k 0. These AVTs cover a wide range, confirming that the chosen model systems offer an appropriate setting for the systematic investigation of the effect of increased transparency on the photoelectronic processes in ST-OPVs.

5.2.2 Impact of the AVT on the Charge Generation Processes

The reduced absorption of photons in the more transparent devices directly results in reduced exciton generation rates and hence reduced charge generation rates. The charge generation rates $G(x, \lambda)$, in dependence on the position x in the active layer (illumination from x = 0 side at normal incidence) and the wavelength λ, are simulated with the optical transfer matrix method and are shown in Figure 5.2d to 1i, based on the device architectures and the optical constants of each layer. The resulting 3D-generation rate profiles visualize the effect of increased AVT on the charge carrier generation under 1 sun AM1.5 illumination. First, the expected reduction of the exciton generation rate in the visible range with increased transparency is apparent. Second, the effects of the reflective Ag back electrode can be seen. To be able to

compare the resulting generation rates, we show the spatially dependent charge generation rate $G(x)$, that is calculated as $\int_{\lambda}^{\lambda'} G(x, \lambda)\, d\lambda = G(x)$, in Figure 5.2c. This plot demonstrates that the strongly reduced backside reflection, caused by the close match of the refractive indices of the active layer and ITO, leads to a reduction of $G(x)$ (maximum from $2.3 \cdot 10^{22}$ cm^{-3} s^{-1} to $2 \cdot 10^{22}$ cm^{-3} s^{-1}) and a shift of its maximum to the side of illumination when replacing Ag with ITO without changing the active layer. The reduction of the absorption in the active layer reduces $G(x)$ further by approximately one order of magnitude (maximum at $0.3 \cdot 10^{22}$ cm^{-3} s^{-1} for the k 0 device). The impact of the changes in the spatially and wavelength-dependent photo-generation rates on the photoelectronic processes in organic solar cells will be discussed in the remaining text.

5.2.3 Impact of the AVT on the V_{oc} and the Charge Recombination Dynamics

First, we consider the impact of the changes in the charge generation on the open circuit-voltage and the charge recombination dynamics of the solar cell. Total charge recombination losses in organic BHJ solar cells are caused by geminate and non-geminate recombination processes.[95,137,200] Geminate recombination annihilates electrons and holes that originate from the same photoexcitation before splitting into free charge carriers, and the latter describes the recombination of free electrons and holes. Non-geminate recombination can be subdivided into bimolecular recombination (electron and hole recombine from band to band) and trap-assisted recombination, in which trap states within the band gap facilitate the recombination process.[198,200,237] These trap states can be further divided into bulk traps and surface traps, causing bulk trap-assisted and surface trap-assisted recombination, respectively.[136,137,295]

Table 5.1. Device parameters, based on the study of the reported PM6:Y6 system, used as input for calculation of the V_{oc}.

parameter	Value
Dielectric constant ε	3
Band gap E_g	1.0 eV
Effective density of States N_c	$2.5 \cdot 10^{19}$ cm^{-3}
Density of surface traps $N_{t,surf}$	10^{12} cm^{-2}
Density of bulk traps $N_{t,bulk}$	10^{16} cm^{-3}
Geminate recombination prefactor P_g	0.95
Temperature T	298 K
Effective mobility μ_{eff}	$5 \cdot 10^{-5}$ cm^2/Vs
Built-in voltage V_{bi}	0.9 V
Langevin prefactor for bimolecular recombination χ	0.005

The device parameters used in this simulation, based on the study of the reported PM6:Y6 system, are summarized in Table 5.1.[215] For the trap densities, typically observed values reported in the literature are chosen, and the value of N_c is used as described by Koster et. al.[159] These parameters are kept constant for all studied systems unless stated otherwise so that the observed changes are only caused by the change in the transparency. The Langevin prefactor χ, the dielectric constant ε and the effective mobility μ_{eff} define the bimolecular recombination coefficient k_{bm} according to Equation 5.1.[137] The density of bulk traps N_t, which facilitates trap-assisted recombination, allows for calculating the bulk trap-assisted recombination coefficient k_{bulk}, as shown in Equation 5.2. The recombination coefficient k_{surf} for surface trap-assisted recombination depends on the density of surface traps $N_{t,surf}$, the built-in field V_{bi} and the open-circuit voltage (V_{oc}). The V_{oc} can be calculated using Equation 5.4, in which the expression $P_g \, I/I_0 \iint G(x,\lambda)dx \, d\lambda$ describes the photogeneration rate of free charge carriers.[137] Here, P_g is a prefactor that describes the reduction of the number of generated charge carriers due to

geminate recombination losses, I is the light intensity and I_0 the light intensity at 1 sun. The calculated V_{oc} at T=298 K is shown in **Figure 5.3a**.

$$k_{bm} = \frac{2\,q\,\mu_{eff}\,\xi}{\varepsilon\varepsilon_0} \qquad (5.1)$$

$$k_{bulk} = \frac{q\,\mu_{eff}N_{bulk}}{\varepsilon\varepsilon_0} \qquad (5.2)$$

$$k_{sf} = \frac{q\,\mu_{eff}N_{sf}}{L\,\varepsilon\varepsilon_0}\,e^{-q\frac{V_{bi}-V_{oc}}{kT}} \qquad (5.3)$$

$$V_{oc} = E_g - \frac{2kT}{q}\cdot\ln\left(\frac{2k_{bm}N_C}{\sqrt{(k_{bulk}+k_{sf})^2+4k_{bm}P_g\,I/I_0\iint G(x,\lambda)dx\,d\lambda}-k_b-k_{sf}}\right) \qquad (5.4)$$
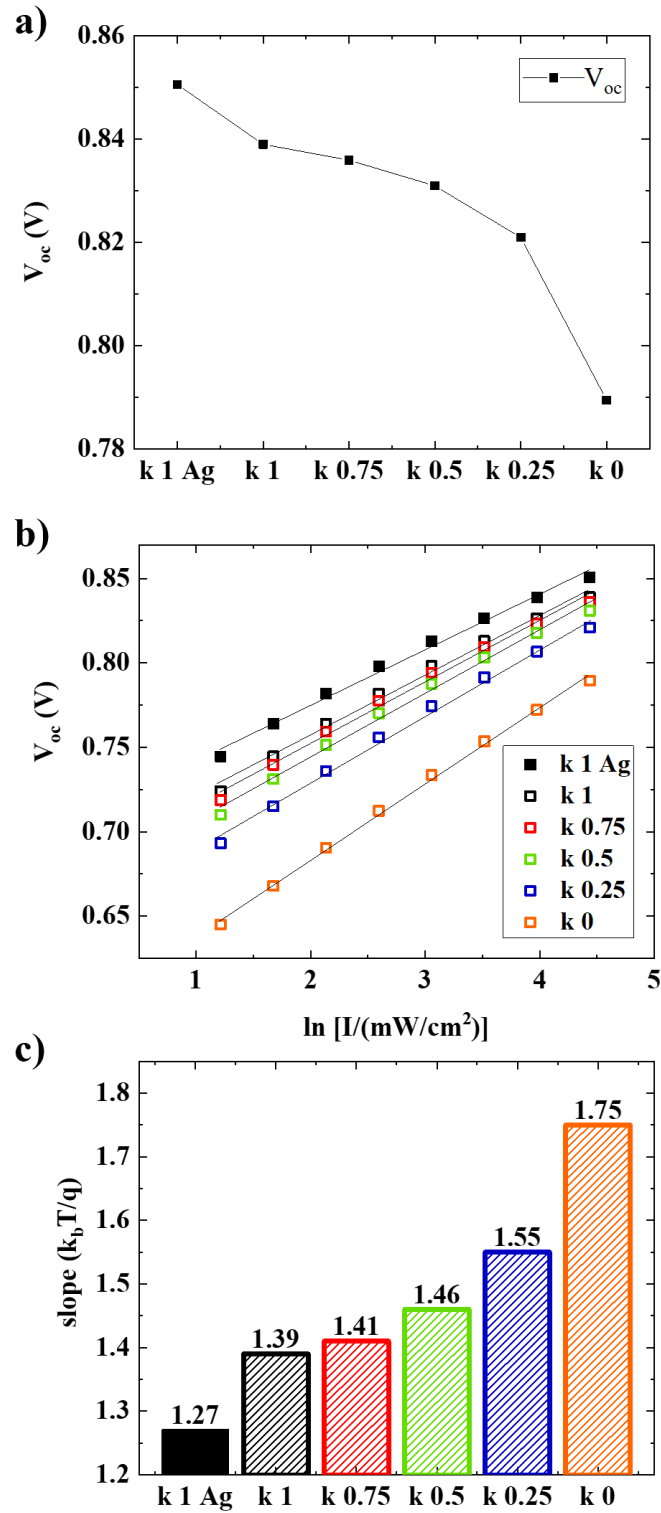
Figure 5.3. a) V_{oc} of the different devices studied. b) Light-intensity dependence of the V_{oc} for the devices with different AVT. c) The slope of the linear regression of the V_{oc} as a function of the natural logarithm of the light intensity.

The model device systems show a change in V_{oc} from 0.85 V (Ag Electrode, k 1) to 0.79 V (transparent ITO electrode with transparent active layer k 0) under 1 sun AM 1.5. As expected from the generation rates, the absence of the backside reflection from the Ag electrode alone leads to a reduction of the V_{oc} (0.83 V) and the further decrease is due to the reduced absorption of the active layer (k 1 to k 0). Next, the calculation of the V_{oc} was repeated to study the dependence on the illumination intensity. The change of V_{oc} with the illumination intensity I is a commonly used indicator of the dominant recombination mechanism.[159,295,300] In the case of pure bimolecular recombination, a slope of unity in the units of kT/q is expected, whereas a slope larger than unity is anticipated due to bulk trap-assisted recombination and a slope below unity due to surface trap-assisted recombination.[137,159,301] Figure 5.3b shows the V_{oc} in dependence on the light intensity. The slope of the linear regression is depicted in Figure 5.3c. An apparent increase of the slope S is observed with increased AVT, from $S = 1.27$ for the opaque device with Ag electrode to $S = 1.39$ for the device with ITO electrode and the same active layer k 1. The slope further increases to 1.41, 1.46, 1.55, and 1.75 upon modification of the active layer from k 0.75 to k 0, indicating an increased relative contribution of recombination *via* traps in the bulk of the active layer.

To quantify this observation, we calculate the recombination rates r_i of all three recombination channels, according to Equations 5.5 to 5.7 and their relative contribution to the total recombination rate $r = r_{bm} + r_{bulk} + r_{sf}$.[137]

$$r_{bm} = k_{bm} n_{oc}^2 \tag{5.5}$$

$$r_{bulk} = k_{bulk} n_{oc} \tag{5.6}$$

$$r_{surf}(V) = k_{sf}(V)\, n_{oc} \tag{5.7}$$

Figure 5.4a shows the resulting charge recombination rates for the different devices. The relative contribution of bimolecular, surface trap-assisted and bulk trap-assisted recombination is shown in Figure 5.4b. The indicated increase in the relative contribution of bulk trap-assisted recombination becomes evident. In the opaque device with Ag electrode, surface trap-assisted (38%) and bimolecular recombination (36%) dominate slightly over bulk trap-assisted recombination (26%) due to the large V_{oc} (see Equation 5.3 for k_{surf}) and due to the high concentration of photogenerated charge carriers (see Equations 5.5 for n_{bm}). The change of the electrode to transparent ITO leads to a slight increase in the relative contribution of bulk trap-assisted recombination to 33% and a decrease of surface trap-assisted recombination, resulting in balanced contributions of all recombination channels. This increasingly dominant bulk-trap contribution continues when the active layer becomes more transparent, increasing to 35%, 38%, 44% and finally 65% for the active layers with k 0.75, k 0.5, k 0.25 and k 0, respectively. The relative contributions of surface and bimolecular recombination thus are reduced, with the more substantial reduction observed for surface trap-assisted recombination (9% for k 0) and a moderate decrease for bimolecular recombination (to 27% for k 0).
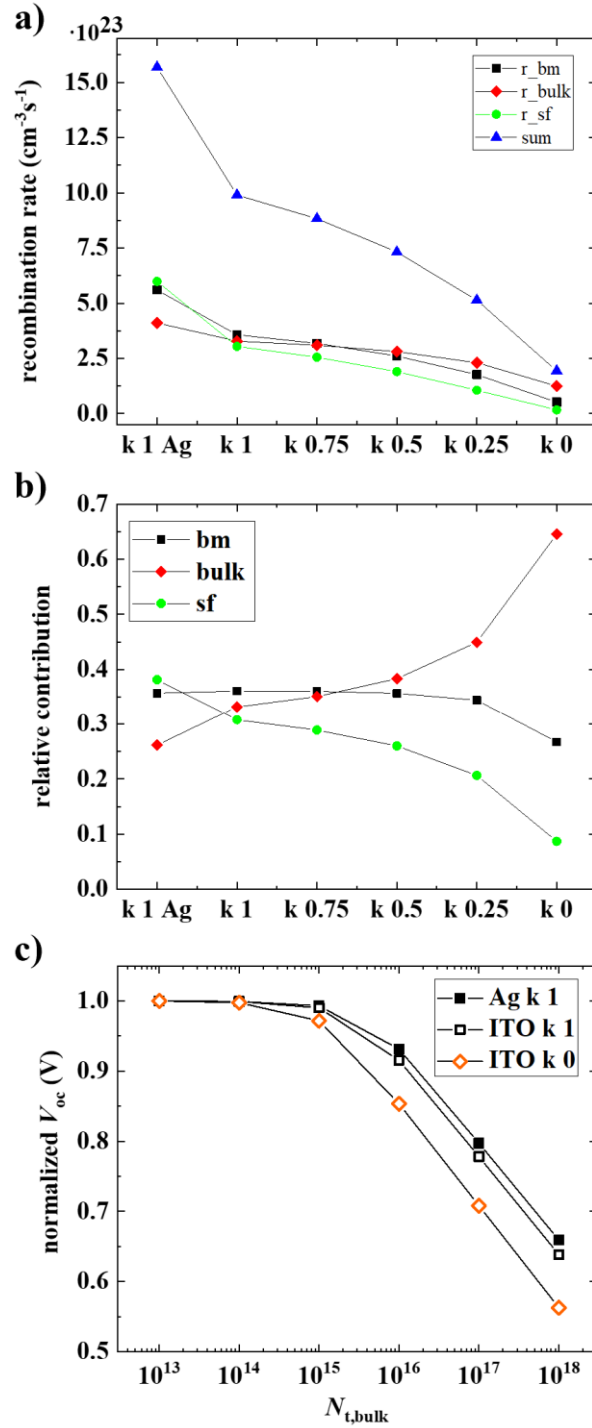
Figure 5.4. Quantitative analysis of the recombination processes in the solar cell under open-circuit conditions. a) The recombination rates for bimolecular recombination, bulk trap-assisted and surface trap-assisted recombination and their sum for the different devices. b) The relative contribution of bimolecular, bulk trap-assisted and surface trap-assisted recombination rates to the devices' total recombination rate with different AVT. c) Normalized V_{oc} versus bulk trap concentration N_t.

Knowing that the contribution of bulk trap-assisted recombination is of increased importance for transparent devices, we now shift our focus entirely to the impact of bulk traps. We calculated the change in the V_{oc} versus the bulk trap concentration N_t for the opaque device with the Ag electrode, the opaque active layer k 1 with the ITO electrode and the device k 0 with the highest AVT. We have previously discussed the absolute change of the V_{oc} with increased transparency; to compare the impact of bulk traps on the different values of V_{oc}, we normalized the V_{oc} to the values obtained at low bulk trap concentration ($N_t = 10^{13}$ cm^{-3}) for each device. The change of this normalized V_{oc} with N_t is shown in Figure 5.4c. In all three devices, the V_{oc} starts to drop noticeably at N_t larger than 10^{15} cm^{-3}. The sole replacement of the Ag electrode with ITO in combination with the same active layer k 1 leads to a slightly larger drop of the V_{oc}. As expected, based on Figure 5.4b, the additional replacement of the active layer with the highly transparent k 0 blend leads to the most extreme decrease of the V_{oc}: For a bulk trap concentration of 10^{18} cm^{-3} (a value at the top of the typically observed range), the V_{oc} decreases by 34% compared to the value obtained at $N_t = 10^{13}$ cm^{-3} in the case of Ag 1 device. Figure 5.4c shows a higher decrease of 36% for the k 1 device with the ITO electrode and an even more dramatic reduction of 44% for the k 0 device. From these results, we infer that the quality of the trap-free active layer blend is of higher importance for (semi)transparent OPVs than for the traditionally opaque devices. Material blends with low bulk trap concentration are necessary to achieve efficient OPVs with high AVT. In contrast, the concentration of surface traps arising at the contact interface (MoO$_3$ or ZnO$_2$) is less crucial for OPVs with higher transparency due to the exponential decrease of the surface recombination coefficient k_{surf} with the decline in of the V_{oc} that accompanies the increase of the AVT. Therefore, there are less strict requirements for the quality of the active layer/transparent electrode interfaces when developing ST-OPVs in comparison to their opaque counterparts. Traps at the interface can arise in the fabrication

process due to a variety of reasons. Parameters of influence include the processing and annealing conditions and the resulting morphologies of both layers, the roughness and homogeneity of the interface, the layers' composition and the resulting changes in surface energy.[216,302,303]

5.2.4 Impact of the AVT on the J_{sc} and the Charge Extraction Efficiency

Having established the understanding of how increased AVT influences the V_{oc} and the multi-channel non-geminate recombination dynamics, we will now shift the focus to the short-circuit current (J_{sc}) and the influence of the altered charge generation on the charge extraction probability. The short-circuit current with neglect of series resistance effects $J_{sc,Rs=0}$ corresponds to the photocurrent (J_{ph}) in the standard solar cell model, described by the equivalent circuit in Figure S5.1. $J_{sc,Rs=0}$ can be calculated based on the charge generation rate $G(x, \lambda)$, the spatially dependent extraction probability $\eta(x)$ and the geminate recombination prefactor P_g as described by Equation 5.8, with P_g ranging from 0 (all charge carriers recombine geminately) to 1 (no geminate losses). The spatially dependent extraction probability $\eta(x)$, with x being the position in the active layer ($x = 0$ position at the interface of the active layer and the front electrode), is formulated by the Hecht equation (Equation 5.9a to 5.9c) as the sum of the extraction efficiencies η_n and η_p for electrons and holes.[254,273] Both depend on the carrier mean free path w and the thickness of the active layer L. The mean free path can be obtained from Equation 5.10, and the lifetime τ can be obtained from the previously derived recombination coefficients (Equation 5.11). We note that the charge carrier density n_{Jsc} used here is the charge carrier density under short-circuit conditions. Due to the weak internal electric field and large injection at V_{oc}, the charge carrier density at V_{oc} is higher than that under short-circuit conditions. To account for this, we use the experimentally determined ratio of n_{oc}/ n_{Jsc} from the published work on the PM6:Y6 system, which is 11.64.[215]

$$J_{sc,Rs=0} = q \cdot P_g \int_{300\ nm}^{1090\ nm} \int_0^L G(x, \lambda)\, \eta(x)\, dx\, d\lambda \tag{5.8}$$

$$\eta(x) = \eta_n(x) + \eta_p(x) \tag{5.9a}$$

$$\eta_n(x) = \frac{w}{L}\left[1 - \exp\left(\frac{-L-x}{w}\right)\right] \tag{5.9b}$$

$$\eta_p(x) = \frac{w}{L}\left[1 - \exp\left(\frac{-x}{w}\right)\right] \tag{5.9c}$$

$$w = \frac{\mu\, \tau\, V_{bi}}{L} \tag{5.10}$$

$$\tau = \frac{1}{k_{sf} + k_{bulk} + k_{bm} n_{Jsc}} \tag{5.11}$$

Figure 5.5a shows the decrease of the $J_{sc,Rs=0}$ with increased AVT. A drop is expected due to the decreased absorption of photons and the reduced charge carrier generation shown in Figure 5.2c. It is not evident though, which role the different shapes of the spatial generation rates in conjunction with altered recombination dynamics and charge carrier densities play in the value of $J_{sc,Rs=0}$. To answer this question, we first calculate the short-circuit current $J_{sc.theo}$ that is predicted by simulation, assuming no geminate recombination nor extraction losses occur, as described in Equation 5.12.

$$J_{sc,theo=0} = q \cdot \int_{300\ nm}^{1090\ nm} \int_0^L G(x, \lambda)\, dx\, d\lambda \tag{5.12}$$

145
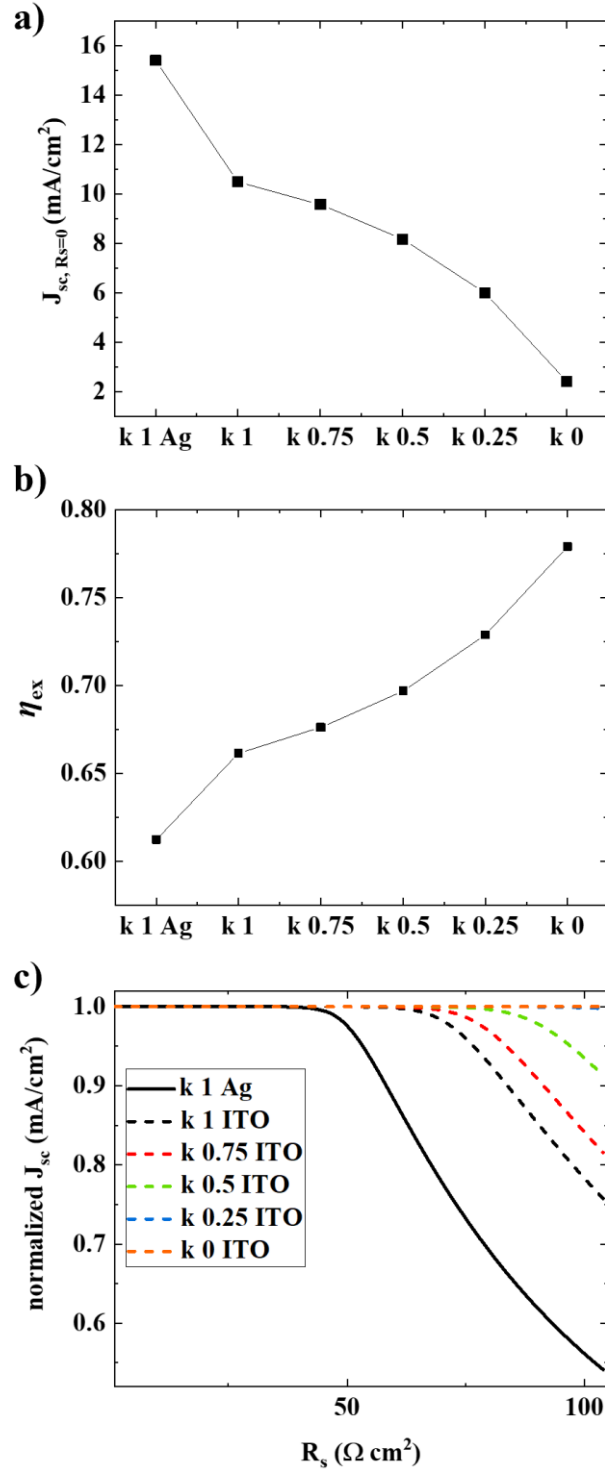
Figure 5.5. a) Short-circuit current J_{sc} of the devices with different AVT, assuming no series resistance R_s. b) Extraction efficiency η_{ex} of the studied devices. c) J_{sc}, normalized to $J_{sc,Rs=0}$ in dependence on series resistance.

It follows that the product of $J_{sc.theo}$ and P_g is the maximum current that would be extracted if all free charge carriers reached the electrodes. Therefore, it is possible to calculate the extraction efficiency η_{ex} as the ratio of the extracted $J_{sc,Rs=0}$ to the product of $J_{sc.theo}$ and P_g. Figure 5.5b shows the resulting extraction efficiencies $\eta_{ex} = J_{sc,Rs=0}/(P_g \cdot J_{sc.theo})$. The opaque Ag 1 device has an extraction efficiency of 0.61, which increases when the Ag electrode is replaced with ITO to 0.66. This can be explained by the increase of the mean free path w (Equation 5.10) in a more transparent device. The altered recombination dynamics and the reduced recombination coefficients (discussed in 2.3) lead to an increased recombination lifetime τ. Since w is proportional to the charge carrier lifetime, this further leads to an increase in the mean free path, which results in higher extraction efficiencies of 0.67, 0.70, 0.72, and 0.77 for k 0.75, k 0.5, k 0.25, and k 0, respectively. Therefore, we conclude that the extraction efficiency increases with the AVT, to some extent counteracting the decrease of the J_{sc} that is expected from the decreased generation rates.

Having established the relationship of the J_{sc} with transparency in neglect of series resistance effects, we now consider the influence of R_s for the devices with different AVT. We calculate the J_{sc} in relation to R_s according to Equation 5.13 with the J_0 as the dark current with a value of $2.14 \cdot 10^{-9}$ mA/cm^2 and the ideality factor n as 1.53, which has been experimentally measured for the reported PM6:Y6 solar cell.[215,304] The relationship is displayed in Figure 5.5c.

$$J_{sc} = J_{sc,Rs=0} - \left[J_0 \cdot \exp\left(\frac{q\,J_{sc}\,R_s}{n\,k\,T}\right) \right] \qquad (5.13)$$

The opaque Ag 1 device's J_{sc} is significantly impacted by the series resistance above R_s values larger than approximately 50 Ω cm^2. From an experimental point of view, we note that this is a value larger than typically achieved for most devices with optimized contacts. Greater transparency increases the threshold value for R_s to about 70 Ω cm^2, 80 Ω cm^2, and 90 Ω cm^2 for

147

the devices with ITO electrode and k 1, k 0.75 and k 0.5 active layer. The devices with the highest AVTs, k 0.25 and k 0, are not noticeably affected by series resistance effects within the range of R_s up to 100 Ω cm^2. This yields the conclusion that for ST-OPVs the choice of ohmic contacts with low series resistance is less important than for conventional opaque OPVs. This may facilitate the application of single-layer graphene electrodes with relatively high sheet resistance and very high transmittance in the whole spectral range.[305–307]

5.2.5 Impact of the Shunt Resistance in Devices with different AVT

Finally, after having reviewed the influence of the series resistance on the J_{sc}, we investigate the impact of the shunt resistance on the V_{oc}. Shunt leakage represents an additional channel of loss of photogenerated charge carriers in the solar cell before they can be extracted to the external electric circuit.[300,308] A high R_{sh} is therefore desired for optimal performance. The relationship of the V_{oc} and R_{sh} is calculated from Equation 5.14 (derivation can be found in SI) and the resulting curves of the normalized V_{oc} versus decreasing R_{sh} are shown in **Figure 5.6**.

$$V_{oc} = \frac{nkT}{q} \cdot \ln\left(\frac{J_{sc,Rs=0} - V_{oc}/R_{sh}}{J_0}\right) \tag{5.14}$$
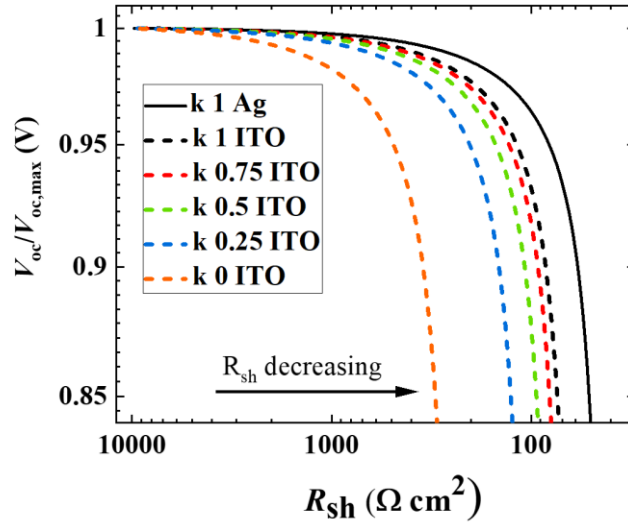
Figure 5.6. Normalized V_{oc} in dependence on the shunt resistance $R_{sh.}$

The more robust a device is towards shunt leakage, the more the R_{sh} would have to be reduced to observe a drop in the V_{oc}. For devices with high AVT, this drop occurs at higher shunt resistance, as can be seen clearly from the trend in Figure 5.6. The device with k 0 active layer's V_{oc} decreases to 90% of its maximum value (large R_{sh}) at $R_{sh} = 347$ Ω cm^2. In contrast, R_{sh} has to be reduced down to 59 Ω cm^2 for the opaque device k 1 Ag to observe a drop of the same magnitude, demonstrating that devices with high AVT are more sensitive to the shunt leakage. Shunt leakage is caused by leakage pathways that arise from the active layer's structural defects, allowing current to flow directly from one electrode to another.[309–311] Therefore, special attention should be paid to avoid structural defects in the active layer in the fabrication of (semi)transparent OPVs to avoid low R_{sh} and the resulting device limitations.

5.3 Conclusion

We have demonstrated changes in ST-OPVs that are concomitant with increased transparency. Reduced generation rates and altered generation rate profiles lead to a reduced V_{oc}

149

and an increased relative bulk trap-assisted recombination contribution, indicating that high-purity and morphologically optimized active layers with low trap density are required. Transparent devices are more sensitive to shunt-leakage reinforces the requirement of a high-quality active layer. The effect of surface recombination at the active layer interfaces becomes less pronounced for systems with higher AVT and limitations due to high series resistance decrease, suggesting that a broader range of materials and deposition techniques can be considered for transparent electrodes. Furthermore, we discussed the reduction of the short-circuit current, and we have shown that the extraction efficiency increases with the AVT, counteracting to a small extent the decreased generation.

5.4 Supplementary Information for Chapter 5

Figure S5.1. Device architectures of the solar cells studied by simulation in this work, related to Figure 5.1.
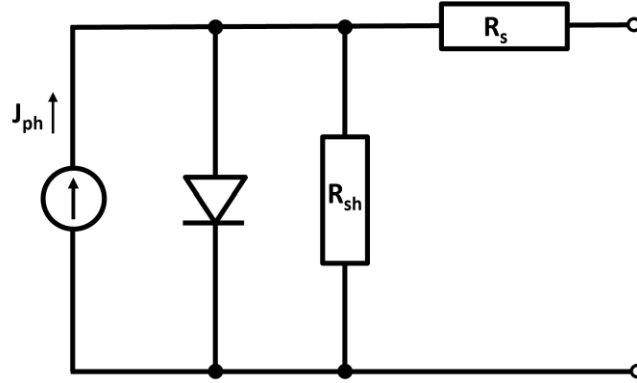
Figure S5.2. Circuit diagram of a solar cell, that was considered for the derivation of mathematical expressions used in this work.[312,313] Related to Equations 5.13 and 5.14.

Mathematical description according to the equivalent circuit in S2. Related to Equations 5.13 and 5.14.

$$J = J_0 \left[\exp\left(\frac{q(V + J R_S)}{n k T}\right) - 1 \right] + \frac{V + J R_S}{R_{sh}} - J_{ph} \tag{S5.1}$$

Thus, at V = 0:

$$J_{sc} = J_0 \left[\exp\left(\frac{q J R_S}{n k T}\right) - 1 \right] + \frac{J R_S}{R_{sh}} - J_{ph} \tag{S5.2}$$

Assuming $R_s \ll R_{sh}$:

$$J_{sc} = J_0 \left[\exp\left(\frac{q J R_S}{n k T}\right) - 1 \right] - J_{ph} \tag{S5.3}$$

For $exp\left(\frac{q J R_S}{n k T}\right) \gg 1$:

$$J_{sc} = J_0 \left[\exp\left(\frac{q J R_S}{n k T}\right) \right] - J_{ph} \tag{S5.4}$$

At J = 0:

$$J_{ph} = J_0 \left[\exp\left(\frac{q\,V_{oc}}{n\,k\,T}\right) - 1 \right] + \frac{V_{oc}}{R_{sh}}$$

<div align="right">(S5.5)</div>

$$V_{oc} = \frac{nkT}{q}\, \ln\left(\frac{J_{ph} - \frac{V_{oc}}{R_{sh}}}{J_0} + 1\right)$$

<div align="right">(S5.6)</div>

For $\dfrac{J_{ph} - \frac{V_{oc}}{R_{sh}}}{J_0} \gg 1$:

$$V_{oc} = \frac{nkT}{q} \cdot \ln\left(\frac{J_{ph} - \frac{V_{oc}}{R_{sh}}}{J_0}\right)$$

<div align="right">(S5.7)</div>

Chapter 6: Understanding Interfacial Recombination Processes in Narrow Band Gap Organic Solar Cells

6.1 Introduction

Organic photovoltaics (OPVs) have emerged as a viable sustainable energy harvesting technology. The inherent properties of the photoactive carbon-based donor:acceptor blends (active layers) allow for energy-efficient and cost-effective solution processing and promise a vast range of integrated energy-harvesting applications.[53,67,170,290,314] In contrast to their inorganic counterparts, OPVs are lightweight, flexible, and optically tunable.[170,275,285,287,315,316] As a result, OPVs can be integrated into windows or greenhouses to increase the energy efficiency of new or existing structures.[52,53,67,69]

In comparison to other emerging technologies, such as perovskite solar cells, OPVs used to lack behind. However, with the development of efficient donor polymers, such as PM6 or D18, and the replacement of fullerene-based acceptors with a new generation of non-fullerene acceptors (NFAs), the picture has changed dramatically.[106,167,169,317] The molecular structures of the state-of-the-art NFAs have been fine-tuned to reach ever-increasing performances, now approaching the 20% power conversion efficiency (PCE) benchmark.[165,214,215,263,318]

With this ongoing improvement of the donor and acceptor materials, understanding the device physics is crucial for the further development of OPVs. Most high-performance OPVs utilize an interfacial layer between the active layer and the electrodes. However, to date, most of the charge recombination studies in the OPV field focus on either only pure bimolecular recombination, or, in some cases bimolecular and bulk trap-assisted recombination. The impacts of interfacial recombination are rarely addressed.

Besides the development of high-performance materials, another major trend in the field of OPVs is the band gap-narrowing of donors and acceptors for (semi) transparent OPVs.[101,275,319–324] These systems exhibit lower open-circuit voltages (V_{oc}), resulting in a less pronounced contribution of interfacial recombination, due to the relationship $k_{sf} \propto e^{V_{oc} - V_{bi}}$, with k_{sf} being the coefficient for surface recombination and V_{bi} the build-in field, and due to an increased relative contribution of bulk-trap assisted recombination, as recently derived in the context of the multi-channel recombination model.[325] However, even in these systems the nature of the active layer–electrode interface plays a significant role as we show in this work.

In this contribution, we chose to combine the most studied donor polymer **PCE10** (poly[4,8-bis(5-(2-ethylhexyl)thiophen-2-yl)benzo[1,2-b;4,5-b']dithiophene-2,6-diyl-alt-(4-(2-ethylhexyl)-3-fluorothieno[3,4-b]thiophene-)-2-carboxylate-2-6-diyl)]) with the narrowest band gap (E_g = 1.10 eV) NFA **COTIC-4F** (2,2'-((2Z,2'Z)-(((4,4-bis(2-ethylhexyl)-4H-cyclopenta[2,1-b:3,4-b']dithiophene-2,6-diyl)bis(4-(heptan-3-yloxy)thiophene-5,2-diyl))bis-(methanylylidene))bis(5,6-difluoro-3-oxo-2,3-dihydro-1H-indene-2,1-diylidene))dimalononitrile), which serves as a model system for future narrow band gap semitransparent OPVs and near infrared (NIR) sensing organic photodetectors (OPDs).[275,326,327]

We investigate the effect of the electrode interface for this blend system by comparing four devices, two in inverted and two in conventional architecture, that have the same active layer thickness (105 nm) but with four different front electrodes, namely ZnO, ZnO functionalized with PFN-Br, PEDOT:PSS and CPE-K. ZnO is commonly used for inverted devices, thanks to its low work function, high stability, transparency, and charge mobility as well as its simplicity of fabrication.[303] PFN-Br has been mentioned in the literature to improve PCEs by increasing the extraction efficiency,[328,329] however, in this work, we focus mainly on using PFN-Br to functionalize ZnO and its effect on surface recombination. PFN-Br has been used to modify the

work function of ZnO to tune the energy level alignment of the cathode layer.[328–330] Most conventional devices employ PEDOT:PSS, however, the acidity of the material has some drawbacks, as it can lead to lower stability.[328,331] A pH-neutral alternative is the self-doped conjugated poly-electrolyte CPE-K, which can be used to replace PEDOT:PSS in OPVs.[332,333] CPE-K has been shown to improve the stability of perovskite solar cells.[331,334]

6.2 Results and Discussion

The chemical structures and the energy levels of the donor, acceptor, CPE-K, and PFN-Br are shown in **Figure 6.1a**, and the material's energy levels as reported in the literature and previous works.[91,215,275,329,331] The device structures are shown in **Figure 6.1c**.
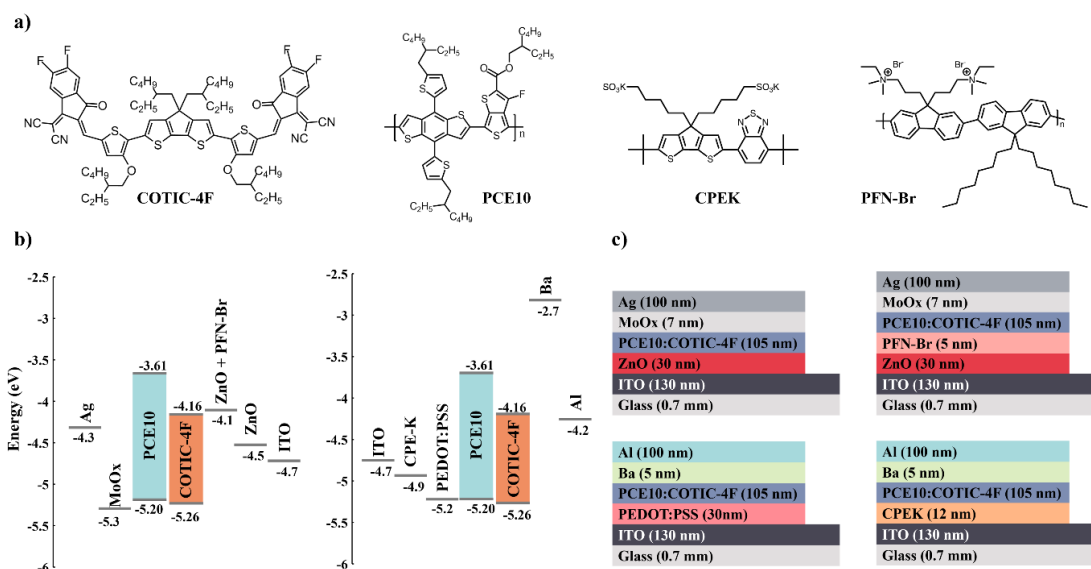
Figure 6.1. a) Chemical structures of the NFA COTIC-4F and the donor polymer PCE10 as well as these of CPE-K and PFN-Br. b) Energy diagram of materials used in inverted (left) and conventional (right) structure. c) Schematic representation of the studied devices.

We systematically address the impact of the various electrodes on charge generation, charge recombination, and charge extraction in these devices, with a focus on interfacial recombination. A comprehensive analysis is necessary because the changes that arise when introducing a new

electrode material are interconnected. For example, changes in the generation rates may influence recombination and extraction processes due to altered charge carrier densities, or, the morphology of the active layer may be altered due to spin-coating onto a different electrode material, leading to various possible changes in recombination and extraction.[335] Thus, it is only possible to gauge the impact of the interfacial processes after having elucidated how much other performance-governing aspects change depending on the device architecture.

It is worth noting, that both the electrode:active layer interface and the active layer:back electrode interface can play a role. However, it is not possible to make a device with only one interface. Therefore, we keep the back electrode constant for the inverted devices (MoOx/Ag) and for the conventional devices (Ba/Al) to draw conclusions about the effects of the front electrode materials on the device performance. The front electrode is expected to have a bigger impact on the overall device performance for two reasons: First, the active layer is deposited on the front electrode, therefore the material choice can impact the film formation and the active layer morphology. Second, the OPV cells are illuminated with the light entering the device from the front electrode:active layer side, typically causing much higher charge generation rates at this interface than at the back electrode, therefore the surface recombination rates at this interface are of more relevance for the net recombination in the device.

In the first step, we obtained the surface topography of the bottom electrode materials with Atomic Force Microscopy, AFM, (Figure S6.1). The ZnO electrode reveals typical round nanoparticle features with homogeneous size distribution and a Roughness Mean Square (RMS) of 1.68 nm. These features remain detectable after the deposition of a thin PFN-Br layer on top, but the roughness of the ZnO+PFN-Br film is reduced and a very smooth film with an RMS of 0.71 nm is obtained. In contrast, PEDOT:PSS and CPE-K lead to films with moderately RMS values of 1.47 nm and 1.46 nm, respectively.

Next, we measured the current-voltage characteristics and external quantum efficiency (EQE) spectra of the four device types (**Figure 6.2a** and 6.2b). The device parameters are summarized in **Table 6.1**.
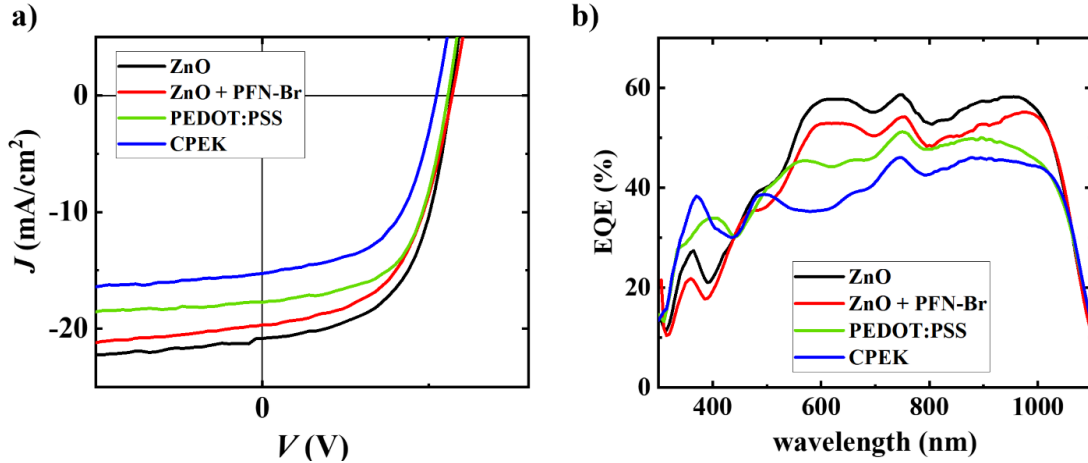
Figure 6.2. a) Current-voltage characteristics of representative devices with four different electrode configurations, measured at 1 sun illumination. b) External quantum efficiency spectra of the same devices.

Table 6.1. Photoelectrical parameters of the fabricated devices and their standard deviations.

PCE10:COTIC-4F, bottom electrode:	J_{sc} (mA/cm²)	V_{oc} (V)	FF (%)	PCE (%)
ZnO	-20.9 ± 0.2	0.57 ± 0.01	55.2 ± 0.8	6.55 ± 0.18
ZnO+PFN-Br	-19.7 ± 0.5	0.57 ± 0.01	53.3 ± 3.3	5.98 ± 0.50
PEDOT:PSS	-17.9 ± 0.5	0.56 ± 0.01	56.1 ± 2.0	5.62 ± 0.26
CPE-K	-16.1 ± 1.1	0.52 ± 0.01	54.5 ± 0.7	4.56 ± 0.15

The inverted devices that are based on ZnO show the highest power conversion efficiency (PCE) of 6.55% owing to a high short-circuit current (J_{sc}) of -20.9 mA/cm², a V_{oc} of 0.57 V, and a fill factor (*FF*) of 55.2%. Devices that additionally have an organic PFN-Br layer on top of the ZnO, showed an unaltered V_{oc}, but a slightly reduced J_{sc} (-19.7 mA/cm²) and *FF* (53.3%), decreasing the average PCE to 5.98%. The 0.57% PCE decrease is attributed to a less favorable

energy alignment of ZnO+PFN-Br with the LUMO of the NFA COTIC-4F. As seen in **Figure 6.1b**, a small energy barrier for electron collection is expected to reduce the driving force for charge extraction. Further, Table S6.1 reveals that the functionalized devices exhibit slightly higher series resistance (2.81 ± 0.18 Ω cm²) than those that use only ZnO (1.92 ± 0.28 Ω cm²), contributing to the slightly lower PCE by reducing the J_{sc} and the *FF*.

A significant drop in the J_{sc} is observed when employing a conventional device architecture. The devices with PEDOT:PSS yield a J_{sc} of -17.9 mA/cm² and a slightly lower V_{oc} of 0.56 V, resulting in a PCE of 5.62%. When replacing PEDOT:PSS with CPE-K, a further reduction in the V_{oc} (0.52 V) and a small decrease in the J_{sc} to -16.1 mA/cm² leads to PCEs of 4.56%. The decrease in the V_{oc} is expected, based on the higher HOMO level of CPE-K (-4.9 eV) compared to PEDOT:PSS (-5.2 eV), since the work function difference of the contacts determines the V_{oc} in the case of non-ohmic contacts.[336] The values of the *FF* are comparable to those observed for inverted ZnO-based devices with 56.1 ± 2.0% and 54.5 ± 0.7%, respectively.

The clear trend in the J_{sc} values is also reflected in the EQE spectra (**Figure 6.2b**) in the range from 500 nm to 1000 nm. In the wavelength region below 500 nm, however, distinct features are visible that can be traced back to the different optical properties of the electrode materials.[97] In the inverted structure, the EQE is reduced in this region due to the strong absorption of ZnO (< 380 nm) and MoOx (< 500 nm). In addition, MoO$_x$ decreases the reflection from the Ag back electrode, leading to lower EQE in this region as well.[335]

The interfacial effects that arise from the electrodes can impact the V_{oc} by causing voltage losses due to energetic disorder in the active layer.[218] As an approximation of the degree of energetic disorder in the devices, the Urbach energy can be extracted from the tail of the EQE spectra at high wavelengths by fitting to the following relationship:

$$E_{U}(E) = \left[\frac{d\ln(\text{EQE})}{dE}\right]^{-1} \qquad (6.1)$$

where E is the photon energy and E_U is the Urbach energy.[141,142] The Urbach energy is often interpreted as the width of the band tail due to localized energy states in the device. Figure S6.2 shows the fits to Equation 6.1 for each device type. The inverted devices have smaller values of E_U: 35.8 meV for devices with ZnO and 34.2 meV for those with ZnO+PFN-Br, indicating less disorder than in the conventional structures (E_U = 42.7 meV for devices with PEDOT:PSS and 42.6 meV for devices with CPE-K). These values provide further explanation for the decreased V_{oc} values for the conventional devices with PEDOT:PSS and CPE-K.

The wavelength region beyond 500 nm in the EQE spectra reflects the performance trend of the studied devices (ZnO > ZnO+PFN-Br > PEDOT:PSS > CPE-K). To understand the origin of this trend we move on to investigate the charge generation, recombination, and extraction of charge carriers within each device structure. First, we address charge generation in the active layer based on the choice of the front electrode and its impact on the performance by employing optical transfer matrix simulations.[130,162] The optical constants of all layers are known from literature and our previous work, except those of CPE-K which were determined in this work (Figure S6.3).[97]
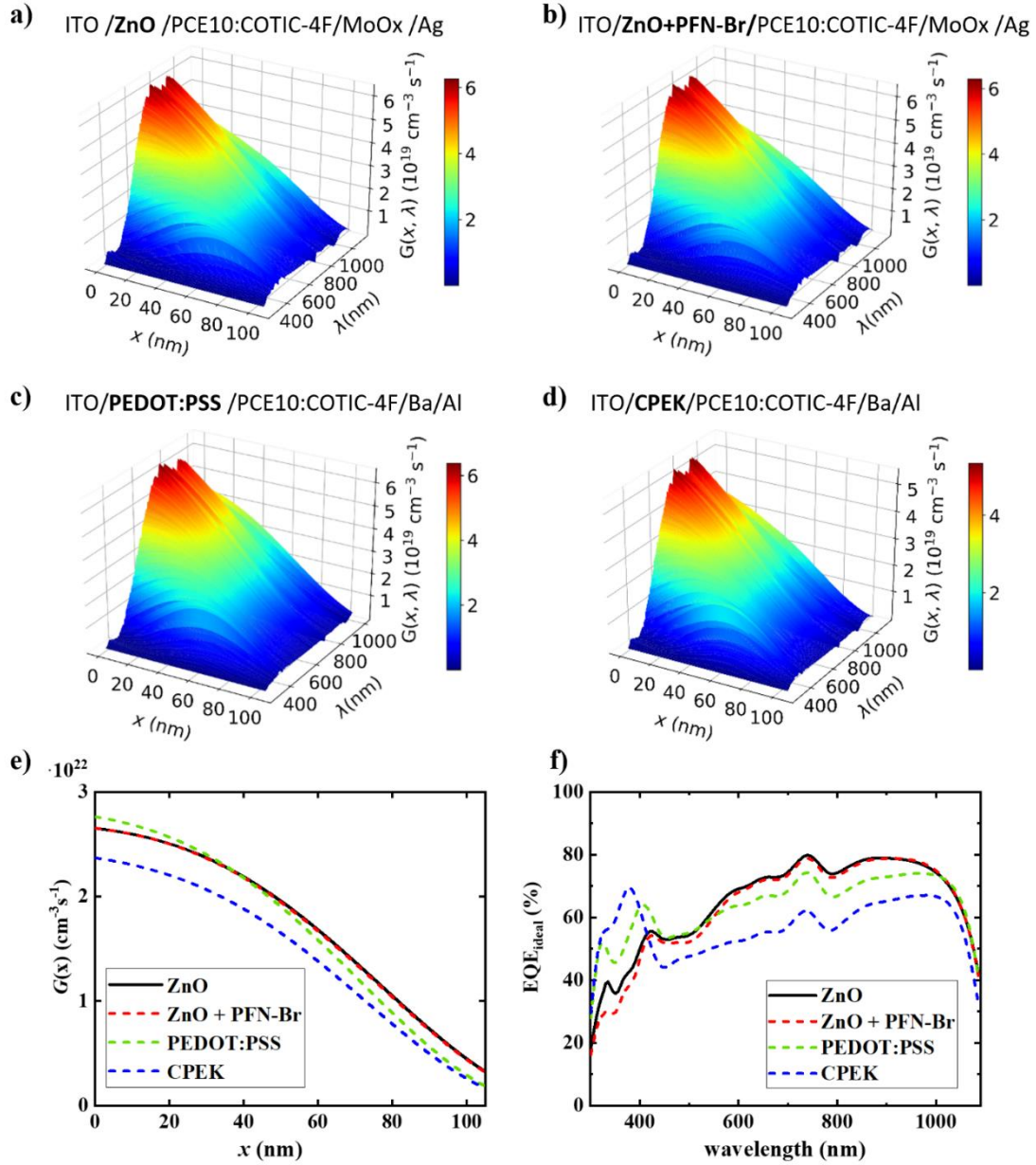
Figure 6.3. a – d) Generation rates $G(x, \lambda)$ for the devices with different front electrodes, depending on wavelength and position in the active layer, for AM 1.5 illumination. e) Spatially dependent generation rate $G(x)$ and the resulting EQE_{ideal} for the four device configurations with varied bottom electrodes.

Figure 6.3a–d shows the spatial and wavelength-dependent generation rates $G(x, \lambda)$, simulated based on the optical properties of each device stack, taking into account reflection at each interface, the absorption in each layer, and the optical interference in the device stack. For

a better comparison, we integrated $G(x, \lambda)$ over the wavelengths to obtain $G(x)$, shown in Figure 6.3e, which depends only on the position in the active layer. The inverted devices show very similar behavior, whereas when using PEDOT:PSS, the generation of charge carriers is higher close to the front electrode:active layer interface ($x=0$), but decays faster, leading to lower generation rates at depths > 40 nm. With CPE-K, $G(x)$ is lower than in all other cases, while following a similar decay as in the inverted structures. To understand the effect of the altered generation rates on the measured device performance, we further calculated the EQE_{ideal}, which would be obtained if no recombination or extraction losses occurred in the device.[97] From Figure 6.3f, it is evident that generation plays a significant role in governing the measured EQE (or J_{sc}) since a clear EQE reduction is observed for PEDOT:PSS and CPE-K based devices in comparison with ZnO based devices. Thus, the reduced generation rates explain the experimentally observed lower EQEs and J_{sc} values in the devices using PEDOT:PSS and CPE-K as bottom electrodes. In contrast, the functionalization of ZnO with PFN-Br has a negligible effect on the generation in the active layer as seen in Figure 6.3f as well, contrasting the experimentally observed reduction of the EQE, and thus highlighting the importance of series resistance and energy barrier effects that were discussed earlier in governing the measured EQE.

In the next step, we investigate the charge carrier recombination and extraction dynamics. First, we investigate the dependence of the V_{oc} on light intensity (V_{oc} vs. $\ln[I]$), and slopes of representative devices are shown in **Figure 6.4a**, which is commonly used to qualitatively infer the dominant recombination mechanism in the organic solar cells.[99,100,159] In the case of pure or strongly dominant bimolecular recombination, a slope of kT/q is expected, with q being the elementary charge, T the temperature, and k the Boltzmann constant. In the presence of bulk traps in the active layer, which facilitate trap-assisted recombination, an increase in the slope can be observed, reaching its maximum at $2\,kT/q$ in the case of dominant trap-assisted

recombination, according to Shockley-Read-Hall statistics.[112,159,198] Interfacial traps, in contrast, lower the slope, and values below kT/q can be obtained.[99,137] The devices with ZnO and ZnO+PFN-Br bottom electrodes exhibit similar slopes of 1.07 and 1.06 kT/q, respectively, indicating the presence of some trap-assisted recombination. In contrast, slopes below kT/q are obtained for the conventional structures, indicating a significant relative contribution of surface traps.[99,137] When using PEDOT:PSS, a lower slope of 0.94 kT/q is found, than for CPE-K electrodes with a slope approaching unity.
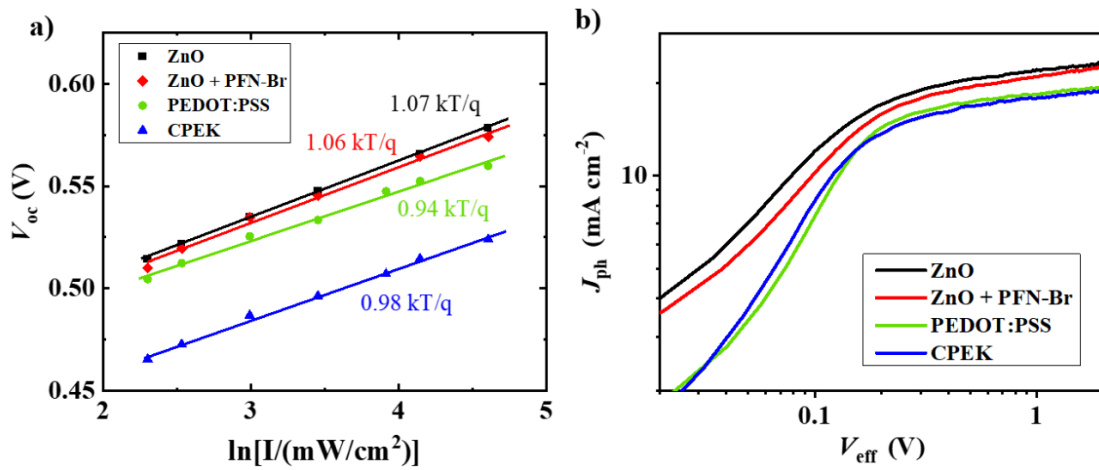
Figure 6.4. a) Dependence of the V_{oc} on the logarithm of the light intensity. b) Photocurrent in dependence on the effective voltage V_{eff}.

To get some first insights into extraction processes, we show the dependence of the photocurrent J_{ph}, calculated as the difference between light and dark JV-curves, $J_l - J_d$, on the effective voltage, V_{eff}. V_{eff} is calculated as $V_{eff} = V_0 - V_{corr}$, where V_0 is the voltage at which the photocurrent is equal to zero and V_{corr} is the applied bias corrected for series resistance effects $(V - JR_s)$. Figure 6.4b reveals that the saturation regime occurs around the same voltage for all systems, indicating comparable rates of extraction.

To make quantitative statements about both recombination and extraction, we employ capacitance spectroscopy, following the approach by Brus and Vollbrecht, as outlined in our

previous works.[136,137] The fits are shown in Figure S6.4. **Figure 6.5a** shows the obtained dimensionless Langevin reduction factors, ξ, as the measure for bimolecular recombination. The choice of the front electrode does not change the bimolecular recombination in the active layer for the studied systems. All values are low compared to other NFA blends and fall within the narrow range of $0.028 - 0.036$, and can be considered the same within the error.[170] This indicates that the morphology of the active layer is comparable within all four devices structures since changes in the morphology would typically be reflected in the bimolecular recombination rate.[337,338] Our surface topography images of the active layers on the different front electrodes support this assumption and no visible changes are evident from the AFM topographic images that were taken in contact mode, shown in Figures S5 and S6, with each film showing similar features and very similar root-mean-square (RMS) roughness values between 1.1 - 1.3 nm. Figure S6.5 and Figure S6.6 also show the photocurrent obtained at -0.5 V and +0.5V sample bias applied to the devices, revealing similar bright-colored donor-rich and dark-colored acceptor rich features. A more in-depth discussion of the pc-AFM scans can be found in the SI.

Figure 6.5b reveals that the densities of bulk traps, N_t, also fall into a narrow range, with values of 2.4×10^{15} cm^{-3}, 2.3×10^{15} cm^{-3}, 1.8×10^{15} cm^{-3}, and 1.7×10^{15} cm^{-3} for devices with ZnO, ZnO+PFN-Br, PEDOT:PSS, and CPE-K, respectively. Considering that only the electrodes have been changed, it is not surprising that only minor changes in the bulk properties are observed. The more interesting aspect is the interfacial recombination at the electrode/active layer interface. Figure 6.5b reveals that the interfacial properties change drastically depending on the choice of the electrode. Surface trap densities for ZnO are low at 1.6×10^{11} cm^{-2}, indicating a minor role in the overall recombination rate. However, we attempted to reduce the interfacial recombination in the inverted structure further by functionalization with PFN-Br. In this case, only a negligible reduction of the surface traps is observed, with the density decreasing to $1.4 \times$

10^{11} cm^{-2}. In contrast, when employing PEDOT:PSS as the electrode layer, we observe a steep increase of surface traps of about one order of magnitude to 1.4×10^{12} cm^{-2}. As a mitigation strategy, we replaced PEDOT:PSS with CPE-K. In fact, the surface recombination is successfully reduced by almost 70% to 4.5×10^{11} cm^{-2}. This indicates that the high density of surface traps in the conventional structure arises primarily from the PEDOT:PSS/active layer interface since the back electrode interface (active layer/Ba) is in both conventional device types unchanged. If Ba would cause high rates of surface recombination, a reduction by replacing PEDOT:PSS with CPE-K would not lead to a significant reduction in the interfacial recombination rate. To further corroborate this, we fabricated devices with PEDOT:PSS bottom electrode and Al back electrode. The V_{oc} vs ln(I) slope is found to be 0.95 kT/q (see Figure S6.7), similar to the 0.94 kT/q for the devices with Ba/Al back electrode, indicating a similar level of surface recombination.

With this knowledge, we can interpret the differences in the V_{oc}-dependence on the light intensity (Figure 6.4a) correctly. The decrease in the slope when using PEDOT:PSS in fact arises from an increase in surface traps, which can be partially recovered when using CPE-K instead. In the inverted devices, surface traps play a smaller role, and recombination *via* bulk traps is dominant, leading to slopes above unity. These findings contrast the often-discussed concerns about ZnO and its interfacial properties. It is well understood that ZnO exhibits a wide range of intrinsic defect levels.[339] We believe that the majority of defect or impurity energy levels created by ZnO are shallow in respect to the HOMO and LUMO levels of the used narrow band gap donor and acceptor. Assuming that the energy positions of defect states introduced by ZnO are fixed, the energetic distance to the HOMO or LUMO levels of donor or acceptor will decrease upon narrowing of the band gap. Such shallow energy levels do not act as efficient recombination centers according to Shockley-Read Hall statistics.[203] Since ZnO has previously been studied in

164

the context of wide band gap systems, the surface defects associated with ZnO served as recombination centers.[340–342] However, in the present narrow band gap system the same defects may serve as shallow traps at the interface which do not contribute as efficiently to the surface recombination. Further investigations that are beyond the scope of this work are necessary to resolve the picture in detail.
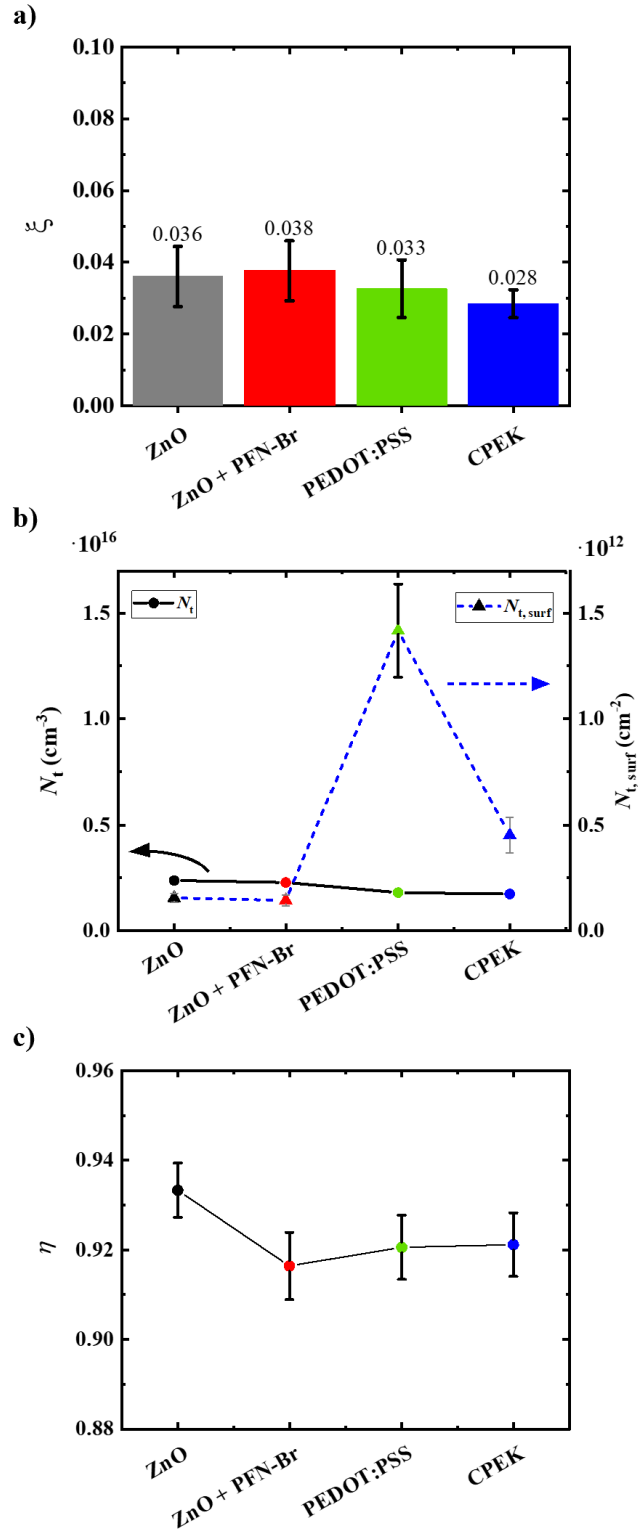
Figure 6.5. a) Langevin prefactor for bimolecular recombination b) bulk trap densities N_t (left axis) and surface trap densities $N_{t,surf}$. c) Extraction probability η at 0 V for the different devices.

Lastly, we investigate the charge extraction in the different devices. We calculated the extraction probability η under short-circuit conditions *via* the simplified Hecht equation (Equation 6.2), assuming that charge carriers are on average located at a distance $L/2$ from the extracting contact, with L being the active layer thickness.[97,254]

$$\eta = \frac{\mu\tau F}{L/2}\left(1 - exp\left(\frac{-L/2}{\mu\tau F}\right)\right) \qquad (6.2)$$

The mobility-lifetime product $\mu\tau$ was obtained from the capacitance spectra, following the approach by Vollbrecht and Brus.[136,137] The internal field, F, in the active layer was obtained according to the relationship $F = (V_{bi} - V_{corr})/L$, with the built-in field V_{bi} obtained from the *JV*-curves in the dark. **Figure 6.5c** reveals minor differences in the charge extraction dynamics. The PEDOT:PSS and CPE-K devices both result in an extraction probability of 92.1%, while the extraction probability in the ZnO/PFN-Br devices is slightly lower at 91.6%. The ZnO devices have the highest extraction probability of 93.3%.

6.3 Conclusions

To summarize, we have studied the differences between inverted OPV devices with either ZnO or PFN-Br functionalized ZnO front electrodes and conventional devices with PEDOT:PSS and CPE-K front electrodes. We elucidated the origins of the performance trend ZnO > ZnO/PFN-Br > PEDOT:PSS > CPE-K and highlighted the role of interfacial recombination. We have found ZnO to be the most suitable electrode for the PCE10:COTIC-4F system, thanks to low interfacial recombination rates, efficient charge extraction, beneficial energy level alignment, and lower energetic disorder than in the conventional device architecture. Similarly, low interfacial recombination rates and no further reduction in surface traps were

observed, when using PFN-Br functionalized ZnO instead. The conventional devices based on the commonly used PEDOT:PSS exhibit high rates of interfacial recombination and reduced photogeneration in the active layer, leading to lower performance compared to the inverted devices. However, the negative effects of the surface traps can be reduced by nearly 70% when replacing PEDOT:PSS with CPE-K. While this is a promising mitigation strategy, it requires further development of the conjugated polyelectrolyte electrode to compete with the PEDOT:PSS electrode; for instance, we found lower PCEs for CPE-K based devices due to lower generation rates and less favorable HOMO level alignment with PCE10. These results encourage further exploration of the surface trap passivation effect of CPE-K in other OPV blend systems and employing thinner CPE-K electrodes to minimize optical losses. Overall, our findings highlight that interfacial recombination can play a significant role in narrow band gap blend systems. Since the role of interfacial effects is expected to be even more dominant in high-performing OPVs, we expect future research in this direction to overcome the anticipated PCE bottleneck arising from interfacial recombination processes.

6.4 Supplementary Information for Chapter 6

Materials

COTIC-4F and CPE-K were prepared according to literature procedure.[275,343] PEDOT:PSS (AL4083) was purchased from Ossila Ltd. ZnO solution and solvents were purchased from Sigma Aldrich.

AFM and pc-AFM

Atomic force images in conductive mode and photocurrent images were obtained with an Asylum Research MFP-3D setup with conductive Pt-Ir-coated probes with a resonant frequency of

13 kHz and a force constant of $0.2 \, N \, m^{-1}$, purchased from Nanoworld. All measurements were carried out under nitrogen. AFM images of the electrodes were collected with an Innova AFM setup in tapping mode.

Device Fabrication

ITO on glass substrates were cleaned by scrubbing with a commercial detergent and distilled water, followed by sonication in acetone and isopropanol. The substrates were dried in an oven overnight at 130 °C. For the inverted devices, the ZnO layer was deposited by spin-coating a 1:2 mixture of diethyl zinc (15% w/w in toluene) and tetrahydrofuran at 4000 rpm in air, followed by annealing at 150 °C for 25 minutes. In the case of using PFN-Br, a 5 nm thick layer was spin-coated at 3000 rpm on top of the ZnO from a PFN-Br solution in methanol with a concentration of 0.5 mg/ml. This solution was stirred for 2 hours at room temperature before spin-coating. The active layer was deposited under nitrogen atmosphere by spin-coating a solution of PCE10:COTIC-4F (1:1.5 ratio, c = 20 mg/ml) in chlorobenzene with 2% (v/v) chloronaphthalene at 1500 rpm. The solution was stirred overnight at 56 °C before spin-coating. The top contact was then deposited by thermal evaporation of molybdenum(VI)oxide and silver in a vacuum deposition chamber (Ångstrom Engineering) at pressures $< 10^{-6}$ torr, using $0.22 \, cm^2$ shadow masks. Devices in the conventional structure were prepared similarly, using barium (5 nm) and aluminum (100 nm) as the top contact. PEDOT:PSS was spin-coated on UV-Ozone treated ITO substrates from an aqueous solution at 4000 rpm, followed by annealing for 20 minutes at 150 °C and CPE-K was spin-coated on UV-Ozone treated ITO substrates from aqueous solution with a concentration of 5 mg/mL at 3000 rpm, followed by annealing at 110 °C for 10 minutes.

Device Characterization

The current-voltage characteristics were measured with a Keithley 2602 semiconductor analyzer system under nitrogen atmosphere. A solar simulator with a 300 W xenon lamp with an AM 1.5 global filter was used to irradiate the devices. The light intensity was calibrated with a standard silicon solar cell with a KG1 filter, calibrated by the National Renewable Energy Laboratory. The illuminated area of the solar cell device was defined by an aperture of 0.094 cm^2. The V_{oc} versus light intensity was measured with the same setup using a set of Newport 5215 neutral density filters. EQE spectra were also measured under nitrogen atmosphere and the intensity of the monochromatic light, chopped at 155 Hz, was determined with a Newport Si photodiode. A Solartron SI1260 analyzer was used to measure the frequency-dependent impedance spectra (10^1-10^6 Hz) under 1 sun and in the dark with a small AC disturbance of 40 mV, starting with a negative sample bias and an increase in bias up to V_{oc}. The thicknesses of the device layers were measured with an Ambios XP-100 profilometer.

Optical Simulation

The available Transfer Matrix software, developed by the McGhee group, was used in combination with or own script to visualize $G(x)$ and EQE_{ideal}.[97,130,163]
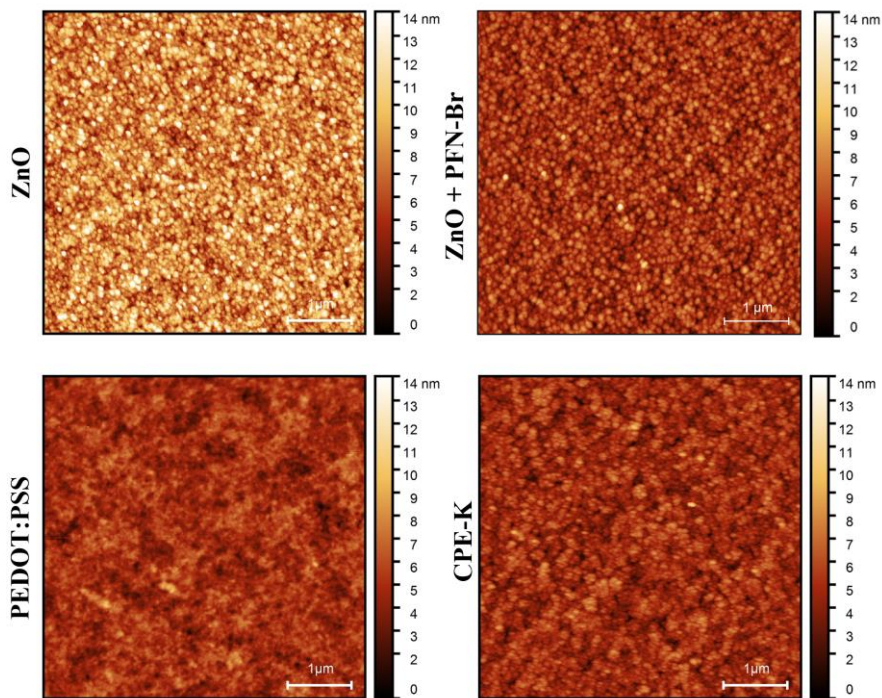
Figure S6.1. Atomic Force Microscopy (AFM) images (5 x 5 µm) of the different electrodes.

Table S6.1. Series and shunt resistance and their standard deviations.

Device	Rs (Ω cm2)	Rshunt (Ω cm2)
ZnO	1.92 ± 0.28	$(8.92 \pm 2.09) \cdot 104$
ZnO + PFN-Br	2.81 ± 0.18	$(4.47 \pm 2.11) \cdot 104$
PEDOT:PSS	2.64 ± 0.29	$(3.69 \pm 3.44) \cdot 104$
CPE-K	3.88 ± 0.21	$(3.17 \pm 1.75) \cdot 104$
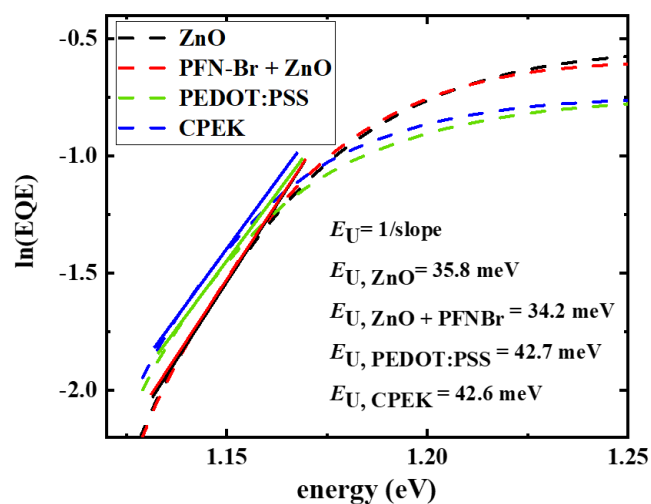
Figure S6.2. Urbach energies obtained from the EQE tail as a measure for energetic disorder.

Optical Properties of CPE-K

The extinction coefficient was obtained from thin-film absorption measurements and the refractive index n was assumed as 2.5. As Burkhard et. al. have shown, the exact value of n leads only to minor differences in the modeled absorption, even when this estimation is applied to the active layer. Since we only estimate n for the CPE-K layer, we expect only a minor error rising from the slightly changed interference pattern in the device stack.[130]
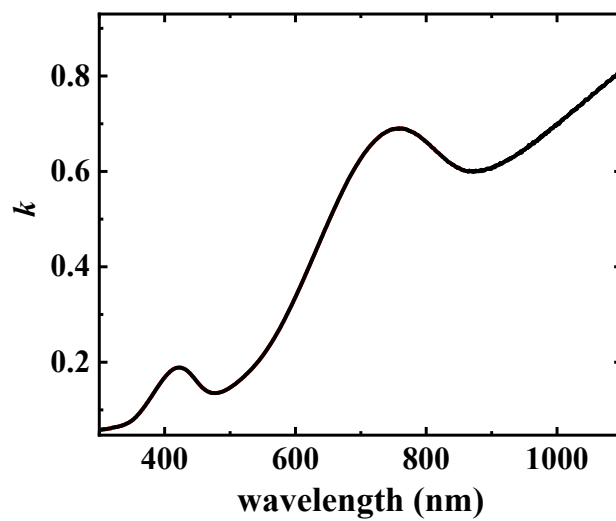
Figure S6.3. Extinction coefficient of CPE-K.
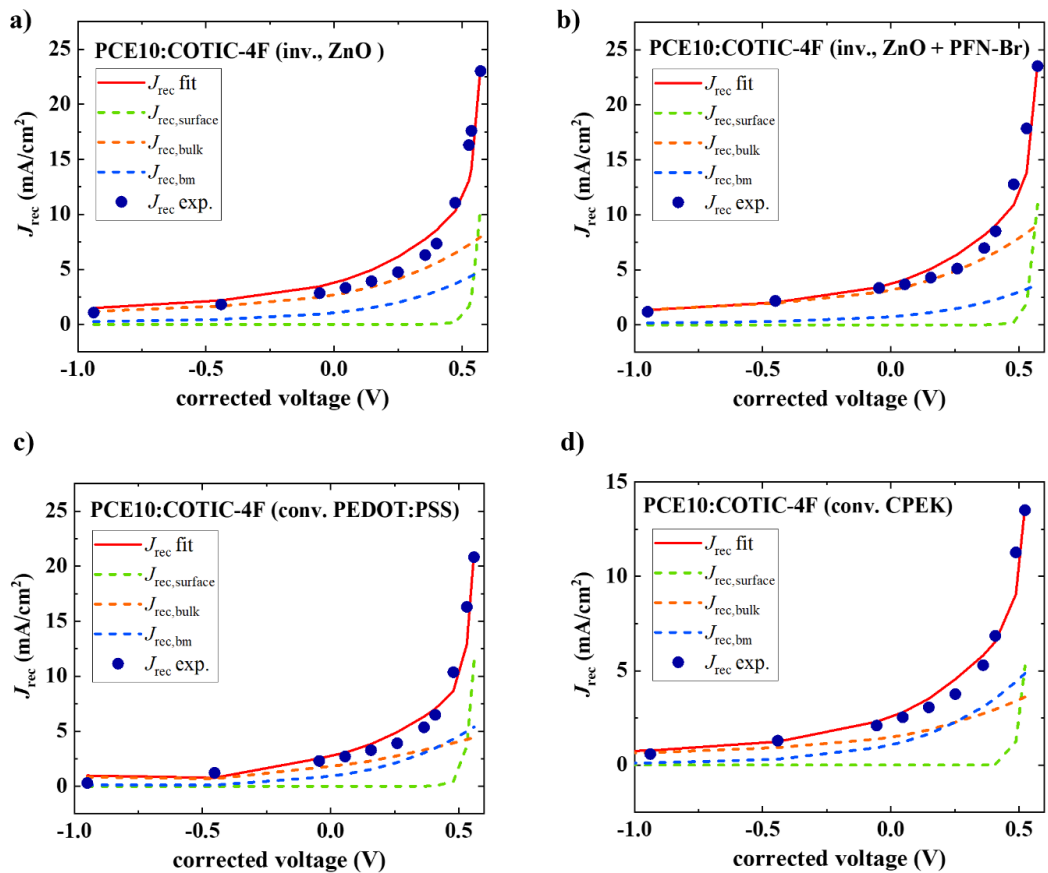
Figure S6.4. Fit of the total recombination current obtained from capacitance spectroscopy (sum of the individual contrition's) to the experimental recombination current.
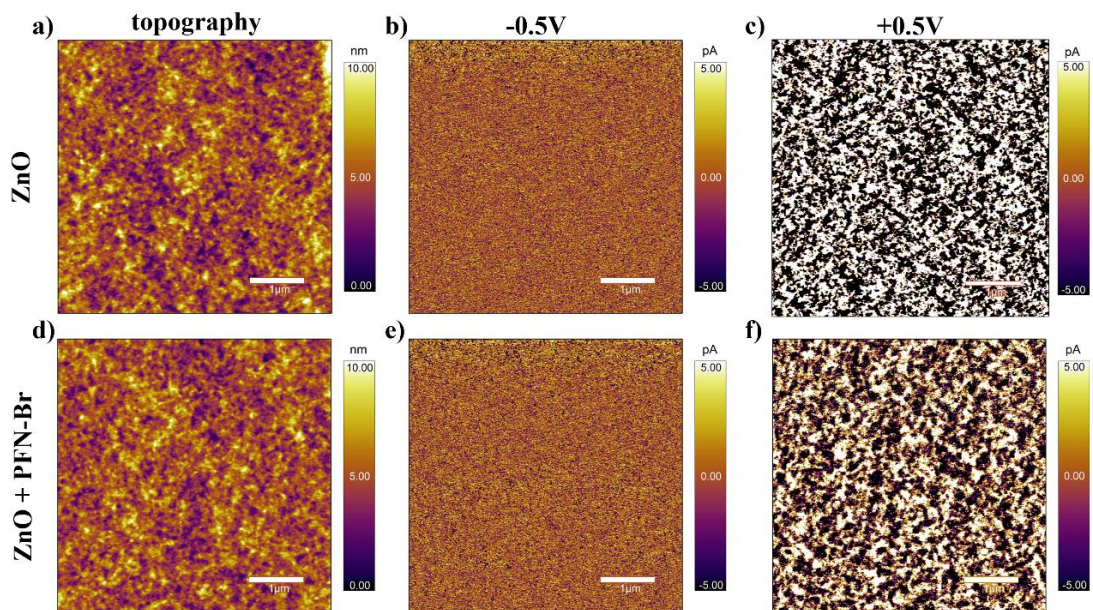
Figure S6.5. Contact mode surface topography and photocurrent images of the inverted devices taken at -0.5 V and +0.5 V sample bias.
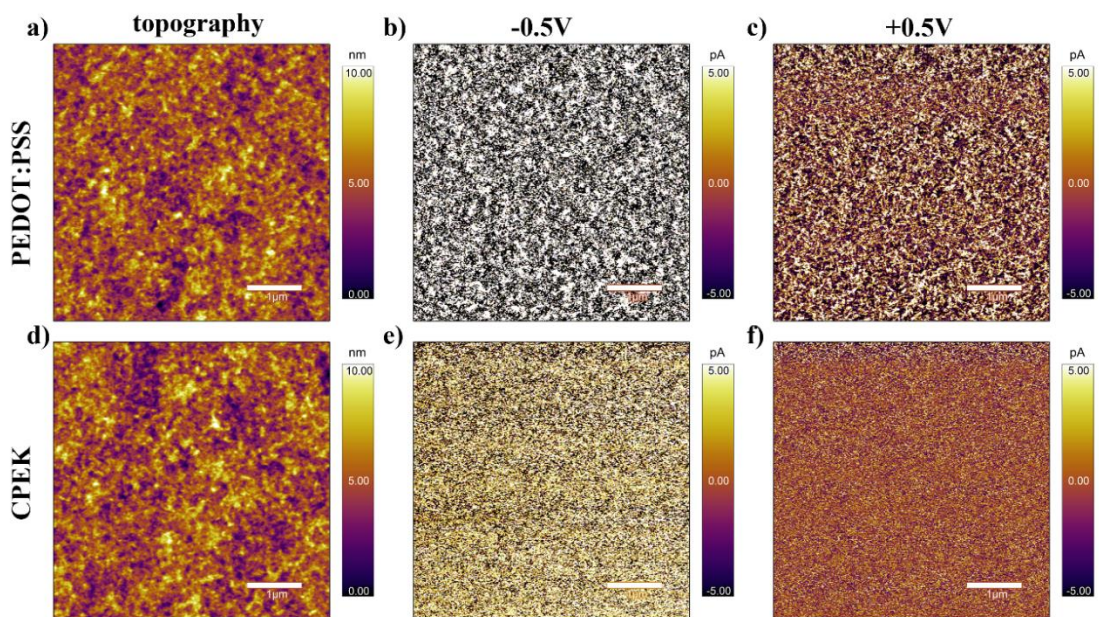
Figure S6.6. Contact mode surface topography and photocurrent images of the conventional devices taken at -0.5 V and +0.5 V sample bias.
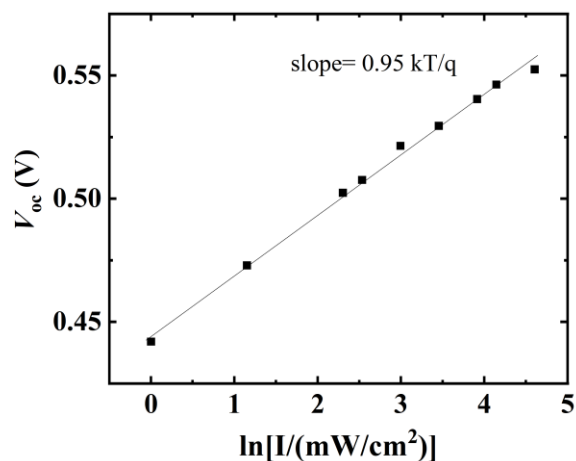
Figure S6.7. Dependence of the V_{oc} on the logarithm of the light intensity for a representative device with Al back electrode.

PC-AFM

When a small positive bias of +0.5 V is applied to the sample, the high work function Pt-coated AFM tip scans the active layer surface and collects photogenerated holes, similar to the working principle of the inverted devices with high work function MoOx/Ag back electrode. Bright features correspond to hole-rich donor domains. The higher contrast in the case of ZnO (Figure S6.6c) indicates a higher nanoscale current compared to the ZnO+PFN-Br devices (Figure S6.6f), in agreement with the observed bulk properties. The features are similar, indicating a similar distribution of donor- and acceptor-rich domains. When reversing the internal field by applying a negative -0.5 V to the samples, the tip collects electrons and no distinct features are revealed (Figure S6.6 b and e) since holes are not collected efficiently by the ZnO or ZnO + PFN-Br electrodes due to the unfavorable energy level alignment (compare Figure 6.1b). In the case of the conventional devices, the tip collects electrons when a negative sample bias is applied and the PEDOT:PSS/ITO or CPE-K/ITO collects holes, similar to the device operating conditions. In this favorable case, similar features can be clearly revealed for the samples based on PEDOT:PSS

(Figure S6.7b), and less distinct features (low current) are observed in the case of CPE-K, possibly originating from the lower photogeneration in these devices. When reversing the field by applying +0.5 V sample bias, the CPE-K/PEDOT:PSS electrodes collect electrons. In this case, again similar features are seen for the PEDOT: PSS-based devices, and no features can be seen for the CPE-K-based devices.

Chapter 7: Unraveling Device Physics of Dilute-Donor Narrow Band Gap Organic Solar Cells with Highly Transparent Active Layers

7.1 Introduction

Organic Photovoltaics promise innovative renewable energy harvesting applications with low environmental impact at low cost.[65,344–348] Thanks to the unique properties of the organic semiconducting materials, being lightweight, flexible, solution-processable, and optically tunable, OPVs are ideal candidates for integrated energy harvesting solutions such as energy-harvesting windows, skylights, or greenhouses.[52,53,65,292,349–352] While the field of OPV research underwent enormous progress in the past decade, resulting in opaque high-performance systems with photoconversion efficiencies (PCEs) of over 18%, (semi-)transparent OPVs (ST-OPVs) still perform far from their theoretical limits.[65,167,214,215,263,291,349,353,354] One inherent challenge for ST-OPVs is to absorb enough photons to obtain a high PCE while maintaining a high average visible transmittance (AVT). Such a combination of high AVT and high PCE can only be achieved if organic semiconductor absorbers with a sufficiently narrow band gap are employed.[66,291,349,352] In fact, it is predicted that the theoretical Shockley–Queisser limit of a fully transparent single junction (100% AVT) approaches an impressive 20% for sufficiently narrow band gaps E_g of 1.0 eV to 1.14 eV.[291,349]

Despite the vast progress in the band gap engineering of non-fullerene acceptors (NFAs) for ST-OPVs, it remains not only a challenge to obtain PCEs comparable to those of opaque devices, but also to meet the high transparency requirements for the intended applications.[85,101,106,167,275,292,344,344,355] While in the scientific literature the term *semitransparency* is

commonly used to refer to OPV devices with an AVT of > 10%, much higher AVTs of > 55% for automotive applications and > 70% for architectural applications are required.[350,356]

In the past, the most common way to achieve transparency was to employ thin active layers, resulting automatically in lower photon harvesting and lower PCEs than in opaque devices. Nowadays, several strategies exist to bypass these limitations. In 2019, Hu et al. reported the *dilute donor approach* and increased the AVT of semitransparent PTB7-Th:IECO-4F OPVs from 23.7% to 27.1% by decreasing the PTB7-Th content in active layers, which was accompanied by a slight PCE decrease from 9.48% to 9.06%.[357] Such dilute donor systems offer a platform for increasing the AVT while maintaining high PCE due to increased IR absorption by a narrow band gap acceptor compound. Xu et al. reported a PCE of 12.91% and an AVT of 22.49% (blend film AVT over 50%) using the wide-band gap donor polymer D18 in combination with the near-IR absorbing N3 acceptor, and Yao et al. reported that PM6:Y6 OPVs with reduced donor content deliver an efficiency over 10% with only 10 wt.% PM6, thanks to efficient charge generation, electron- and hole transport, slow charge recombination, and field-insensitive extraction.[358,359] Another strategy is to employ ternary blends with two narrow-band gap acceptors to achieve efficient ST-OPVs.[360,361] For example, Hu et al reported ternary blends with an active layer AVT of 50.1%, leading to ST-OPVs with 20.2% and a PCE of 13.02% when employing D18-Cl:Y6-1O:Y6 in a 0.7:0.8: 0.8 wt/wt ratio.[362]

To date, only a few examples in the literature demonstrate OPVs with AVTs of > 60%. To reach such high AVTs, highly-transparent electrodes and active layers have to be employed. Typically, a strong focus lies on the intended applications which dominates over efforts to create an in-depth understanding of ST-OPVs.[349,350,352,363–365,365–367] Nevertheless, to close the gap between the current performance and the theoretical limitations of ST-OPVs, an in-depth

understanding of the photoelectronic processes in the devices comprising highly transparent active layers is necessary to improve ST-OPVs for widespread application.

7.2 Results and Discussion

Here, we focus on the commonly used donor polymer **PCE10** (poly[4,8-bis(5-(2-ethylhexyl)thiophen-2-yl)benzo[1,2-b;4,5-b']dithiophene-2,6-diyl-alt-(4-(2-ethylhexyl)-3-fluorothieno[3,4-b]thiophene-)-2-carboxylate-2-6-diyl)]) and the narrowest band gap (E_g=1.10 eV) NFA, **COTIC-4F** (2,2'-((2Z,2'Z)-(((4,4-bis(2-ethylhexyl)-4H-cyclopenta[2,1-b:3,4-b']dithiophene-2,6-diyl)bis(4-(heptan-3-yloxy)thiophene-5,2-diyl))bis(methanylylidene))bis(5,6-difluoro-3-oxo-2,3-dihydro-1H-indene-2,1-diylidene))dimalononitrile, shown in **Figure 7.1a**. The combination of PCE10:COTIC-4F serves as a model system for state-of-the-art NFA-based narrow band gap systems and has been the focus of previous studies of devices with optimized D:A ratio.[97,275] The narrow band gap acceptor favorably absorbs in the near IR with an absorption peak at 960 nm, whereas PCE10 limits the AVT of the blend due to absorption in the visible range with absorption maxima between 600 nm and 800 nm (Figure S7.1). In this work, we systematically increase the transparency of the BHJ active layers by two means. First, we employ the *dilute donor approach*, varying the donor:acceptor ratio from 40:60 to 30:70 and 20:80, in the remainder of the text referred to as 40%, 30%, and 20%. Second, to achieve higher transparency, significantly thinner films are employed than in previous works, ranging from 92 nm to 83 nm and 78 nm, for 40%, 30%, and 20% donor concentration, respectively, instead of the optimized 140 nm shown in previous works.[97,100]

We use a highly reproducible opaque back electrode configuration in order to elucidate the changes in the photoelectric processes that arise from the dilution of the donor. The devices

studied in this work and the respective energy level diagram are shown schematically in Figure 7.1b and c.
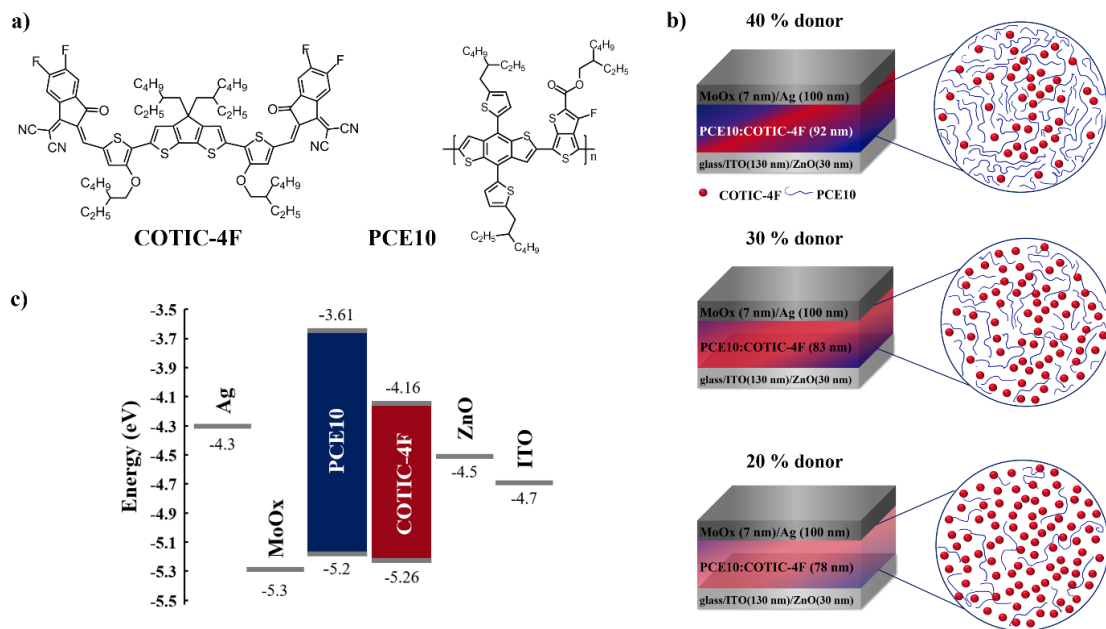
Figure 7.1. a) Chemical structures of the non-fullerene acceptor COTIC-4F and the donor polymer PCE10. b) Schematic device structures of the studied OPVs with different donor:acceptor ratios in the active layer. c) Energy level diagram of the devices.

To start, we characterize the morphology of the three different blend films with photoconductive atomic force microscopy (pc-AFM), which allows obtaining information on the surface topography and the nano-scale photocurrent simultaneously, therefore providing information on the nanoscale charge generation.[113,114] A small positive bias was applied to the sample to direct the flow of photogenerated electrons toward the ITO/ZnO substrate. As the high work function Pt-coated tip collects holes from the blend, a high photocurrent signal corresponds to efficient hole extraction from a donor-rich domain. Consequently, dark domains correspond to the collection of electrons from acceptor-rich domains.[91,112,113]

Figure S7.2 a,e and i show 5 µm x 5µm surface topography images of the 40%, 30%, and 20% blends, revealing similar features and low surface roughness (0.82 nm to 0.89 nm) for all films.

Due to this similarity, we can conclude that the surface roughness is not a significant factor in the performance of the studied cells. Figure S7.2 b-d,f-h and j-l show the photocurrent images of the same blends at 0 V, +0.5 V, and +1 V bias applied to the sample. In contrast to the topography scans, the photocurrent images reveal significant differences. As expected, with higher sample bias, holes are extracted more efficiently, leading to higher contrast in the images and higher RMS values (Table S7.1) with increasing sample bias, therefore resolving the features most distinctly at +1 V. The 20% films show a low photocurrent response at all voltages, and the features cannot be resolved as clearly as for the other blends. Such a reduced photocurrent can originate from lower charge carrier generation, higher rates of recombination, and poor extraction, hinting toward a reduced OPV performance. When comparing the other two blends, it is evident that the 30% film reveals larger features than the 40% blend, indicating a higher degree of phase separation. This observation is confirmed by higher resolution scans, shown in Figure S7.3.

Next, we carried out Transmission Electron Microscopy (TEM) measurements, shown in Figure S7.4, taken at 20kx and 30kx total magnification. Brighter and darker areas are visible, which correspond to regions with different scattering contrast, e.g., donor-rich or acceptor-rich phases with a higher or lower degree of crystallinity and aggregation. With reduced donor content these features visibly increase in size. An analysis of the average domain sizes confirms the visible trend and for the bright features, $(31,400 \pm 14,500)$ nm^2, $(18,900 \pm 11,300)$ nm^2, and (6700 ± 3600) nm^2 are found for 40%, 30%, and 20%, respectively.

To gain additional morphological insights, we obtained information about the molecular ordering of the PTB7-Th:COTIC-4F blends by carrying out GIWAXs measurements. The GIWAXs analysis reveals that the crystal structure of donor and acceptor prefers to retain a face-on orientation, regardless of the differences in the thickness and composition of the films, as seen in Figure S7.5a. An expected decrease in the scattering intensity is observed with the reduced

thickness from 40% to 20% donor content in the film. The crystal information for the NFA has not been assigned and overlaps with features from PTB7-Th, however, the observed scattering pattern for the 40% film agrees well with what is reported in the literature for this blend.[327] As shown in the out-of-plane line cut, the lamellar packing (100) distance of PTB7-Th does not change with the donor concentration (Figure S7.5b and Table S2). However, a minor increase in the crystal size can be observed from 8.84 nm for 40% to 9.29 nm and 9.67 nm for 30% and 20%, respectively. This correlation with the above-mentioned TEM results indicates that an increased crystallinity may contribute to the larger area features in the blends with a lower donor concentration.

In the case of π-π (010) stacking, both size and lattice are preserved. Overall, the morphology characterization results indicate changes in the phase separation and in the molecular ordering, which are expected to have an effect on the OPV performance. However, we expect that the PCE values are governed by other factors as well, which we will address in the remaining text.

Next, we investigate the optical properties of the active layer blends by carrying out transmission measurements of the blend films on glass, shown in Figure 7.2, to determine the AVT. The AVT is the standardized measure for the transparency in the visible range and is calculated based on the transmittance of the device stack, the spectral intensity distribution of the AM1.5 spectrum I(λ), and the photopic spectral response of the human eye V(λ), as

$$AVT = \frac{\int I(\lambda) \cdot T(\lambda) \cdot V(\lambda) \, d\lambda}{\int T(\lambda) \cdot V(\lambda) \, d\lambda}$$[65,325,350] The reduction of the donor content leads to a monotonous increase in the transmittance in the visible range up to 760 nm, resulting in blend AVTs of 64%, 70%, and 77%, respectively. The most transparent devices reported comprise active layers with up to 68% blend AVT, and other dilute-donor studies reported AVTs of ≈ 50% blend AVT.[358,362,368,369] Therefore, best to our knowledge, the present blends are among the most transparent BHJ active layers reported to date, making them excellent candidates for ST-OPVs.
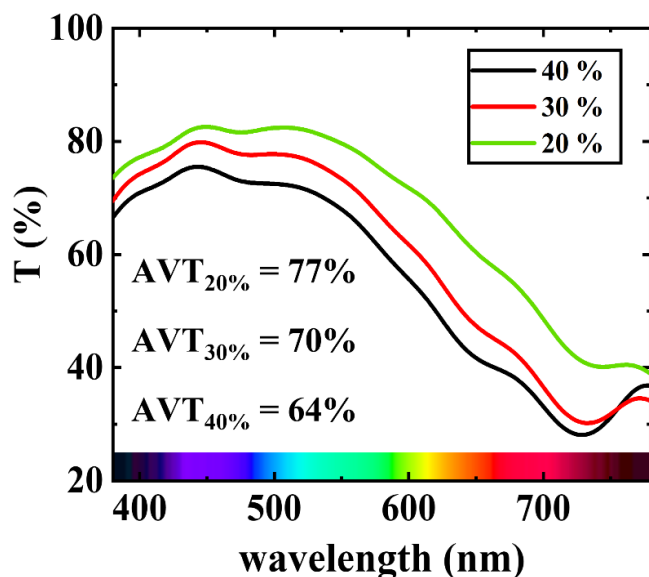
Figure 7.2. Transmittance spectra of the dilute donor active layers, leading to high blend AVTs of 64%, 70%, and 77%.

Having resolved differences in the morphology and optical properties of the blends, we now focus on the impact of the donor concentration on the OPV device performance. To create an in-depth understanding of the optoelectronic processes in dependence on the donor concentration, we fabricate devices in inverted structure with a well-established opaque MoOx(7 nm)/Ag(100 nm) electrode configuration. The current-density voltage (JV)-characteristics of representative devices are shown in **Figure 7.3a**. The photoelectrical parameters are summarized in **Table 7.1**, obtained from 8 devices of each blend type.

Table 7.1. Photoelectrical parameters of the solar cells used in this work under 1 sun illumination, obtained from the fabrication of 8 devices for each blend.

donor (%)	J_{sc} (mA/cm²)	V_{OC} (V)	FF(%)	PCE (%)	AVT (%) of active layer
40%	20.6 ± 0.8	0.567 ± 0.003	60.1 ± 0.7	7.0 ± 0.3	63.8
30%	19.0 ± 1.5	0.563 ± 0.002	60.7 ± 2.7	6.5 ± 0.2	69.8
20%	12.2 ± 0.4	0.555 ± 0.004	60.3 ± 1.5	4.1 ± 0.1	76.8

With decreasing donor concentration from 40% to 30% and 20%, the short-circuit current J_{sc} decreases most noticeably from 20.6 mA/cm² to 19.0 mA/cm² (8% decrease) and 12.2 mA/cm² (41% decrease). While the open-circuit voltage V_{oc} follows the same trend, the differences are minor. The 40% reference system exhibits a V_{oc} of 0.567 V, which is decreased by 1% to 0.563 V and by 2% to 0.555 V for the 30% and 20% devices, respectively. All devices maintain a fill factor FF of over 60%, leading to PCEs of 7.0%, 6.5%, and 4.1%. Before weighing the observed drop in performance against the gain in transparency with decreased PCE10 content, we aim to understand the origins of the observed performance trend in the three systems by elucidating charge carrier generation, charge carrier recombination, and extraction dynamics.
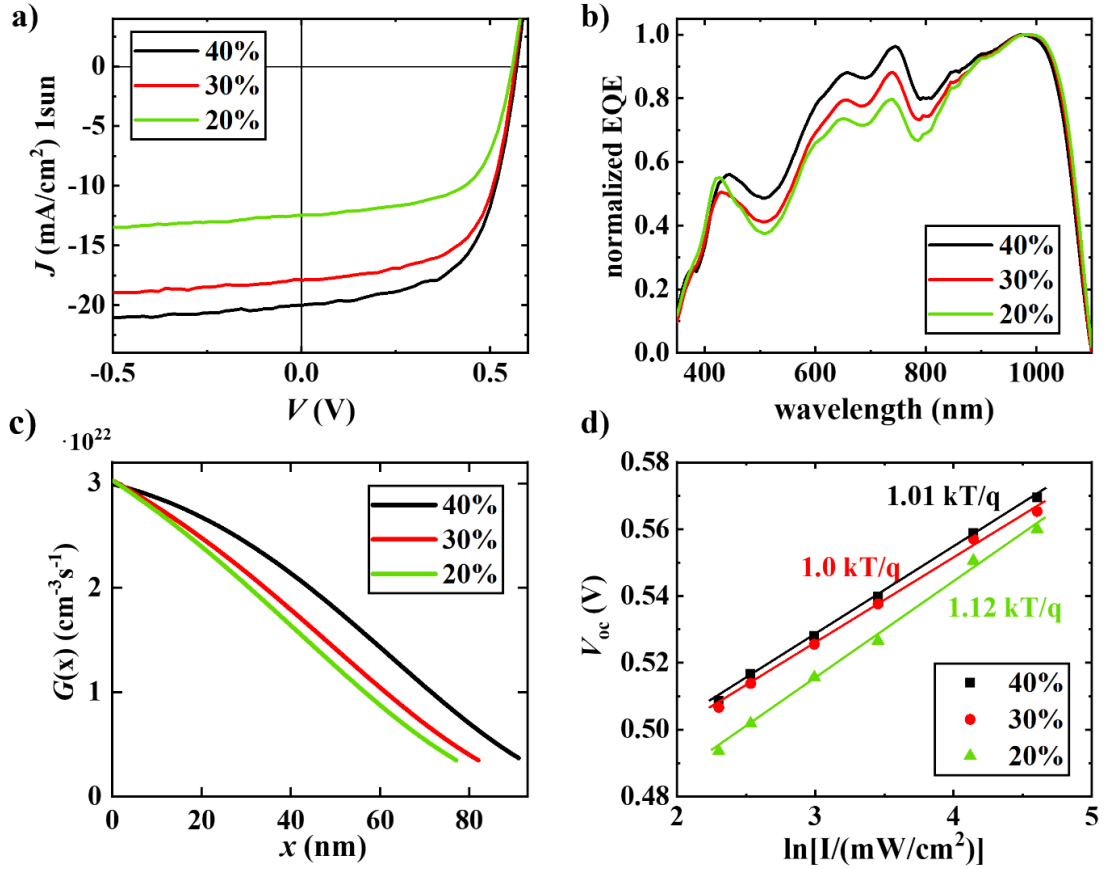
Figure 7.3. a) Experimental current-voltage characteristics of the studied OPVs with the different donor:acceptor ratios. b) Experimental normalized EQE spectra of the same devices. c) Simulated generation rates as a function of the spatial position in the active layer, x = 0 being the bottom electrode:active layer interface. d) Experimental dependence of the V_{oc} on the light intensity and linear fits.

A more in-depth analysis of the JV-characteristics, by obtaining the differential resistance dV/dJ in dependance on the voltage, reveals that the series resistance R_s is unaffected and low, with values of 1.87 ± 0.06 Ω cm^2, 1.69 ± 0.21 Ω cm^2 and 1.71 ± 0.23 Ω cm^2 for the 40%, 30%, and 20% devices, respectively, as summarized in Table S7.2. Another potential cause for performance losses is leakage current, as quantified by the shunt resistance R_{shunt}. All devices maintain high R_{shunt} values of $> 4.28 \cdot 10^4$ Ω cm^2, demonstrating that the deviation from the optimized donor:acceptor ratio does not result in undesired leakage current pathways in the devices. The analysis of the dark JV-characteristics shows a small increase in the ideality

coefficient n from 1.33± 0.04 to 1.38 ± 0.03 and 1.39 ± 0.01 when reducing the donor concentration (Table S7.3), which can be caused by an increase in trap-assisted recombination. Concomitantly, an increase in the reverse bias dark current J_0 is observed from $(2.64 \pm 1.30) \cdot 10^{-7}$ mA/cm^2 to $(4.89 \pm 2.19) \cdot 10^{-7}$ mA/cm^2 and $(5.55 \pm 1.20) \cdot 10^{-7}$ mA/cm^2, which may arise from the reducing active layer thickness, trapped charge carriers or changes in the energetic disorder.[370,371]

Figure 7.3b displays the normalized EQE spectra of the studied devices, normalized to the acceptor absorption at 975 nm. The absolute EQE spectra match the trend in the J_{sc} values obtained from the JV-curves (Figure S7.6). The normalization allows visualizing that the reduction of the donor content results in a reduced EQE in the donor absorption range (Figure S7.1) below 800 nm in the 30% and 20% donor devices, hinting towards the desired increase in the transparency in the visible range (370 nm – 770 nm). The relative donor:acceptor peak ratios range from 0.96:1 (40%) to 0.88:1 (30%) and 0.79:1 (20%).

Next, we aim to quantify the role of charge generation. To obtain the charge carrier generation rates depending on the spatial position $G(x)$ in the active layer, we obtained the optical properties of the blends with variable angle spectroscopic ellipsometry (VASE) and combined them with the already known optical properties of the other materials used in the device stack to serve as the input for optical transfer matrix simulations (TMM).[97,335] The resulting $G(x)$ curves are shown in Figure 7.3c. Here, too, a clear trend can be seen with $G(x)$ being reduced noticeably as the donor concentration is reduced from 40% to 30% and 20%. This observation implies that the absorption of the NFA in the IR cannot compensate for the reduced donor absorption in the visible range. Such a reduction in $G(x)$ is expected to directly translate to the J_{sc}, which linearly depends on $G(x)$. In contrast, the V_{oc} has a logarithmic dependence. $V_{oc} \propto \ln(G(x))$, explaining the small observed reduction in the V_{oc} with decreasing donor content.[159,372] However, these

changes cannot explain the observed performance changes alone. For example, a drop in J_{sc} of 8% is observed when reducing the donor concentration from 40% to 30%, but the reduced charge generation explains only a reduction of 3%. Therefore, we shift our focus to the charge carrier recombination and extraction processes in the different blends.

As a first glance into recombination in the devices with different donor concentrations, we consider the relationship of the V_{oc} with the light intensity, presented in Figure 7.3d. In all cases a linear relationship is found, confirming low leakage contributions, with slopes of 1.01, 1.00, and 1.12 kT/q. It is commonly assumed that for slopes of 1 kT/q pure or dominant bimolecular recombination occurs in the devices, whereas slopes > 1 kT/q indicate bulk trap-assisted recombination.[99,100,159] Thus, the data suggest an increase in trap-assisted recombination only for the 20% system. In the presence of surface trap-assisted recombination, the slopes are reduced and values < 1 kT/q indicate a strong relative contribution of surface recombination.[99,100,137] However, it is also possible that the effect of bulk and surface trap-assisted recombination contributions on the slope balance each other out, leading to slopes of exactly 1 kT/q, as demonstrated in detail in our previous work.[99,100] For the present PCE10:COTIC-4F systems, a combination of the three recombination mechanisms is expected, based on previous results of the optimized opaque device structures with 40% donor and a thicker active layer. In addition, the relative contribution of bimolecular recombination has previously been found to be low in these devices with a Langevin prefactor $\xi = 0.02$.[100] With the observed reduction in the generation rates for the 30% and 20% donor devices, lower charge carrier concentrations n are anticipated, decreasing the relative contribution of bimolecular recombination even further due to its $\propto n^2$ dependence. Therefore, the slopes close to 1 kT/q may not indicate dominant bimolecular recombination and a more in-depth analysis of the recombination pathways is necessary to interpret the results correctly.

To draw a more detailed picture of the occurring recombination processes, we employed the voltage-capacitance spectroscopy technique, following the approach developed by Brus and Vollbrecht.[136,137] The method provides information about the effective mobility μ_{eff}, effective lifetime τ_{eff}, and charge carrier concentration n, and the fit of the calculated recombination current $J_{rec,fit}$ to the experimental recombination current $J_{rec,exp}$, shown in Figure S7.7a-c, yields information on the multi-mechanism recombination contributions and trap concentrations.

Figure S7.7d shows μ_{eff} for devices with the different donor concentrations as a function of the corrected voltage $V_{corr} = V\text{-}JR_s$ in the relevant working regime from 0 V to the V_{oc}. Under forward bias > 0.4 V, the μ_{eff} of the 40% and 30% are indistinguishable, whereas the 20% donor blend shows slightly lower mobility values. The lower μ_{eff} of the 20% system might originate from a less optimal morphology in the BHJ at low donor concentrations, as indicated by TEM and GIWAXs measurements, such as changes in the percolation network, increased domain size, and the changed crystal size. All in all, the changes in the mobility values with decreased donor concentration are minor and their dependence on the voltage follows a similar trend.

Figure S7.7e gives insights into the evolution of the effective lifetime τ_{eff} with decreased donor concentration. Here, a clear trend can be seen, with the 40% devices exhibiting more than twice as high τ_{eff} around 0 V than the other blends with $4.8 \cdot 10^{-6}$ s compared to $2.1 \cdot 10^{-6}$ s and $1.9 \cdot 10^{-6}$ s for 30% and 20%, respectively. However, towards the V_{oc} these differences subside, and values close to 10^{-6} s are found for all systems.

The evolution of the charge carrier densities n, shown in Figure S7.7f, follows the same trend with 40% > 30% > 20%. The trend in n at all biases reflects very well the charge photogeneration rates G that we presented earlier, obtained from the independent method of optical TMM simulations.

Around 0V the charge carrier extraction dominates over recombination, opposite to the open-circuit condition. As shown here down the extraction efficiency of photogenerated charge carriers is high and comparable for all systems. Thus, the trend in n at low forward bias is fully governed by the decrease of G with donor dilution. At V_{oc} all photogenerated charge carriers recombine without being extracted to the external circuit. Therefore, the charge carrier concentration can be estimated as $n = \tau_{eff}G$.[373] Since τ_{eff} at V_{oc} remains almost the same for all systems, the trend in n at large forward bais close to V_{oc} is also determined dominantly by the change in the charge photogeneration rate. We can therefore confirm, that with lower donor concentration, the charge carrier densities in the BHJ are reduced significantly within the whole operating bias range.

The 40% system exhibits already a relatively low charge carrier density of less than $1.7 \cdot 10^{16}$ cm^{-3} at V_{oc}, which is reduced even further for the 30% and 20% systems to values below $1.4 \cdot 10^{16}$ cm^{-3} and $1.1 \cdot 10^{16}$ cm^{-3}. For reference, most systems exhibit higher charge carrier densities, sometimes exceeding $1 \cdot 10^{17}$ cm^{-3}.[100,215,348]

As discussed, such low charge carrier densities render the bimolecular recombination of free charge carriers less dominant as they are encounter-limited. In addition, the Langevin prefactor for bimolecular recombination was found to be low with a value of 0.015 for the 40% system, confirming the minimal role of bimolecular recombination. With further reduction of n in the 30% and 20% devices, the role of bimolecular recombination diminishes even further due to the n^2 dependence of the bimolecular recombination rate.
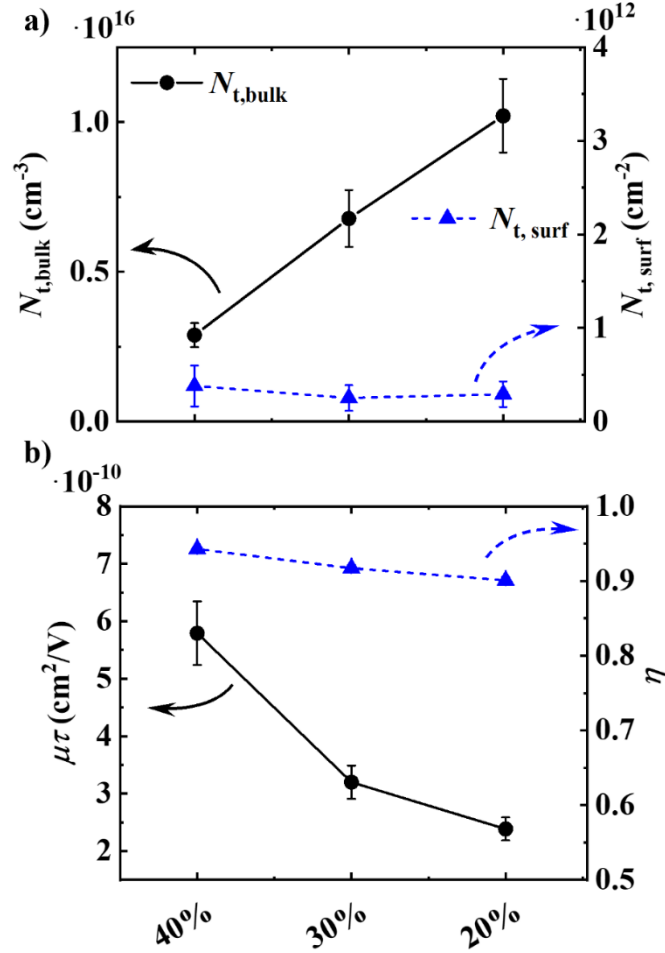
Figure 7.4. a) Concentration of bulk traps $N_{t,bulk}$ in the active layer of the studied devices (left axis) and concentration of surface traps $N_{t,surf}$ at the bottom electrode:active layer interface (right axis). b) The $\mu\tau$ product (left axis) and the extraction efficiency η in the studied devices with different donor concentrations.

Therefore, bulk and surface trap-assisted recombination are the relevant recombination channels in these devices, despite the narrow band gap that according to Shockley-Read-Hall model does not favor the dominance of trap-assisted recombination.[100,198,203,204] **Figure 7.4a** shows the bulk trap and the surface trap concentrations obtained from the capacitance spectroscopy method. The different donor concentrations do not impact the surface trap concentrations significantly, and values below $N_{t,surf} = 1 \cdot 10^{12}$ cm^{-2} are found that are the same within the error for all systems. In contrast, the bulk trap densities increase from $N_{t,bulk} = 2.9 \cdot 10^{15}$

cm^{-3} to $6.8 \cdot 10^{15}$ cm^{-3} and $1.0 \cdot 10^{16}$ cm^{-3}. The origins of bulk traps can be various; impurities, such as side products from synthesis, oxygen, water, and also local morphological variations can trap charge carriers.[84,103,112,193,302] All three systems consist of the same donor and acceptor material from the same batch of synthesis and were processed in the same manner, thus impurities are unlikely the source of traps in this case. Moreover, an increase in traps due to impurities with an increase of the NFA concentration is in general unlikely, because small molecule NFAs are much easier to purify than polymeric donor materials.[112,177] Therefore, the increase in traps is most likely due to morphological causes. The reduction of the donor content, specifically in the 20% active layers, may cause disturbances in the percolation pathway and give rise to isolated acceptor islands in which charges can get trapped.[84,374] The increased domain size that we have reported based on pc-AFM and TEM as well as the increased crystal size (GIWAXs) support this argument. Moreover, similar behavior has been reported for fullerene-based OPVs with reduced acceptor content.[84] The trapping of charge carriers in isolated acceptor regions explains the observed increase in the slope of the V_{oc} depending on ln(I). A comparison with other device systems fabricated in the same device configuration is conducive to understanding the scale and impact of the observed trap increases. While the $\approx$ 2-fold increase in $N_{t,bulk}$ upon donor content reduction is a significant, much larger system to system variations have been observed before. For example, the mere substitution of the solvent has been shown to lead to > 1 order of magnitude changes in the bulk trap concentration, and equally large changes have been observed upon the addition of impurities to the active layer blend.[112,348]

With these quantitative insights into non-geminate charge recombination, we can confirm our earlier discussion of the dependence of the V_{oc} on the light intensity. Indeed, the slopes close to unity are not a reflection of dominant bimolecular recombination. We further learn that the $\approx$ 2-fold increase in N_t for the 30% is not large enough to cause an increase in the slope, but the about

$\approx$ 3-fold increase in N_t in the 20% system is sufficient to outweigh the constant contribution from the surface recombination and causes a small deviation to 1.1 kT/q.

Next, we address the impact of the donor concentration on the charge carrier extraction. The mobility-lifetime product $\mu\tau$ can be derived from the presented capacitance spectroscopy results and is proportional to the mean free path w that charge carriers travel in the active layer before they recombine.[97,254,273] The extraction efficiency η can then be calculated from w and the active layer thickness.[97,254,273] Both $\mu\tau$ and η under short-circuit conditions are displayed in Figure 7.4b. The $\mu\tau$ drops from $5.8 \cdot 10^{-10}$ cm^2/V to $3.2 \cdot 10^{-10}$ cm^2/V when decreasing the donor concentration from 40% to 30%. A further reduction is observed for the 20% system to $2.4 \cdot 10^{-10}$ cm^2/V, indicating a steady increase in combined non-geminate and extraction losses (Figure 7.5b, solid line, left axis). This variation in the $\mu\tau$ product by nearly 60% from $5.8 \cdot 10^{-10}$ cm^2/V to $2.4 \cdot 10^{-10}$ cm^2/V strikes as a substantial change, that exceeds even system-to-system variations for unrelated BHJ blend systems. For example, it exceeds the difference in $\mu\tau$ of PM6:Y6 vs P3HT:PCBM or PM6:Y6 vs PCE10:IOTIC-2F.[97] However, since the processing conditions were kept the same for all three device types, thinner active layers were obtained when using lower polymer donor concentrations (Figure 7.1b). This reduced active layer thicknesses partially compensate the drop in $\mu\tau$, leading to η = 0.94, η = 0.92, and η = 0.90, indicating efficient charge extraction in all cases (Figure 7.5b. dashed line, right axis).

As discussed earlier, all active layers have an exceptional AVT of over 60% (Figure 7.2). We measured AVT values of 64%, 71%, and 76% for the glass/ITO/ZnO/BHJ stacks without back electrodes, which demonstrates the great potential of these blends for ST-OPVs. Therefore, after this detailed discussion of the photoelectronic processes in the three systems, we lastly give a brief outlook on their application potential for integrated energy harvestings solutions that require high transparency.

We fabricated devices with semitransparent MoOx(7 nm)/Au(10 nm) back electrodes and obtained PCEs of 3.3%, 2.9%, and 1.7% while measuring device stack AVTs of 41.9%, 47.1%, and 48.9% for stacks comprising the blends with 40%, 30% and 20% donor polymer, as summarized in Table S7.4. Figure S7.8 shows the transmittance spectra of the transparent electrode, the transmittance spectra of the whole device stack, and the experimental AVTs as well as AVT values of literature systems as a function of the PCE, as well as those of this work.[88,299,350,352,365–367,375–389] Further we show the EQEs of representative semitransparent devices and the QUE in Figure S7.9 a and b, respectively. Lastly, to estimate the AVT of devices with more transparent electrodes, we *simulated* the AVT of a device stack with Ag nanowires as back electrodes and obtained AVT values of 61%, 67%, and 71% are found for the device stacks with 40%, 30%, and 20% donor content, suggesting that specifically, the 30% and 20% blends are promising candidates for highly transparent OPVs. Future works are necessary to gauge the PCE of such devices.

7.3 Conclusions

To summarize, the three PCE10:COTIC-4F active layer systems with donor concentrations of 40%, 30%, and 20% provide exceptionally high AVTs of 64% to 77%. The AVT increases with decreasing donor concentration owing to reduced donor absorption in the visible range and increased near-IR acceptor absorption. We found that the donor:acceptor ratio impacts the nanoscale morphology and the domain sizes, however, the thin active layers allow for efficient charge extraction ($\eta > 90\%$) in all systems. The PCEs of 7.0%, 6.5%, and 4.1% follow a clear trend with decreasing donor content due to reduced J_{sc} values, which originate from reduced charge carrier generation, reduced lifetime, and increased bulk trap-assisted recombination. Higher degrees of intermixing in the 30% devices and maintained effective mobility, explaining

why only a moderate drop in the PCE is observed when reducing the donor content from 40% to 30%. We further found very low bimolecular recombination contributions and low charge carrier densities in all devices, rendering surface or bulk trap-assisted recombination channels dominant. While surface trap contributions remain constant, an increase in bulk trap-assisted recombination with decreased donor content may be due to morphological changes such as isolated donor islands.

On the one side, such increased bulk trap-assisted recombination has a reducing effect on the FF. On the other side, charge extraction remains efficient due to thinner active layers, and a smaller voltage drop over the series resistance ($J_{sc}R_s$) should improve the FF. The counterbalance of these effects explains the observed constant FF values.

The decreased charge generation is reflected in the small decreases in V_{oc} as well; however, the V_{oc} is impacted far less than the J_{sc} due to the weaker non-linear dependence on the charge carrier density. The increased bulk trap-assisted recombination reduces J_{sc} but has a minor effect on the V_{oc}, which is dominantly governed by surface trap-assisted and bimolecular recombination.

To conclude, further optimization of the interfaces and the active layer morphology might reduce the observed loss factors. Besides employing different transparent back-electrodes, a future direction might therefore involve ternary systems to improve PCE and AVT of the present blend system further. Overall, more synthetic efforts to obtain high-performing ultra-narrow band gap NFAs with band gaps of ≈ 1.12 eV are desirable to overcome the low AVT bottleneck and establish OPV blends with high AVTs > 70%.

7.4 Experimental Section

Materials

The donor polymer PCE10 was purchased from 1-Material Inc. and the acceptor COTIC-4F was synthesized following the literature procedure.[275]

Thin Film Characterization

Photoconductive Atomic Force Microscopy images were obtained in contact mode with an Asylum Research MFP-3D setup using platinum-coated probes. Measurements were carried out under a nitrogen atmosphere at a sample bias of 0V, +0.5 V, and +1 V, applied to the ITO bottom electrode. Photocurrent images were obtained by illuminating the samples with a white light source. The small current value in the dark at the respective bias was used as the current offset to obtain the photocurrent images. All images were obtained using the same tip and the same contact force.

Transmission Electron Microscopy images were obtained with a Jeol JEM-1400 Plus setup. The films were spin-coated as the active layers in devices on Glass/ITO/PSS substrates. Then, each film was carefully detached from the substrate by dissolving the PSS layer in distilled water so that the film could be transferred to a copper 100 mesh TEM grid. The active layer analysis was performed at an accelerating voltage of 120 kV.

GIWAXS measurements were carried out at the PLS-II 5A beamline of the Pohang Accelerator Laboratory in South Korea. The 2D images were taken by using a Mar CCD detector with a sample-to-detector distance of 414.58mm at 11.57 keV (1.07156 Å).

The *optical properties* of materials not reported in previous works were obtained with a SER850 DUV spectroscopic ellipsometer (SENTECH Instruments GmbH, Berlin) with a spectral range of 190 nm – 2500 nm. First, the SiO_2/Si substrates were modeled with a Sellmeier oscillator model. Then, the active layers were modeled as uniaxial anisotropic, and measurements were carried out at angles of 50°, 60°, and 70°.

Device Fabrication

Substrates of ITO on glass were cleaned by scrubbing with an aqueous solution of commercial detergent, followed by subsequent sonication in acetone and isopropanol and drying overnight in an oven at 130 °C. Next, the ZnO layer was deposited by spin-coating a mixture of diethyl zinc (15% w/w in toluene) and tetrahydrofuran in a 1:2 ratio at 4000 rpm in air. The films were annealed at 150 °C for 25 minutes before the active layers were deposited under nitrogen atmosphere by spin-coating a solution of PCE10:COTIC-4F (1:1.5 ratio, c = 20 mg/ml) in chlorobenzene with 2% (v/v) chloronaphthalene at 2000 rpm. The back electrodes (0.22 cm^2) were deposited by thermal evaporation of molybdenum(VI) oxide and silver in a vacuum deposition chamber (Ångstrom Engineering) at pressures < 10^{-6} torr. The same procedure was followed for the ST-OPV devices, but thinner Ag electrodes were evaporated (15 nm instead of 100 nm).

Device Characterization

The current-voltage characteristics were obtained with a Keithley 2602 semiconductor analyzer system under nitrogen atmosphere. For measurements under 1 sun, a solar simulator with a 300 W Xenon lamp with an AM 1.5 global filter was used to irradiate the devices. The light intensity was calibrated with a standard silicon solar cell with a KG1 filter, calibrated by the National

Renewable Energy Laboratory. An aperture of 0.123 cm^2 was used to define the illuminated area of the cells. The V_{oc} dependence on the light intensity was measured with the same setup using a set of Newport 5215 neutral density filters. EQE spectra were obtained using monochromatic light chopped at 155 Hz with defined intensity as determined with a Newport Si photodiode as reference. A Solartron SI1260 analyzer was used to measure the frequency-dependent impedance spectra (10^1-10^6 Hz) under 1 sun and in the dark, applying a small AC disturbance of 40 mV. The measurements were carried out starting with a negative sample bias that was gradually increased up to the respective V_{oc}. The thicknesses of the device layers were measured with an Ambios XP-100 profilometer.

Optical Simulation

The available Transfer Matrix software, developed by the McGhee group, was used in combination with our script to visualize $G(x)$.[97,130,163]

Statistical Analysis

Statistical Analysis was conducted using Microsoft® Excel® for Microsoft 365 MSO (Version 2205 Build 16.0.15225.20172) 64-bit. Data in tables is presented as mean ± SD and the sample size n_s for each statistical analysis is given in the respective figure legends. For the recombination current analysis, fitting errors were determined in Python 3.7 using scipy. optimize.curve_fit for the fitting procedure, yielding the estimated covariance of the optimized parameters (trap densities N_b, N_{sf}, and Langevin prefactor χ) as a 2D-array. The array's diagonals provide the variance of the optimized parameter estimate, thus one standard deviation errors on the parameters were obtained as perr = np.sqrt(np.diag(pcov)). Further documentation can be found in the SciPy documentation on scipy.optimize.curve_fit. The errors obtained for the thickness-

dependent quantities ($\mu\tau$ and η) were assumed to be dominated by the uncertainty of the profilometry measurement, which was estimated as ± 5 nm. Errors were obtained by carrying out the recombination current analysis for the measured thickness + 5 nm and for the measured thickness-5 nm.

7.5 Supplementary Information for Chapter 7
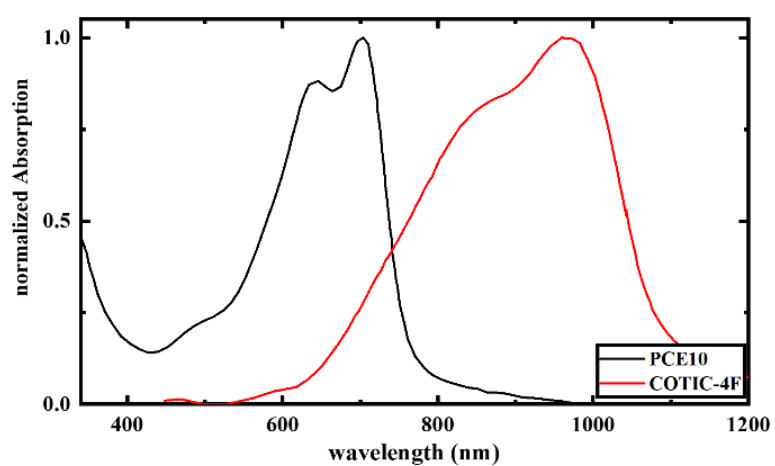
Figure S7.1. Normalized Absorption spectra of the donor polymer PCE10 and the non-fullerene acceptor COTIC-4F.
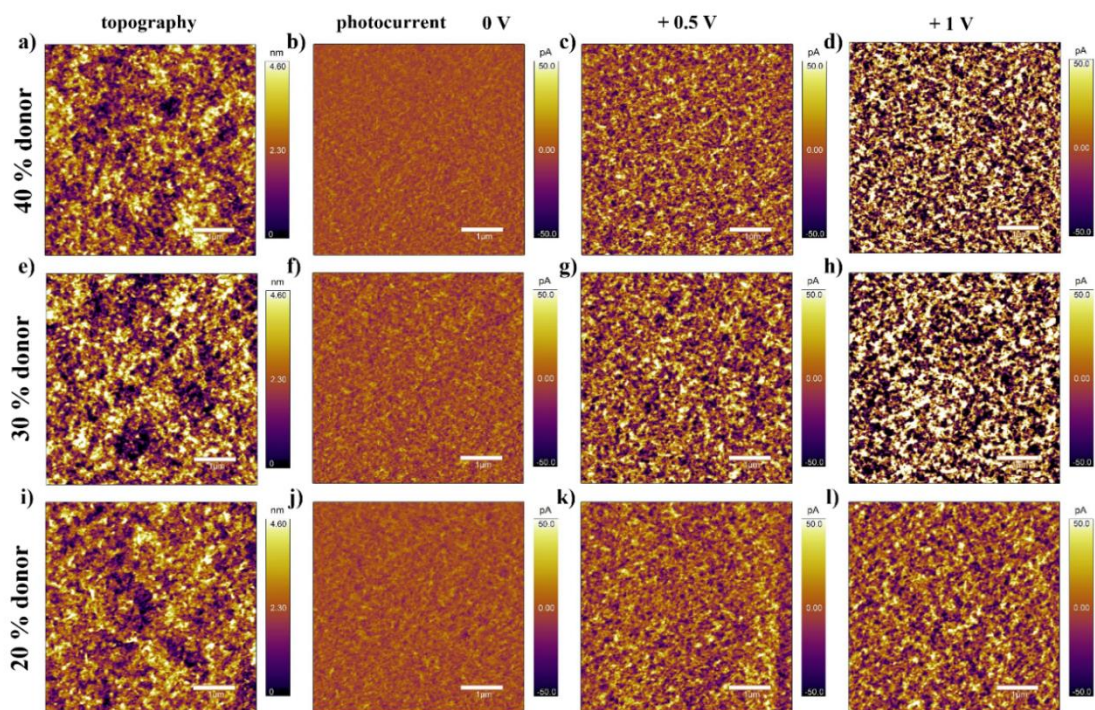
Figure S7.2. 5 μm x 5 μm surface topography (left) and photoconductive atomic force microscopy (pc-AFM) scans of the blends with different donor concentrations at different sample biases of 0V, +0.5 V, and +1 V.
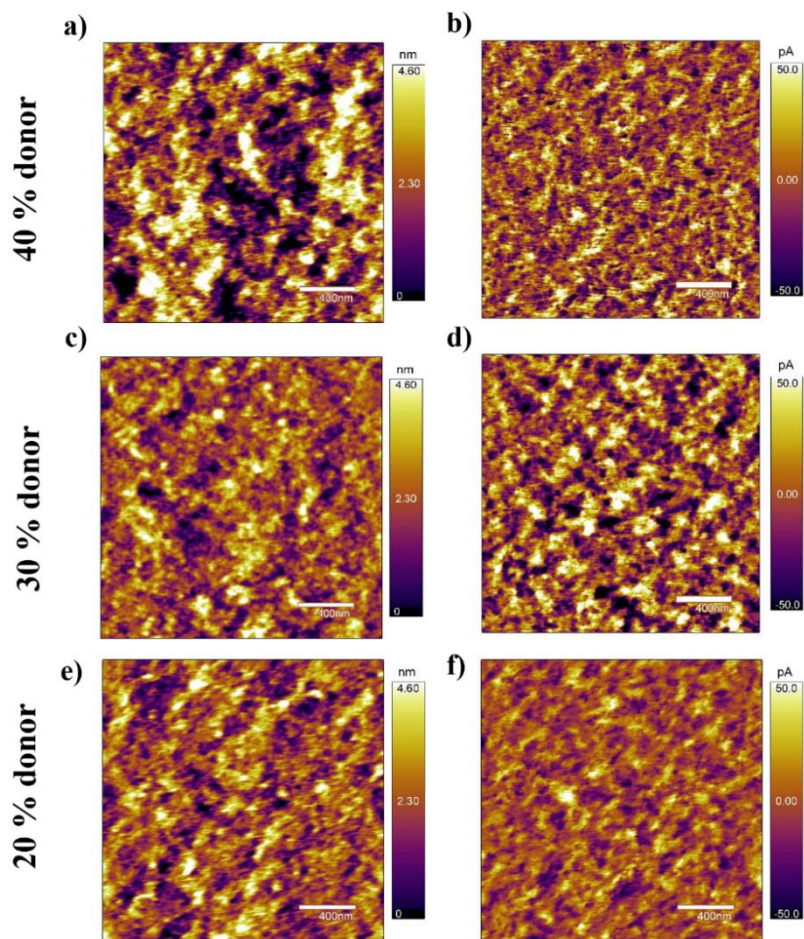
Figure S7.3. 2 μm x 2 μm surface topography (left) and photocurrent images (right) taken at +0.5 V sample bias of the blends with different donor concentrations.

Table S7.1. Roughness Mean Squared (RMS) values obtained from pc-AFM images for the surface roughness and for the current images of representative films.

c(donor)	RMS (nm)	RMS 0 V (pA)	RMS +0.5 V (pA)	RMS +1V (pA)
40%	0.82	4.65	15.41	33.89
30%	0.89	7.02	18.63	37.89
20%	0.82	5.27	12.81	15.94
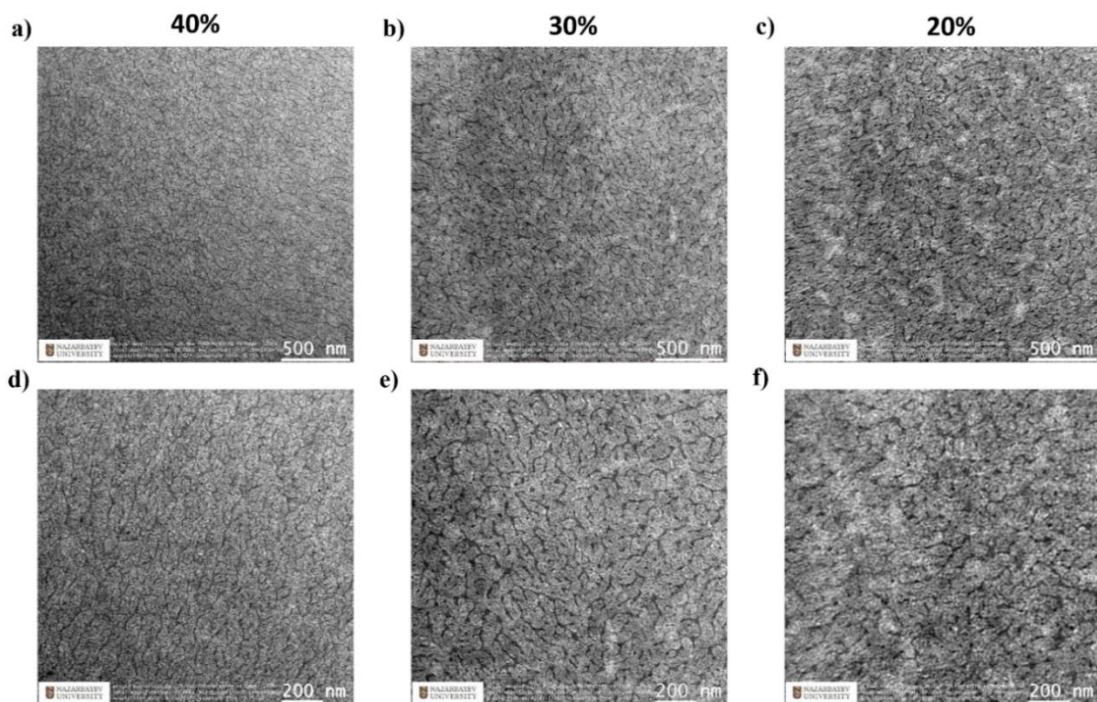
Figure S7.4. TEM images of representative blend films with 40%, 30% and 20% PCE10 donor polymer at 20kx (a-c) and 30kx total magnification (d-f).
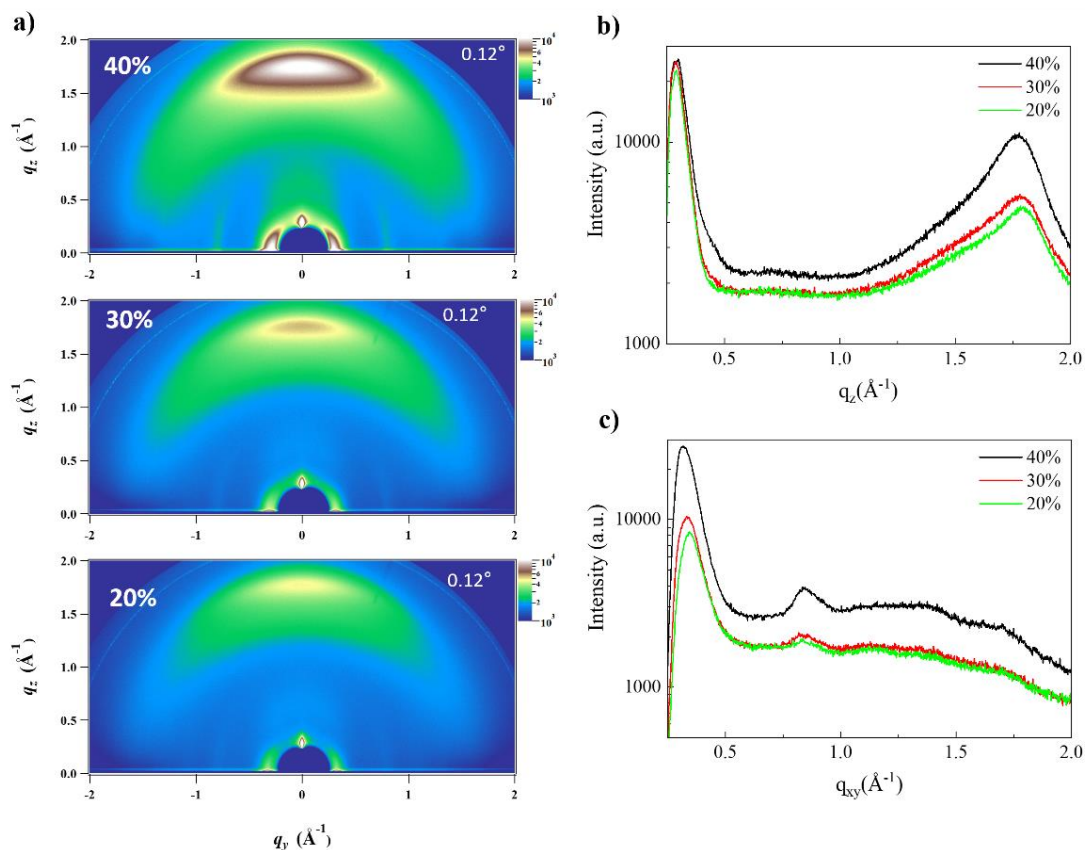
Figure S7.5. a) Scattering Intensities obtained in a grazing incidence angle of 0.12° for the 40%, 30% and 20% donor blends. b) GIWAXs 1D-linecuts showing the scattered intensity in the q_z plane, perpendicular to the substrate. c) GIWAXs 1D-linecuts showing the scattered intensity in the q_{xy} plane (parallel to the substrate).

Table S7.2. Peak positions, FWHM, lamellar packing lattice distance and crystallite size.

Out-of-plane		Peak (Å^{-1})	FWHM (Å^{-1})	Lattice (nm)	Size (nm)
40wt%	[100]	0.296	0.071	2.122	8.843
	π-π	1.775	0.209	0.354	3.009
30wt%	[100]	0.292	0.068	2.154	9.292
	π-π	1.788	0.206	0.351	3.055
20wt%	[100]	0.293	0.065	2.147	9.674
	π-π	1.790	0.210	0.351	2.988

Table S7.3. Series and shunt resistance, ideality coefficient n, and reverse bias dark current J_0 in dependance on the donor concentration of the studied PCE10:COTIC-4F devices. Sample sizes for the analysis are $n_s = 8$.

c(*donor*)	R_s (Ω cm²)	R_{shunt} (Ω cm²)	n	J_0 (mA/cm²)
40%	1.87 ± 0.06	(5.56 ± 6.09) · 10^4	1.33 ± 0.04	(2.64 ± 1.30) · 10^{-7}
30%	1.69 ± 0.21	(5.66 ± 2.59) · 10^4	1.38 ± 0.03	(4.89 ± 2.19) · 10^{-7}
20%	1.71 ± 0.23	(4.28 ± 3.38) · 10^4	1.39 ± 0.01	(5.55 ± 1.20) · 10^{-7}
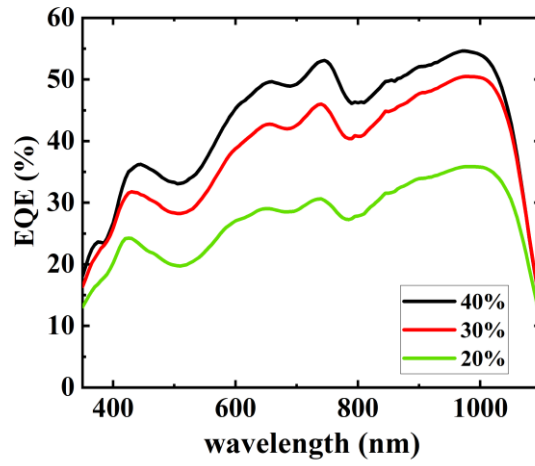
Figure S7.6. EQEs of the studied opaque PCE10:COTIC-4F devices with different donor content.
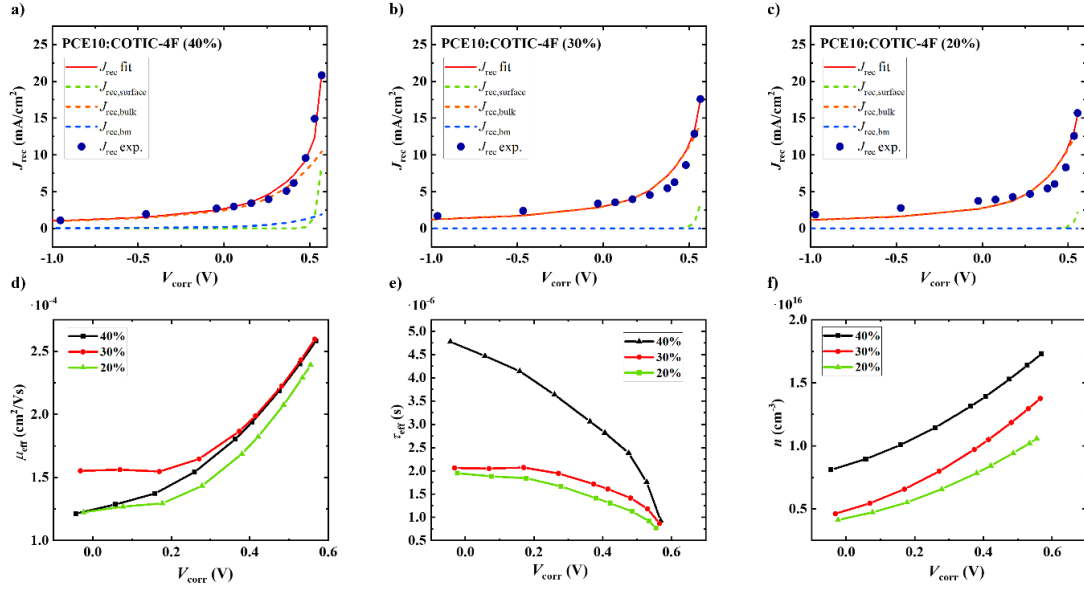
Figure S7.7. a)-c) Fit of the recombination current $J_{rec,fit}$, and its components for surface, bulk, and bimolecular recombination, to the experimental recombination current $J_{rec,exp}$ based on the analysis of capacitance spectra of the different device types with 40%, 30%, and 20% donor. d)-f) The effective mobility μ_{eff}, effective lifetime τ_{eff}, and charge carrier concentration n in dependence on the corrected voltage V_{corr}.

Table S7.4. Device performance of ST-OPV devices with MoOx(7 nm)/Au(10 nm) back electrode, obtained from the fabrication of 8 devices for each blend.

donor (%)	J_{sc} (mA/cm²)	V_{OC} (V)	FF(%)	PCE (%)	AVT$_{stack}$ (%)
40%	-14.14 ± 0.49	0.540 ± 0.002	0.43 ± 0.02	3.27% ± 0.14	41.9
30%	-10.89 ± 0.33	0.555 ± 0.002	0.48 ± 0.01	2.89% ± 0.05	47.1
20%	-7.50 ± 0.44	0.542 0.022	0.40 ± 0.04	1.65% ± 0.26	48.9
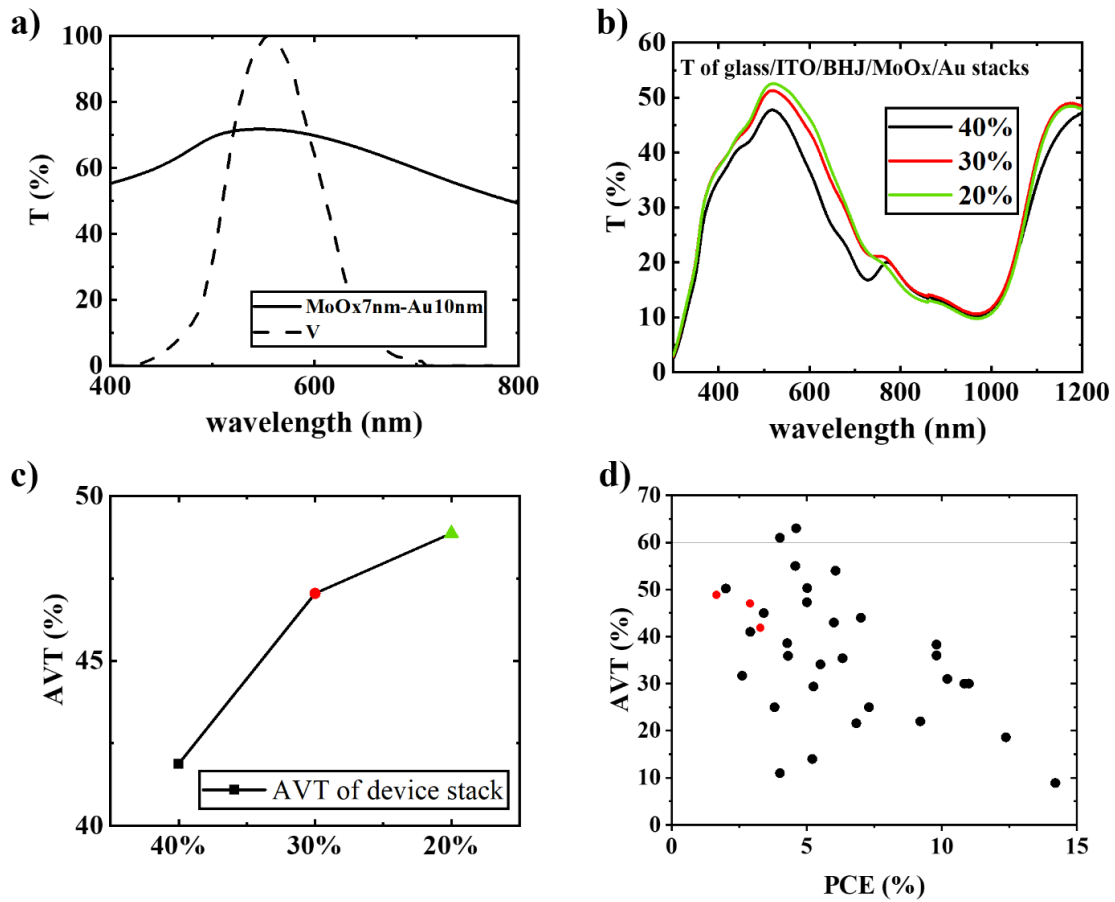
Figure S7.8. a) Transmittance of MoOx/Au gold electrodes in the visible range with different Au thicknesses and photopic response V. b) Experimental transmittance spectra of the device stacks with thin electrodes. c) Experimental AVTs of the device stacks. d) AVTs reported in literature in dependance on the PCE (black) and our work (red), demonstrating the system's potential for ST-OPV applications upon further optimization.
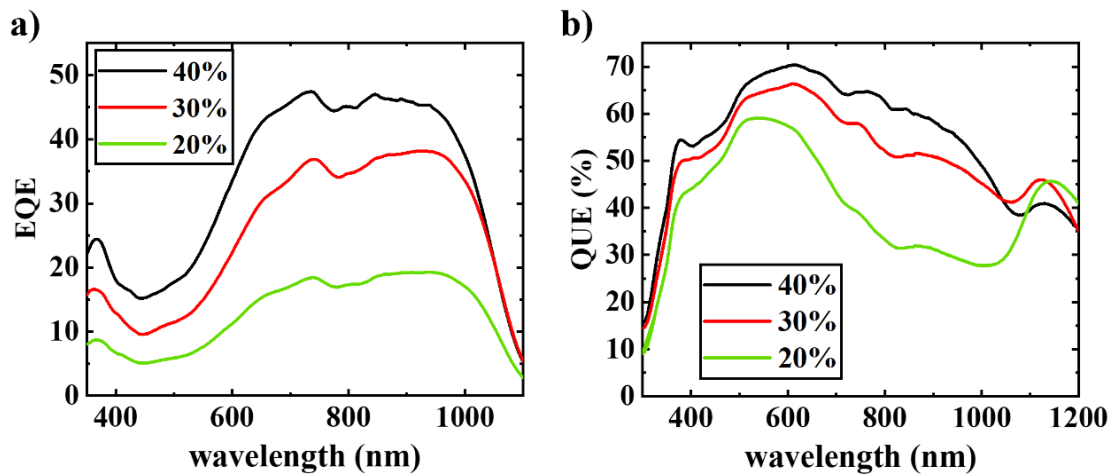
Figure S7.9. a) EQE spectra and b) Quantum Utilization Efficiency QUE for the ST-OPV devices with MoOx/Au electrode.

Summary and Outlook

This thesis work has elucidated various limitations of organic photovoltaics. The working principles of OPVs have been discussed in Chapter 1, followed by the description of various characterization techniques used in OPV research in Chapter 2.

Chapter 3 has focused on the residual cross-coupling catalyst $Pd(PPh_3)_4$ and has shown that small amounts of the catalyst, typically not exceeded after the material purification, do not harm the performance of OPVs significantly. Therefore, we have concluded that residual catalysts traces are not a major concern in the studied PCE10:IOTIC-4F system. Other factors that can lead to batch-to-batch variations are the molecular weight, polydispersity, and other trace impurities. Addressing these factors in the future to understand their influence on the common batch-to-batch-variations may help to achieve higher batch-to-batch reproducibility.

In Chapter 4 we have presented a new approach to unravel the optoelectronic processes under short-circuit conditions. We have shown how to obtain the geminate prefactor P_g, the mobility-lifetime product $\mu\tau$, and the extraction efficiency η, using only standard measurements and simulations. Due to the good agreement with impedance spectroscopy results, we encourage the implementation of the new approach. Since our simple method can predict the optimal device configuration and active layer thickness from a single device, the use of this approach is in particular of interest when the availability of the OPV materials is limited.

Chapter 5 has derived changes in ST-OPVs that are arise from an increased transparency. We have found that a reduced generation of charge carriers and an altered generation rate profile leads to lower Open-circuit Voltages (V_{oc}) and changes in the recombination dynamics. We have further shown that high-purity and low-trap-density active layers are necessary for ST-OPVs and that transparent devices are more sensitive to shunt-leakage. We encourage the exploration of a

wider range of transparent electrodes since the impact of surface recombination and of the series resistance decrease with increased AVT. The insights of this simulation-based study are experimentally not accessible, since no such systematic variation of the optical constants is feasible without alteration of other material parameters. Therefore, this project highlights the importance of combining experiment and simulation to advance the OPV field.

Chapter 6 has investigated the role of the interfacial recombination in the narrow-band gap system PCE10:COTIC-4F. We have shown that ZnO is the most suitable front electrode due to low interfacial recombination, efficient charge extraction, and favorable energy level alignment, contrasting the common notion in the community that ZnO introduces surface traps. This highlights the need for a re-assessment of established device fabrication guidelines when working with narrow band gap OPVs.

In Chapter 7 we have investigated OPVs with highly transparent active layers based on the 'dilute donor approach with high AVT values up to 77%. The systematic dilution of the donor in combination with the near IR acceptor COTIC-4F has resulted in active layers with systematically increased AVT and moderately reduced PCE. This work highlights that highly transparent OPVs are within reach and that existing narrow band gap systems can be modified and tuned to meet application-specific transparency requirements.

All in all, this work has given insights into opaque and transparent OPV systems and has provided the reader with an in-depth understanding of the processes and limitation of the different devices. Moreover, it has outlined guidelines and approaches for the fabrication and characterization of OPVs. Based on the vast progress in the OPV field in recent years, a more widespread application is expected to occur as soon as the few remaining challenges, such as long-term stability, temperature-sensitivity, and losses due to up-scaling are addressed and improved.

Bibliography

[1]   U.S. Energy Information Administration, *Annual Energy Outlook 2022 (AEO2022)*, **2022**.

[2]   "EIA projects that renewable generation will supply 44% of U.S. electricity by 2050," can be found under https://www.eia.gov/todayinenergy/detail.php?id=51698, **2022**.

[3]   U.S. Energy Information Administration, "Coal explained," can be found under https://www.eia.gov/energyexplained/coal/, **2022**.

[4]   J. M. K. O'Keefe, A. Bechtel, K. Christanis, S. Dai, W. A. DiMichele, C. F. Eble, J. S. Esterle, M. Mastalerz, A. L. Raymond, B. V. Valentim, N. J. Wagner, C. R. Ward, J. C. Hower, *International Journal of Coal Geology* **2013**, *118*, 58.

[5]   E. Amster, C. Lew Levy, *International Journal of Environmental Research and Public Health* **2019**, *16*, 2008.

[6]   R. B. Finkelman, L. Tian, *International Geology Review* **2018**, *60*, 579.

[7]   S. M. Melody, F. H. Johnston, *International Journal of Coal Geology* **2015**, *152*, 1.

[8]   U.S. Energy Information Administration, "Where our natural gas comes from," can be found under https://www.eia.gov/energyexplained/natural-gas/where-our-natural-gas-comes-from.php, **2022**.

[9]   U.S. Energy Information Administration, "Nuclear explained," can be found under https://www.eia.gov/energyexplained/nuclear/, **2022**.

[10]   N. Muellner, N. Arnold, K. Gufler, W. Kromp, W. Renneberg, W. Liebert, *Energy Policy* **2021**, *155*, 112363.

[11]   K. Saidi, A. Omri, *Progress in Nuclear Energy* **2020**, *126*, 103425.

[12]   J. Markard, N. Bento, N. Kittner, A. Nuñez-Jimenez, *Energy Research & Social Science* **2020**, *67*, 101512.

[13]   "Fallout from the Chernobyl Nuclear Disaster and Congenital Malformations in Europe: Archives of Environmental Health: An International Journal: Vol 56, No 6," can be found under https://www.tandfonline.com/doi/abs/10.1080/00039890109602895, **2010**.

[14]   "Chernobyl Disaster: Cancer following the Accident at the Chernobyl Nuclear Power Plant," can be found under https://academic.oup.com/epirev/article/27/1/56/520833, **2005**.

[15]   N. Behling, M. C. Williams, T. G. Behling, S. Managi, *Energy Policy* **2019**, *126*, 411.

[16]   J. Shigemura, T. Terayama, M. Kurosawa, Y. Kobayashi, H. Toda, M. Nagamine, A. Yoshino, *CNS Spectrums* **2021**, *26*, 14.

[17]   "The true long-term cost of nuclear power," can be found under https://environment-review.yale.edu/true-long-term-cost-nuclear-power, **2019**.

[18]   J. F. Ahearne, *Risk Analysis* **2000**, *20*, 763.

[19]   McKinsey, "How global business could mitigate climate change," can be found under https://www.mckinsey.com/capabilities/sustainability/our-insights/climate-math-what-a-1-point-5-degree-pathway-would-take, **2020**.

[20]   Q. You, Z. Jiang, X. Yue, W. Guo, Y. Liu, J. Cao, W. Li, F. Wu, Z. Cai, H. Zhu, T. Li, Z. Liu, J. He, D. Chen, N. Pepin, P. Zhai, *npj Clim Atmos Sci* **2022**, *5*, 1.

[21]   P. A. Owusu, S. Asumadu-Sarkodie, *Cogent Engineering* **2016**, *3*, 1167990.

[22]   A. Raza, A. Razzaq, S. S. Mehmood, X. Zou, X. Zhang, Y. Lv, J. Xu, *Plants* **2019**, *8*, 34.

[23]   A. M. Vicedo-Cabrera, N. Scovronick, F. Sera, D. Royé, R. Schneider, A. Tobias, C. Astrom, Y. Guo, Y. Honda, D. M. Hondula, R. Abrutzky, S. Tong, M. de S. Z. S. Coelho, P. H. N. Saldiva, E. Lavigne, P. M. Correa, N. V. Ortega, H. Kan, S. Osorio, J. Kyselý, A. Urban, H. Orru, E. Indermitte, J. J. K. Jaakkola, N. Ryti, M. Pascal, A. Schneider, K. Katsouyanni, E. Samoli, F. Mayvaneh, A. Entezari, P. Goodman, A. Zeka, P. Michelozzi, F. de'Donato, M. Hashizume, B. Alahmad, M. H. Diaz, C. D. L. C. Valencia, A. Overcenco, D. Houthuijs, C. Ameling, S. Rao,

F. Di Ruscio, G. Carrasco-Escobar, X. Seposo, S. Silva, J. Madureira, I. H. Holobaca, S. Fratianni, F. Acquaotta, H. Kim, W. Lee, C. Iniguez, B. Forsberg, M. S. Ragettli, Y. L. L. Guo, B. Y. Chen, S. Li, B. Armstrong, A. Aleman, A. Zanobetti, J. Schwartz, T. N. Dang, D. V. Dung, N. Gillett, A. Haines, M. Mengel, V. Huber, A. Gasparrini, *Nat. Clim. Chang.* **2021**, *11*, 492.

[24]   S. D. Ahmed, F. S. M. Al-Ismail, M. Shafiullah, F. A. Al-Sulaiman, I. M. El-Amin, *IEEE Access* **2020**, *8*, 10857.

[25]   G. M. Joselin Herbert, S. Iniyan, E. Sreevalsan, S. Rajapandian, *Renewable and Sustainable Energy Reviews* **2007**, *11*, 1117.

[26]   G. Msigwa, J. O. Ighalo, P.-S. Yap, *Science of The Total Environment* **2022**, *849*, 157755.

[27]   J.-É. Klimpt, C. Rivero, H. Puranen, F. Koch, *Energy Policy* **2002**, *30*, 1305.

[28]   A. M. Bagher, M. Vahid, M. Mohsen, D. Parvin, **2015**.

[29]   J. D. C. Little, *OR* **1955**, *3*, 187.

[30]   T. Moeller, J. C. Bailar, J. Kleinberg, C. O. Guss, M. E. Castellion, C. Metz, in *Chemistry*, Academic Press, **1980**, pp. 197–231.

[31]   E. Weston, *UNITED STATES PATENT OFFICE.*, **1888**, US389124A.

[32]   B. Zaidi, *Solar Panels and Photovoltaic Materials*, BoD – Books On Demand, **2018**.

[33]   W. Tress, *Organic Solar Cells: Theory, Experiment, and Device Simulation*, Springer, **2014**.

[34]   V. Petrova-Koch, Ed., *High-Efficient Low-Cost Photovoltaics: Recent Developments*, Springer, Berlin Heidelberg, **2009**.

[35]   R. A. Marques Lameirinhas, J. P. N. Torres, J. P. de Melo Cunha, *Energies* **2022**, *15*, 1823.

[36]   M. V. Dambhare, B. Butey, S. V. Moharil, *J. Phys.: Conf. Ser.* **2021**, *1913*, 012053.

[37]   NREL, "Best Research-Cell Efficiency Chart," can be found under https://www.nrel.gov/pv/cell-efficiency.html, **2022**.

[38] M. Woodhouse, D. Feldman, R. Fu, K. Horowitz, D. Chung, *On the Path to SunShot: The Role of Advancements in Solar Photovoltaic Efficiency, Reliability, and Costs*, **2016**.

[39] "Documenting a Decade of Cost Declines for PV Systems," can be found under https://www.nrel.gov/news/program/2021/documenting-a-decade-of-cost-declines-for-pv-systems.html, **2021**.

[40] C. Ballif, F.-J. Haug, M. Boccard, P. J. Verlinden, G. Hahn, *Nat Rev Mater* **2022**, *7*, 597.

[41] A. H. Alami, M. Ramadan, M. A. Abdelkareem, J. J. Alghawi, N. T. Alhattawi, H. A. Mohamad, A.-G. Olabi, *Thermal Science and Engineering Progress* **2022**, *29*, 101208.

[42] V. V. Brus, J. Lee, B. R. Luginbuhl, S.-J. Ko, G. C. Bazan, T.-Q. Nguyen, *Advanced Materials* **2019**, *31*, 1900904.

[43] G. Apostolou, A. H. M. E. Reinders, *Energy Technology* **2014**, *2*, 229.

[44] C. Egbon, A. Oyekola, T.-T. Lie, in *2018 Australasian Universities Power Engineering Conference (AUPEC)*, **2018**, pp. 1–6.

[45] M. Esmailzadeh, S. Noori, A. Aliahmadi, H. Nouralizadeh, M. Bogers, *Sustainability* **2020**, *12*, 2049.

[46] S. Lizin, S. Van Passel, E. De Schepper, L. Vranken, *Solar Energy Materials and Solar Cells* **2012**, *103*, 1.

[47] P. Shapira, J. Youtie, in *Green Processes for Nanotechnology: From Inorganic to Bioinspired Nanomaterials* (Eds.: V. A. Basiuk, E. V. Basiuk), Springer International Publishing, Cham, **2015**, pp. 409–434.

[48] M. A. A. Mamun, P. Dargusch, D. Wadley, N. A. Zulkarnain, A. A. Aziz, *Renewable and Sustainable Energy Reviews* **2022**, *161*, 112351.

[49] R. Waller, M. Kacira, E. Magadley, M. Teitel, I. Yehia, *AgriEngineering* **2022**, *4*, 969.

[50] J. Xue, *Renewable and Sustainable Energy Reviews* **2017**, *73*, 1.

[51]   E. Ravishankar, M. Charles, Y. Xiong, R. Henry, J. Swift, J. Rech, J. Calero, S. Cho, R. E. Booth, T. Kim, A. H. Balzer, Y. Qin, C. Hoi Yi Ho, F. So, N. Stingelin, A. Amassian, C. Saravitz, W. You, H. Ade, H. Sederoff, B. T. O'Connor, *Cell Reports Physical Science* **2021**, *2*, 100381.

[52]   C. J. M. Emmott, J. A. Röhr, M. Campoy-Quiles, T. Kirchartz, A. Urbina, N. J. Ekins-Daukes, J. Nelson, *Energy & Environmental Science* **2015**, *8*, 1317.

[53]   E. Ravishankar, R. E. Booth, C. Saravitz, H. Sederoff, H. W. Ade, B. T. O'Connor, *Joule* **2020**, *4*, 490.

[54]   F. Hussin, G. Issabayeva, M. K. Aroua, *Reviews in Chemical Engineering* **2018**, *34*, 503.

[55]   N. Schopp, V. V. Brus, *Energies* **2022**, *15*, 4639.

[56]   S. O. Kasap, *Principles of Electronic Materials and Devices*, Tata McGraw-Hill, **2006**.

[57]   First Solar, "Our Technology," can be found under https://www.firstsolar.com:443/Technology/CadTel, **2023**.

[58]   S. Johnston, C. Xiao, M. G. Deceglie, A. Gaulding, C.-S. Jiang, H. Guthrey, D. B. Kern, G. F. Kroeger, M. Al-Jassim, I. L. Repins, in *2021 IEEE 48th Photovoltaic Specialists Conference (PVSC)*, **2021**, pp. 2276–2278.

[59]   Market Watch, "CdTe Thin Film Solar Cell Market Size, Latest Trends, Share, Top Players, Revenue and Forecast 2028," can be found under https://www.marketwatch.com/press-release/cdte-thin-film-solar-cell-market-size-latest-trends-share-top-players-revenue-and-forecast-2028-2023-01-09, **2023**.

[60]   B. J. Stanbery, D. Abou-Ras, A. Yamada, L. Mansfield, *J. Phys. D: Appl. Phys.* **2021**, *55*, 173001.

[61]   B. J. Stanbery, *Critical Reviews in Solid State and Materials Sciences* **2002**, *27*, 73.

[62]   B. Gai, Y. Sun, H. Lim, H. Chen, J. Faucher, M. L. Lee, J. Yoon, *ACS Nano* **2017**, *11*, 992.

[63]   Q. Xue, R. Xia, C. J. Brabec, H.-L. Yip, *Energy & Environmental Science* **2018**, *11*, 1688.

[64]   V. V. Brus, F. Lang, J. Bundesmann, S. Seidel, A. Denker, B. Rech, G. Landi, H. C. Neitzert, J. Rappich, N. H. Nickel, *Advanced Electronic Materials* **2017**, *3*, 1600438.

[65]   V. V. Brus, J. Lee, B. R. Luginbuhl, S.-J. Ko, G. C. Bazan, T.-Q. Nguyen, *Advanced Materials* **2019**, *31*, 1970219.

[66]   Y. Cui, C. Yang, H. Yao, J. Zhu, Y. Wang, G. Jia, F. Gao, J. Hou, *Advanced Materials* **2017**, *29*, 1703080.

[67]   A. Anctil, E. Lee, R. R. Lunt, *Applied Energy* **2020**, *261*, 114429.

[68]   C. Ballif, L.-E. Perret-Aebi, S. Lufkin, E. Rey, *Nature Energy* **2018**, *3*, 438.

[69]   E. Biyik, M. Araz, A. Hepbasli, M. Shahrestani, R. Yao, L. Shao, E. Essah, A. C. Oliveira, T. del Caño, E. Rico, J. L. Lechón, L. Andrade, A. Mendes, Y. B. Atlı, *Engineering Science and Technology, an International Journal* **2017**, *20*, 833.

[70]   W. Brütting, *Physics of Organic Semiconductors*, John Wiley & Sons, **2006**.

[71]   Y. Hu, Z. D. Rengert, C. McDowell, M. J. Ford, M. Wang, A. Karki, A. T. Lill, G. C. Bazan, T.-Q. Nguyen, *ACS nano* **2018**, *12*, 3938.

[72]   B. Amna, H. M. Siddiqi, A. Hassan, T. Ozturk, *RSC Adv.* **2020**, *10*, 4322.

[73]   M. Volmer, *Annalen der Physik* **1913**, *345*, 775.

[74]   "The Nobel Prize in Chemistry 2000," can be found under https://www.nobelprize.org/prizes/chemistry/2000/summary/, **2023**.

[75]   A. Köhler, H. Bässler, *Electronic Processes in Organic Semiconductors: An Introduction*, Wiley-VCH Verlag GmbH & Co. KGaA, Weinheim, Germany, **2015**.

[76]   W. R. Salaneck, R. H. Friend, J. L. Brédas, *Physics Reports* **1999**, *319*, 231.

[77]   P. W. Atkins, R. S. Friedman, *Molecular Quantum Mechanics*, OUP Oxford, **2011**.

[78]   D. Liu, B. Kan, X. Ke, N. Zheng, Z. Xie, D. Lu, Y. Liu, *Advanced Energy Materials* **2018**, *8*, 1801618.

[79] R. A. Street, *Advanced Materials* **2016**, *28*, 3814.

[80] I. J. Curtin, D. W. Blaylock, R. J. Holmes, *Appl. Phys. Lett.* **2016**, *108*, 163301.

[81] M. P. Hughes, K. D. Rosenthal, N. A. Ran, M. Seifrid, G. C. Bazan, T.-Q. Nguyen, *Advanced Functional Materials* **2018**, *28*, 1801542.

[82] S. Torabi, F. Jahani, I. V. Severen, C. Kanimozhi, S. Patil, R. W. A. Havenith, R. C. Chiechi, L. Lutsen, D. J. M. Vanderzande, T. J. Cleij, J. C. Hummelen, L. J. A. Koster, *Advanced Functional Materials* **2015**, *25*, 150.

[83] A. L. Ayzner, C. J. Tassone, S. H. Tolbert, B. J. Schwartz, *J. Phys. Chem. C* **2009**, *113*, 20050.

[84] J. A. Bartelt, Z. M. Beiley, E. T. Hoke, W. R. Mateker, J. D. Douglas, B. A. Collins, J. R. Tumbleston, K. R. Graham, A. Amassian, H. Ade, J. M. J. Fréchet, M. F. Toney, M. D. McGehee, *Advanced Energy Materials* **2013**, *3*, 364.

[85] A. Armin, W. Li, O. J. Sandberg, Z. Xiao, L. Ding, J. Nelson, D. Neher, K. Vandewal, S. Shoaee, T. Wang, H. Ade, T. Heumüller, C. Brabec, P. Meredith, *Advanced Energy Materials* **2021**, *11*, 2003570.

[86] P. W. M. Blom, V. D. Mihailetchi, L. J. A. Koster, D. E. Markov, *Advanced Materials* **2007**, *19*, 1551.

[87] S. R. Cowan, A. Roy, A. J. Heeger, *Phys. Rev. B* **2010**, *82*, 245207.

[88] D. J. Lee, D. K. Heo, C. Yun, Y. H. Kim, M. H. Kang, *ECS J. Solid State Sci. Technol.* **2019**, *8*, Q32.

[89] C. Zhu, J. Yuan, F. Cai, L. Meng, H. Zhang, H. Chen, J. Li, B. Qiu, H. Peng, S. Chen, Y. Hu, C. Yang, F. Gao, Y. Zou, Y. Li, *Energy Environ. Sci.* **2020**, *13*, 2459.

[90] V. V. Brus, M. I. Ilashchuk, I. G. Orletskyi, M. M. Solovan, G. P. Parkhomenko, I. S. Babichuk, N. Schopp, G. O. Andrushchak, A. I. Mostovyi, P. D. Maryanchuk, *Nanotechnology* **2020**, *31*, 505706.

[91] A. Karki, J. Vollbrecht, A. J. Gillett, S. Shuyong Xiao, Y. Yang, Z. Peng, N. Schopp, A. L. Dixon, S. Yoon, M. Schrock, H. Ade, G. N. Manjunatha Reddy, R. H. Friend, T.-Q. Nguyen, *Energy & Environmental Science* **2020**, *13*, 3679.

[92] T.-Y. Huang, H. Yan, M. Abdelsamie, V. Savikhin, S. A. Schneider, N. A. Ran, T.-Q. Nguyen, G. C. Bazan, M. F. Toney, *RSC advances* **2019**, *9*, 4106.

[93] A. Karki, J. Vollbrecht, A. L. Dixon, N. Schopp, M. Schrock, G. N. M. Reddy, T.-Q. Nguyen, *Advanced Materials* **2019**, *31*, 1903868.

[94] A. Kahn, *Mater. Horiz.* **2015**, *3*, 7.

[95] C. M. Proctor, S. Albrecht, M. Kuik, D. Neher, T.-Q. Nguyen, *Advanced Energy Materials* **2014**, *4*, 1400230.

[96] J. G. Müller, J. M. Lupton, J. Feldmann, U. Lemmer, M. C. Scharber, N. S. Sariciftci, C. J. Brabec, U. Scherf, *Phys. Rev. B* **2005**, *72*, 195208.

[97] N. Schopp, V. V. Brus, J. Lee, G. C. Bazan, T.-Q. Nguyen, *Advanced Energy Materials* **2021**, *11*, 2002760.

[98] L. Perdigón-Toro, H. Zhang, A. Markina, J. Yuan, S. M. Hosseini, C. M. Wolff, G. Zuo, M. Stolterfoht, Y. Zou, F. Gao, D. Andrienko, S. Shoaee, D. Neher, *Advanced Materials* **2020**, *32*, 1906763.

[99] V. V. Brus, *Organic Electronics* **2016**, *29*, 1.

[100] V. V. Brus, N. Schopp, S.-J. Ko, J. Vollbrecht, J. Lee, A. Karki, G. C. Bazan, T.-Q. Nguyen, *Advanced Energy Materials* **2021**, *11*, 2003091.

[101] J. Vollbrecht, J. Lee, S.-J. Ko, V. V. Brus, A. Karki, W. Le, M. Seifrid, M. J. Ford, K. Cho, G. C. Bazan, T.-Q. Nguyen, *J. Mater. Chem. C* **2020**, *8*, 15175.

[102] R. A. Street, M. Schoendorf, in *2010 35th IEEE Photovoltaic Specialists Conference*, **2010**, pp. 000079–000084.

[103] Z. Chen, T. Wang, Z. Wen, P. Lu, W. Qin, H. Yin, X.-T. Hao, *ACS Energy Lett.* **2021**, 3203.

[104] S. R. Cowan, W. L. Leong, N. Banerji, G. Dennler, A. J. Heeger, *Advanced Functional Materials* **2011**, *21*, 3083.

[105] O. V. Mikhnenko, M. Kuik, J. Lin, N. van der Kaap, T.-Q. Nguyen, P. W. Blom, *Advanced Materials* **2014**, *26*, 1912.

[106] R. S. Gurney, D. G. Lidzey, T. Wang, *Rep. Prog. Phys.* **2019**, *82*, 036601.

[107] G. Binnig, C. F. Quate, Ch. Gerber, *Phys. Rev. Lett.* **1986**, *56*, 930.

[108] F. J. Giessibl, *Rev. Mod. Phys.* **2003**, *75*, 949.

[109] Á. S. Paulo, R. García, *Phys. Rev. B* **2002**, *66*, 041406.

[110] Á. S. Paulo, R. García, *Phys. Rev. B* **2001**, *64*, 193411.

[111] "Gwyddion," can be found under http://gwyddion.net/, **2022**.

[112] N. Schopp, V. V. Brus, J. Lee, A. Dixon, A. Karki, T. Liu, Z. Peng, K. R. Graham, H. Ade, G. C. Bazan, T.-Q. Nguyen, *Advanced Functional Materials* **2021**, *31*, 2009363.

[113] X.-D. Dang, A. B. Tamayo, J. Seo, C. V. Hoven, B. Walker, T.-Q. Nguyen, *Advanced Functional Materials* **2010**, *20*, 3314.

[114] D. C. Coffey, O. G. Reid, D. B. Rodovsky, G. P. Bartholomew, D. S. Ginger, *Nano Lett.* **2007**, *7*, 738.

[115] N. Schopp, G. Akhtanova, P. Panoy, A. Arbuz, S. Chae, A. Yi, H. J. Kim, V. Promarak, T.-Q. Nguyen, V. V. Brus, *Advanced Materials* **2022**, *34*, 2203796.

218

[116]   A. Mahmood, J.-L. Wang, *Solar RRL* **2020**, *4*, 2000337.

[117]   C. D. Liman, S. Choi, D. W. Breiby, J. E. Cochran, M. F. Toney, E. J. Kramer, M. L. Chabinyc, *J. Phys. Chem. B* **2013**, *117*, 14557.

[118]   C. Wang, C. Zuo, Q. Chen, L. Ding, *J. Semicond.* **2021**, *42*, 060201.

[119]   "Electron Microscopy Tutorial," can be found under https://advanced-microscopy.utah.edu/education/electron-micro/, **2011**.

[120]   C. Y. Tang, Z. Yang, in *Membrane Characterization* (Eds.: N. Hilal, A. F. Ismail, T. Matsuura, D. Oatley-Radcliffe), Elsevier, **2017**, pp. 145–159.

[121]   M. Winey, J. B. Meehl, E. T. O'Toole, T. H. Giddings, *MBoC* **2014**, *25*, 319.

[122]   C. Wang, B. Watts, T. Araki, H. Ade, A. Hexemer, A. Garcia, T.-Q. Nguyen, G. Bazan, K. Sohn, E. Kramer, in *APS Southeastern Section Meeting Abstracts*, **2008**.

[123]   F. Liu, M. A. Brady, C. Wang, *European Polymer Journal* **2016**, *81*, 555.

[124]   H. Ade, C. Wang, A. Garcia, H. Yan, K. Sohn, A. Hexemer, G. Bazan, T.-Q. Nguyen, E. Kramer, *Journal of Polymer Science Part B: Polymer Physics* **2009**, *47*, 1291.

[125]   Y. I. Uhanov, *Optical Properties of Semiconductors*, Nauka, Moscow, **1977**.

[126]   B. M. Tissue, in *Characterization of Materials*, John Wiley & Sons, Ltd, **2002**.

[127]   J. I. Pankove, *Optical Processes in Semiconductors*, Prentice-Hall, **1971**.

[128]   H. Ishii, K. Seki, *IEEE Transactions on Electron Devices* **1997**, *44*, 1295.

[129]   R. Kerremans, C. Kaiser, W. Li, N. Zarrabi, P. Meredith, A. Armin, *Advanced Optical Materials* **2020**, *8*, 2000319.

[130]   G. F. Burkhard, E. T. Hoke, M. D. McGehee, *Adv. Mater.* **2010**, *22*, 3293.

[131]   K. Hinrichs, K.-J. Eichhorn, Eds., *Ellipsometry of Functional Organic Surfaces and Films*, Springer Berlin Heidelberg, New York, NY, **2018**.

[132]   J.A. Woollam, "Ellipsometry Measurements," **2022**.

[133] M. Dressel, B. Gompf, D. Faltermeier, A. K. Tripathi, J. Pflaum, M. Schubert, *Opt. Express, OE* **2008**, *16*, 19770.

[134] M. Losurdo, M. M. Giangregorio, P. Capezzuto, G. Bruno, F. Babudri, D. Colangiuli, G. M. Farinola, F. Naso, *Synthetic Metals* **2003**, *138*, 49.

[135] J. Bergqvist, H. Arwin, O. Inganäs, *ACS Photonics* **2018**, *5*, 3023.

[136] V. V. Brus, C. M. Proctor, N. A. Ran, T.-Q. Nguyen, *Advanced Energy Materials* **2016**, *6*, 1502250.

[137] J. Vollbrecht, V. V. Brus, S.-J. Ko, J. Lee, A. Karki, D. X. Cao, K. Cho, G. C. Bazan, T.-Q. Nguyen, *Advanced Energy Materials* **2019**, 1901438.

[138] P. Caprioglio, M. Stolterfoht, C. M. Wolff, T. Unold, B. Rech, S. Albrecht, D. Neher, *Advanced Energy Materials* **2019**, *9*, 1901631.

[139] L. Jiang, J. H. Lyou, S. Rane, E. A. Schiff, Q. Wang, Q. Yuan, *MRS Proc.* **2000**, *609*, A18.3.

[140] P. Hartnagel, S. Ravishankar, B. Klingebiel, O. Thimm, T. Kirchartz, *Advanced Energy Materials*, 2300329.

[141] A. Karki, G.-J. A. Wetzelaer, G. N. M. Reddy, V. Nádaždy, M. Seifrid, F. Schauer, G. C. Bazan, B. F. Chmelka, P. W. Blom, T.-Q. Nguyen, *Advanced Functional Materials* **2019**, *29*, 1901109.

[142] C. Kaiser, O. J. Sandberg, N. Zarrabi, W. Li, P. Meredith, A. Armin, *Nat Commun* **2021**, *12*, 3988.

[143] ThermoFischer Scientific, "Ultraviolet Photoelectron Spectroscopy," can be found under https://www.thermofisher.com/us/en/home/materials-science/learning-center/surface-analysis/uv-photoelectron-spectroscopy.html, **2022**.

[144] S. Olthof, *Advanced Optical Materials* **2021**, *9*, 2100227.

[145] "Surface Spectroscopy: UPS vs XPS," can be found under https://www.azooptics.com/Article.aspx?ArticleID=1316, **2018**.

[146] N. Elgrishi, K. J. Rountree, B. D. McCarthy, E. S. Rountree, T. T. Eisenhart, J. L. Dempsey, *J. Chem. Educ.* **2018**, *95*, 197.

[147] R. G. Compton, C. E. Banks, *Understanding Voltammetry*, World Scientific, **2007**.

[148] C. G. Zoski, *Handbook of Electrochemistry*, Elsevier, **2007**.

[149] S. Janietz, D. D. C. Bradley, M. Grell, C. Giebeler, M. Inbasekaran, E. P. Woo, *Appl. Phys. Lett.* **1998**, *73*, 2453.

[150] S. Admassie, O. Inganäs, W. Mammo, E. Perzon, M. R. Andersson, *Synthetic Metals* **2006**, *156*, 614.

[151] J. L. Bredas, R. Silbey, D. S. Boudreaux, R. R. Chance, *J. Am. Chem. Soc.* **1983**, *105*, 6555.

[152] J. Pei, W.-L. Yu, J. Ni, Y.-H. Lai, W. Huang, A. J. Heeger, *Macromolecules* **2001**, *34*, 7241.

[153] S. N. Inamdar, P. P. Ingole, S. K. Haram, *ChemPhysChem* **2008**, *9*, 2574.

[154] J.-H. Tsai, W.-R. Tu, C.-L. Liu, W.-C. Wu, W.-C. Chen, *Polym. J.* **2009**, *41*, 363.

[155] P. T. Kissinger, W. R. Heineman, *Journal of Chemical Education* **1983**, *60*, 5.

[156] J. Kurpiers, T. Ferron, S. Roland, M. Jakoby, T. Thiede, F. Jaiser, S. Albrecht, S. Janietz, B. A. Collins, I. A. Howard, D. Neher, *Nat Commun* **2018**, *9*, 1.

[157] D. Credgington, F. C. Jamieson, B. Walker, T.-Q. Nguyen, J. R. Durrant, *Advanced Materials* **2012**, *24*, 2135.

[158] R. A. Street, S. Cowan, A. J. Heeger, *Phys. Rev. B* **2010**, *82*, 121301.

[159] L. J. A. Koster, V. D. Mihailetchi, R. Ramaker, P. W. M. Blom, *Applied Physics Letters* **2005**, *86*, 123509.

[160] E. von Hauff, *J. Phys. Chem. C* **2019**, *123*, 11329.

[161] V. V. Brus, *Semicond. Sci. Technol.* **2012**, *27*, 035024.

[162] L. A. A. Pettersson, L. S. Roman, O. Inganäs, *Journal of Applied Physics* **1999**, *86*, 487.

[163] G. F. Burkhard, E. T. Hoke, M. Group, **2011**, 6.

[164]   George F. Burkhard, Eric T. Hoke, Kamil Mielczarek, "Transfer Matrix Python Code," can   be   found   under https://github.com/erichoke/Stanford/blob/8305770167003daf164891f98d2a811344049653/ TransferMatrix_Python/transfermatrix.py, **2010**.

[165]   B. Fan, D. Zhang, M. Li, W. Zhong, Z. Zeng, L. Ying, F. Huang, Y. Cao, *Sci. China Chem.* **2019**, *62*, 746.

[166]   P. Cheng, G. Li, X. Zhan, Y. Yang, *Nature Photon* **2018**, *12*, 131.

[167]   A. Wadsworth, M. Moser, A. Marks, M. S. Little, N. Gasparini, C. J. Brabec, D. Baran, I. McCulloch, *Chem. Soc. Rev.* **2019**, *48*, 1596.

[168]   Y. Hu, D. X. Cao, A. T. Lill, L. Jiang, C.-A. Di, X. Gao, H. Sirringhaus, T.-Q. Nguyen, *Advanced Electronic Materials* **2018**, *4*, 1800175.

[169]   Q. Liu, Y. Jiang, K. Jin, J. Qin, J. Xu, W. Li, J. Xiong, J. Liu, Z. Xiao, K. Sun, S. Yang, X. Zhang, L. Ding, *Science Bulletin* **2020**, *65*, 272.

[170]   V. V. Brus, J. Lee, B. R. Luginbuhl, S.-J. Ko, G. C. Bazan, T.-Q. Nguyen, *Advanced Materials* **2019**, *31*, 1970219.

[171]   Y. Cui, Y. Wang, J. Bergqvist, H. Yao, Y. Xu, B. Gao, C. Yang, S. Zhang, O. Inganäs, F. Gao, J. Hou, *Nature Energy* **2019**, *4*, 768.

[172]   T. Wang, G. Kupgan, J.-L. Brédas, *Trends in Chemistry* **2020**, DOI 10.1016/j.trechm.2020.03.006.

[173]   T. Zhang, E. Birgersson, J. Luther, *Physica B: Condensed Matter* **2015**, *456*, 267.

[174]   S. Lacic, O. Inganäs, *Journal of Applied Physics* **2005**, *97*, 124901.

[175]   L. J. A. Koster, E. C. P. Smits, V. D. Mihailetchi, P. W. M. Blom, *Phys. Rev. B* **2005**, *72*, 085205.

[176]   W. R. Mateker, M. D. McGehee, *Adv. Mater.* **2017**, *29*, 1603940.

[177] J. H. Bannock, N. D. Treat, M. Chabinyc, N. Stingelin, M. Heeney, J. C. de Mello, *Sci Rep* **2016**, *6*, 1.

[178] A. Biffis, P. Centomo, A. Del Zotto, M. Zecca, *Chem. Rev.* **2018**, *118*, 2249.

[179] L. Lu, T. Zheng, Q. Wu, A. M. Schneider, D. Zhao, L. Yu, *Chem. Rev.* **2015**, *115*, 12666.

[180] S. Li, C.-Z. Li, M. Shi, H. Chen, *ACS Energy Lett.* **2020**, *5*, 1554.

[181] C. Sun, F. Pan, S. Chen, R. Wang, R. Sun, Z. Shang, B. Qiu, J. Min, M. Lv, L. Meng, C. Zhang, M. Xiao, C. Yang, Y. Li, *Advanced Materials* **2019**, *31*, 1905480.

[182] F. Cai, C. Zhu, J. Yuan, Z. Li, L. Meng, W. Liu, H. Peng, L. Jiang, Y. Li, Y. Zou, *Chem. Commun.* **2020**, *56*, 4340.

[183] P. Sonar, E. L. Williams, S. P. Singh, A. Dodabalapur, *Journal of Materials Chemistry* **2011**, *21*, 10532.

[184] J. K. Stille, *Angewandte Chemie International Edition in English* **1986**, *25*, 508.

[185] N. Miyaura, K. Yamada, H. Suginome, A. Suzuki, *J. Am. Chem. Soc.* **1985**, *107*, 972.

[186] E. Negishi, *Acc. Chem. Res.* **1982**, *15*, 340.

[187] K. Sonogashira, *Journal of Organometallic Chemistry* **2002**, *653*, 46.

[188] K. T. Nielsen, K. Bechgaard, F. C. Krebs, *Macromolecules* **2005**, *38*, 658.

[189] F. C. Krebs, R. B. Nyberg, M. Jørgensen, *Chem. Mater.* **2004**, *16*, 1313.

[190] R. Ul Islam, M. J. Witcomb, M. S. Scurrell, E. van der Lingen, W. V. Otterlo, K. Mallick, *Catalysis Science & Technology* **2011**, *1*, 308.

[191] M. P. Nikiforov, B. Lai, W. Chen, S. Chen, R. D. Schaller, J. Strzalka, J. Maser, S. B. Darling, *Energy & Environmental Science* **2013**, *6*, 1513.

[192] L. Kaake, X.-D. Dang, W. L. Leong, Y. Zhang, A. Heeger, T.-Q. Nguyen, *Advanced Materials* **2013**, *25*, 1706.

[193]   S. R. Cowan, W. L. Leong, N. Banerji, G. Dennler, A. J. Heeger, *Advanced Functional Materials* **2011**, *21*, 3083.

[194]   A. Aghassi, C. D. Fay, *Phys. Chem. Chem. Phys.* **2019**, *21*, 13176.

[195]   M. M. Mandoc, F. B. Kooistra, J. C. Hummelen, B. de Boer, P. W. M. Blom, *Appl. Phys. Lett.* **2007**, *91*, 263505.

[196]   W. R. Mateker, J. D. Douglas, C. Cabanetos, I. T. Sachs-Quintana, J. A. Bartelt, E. T. Hoke, A. E. Labban, P. M. Beaujuge, J. M. J. Fréchet, M. D. McGehee, *Energy Environ. Sci.* **2013**, *6*, 2529.

[197]   W. L. Leong, G. C. Welch, L. G. Kaake, C. J. Takacs, Y. Sun, G. C. Bazan, A. J. Heeger, *Chem. Sci.* **2012**, *3*, 2103.

[198]   R. A. Street, A. Krakaris, S. R. Cowan, *Advanced Functional Materials* **2012**, *22*, 4608.

[199]   N. Camaioni, F. Tinti, L. Franco, M. Fabris, A. Toffoletti, M. Ruzzi, L. Montanari, L. Bonoldi, A. Pellegrino, A. Calabrese, R. Po, *Organic Electronics* **2012**, *13*, 550.

[200]   M. Kuik, L. J. A. Koster, G. A. H. Wetzelaer, P. W. M. Blom, *Phys. Rev. Lett.* **2011**, *107*, 256805.

[201]   L. F. Hernández-García, O. Ramírez-Sánchez, V. Cabrera-Arenas, L. M. Reséndiz-Mendoza, *Journal of Computational Electronics* **2016**, *15*, 1103.

[202]   A. Bourdick, M. Reichenberger, A. Stradomska, G. C. Bazan, T.-Q. Nguyen, A. Köhler, S. Gekle, *The Journal of Physical Chemistry B* **2018**, *122*, 9191.

[203]   W. Shockley, W. T. Read, *Phys. Rev.* **1952**, *87*, 835.

[204]   R. N. Hall, *Phys. Rev.* **1952**, *87*, 387.

[205]   W. L. Leong, G. Hernandez-Sosa, S. R. Cowan, D. Moses, A. J. Heeger, *Advanced Materials* **2012**, *24*, 2273.

[206]   J. Schafferhans, A. Baumann, A. Wagenpfahl, C. Deibel, V. Dyakonov, *Organic Electronics* **2010**, *11*, 1693.

[207]   A. Seemann, T. Sauermann, C. Lungenschmied, O. Armbruster, S. Bauer, H.-J. Egelhaaf, J. Hauch, *Solar Energy* **2011**, *85*, 1238.

[208]   A. Weu, J. A. Kress, F. Paulus, D. Becker-Koch, V. Lami, A. A. Bakulin, Y. Vaynzof, *ACS Appl. Energy Mater.* **2019**, *2*, 1943.

[209]   M. Hermenau, M. Riede, K. Leo, S. A. Gevorgyan, F. C. Krebs, K. Norrman, *Solar Energy Materials and Solar Cells* **2011**, *95*, 1268.

[210]   B. Arredondo, B. Romero, M. J. Beliatis, G. del Pozo, D. Martín-Martín, J. C. Blakesley, G. Dibb, F. C. Krebs, S. A. Gevorgyan, F. A. Castro, *Solar Energy Materials and Solar Cells* **2018**, *176*, 397.

[211]   C. Wang, S. Ni, S. Braun, M. Fahlman, X. Liu, *J. Mater. Chem. C* **2019**, *7*, 879.

[212]   C. Bracher, H. Yi, N. W. Scarratt, R. Masters, A. J. Pearson, C. Rodenburg, A. Iraqi, D. G. Lidzey, *Organic Electronics* **2015**, *27*, 266.

[213]   A. Saeki, M. Tsuji, S. Seki, *Advanced Energy Materials* **2011**, *1*, 661.

[214]   J. Yuan, Y. Zhang, L. Zhou, G. Zhang, H.-L. Yip, T.-K. Lau, X. Lu, C. Zhu, H. Peng, P. A. Johnson, M. Leclerc, Y. Cao, J. Ulanski, Y. Li, Y. Zou, *Joule* **2019**, *3*, 1140.

[215]   A. Karki, J. Vollbrecht, A. L. Dixon, N. Schopp, M. Schrock, G. N. M. Reddy, T.-Q. Nguyen, *Advanced Materials* **2019**, *31*, 1903868.

[216]   A. Karki, J. Vollbrecht, A. J. Gillett, S. S. Xiao, Y. Yang, Z. Peng, N. Schopp, A. L. Dixon, S. Yoon, M. Schrock, H. Ade, G. N. M. Reddy, R. H. Friend, T.-Q. Nguyen, *Energy Environ. Sci.* **2020**, 10.1039.D0EE01896A.

[217]   H. Yao, Y. Cui, R. Yu, B. Gao, H. Zhang, J. Hou, *Angewandte Chemie International Edition* **2017**, *56*, 3045.

[218]   A. Karki, J. Vollbrecht, A. J. Gillett, P. Selter, J. Lee, Z. Peng, N. Schopp, A. L. Dixon, M. Schrock, V. Nádaždy, F. Schauer, H. Ade, B. F. Chmelka, G. C. Bazan, R. H. Friend, T.-Q. Nguyen, *Advanced Energy Materials* **2020**, *10*, 2001203.

[219]   N. A. Ran, J. A. Love, M. C. Heiber, X. Jiao, M. P. Hughes, A. Karki, M. Wang, V. V. Brus, H. Wang, D. Neher, others, *Advanced Energy Materials* **2018**, *8*, 1701073.

[220]   B. A. Collins, Z. Li, J. R. Tumbleston, E. Gann, C. R. McNeill, H. Ade, *Advanced Energy Materials* **2013**, *3*, 65.

[221]   L. Ye, H. Hu, M. Ghasemi, T. Wang, B. A. Collins, J.-H. Kim, K. Jiang, J. H. Carpenter, H. Li, Z. Li, T. McAfee, J. Zhao, X. Chen, J. L. Y. Lai, T. Ma, J.-L. Bredas, H. Yan, H. Ade, *Nature Materials* **2018**, *17*, 253.

[222]   X. Jiao, L. Ye, H. Ade, *Advanced Energy Materials* **2017**, *7*, 1700084.

[223]   J. A. Love, C. M. Proctor, J. Liu, C. J. Takacs, A. Sharenko, T. S. van der Poll, A. J. Heeger, G. C. Bazan, T.-Q. Nguyen, *Advanced Functional Materials* **2013**, *23*, 5019.

[224]   F. Zhao, C. Wang, X. Zhan, *Advanced Energy Materials* **2018**, *8*, 1703147.

[225]   W. Huang, E. Gann, N. Chandrasekaran, L. Thomsen, S. K. K. Prasad, J. M. Hodgkiss, D. Kabra, Y.-B. Cheng, C. R. McNeill, *Energy Environ. Sci.* **2017**, *10*, 1843.

[226]   L. Ye, S. Li, X. Liu, S. Zhang, M. Ghasemi, Y. Xiong, J. Hou, H. Ade, *Joule* **2019**, *3*, 443.

[227]   N. A. Ran, S. Roland, J. A. Love, V. Savikhin, C. J. Takacs, Y.-T. Fu, H. Li, V. Coropceanu, X. Liu, J.-L. Brédas, others, *Nature communications* **2017**, *8*, 79.

[228]   X. Song, N. Gasparini, L. Ye, H. Yao, J. Hou, H. Ade, D. Baran, *ACS Energy Letters* **2018**, *3*, 669.

[229]   D. M. Smilgies, *J Appl Crystallogr* **2009**, *42*, 1030.

[230]   T. Wang, A. J. Pearson, D. G. Lidzey, *J. Mater. Chem. C* **2013**, *1*, 7266.

[231]   Y. Lin, F. Zhao, Q. He, L. Huo, Y. Wu, T. C. Parker, W. Ma, Y. Sun, C. Wang, D. Zhu, A. J. Heeger, S. R. Marder, X. Zhan, *J. Am. Chem. Soc.* **2016**, *138*, 4955.

[232]   H. Zhang, X. Wang, L. Yang, S. Zhang, Y. Zhang, C. He, W. Ma, J. Hou, *Advanced Materials* **2017**, *29*, 1703777.

[233]   C. Lee, Y. Li, W. Lee, Y. Lee, J. Choi, T. Kim, C. Wang, E. D. Gomez, H. Y. Woo, B. J. Kim, *Macromolecules* **2016**, *49*, 5051.

[234]   F. Liu, W. Zhao, J. R. Tumbleston, C. Wang, Y. Gu, D. Wang, A. L. Briseno, H. Ade, T. P. Russell, *Advanced Energy Materials* **2014**, *4*, 1301377.

[235]   K. Celebi, P. J. Jadhav, K. M. Milaninia, M. Bora, M. A. Baldo, *Appl. Phys. Lett.* **2008**, *93*, 083308.

[236]   H. Bässler, *physica status solidi (b)* **1993**, *175*, 15.

[237]   C. M. Proctor, C. Kim, D. Neher, T.-Q. Nguyen, *Advanced Functional Materials* **2013**, *23*, 3584.

[238]   D. Credgington, F. C. Jamieson, B. Walker, T.-Q. Nguyen, J. R. Durrant, *Advanced Materials* **2012**, *24*, 2135.

[239]   G. F. A. Dibb, F. C. Jamieson, A. Maurano, J. Nelson, J. R. Durrant, *J. Phys. Chem. Lett.* **2013**, *4*, 803.

[240]   F. Laquai, D. Andrienko, C. Deibel, D. Neher, in *Elementary Processes in Organic Photovoltaics* (Ed.: K. Leo), Springer International Publishing, Cham, **2017**, pp. 267–291.

[241]   N. Schopp, V. Brus*, J. Lee, G. C. Bazan, T.-Q. Nguyen*, *Advanced Energy Materials* **2020**, DOI 10.1002/aenm.202002760.

[242]   V. Arkhipov, E. Emelianova, H. Bässler, *Phys. Rev. B* **2004**, *70*, 205205.

[243]   O. V. Mikhnenko, P. W. M. Blom, T.-Q. Nguyen, *Energy & Environmental Science* **2015**, *8*, 1867.

[244]   N. Schopp, V. V. Brus, T.-Q. Nguyen, *Advanced Optical Materials* **2021**, *9*, 2001484.

[245]   C. M. Proctor, S. Albrecht, M. Kuik, D. Neher, T.-Q. Nguyen, *Advanced Energy Materials* **2014**, *4*, 1400230.

[246]   I. A. Howard, R. Mauer, M. Meister, F. Laquai, *Journal of the American Chemical Society* **2010**, *132*, 14866.

[247]   C. M. Proctor, C. Kim, D. Neher, T.-Q. Nguyen, *Advanced Functional Materials* **2013**, *23*, 3584.

[248]   B. Y. Finck, B. J. Schwartz, *Phys. Rev. Applied* **2015**, *4*, 034006.

[249]   Y. Zou, R. J. Holmes, *Advanced Energy Materials* **2015**, *5*, 1500019.

[250]   S. Albrecht, J. R. Tumbleston, S. Janietz, I. Dumsch, S. Allard, U. Scherf, H. Ade, D. Neher, *J. Phys. Chem. Lett.* **2014**, *5*, 1131.

[251]   V. D. Mihailetchi, J. Wildeman, P. W. M. Blom, *Phys. Rev. Lett.* **2005**, *94*, 126602.

[252]   M. Kuik, G.-J. A. H. Wetzelaer, H. T. Nicolai, N. I. Craciun, D. M. D. Leeuw, P. W. M. Blom, *Advanced Materials* **2014**, *26*, 512.

[253]   V. V. Brus, H. K. Lee, C. M. Proctor, M. Ford, X. Liu, M. A. Burgers, J. Lee, G. C. Bazan, T.-Q. Nguyen, *Advanced Energy Materials* **2018**, *8*, 1801807.

[254]   K. Hecht, *Zeitschrift fuer Physik* **1932**, *77*, 235.

[255]   E. Gann, A. T. Young, B. A. Collins, H. Yan, J. Nasiatka, H. A. Padmore, H. Ade, A. Hexemer, C. Wang, *Review of Scientific Instruments* **2012**, *83*, 045110.

[256]   A. R. Zanatta, I. Chambouleyron, *Phys. Rev. B* **1996**, *53*, 3833.

[257]   F. Urbach, *Phys. Rev.* **1953**, *92*, 1324.

[258]   A. Karki, G.-J. A. Wetzelaer, G. N. M. Reddy, V. Nádaždy, M. Seifrid, F. Schauer, G. C. Bazan, B. F. Chmelka, P. W. Blom, T.-Q. Nguyen, *Advanced Functional Materials* **2019**, *29*, 1901109.

[259]   Ю. И. Уханов, *Оптические Свойства Полупроводников (Optical Properties of Semiconductors)*, ИЗДАТЕЛЬСТВО НАУКА (Nauka), Moscow, **1977**.

[260]   S. Park, S. W. Heo, W. Lee, D. Inoue, Z. Jiang, K. Yu, H. Jinno, D. Hashizume, M. Sekino, T. Yokota, K. Fukuda, K. Tajima, T. Someya, *Nature* **2018**, *561*, 516.

[261]   F. C. Krebs, *Solar Energy Materials and Solar Cells* **2009**, *93*, 394.

[262]   W. Chen, Q. Zhang, *J. Mater. Chem. C* **2017**, *5*, 1275.

[263]   Y. Cui, H. Yao, J. Zhang, T. Zhang, Y. Wang, L. Hong, K. Xian, B. Xu, S. Zhang, J. Peng, Z. Wei, F. Gao, J. Hou, *Nature Communications* **2019**, *10*, 1.

[264]   W. Qarony, M. I. Hossain, V. Jovanov, D. Knipp, Y. H. Tsang, *Appl Nanosci* **2018**, *8*, 339.

[265]   C. Deibel, T. Strobel, V. Dyakonov, *Advanced Materials* **2010**, *22*, 4097.

[266]   S. Shoaee, M. Stolterfoht, D. Neher, *Advanced Energy Materials* **2018**, *8*, 1703355.

[267]   J. D. Servaites, B. M. Savoie, J. B. Brink, T. J. Marks, M. A. Ratner, *Energy Environ. Sci.* **2012**, *5*, 8343.

[268]   S. De, T. Pascher, M. Maiti, K. G. Jespersen, T. Kesti, F. Zhang, O. Inganäs, A. Yartsev, V. Sundström, *J. Am. Chem. Soc.* **2007**, *129*, 8466.

[269]   J. Kurpiers, D. Neher, *Scientific Reports* **2016**, *6*, 1.

[270]   A. F. Nogueira, I. Montanari, J. Nelson, J. R. Durrant, C. Winder, N. S. Sariciftci, C. Brabec, *J. Phys. Chem. B* **2003**, *107*, 1567.

[271]   R. A. Street, M. Schoendorf, A. Roy, J. H. Lee, *Phys. Rev. B* **2010**, *81*, 205307.

[272]   L. G. Gerling, S. Mahato, S. Galindo, C. Voz, J. Puigdollers, R. Alcubilla, J. M. Asensi, in *2015 10th Spanish Conference on Electron Devices (CDE)*, **2015**, pp. 1–4.

[273]   S. Miyajima, K. Imagawa, M. Matsumoto, *Med Phys* **2002**, *29*, 1421.

[274]   A. Ruzin, Y. Nemirovsky, *Journal of Applied Physics* **1997**, *82*, 4166.

[275] J. Lee, S.-J. Ko, M. Seifrid, H. Lee, B. R. Luginbuhl, A. Karki, M. Ford, K. Rosenthal, K. Cho, T.-Q. Nguyen, G. C. Bazan, *Advanced Energy Materials* **2018**, *8*, 1801212.

[276] D. W. Sievers, V. Shrotriya, Y. Yang, *Journal of Applied Physics* **2006**, *100*, 114509.

[277] W.E. Mueller, *Phys. kondens. Materie* **1967**, *6*, 243.

[278] A. D. Rakić, *Appl. Opt.* **1995**, *34*, 4755.

[279] C.-W. Chen, S.-Y. Hsiao, C.-Y. Chen, H.-W. Kang, Z.-Y. Huang, H.-W. Lin, *J. Mater. Chem. A* **2015**, *3*, 9152.

[280] D. Baran, N. Gasparini, A. Wadsworth, C. H. Tan, N. Wehbe, X. Song, Z. Hamid, W. Zhang, M. Neophytou, T. Kirchartz, C. J. Brabec, J. R. Durrant, I. McCulloch, *Nat Commun* **2018**, *9*, 1.

[281] D. Credgington, F. C. Jamieson, B. Walker, T.-Q. Nguyen, J. R. Durrant, *Advanced Materials* **2012**, *24*, 2135.

[282] D. Rauh, C. Deibel, V. Dyakonov, *Advanced Functional Materials* **2012**, *22*, 3371.

[283] T. Zhang, R. J. Holmes, *Journal of Materials Chemistry C* **2017**, *5*, 11885.

[284] W. H. Lee, S. Y. Chuang, H. L. Chen, W. F. Su, C. H. Lin, *Thin Solid Films* **2010**, *518*, 7450.

[285] M. Kaltenbrunner, M. S. White, E. D. Głowacki, T. Sekitani, T. Someya, N. S. Sariciftci, S. Bauer, *Nature Communications* **2012**, *3*, 770.

[286] Y.-X. Zhang, J. Fang, W. Li, Y. Shen, J.-D. Chen, Y. Li, H. Gu, S. Pelivani, M. Zhang, Y. Li, J.-X. Tang, *ACS Nano* **2019**, *13*, 4686.

[287] K.-W. Seo, J. Lee, J. Jo, C. Cho, J.-Y. Lee, *Advanced Materials* **2019**, *31*, 1902447.

[288] A. A. F. Husain, W. Z. W. Hasan, S. Shafie, M. N. Hamidon, S. S. Pandey, *Renewable and Sustainable Energy Reviews* **2018**, *94*, 779.

[289] K. Kapsis, A. K. Athienitis, *Solar Energy* **2015**, *115*, 120.

[290] Z. Ding, V. Stoichkov, M. Horie, E. Brousseau, J. Kettle, *Solar Energy Materials and Solar Cells* **2016**, *157*, 305.

[291] R. R. Lunt, *Appl. Phys. Lett.* **2012**, *101*, 043902.

[292] R. R. Lunt, V. Bulovic, *Appl. Phys. Lett.* **2011**, *98*, 113305.

[293] J. Wang, S. Xie, D. Zhang, R. Wang, Z. Zheng, H. Zhou, Y. Zhang, *J. Mater. Chem. A* **2018**, *6*, 19934.

[294] X. Li, H. Huang, H. Bin, Z. Peng, C. Zhu, L. Xue, Z.-G. Zhang, Z. Zhang, H. Ade, Y. Li, *Chemistry of Materials* **2017**, *29*, 10130.

[295] V. V. Brus, *Organic Electronics* **2016**, *29*, 1.

[296] G. F. Burkhard, E. T. Hoke, M. D. McGehee, *Advanced Materials* **2010**, *22*, 3293.

[297] "RefractiveIndex.INFO," can be found under https://refractiveindex.info, **2020**.

[298] J. Schwiegerling, in *Field Guide to Visual and Ophthalmic Optics*, SPIE, **2004**.

[299] R. Xia, C. J. Brabec, H.-L. Yip, Y. Cao, *Joule* **2019**, *3*, 2241.

[300] C. M. Proctor, T.-Q. Nguyen, *Applied Physics Letters* **2015**, *106*, 23_1.

[301] A. K. K. Kyaw, D. H. Wang, C. Luo, Y. Cao, T.-Q. Nguyen, G. C. Bazan, A. J. Heeger, *Advanced Energy Materials* **2014**, *4*, 1301469.

[302] G. Canning, A. K. Thomas, D. H. Dunlap, J. K. Grey, *ACS Appl. Mater. Interfaces* **2018**, *10*, 19853.

[303] Z. Yin, J. Wei, Q. Zheng, *Advanced Science* **2016**, *3*, 1500362.

[304] V. V. Brus, *Solar Energy* **2012**, *86*, 786.

[305] X. Wang, L. Zhi, K. Müllen, *Nano Lett.* **2008**, *8*, 323.

[306] J. Wu, H. A. Becerril, Z. Bao, Z. Liu, Y. Chen, P. Peumans, *Appl. Phys. Lett.* **2008**, *92*, 263302.

[307] V. V. Brus, M. A. Gluba, X. Zhang, K. Hinrichs, J. Rappich, N. H. Nickel, *physica status solidi (a)* **2014**, *211*, 843.

[308] S. Dongaonkar, J. D. Servaites, G. M. Ford, S. Loser, J. Moore, R. M. Gelfand, H. Mohseni, H. W. Hillhouse, R. Agrawal, M. A. Ratner, T. J. Marks, M. S. Lundstrom, M. A. Alam, *Journal of Applied Physics* **2010**, *108*, 124509.

[309] K. H. Wong, K. Ananthanarayanan, M. D. Heinemann, J. Luther, P. Balaya, *Solar Energy* **2012**, *86*, 3190.

[310] J. D. Servaites, M. A. Ratner, T. J. Marks, *Energy & Environmental Science* **2011**, *4*, 4410.

[311] H. Hoppe, J. Bachmann, B. Muhsin, K.-H. Drüe, I. Riedel, G. Gobsch, C. Buerhop-Lutz, C. J. Brabec, V. Dyakonov, *Journal of Applied Physics* **2010**, *107*, 014505.

[312] S. M. Sze, K. K. Ng, *Physics of Semiconductor Devices*, John Wiley & Sons, **2006**.

[313] A. L. Fahrenbruch, R. H. Bube, *Fundamentals of Solar Cells: Photovoltaic Solar Energy Conversion*, Academic Press, **1983**.

[314] R. R. Lunt, *Applied Physics Letters* **2012**, *101*, 043902.

[315] Y. Li, G. Xu, C. Cui, Y. Li, *Advanced Energy Materials* **2018**, *8*, 1701791.

[316] Y. Park, L. Bormann, L. Müller-Meskamp, K. Vandewal, K. Leo, *Organic Electronics* **2016**, *36*, 68.

[317] S. Zhang, Y. Qin, J. Zhu, J. Hou, *Advanced Materials* **2018**, *30*, 1800868.

[318] Y. Cui, H. Yao, J. Zhang, K. Xian, T. Zhang, L. Hong, Y. Wang, Y. Xu, K. Ma, C. An, C. He, Z. Wei, F. Gao, J. Hou, *Advanced Materials* **2020**, *32*, 1908205.

[319] M. Seifrid, G. C. Bazan, J. Lee, T.-Q. Nguyen, B. Luginbuhl, S.-J. Ko, *Narrow Bandgap Non-Fullerene Acceptors and Devices Including Narrow Bandgap Non-Fullerene Acceptors*, Google Patents, **2019**.

[320]   J. Chen, G. Li, Q. Zhu, X. Guo, Q. Fan, W. Ma, M. Zhang, *Journal of Materials Chemistry A* **2019**, *7*, 3745.

[321]   G. Kim, H. Kim, M. Jang, Y. Kyung Jung, J. Hak Oh, C. Yang, *Journal of Materials Chemistry C* **2016**, *4*, 9554.

[322]   D. Liu, T. Wang, X. Ke, N. Zheng, Z. Chang, Z. Xie, Y. Liu, *Materials Chemistry Frontiers* **2019**, *3*, 2157.

[323]   H. Xu, Y. Yang, C. Zhong, X. Zhan, X. Chen, *Journal of Materials Chemistry A* **2018**, *6*, 6393.

[324]   J. H. Kim, A. Liess, M. Stolte, A.-M. Krause, V. Stepanenko, C. Zhong, D. Bialas, F. Spano, F. Würthner, *Advanced Materials* **2021**, *33*, 2100582.

[325]   N. Schopp, V. V. Brus, T.-Q. Nguyen, *Advanced Optical Materials* **2021**, *9*, 2001484.

[326]   J. Huang, J. Lee, M. Schrock, A. L. Dixon, A. T. Lill, K. Cho, G. C. Bazan, T.-Q. Nguyen, *Mater. Horiz.* **2020**, *7*, 3234.

[327]   J. Lee, S.-J. Ko, H. Lee, J. Huang, Z. Zhu, M. Seifrid, J. Vollbrecht, V. V. Brus, A. Karki, H. Wang, K. Cho, T.-Q. Nguyen, G. C. Bazan, *ACS Energy Lett.* **2019**, *4*, 1401.

[328]   S. Bi, X. Leng, Y. Li, Z. Zheng, X. Zhang, Y. Zhang, H. Zhou, *Advanced Materials* **2019**, *31*, 1805708.

[329]   T. Yang, M. Wang, C. Duan, X. Hu, L. Huang, J. Peng, F. Huang, X. Gong, *Energy Environ. Sci.* **2012**, *5*, 8208.

[330]   B. Xiao, H. Wu, Y. Cao, *Materials Today* **2015**, *18*, 385.

[331]   H. Choi, C.-K. Mai, H.-B. Kim, J. Jeong, S. Song, G. C. Bazan, J. Y. Kim, A. J. Heeger, *Nat Commun* **2015**, *6*, 7348.

[332]   H. Zhou, Y. Zhang, C.-K. Mai, J. Seifter, T.-Q. Nguyen, G. C. Bazan, A. J. Heeger, *ACS Nano* **2015**, *9*, 371.

[333]   H. Zhou, Y. Zhang, C.-K. Mai, S. D. Collins, G. C. Bazan, T.-Q. Nguyen, A. J. Heeger, *Advanced Materials* **2015**, *27*, 1767.

[334]   S. Moon, S. Khadtare, M. Wong, S.-H. Han, G. C. Bazan, H. Choi, *Journal of Colloid and Interface Science* **2018**, *518*, 21.

[335]   N. Schopp, T.-Q. Nguyen, V. V. Brus, *ACS Appl. Mater. Interfaces* **2021**, *13*, 27217.

[336]   V. D. Mihailetchi, P. W. M. Blom, J. C. Hummelen, M. T. Rispens, *Journal of Applied Physics* **2003**, *94*, 6849.

[337]   G. Lakhwani, A. Rao, R. H. Friend, *Annual Review of Physical Chemistry* **2014**, *65*, 557.

[338]   V. Coropceanu, J.-L. Brédas, S. Mehraeen, *J. Phys. Chem. C* **2017**, *121*, 24954.

[339]   L. Schmidt-Mende, J. L. MacManus-Driscoll, *Materials Today* **2007**, *10*, 40.

[340]   L. Nian, W. Zhang, S. Wu, L. Qin, L. Liu, Z. Xie, H. Wu, Y. Ma, *ACS Appl. Mater. Interfaces* **2015**, *7*, 25821.

[341]   E. Cieplechowicz, R. Munir, M. A. Anderson, E. L. Ratcliff, G. C. Welch, *ACS Appl. Mater. Interfaces* **2021**, *13*, 49096.

[342]   M. Abd-Ellah, J. Cann, S. V. Dayneko, A. Laventure, E. Cieplechowicz, G. C. Welch, *ACS Appl. Electron. Mater.* **2019**, *1*, 1590.

[343]   C.-K. Mai, R. A. Schlitz, G. M. Su, D. Spitzer, X. Wang, S. L. Fronk, D. G. Cahill, M. L. Chabinyc, G. C. Bazan, *J. Am. Chem. Soc.* **2014**, *136*, 13478.

[344]   C. Yan, S. Barlow, Z. Wang, H. Yan, A. K.-Y. Jen, S. R. Marder, X. Zhan, *Nature Reviews Materials* **2018**, *3*, 18003.

[345]   J. Ajayan, D. Nirmal, P. Mohankumar, M. Saravanan, M. Jagadesh, L. Arivazhagan, *Superlattices and Microstructures* **2020**, *143*, 106549.

[346]   C. J. Brabec, A. Distler, X. Du, H.-J. Egelhaaf, J. Hauch, T. Heumueller, N. Li, *Advanced Energy Materials* **2020**, *10*, 2001864.

[347] D. Corzo, E. Bihar, E. B. Alexandre, D. Rosas-Villalva, D. Baran, *Advanced Functional Materials* **2021**, *31*, 2005763.

[348] Z. Du, M. Mainville, J. Vollbrecht, A. L. Dixon, N. Schopp, M. Schrock, Z. Peng, J. Huang, S. Chae, H. Ade, M. Leclerc, G. N. M. Reddy, T.-Q. Nguyen, *Solar RRL* **2021**, *5*, 2100213.

[349] C. J. Traverse, R. Pandey, M. C. Barr, R. R. Lunt, *Nature Energy* **2017**, *2*, 849.

[350] Z. Hu, J. Wang, X. Ma, J. Gao, C. Xu, K. Yang, Z. Wang, J. Zhang, F. Zhang, *Nano Energy* **2020**, *78*, 105376.

[351] A. A. F. Husain, W. Z. W. Hasan, S. Shafie, M. N. Hamidon, S. S. Pandey, *Renewable and Sustainable Energy Reviews* **2018**, *94*, 779.

[352] S.-Y. Chang, P. Cheng, G. Li, Y. Yang, *Joule* **2018**, *2*, 1039.

[353] Z.-C. Wen, H. Yin, X.-T. Hao, *Surfaces and Interfaces* **2021**, *23*, 100921.

[354] J. Hou, O. Inganäs, R. H. Friend, F. Gao, *Nature Materials* **2018**, *17*, 119.

[355] L. Ma, S. Zhang, J. Wang, Y. Xu, J. Hou, *Chemical Communications* **2020**, *56*, 14337.

[356] C. Tuchinda, S. Srivannaboon, H. W. Lim, *Journal of the American Academy of Dermatology* **2006**, *54*, 845.

[357] Z. Hu, Z. Wang, F. Zhang, *Journal of Materials Chemistry A* **2019**, *7*, 7025.

[358] C. Xu, K. Jin, Z. Xiao, Z. Zhao, X. Ma, X. Wang, J. Li, W. Xu, S. Zhang, L. Ding, F. Zhang, *Advanced Functional Materials* **2021**, *31*, 2107934.

[359] N. Yao, Y. Xia, Y. Liu, S. Chen, M. P. Jonsson, F. Zhang, *ACS Appl. Energy Mater.* **2021**, *4*, 14335.

[360] Z. Hu, J. Wang, Z. Wang, W. Gao, Q. An, M. Zhang, X. Ma, J. Wang, J. Miao, C. Yang, F. Zhang, *Nano Energy* **2019**, *55*, 424.

[361] X. Ma, Z. Xiao, Q. An, M. Zhang, Z. Hu, J. Wang, L. Ding, F. Zhang, *J. Mater. Chem. A* **2018**, *6*, 21485.

235

[362]   Z. Hu, J. Wang, X. Ma, J. Gao, C. Xu, X. Wang, X. Zhang, Z. Wang, F. Zhang, *J. Mater. Chem. A* **2021**, *9*, 6797.

[363]   S. Choi, Y. Zhou, W. Haske, J. W. Shim, C. Fuentes-Hernandez, B. Kippelen, *Organic Electronics* **2015**, *17*, 349.

[364]   S. Strohm, F. Machui, S. Langner, P. Kubis, N. Gasparini, M. Salvador, I. McCulloch, H.-J. Egelhaaf, C. J. Brabec, *Energy Environ. Sci.* **2018**, *11*, 2225.

[365]   T. Jiang, G. Zhang, R. Xia, J. Huang, X. Li, M. Wang, H.-L. Yip, Y. Cao, *Materials Today Energy* **2021**, *21*, 100807.

[366]   Z. Hu, Z. Wang, Q. An, F. Zhang, *Science Bulletin* **2020**, *65*, 131.

[367]   C. Yang, M. Moemeni, M. Bates, W. Sheng, B. Borhan, R. R. Lunt, *Advanced Optical Materials* **2020**, *8*, 1901536.

[368]   C.-C. Chen, L. Dou, R. Zhu, C.-H. Chung, T.-B. Song, Y. B. Zheng, S. Hawks, G. Li, P. S. Weiss, Y. Yang, *ACS Nano* **2012**, *6*, 7185.

[369]   Y. Li, C. He, L. Zuo, F. Zhao, L. Zhan, X. Li, R. Xia, H.-L. Yip, C.-Z. Li, X. Liu, H. Chen, *Advanced Energy Materials* **2021**, *11*, 2003408.

[370]   J. Kublitski, A. Hofacker, B. K. Boroujeni, J. Benduhn, V. C. Nikolis, C. Kaiser, D. Spoltore, H. Kleemann, A. Fischer, F. Ellinger, K. Vandewal, K. Leo, *Nat Commun* **2021**, *12*, 551.

[371]   G. Simone, M. J. Dyson, C. H. L. Weijtens, S. C. J. Meskers, R. Coehoorn, R. A. J. Janssen, G. H. Gelinck, *Advanced Optical Materials* **2020**, *8*, 1901568.

[372]   D. Rauh, A. Wagenpfahl, C. Deibel, V. Dyakonov, *Appl. Phys. Lett.* **2011**, *98*, 133301.

[373]   S. M. Sze, K. K. Ng, *Physics of Semiconductor Devices*, John Wiley & Sons, **2006**.

[374]   K. Wang, S. Dong, K. Zhang, Z. Li, J. Huang, M. Wang, *Organic Electronics* **2021**, *99*, 106319.

[375]   M. B. Upama, M. Wright, N. K. Elumalai, M. A. Mahmud, D. Wang, C. Xu, A. Uddin, *ACS Photonics* **2017**, *4*, 2327.

[376]   G. Sun, M. Shahid, Z. Fei, S. Xu, F. D. Eisner, T. D. Anthopolous, M. A. McLachlan, M. Heeney, *Mater. Chem. Front.* **2019**, *3*, 450.

[377]   W. Yu, X. Jia, Y. Long, L. Shen, Y. Liu, W. Guo, S. Ruan, *ACS Appl. Mater. Interfaces* **2015**, *7*, 9920.

[378]   G. Ji, Y. Wang, Q. Luo, K. Han, M. Xie, L. Zhang, N. Wu, J. Lin, S. Xiao, Y.-Q. Li, L.-Q. Luo, C.-Q. Ma, *ACS Appl. Mater. Interfaces* **2018**, *10*, 943.

[379]   M. Koppitz, E. Wegner, T. Rödlmeier, A. Colsmann, *Energy Technology* **2018**, *6*, 1275.

[380]   H. Park, J.-H. Lee, S. Lee, S. Y. Jeong, J. W. Choi, C.-L. Lee, J.-H. Kim, K. Lee, *ACS Appl. Mater. Interfaces* **2020**, *12*, 2276.

[381]   M. M. Tavakoli, R. Po, G. Bianchi, A. Cominetti, C. Carbonera, N. Camaioni, F. Tinti, J. Kong, *PNAS* **2019**, *116*, 22037.

[382]   B. Jia, S. Dai, Z. Ke, C. Yan, W. Ma, X. Zhan, *Chem. Mater.* **2018**, *30*, 239.

[383]   Z. Yin, J. Wei, S.-C. Chen, D. Cai, Y. Ma, M. Wang, Q. Zheng, *J. Mater. Chem. A* **2017**, *5*, 3888.

[384]   Y. Q. Wong, H.-F. Meng, H. Y. Wong, C. S. Tan, C.-Y. Wu, P.-T. Tsai, C.-Y. Chang, S.-F. Horng, H.-W. Zan, *Organic Electronics* **2017**, *43*, 196.

[385]   Y. Zhang, Z. Peng, C. Cai, Z. Liu, Y. Lin, W. Zheng, J. Yang, L. Hou, Y. Cao, *J. Mater. Chem. A* **2016**, *4*, 11821.

[386]   Y. Song, S. Chang, S. Gradecak, J. Kong, *Advanced Energy Materials* **2016**, *6*, 1600847.

[387]   J. Min, C. Bronnbauer, Z.-G. Zhang, C. Cui, Y. N. Luponosov, I. Ata, P. Schweizer, T. Przybilla, F. Guo, T. Ameri, K. Forberich, E. Spiecker, P. Bäuerle, S. A. Ponomarenko, Y. Li, C. J. Brabec, *Advanced Functional Materials* **2016**, *26*, 4543.

[388] G. Xu, L. Shen, C. Cui, S. Wen, R. Xue, W. Chen, H. Chen, J. Zhang, H. Li, Y. Li, Y. Li, *Advanced Functional Materials* **2017**, *27*, 1605908.

[389] X. Li, H. Meng, F. Shen, D. Su, S. Huo, J. Shan, J. Huang, C. Zhan, *Dyes and Pigments* **2019**, *166*, 196.